AFRL-SR-BL-TR-98-
0494

1997

Technical

Digest Series

Volume 9

Quantum Optoelectronics

Technical Digest

DISTRIBUTION STATEMENT A
Approved for public release;
Distribution Unlimited

March 19–21, 1997

Hyatt Regency Lake Tahoe
Incline Village, Nevada

Postconference Edition

1997 OSA Technical Digest Series

Vol. 1 VISION SCIENCE AND ITS APPLICATIONS
Santa Fe, NM (January)
List Price $92 Member Price $60

Vol. 2 CHEMISTRY AND PHYSICS OF SMALL STRUCTURES
Santa Fe, NM (February)
List Price $66 Member Price $43

Vol. 3 FOURIER TRANSFORM SPECTROSCOPY
Santa Fe, NM (February)
List Price $66 Member Price $43

Vol. 4 LIGHT AND COLOR IN THE OPEN AIR
Santa Fe, NM (February)
List Price $66 Member Price $43

Vol. 5 OPTICAL REMOTE SENSING OF THE ATMOSPHERE
Santa Fe, NM (February)
List Price $92 Member Price $60

Vol. 6 OPTICAL FIBER COMMUNICATION CONFERENCE (OFC)
Dallas, TX (February)
List Price $92 Member Price $60

Vol. 7 APPLICATIONS OF HIGH FIELD AND SHORT WAVELENGTH SOURCES
Santa Fe, NM (March)
List Price $75 Member Price $48

Vol. 8 OPTICS IN COMPUTING
Lake Tahoe, NV (March)
List Price $75 Member Price $48

Vol. 9 QUANTUM OPTOELECTRONICS
Lake Tahoe, NV (March)
List Price $75 Member Price $48

Vol. 10 PHOTONICS IN SWITCHING
Stockholm, Sweden (April)
List Price $75 Member Price $48

Vol. 11 CONFERENCE ON LASERS AND ELECTRO-OPTICS (CLEO)
Baltimore, MD (May)
List Price $92 Member Price $60

Vol. 12 QUANTUM ELECTRONICS AND LASER SCIENCE CONFERENCE (QELS)
Baltimore, MD (May)
List Price $92 Member Price $60

Vol. 13 NONASTRONOMICAL ADAPTIVE OPTICS
Munich, Germany (June)
List Price $75 Member Price $48

Vol 14 ORGANIC THIN FILMS
Long Beach, CA (October)
List Price $75 Member Price $48

Vol. 15 LASERS IN DERMATOLOGY
Long Beach, CA (October)
List Price $75 Member Price $48

Vol. 16 OPTICAL FIBER SENSORS
Williamsburg, VA (October)
List Price $75 Member Price $48

Vol. 17 BRAGG GRATINGS, PHOTOSENSITIVITY, AND POLING IN GLASS FIBERS AND WAVEGUIDES: APPLICATIONS AND FUNDAMENTALS
Williamsburg, VA (October)
List Price $75 Member Price $48

Also: EIGHTH EUROPEAN CONFERENCE ON INTEGRATED OPTICS (ECIO)
Stockholm, Sweden (April)
List Price $75 Member Price $48

SOLID STATE LASERS MATERIALS AND APPLICATIONS
Tianjin, People's Republic of China (July)
List Price $75 Member Price $48

Order by mail, phone, fax, or Internet

OSA Customer Service, 2010 Massachusetts Ave. NW, Washington DC 20036-1023
Phone 202/416-1907 ■ Fax 202/416-6140 ■ E-mail: Cust.serv@osa.org

OSA
Optical Society of America

Quantum Optoelectronics

March 19–21, 1997
Hyatt Regency Lake Tahoe
Incline Village, Nevada

POSTCONFERENCE EDITION

Sponsored and managed by
Optical Society of America

Optical Society of America
2010 Massachusetts Avenue NW
Washington DC 20036-1023

Articles in this publication may be cited in other publications. To facilitate access to the original publication source, the following form for the citation is suggested:

Name of Author(s), "Title of Paper," in *Quantum Optoelectronics*, Vol. 9, 1997 OSA Technical Digest Series (Optical Society of America, Washington DC, 1997), pp. xx-xx.

Optical Society of America

ISBN

Conference Edition	1-55752-492-0
Postconference Edition	1-55752-493-9
(Note: Postconference Edition includes postdeadline papers.)	
1997 Technical Digest Series	1-55752-485-8

Library of Congress Catalog Card Number

Conference Edition	97-65499
Postconference Edition	97-65500

Copyright © 1997, Optical Society of America

Individual readers of this digest and libraries acting for them are permitted to make fair use of the material in it, such as to copy an article for use in teaching or research, without payment of fee, provided that such copies are not sold. Copying for sale is subject to payment of copying fees. The code 1-55752-485-8/97/$6.00 gives the per-article copying fee for each copy of the article made beyond the free copying permitted under Sections 107 and 108 of the U.S. Copyright Law. The fee should be paid through the Copyright Clearance Center, Inc., 21 Congress Street, Salem, MA 01970.

Permission is granted to quote excerpts from articles in this digest in scientific works with the customary acknowledgment of the source, including the author's name and the name of the digest, page, year, and name of the Society. Reproduction of figures and tables is likewise permitted in other articles and books provided that the same information is printed with them and notification is given to the Optical Society of America. In addition, the Optical Society may require that permission also be obtained from one of the authors. Address inquiries and notices to Director of Publications, Optical Society of America, 2010 Massachusetts Avenue, NW, Washington, DC 20036-1023. In the case of articles whose authors are employees of the United States Government or its contractors or grantees, the Optical Society of America recognizes the right of the United States Government to retain a nonexclusive, royalty free license to use the author's copyrighted article for United States Government purposes.

Printed in the U.S.A.

Contents

QUANTUM OPTOELECTRONICS
TECHNICAL PROGRAM COMMITTEE

Wayne Knox, *Bell Laboratories, Lucent Technologies, General Co-Chair*
Jurgen Kuhl, *Max-Planck Institut, Stuttgart, Germany, General Co-Chair*
Kohroh Kobayashi, *NEC Corporation, Japan, General Co-Chair*
Philippe Fauchet, *University of Rochester, Program Co-Chair*
Shigehisa Arai, *Tokyo Institute of Technology, Japan*
Yasuhiko Arakawa, *University of Tokyo, Japan*
Israel Bar-Joseph, *Weizmann Institute of Science, Israel*
Moungi Bawendi, *Massachusetts Institute of Technology*
David Citrin, *Washington State University*
Jochen Feldmann, *Ludwig-Maximilians Universitat, Munich, Germany*
Steve Forrest, *Princeton University*
Manuel Joffre, *ENSTA-Ecole Polytechnique, France*
Jacob Khurgin, *Johns Hopkins University*
Jerry Meyer, *U.S. Naval Research Laboratory*
John Ryan, *Oxford University, U.K.*
Arthur Smirl, *University of Iowa*
Toshihide Takagahara, *NTT Basic Research Laboratories, Japan*

SALON A

1:30pm–3:00pm

QWA • Microcavity Lasers and Quantum Dots

Kenichi Iga, *Tokyo Institute of Technology, Japan, Presider*

1:30pm (Invited)

QWA1 • Practical microcavities?, Jack Jewell, *Picolight, Inc.* Abstract not available. **(p. 2)**

2:00 (Invited)

QWA2 • Vertical cavity surface emitting laser with self-assembled quantum dots, Kenichi Nishi, Hideaki Saito, Shigeo Sugou, *NEC Corp., Japan.* Continuous wave operation at room temperature has been achieved in a surface-emitting laser with ten periods of self-assembly formed quantum dot active layers. **(p. 3)**

2:30pm (Invited)

QWA3 • Optical probing of mesoscopic and nano-structures, Yasuhiko Arakawa, *Univ. Tokyo, Japan.* We investigate the dynamics of 2D electrons in mesoscopic and point-contact structures using a micro-photoluminescence probing technique. NSOM observation of photoluminescence from quantum dots is also demonstrated. **(p. 6)**

3:00pm–3:30pm

Coffee Break

SALON A

3:30pm–5:15pm

QWB • Quantum Coherence

Duncan Steel, *University of Michigan, Presider*

3:30pm

QWB1 • Quantum coherence of hole-continuum states in GaAs quantum wells, T. Dekorsy, A. M. T. Kim, G. C. Cho, S. Hunsche, H. J. Bakker, H. Kurz, *RWTH Aachen, Germany;* S. L. Chuang, *Univ. Illinois;* K. Köhler, *Fraunhofer Institut für Angewandte Festkörperphysik, Germany.* We observe quantum beats under excitation well above the fundamental excitonic transitions. The data give evidence for the intersubband coherence of continuum states in the valence band. **(p. 8)**

3:45pm

QWB2 • Interferometric four-wave-mixing spectroscopy on semiconductors, M. U. Wehner, J. Hetzler, M. Wegener, *Univ. Karlsruhe, Germany.* Interferometric four-wave-mixing spectroscopy is introduced as a sensitive tool for quantifying the influence of contributions beyond the third order perturbational limit on the nonlinear response. **(p. 11)**

4:00pm (Invited)

QWB3 • Coherent control of semiconductor optoelectronic properties, A. Haché, Y. Kostoulas, R. Atanasov, J. Fraser, J. E. Sipe, H. M. van Driel, *Univ. Toronto, Canada.* We discuss recent experiments on the use of phased laser beams to generate and control carrier density and electrical currents in unbiased GaAs via band-band transitions at room temperature. **(p. 14)**

4:30pm

QWB4 • Time-resolved amplitude and phase of coherent four-wave-mixing emission from GaAs quantum wells, Wojciech J. Walecki, David N. Fittinghoff, Arthur L. Smirl, *Univ. Iowa.* We demonstrate that spectral interferometry, in conjunction with a well-characterized reference pulse, can be used to directly determine the dynamics of both the phase and the amplitude of coherent four-wave-mixing emission from multiple quantum wells. **(p. 15)**

4:45pm

QWB5 • Excitation- and disorder-induced reduction of the superradiant excitonic decay in GaAs quantum well Bragg structures, J. Kuhl, M. Hübner, *Max-Planck-Institut für Festkörperforschung, Germany;* T. Stroucken, B. Grote, A. Knorr, S. W. Koch, *Philipps Univ., Germany;* R. Hey, K. Ploog, *Paul-Drude-Institut für Festkörperelektronik, Germany.* Geometric or energetic disorder strongly reduce the interwell radiative coupling of excitons in multiple-quantum-well Bragg samples. Excitation-induced exciton/exciton intrawell scattering supresses the superradiant decay. **(p. 18)**

5:00pm

QWB6 • Probing radial electron-hole wave-packet dynamics in quantum wells with terahertz pulses, A. Maslov, D. S. Citrin, *Washington State Univ.* Partial recurrences in the dynamics of electron-hole relative-motion wave packets under ultrafast optical excitation are predicted to be manifested in the oscillations in time-dependent coherent optical emission and induced THz absorption. **(p. 21)**

SALON A

8:30am–10:00am
QThA • Photonic Bandgaps
Eli Yablonovitch, *University of California–Los Angeles, Presider*

8:30am
QThA1 • Reflection properties and defect formation in metallic photonic crystals, Ekmel Özbay, Burak Temelkuran, *Bilkent Univ., Turkey;* M. Sigalas, G. Tuttle, C. M. Soukoulis, K. M. Ho, *Iowa State Univ.* Reflection-phase properties and a Fabry–Perot cavity analogy were used to predict defect formation in metallic photonic crystals. **(p. 26)**

8:45am
QThA2 • Observation of photonic bandgap in GaAs 2-D crystal fabricated by selective growth, Tetsuko Hamano, Hideki Hirayama, Yoshinobu Aoyagi, *The Institute of Physical and Chemical Research (RIKEN), Japan.* We have fabricated GaAs two-dimensional photonic bandgap crystals by selective growth and observed the bandgaps and their dependence on the polarizations. By the photoluminescence in the parallel direction of the substrate, discontinuous spectra were obtained as a result of bandgaps. **(p. 29)**

9:00am
QThA3 • Observation of photonic bandgap in GaInAsP/InP 2-D photonic crystals by equivalent transmission measurement, T. Baba, M. Ikeda, N. Kamizawa, *Yokohama National Univ., Japan.* We have theoretically predicted spontaneous emission control effects in 2-D photonic crystals and demonstrated a 2-D photonic bandgap in 1.55 μm GaInAsP/InP column arrays by evaluating equivalent transmission characteristics. **(p. 32)**

9:15am
QThA4 • Subwavelength multilayer binary grating design for implementing photonic crystals, Rong-Chung Tyan, Pang-Chen Sun, Yeshayahu Fainman, *Univ. California–San Diego;* Atul A. Salvekar, Hou-Pu Chou, Chuan-Cheng Cheng, Fang Xu, Axel Scherer, *California Institute of Technology.* Subwavelength multilayer binary gratings are used for design, fabrication, and testing of polarization sensitive microdevices as well as photonic crystals. **(p. 35)**

9:30am (Invited)
QThA5 • Microfabrication of photonic crystal mirrors for optoelectronic devices, A. Scherer, J. O'Brien, C. C. Cheng, O. Painter, R. Lee, A. Yariv, *Caltech;* E. Yablonovitch, *UC–Los Angeles.* We describe measurements from lasers which include two-dimensional and three-dimensional photonic crystals as end-mirrors, and show the fabrication methods used to define these "photonic crystal mirrors". **(p. 38)**

10:00am–10:30am
Coffee Break

SALON A

10:30am–12:00m
QThB • QED?
Galina Khitrova, *University of Arizona, Presider*

10:30am (Invited)
QThB1 • Quantum statistical effects of microcavity exciton polaritons, H. Cao, S. Pau, F. Tassone, R. Huang, Y. Yamamoto, *Stanford Univ.;* G. Björk, *KTH Electrum, Sweden.* We have shown two quantum statistical effects of microcavity exciton polaritons: one is the stimulated generation of exciton polaritons, the other is the biexcitonic effect. **(p. 42)**

11:00am
QThB2 • Anomalous diffusion of repulsive bosons in a two-dimensional random potential, T. Fukuzawa, *Tokyo Research Laboratory, Japan;* S. Y. Kim, T. K. Gustafson, E. E. Haller, *Univ. California–Berkeley;* E. Yamada, *Meisei Univ., Japan.* A possibility of exciton superfluidity was found in dipole-oriented two-dimensional excitons in a random potential by studying boson diffusion in energy space. **(p. 45)**

11:15am
QThB3 • Cavity-polariton formation and relaxation dynamics in semiconductor microcavities, J. D. Berger, O. Lyngnes, G. Khitrova, H. M. Gibbs, *Univ. Arizona;* S. Hallstein, *Max-Planck-Institut für Festkörperforschung, Germany;* W. W. Rühle, M. Kira, F. Jahnke, S. W. Koch, *Fachbereich Physik der Philipps-Univ., Germany.* We investigate cavity-polariton emission dynamics in a semiconductor microcavity in the strong coupling regime. A microscopic theory explains the emission properties in the context of carrier cooling observed through a normal mode coupling microcavity. **(p. 48)**

11:30am
QThB4 • Quantum mode correlations in vertical-cavity surface-emitting lasers, D. C. Kilper, P. A. Roos, J. L. Carlsten, *Montana State Univ.;* K. L. Lear, *Sandia National Laboratories.* Correlated photon-number fluctuations between two transverse modes in a microcavity laser are shown to extend below the shot-noise level, resulting in photon-number squeezed output. **(p. 51)**

11:45am
QThB5 • Fluorescence lifetimes of oriented molecules in microdroplets, M. D. Barnes, N. Lermer, W. B. Whitten, J. M. Ramsey, *Oak Ridge National Laboratory;* S. Arnold, *Polytechnic Univ.* Fluorescence lifetime measurements of molecules localized and oriented at the surface of dielectric microspheres are discussed. **(p. 54)**

12:00m–1:30pm
Lunch Break

SALON A

1:30pm–3:00pm
QThC • Postdeadline Session
Philippe M. Fauchet, *University of Rochester, Presider*

3:00pm–3:30pm
Coffee Break

SALON A

3:30pm–5:30pm
QThD • Physics in Quantum Structures
A. L. Smirl, *University of Iowa, Presider*

3:30pm (Invited)
QThD1 • Radiationless stimulated exciton emission, E. Benson, E. Fortin, *Univ. Ottawa, Canada;* A. Mysyrowicz, *LOA, ENSTA, France.* Experiments investigating the process of Bose–Einstein condensation of excitons in Cu_2O will be reviewed. The exciton flux reaching the back surface of mm-thick single crystals is investigated following creation of a high density of excitons close to the front surface with a pulsed laser. Finally, recent experimental results showing interference effects between two independent excitonic condensates will be briefly described. **(p. 58)**

4:00pm (Invited)
QThD2 • Femtosecond luminescence of semiconductor nanostructures, B. Deveaud, S. Haacke, M. Hartig, R. Ambigapathy, *EPFL-DP-IMO-LOEQ, Switzerland;* I. Bar Joseph, *Weizmann Institute, Israel;* R. A. Taylor, *Oxford Univ. U.K.* We report the importance of carrier-carrier scattering for intersubband scattering, the excitonic contribution at high densities in QWRs, we separate excitonic luminescence and Rayleigh in QWs. **(p. 59)**

4:30pm
QThD3 • Coulomb contributions to room temperature exciton saturation in GaAs-Al_xGa_{1-x}As multiple quantum wells, M. Holden, G. T. Kennedy, A. Miller, *Univ. St. Andrews, U.K.* Spin-dependent and spin-independent saturation mechanisms for heavy hole excitons are resolved in room temperature GaAs-Al_xGa_{1-x}As quantum wells using circularly polarized ultrashort pulses. **(p. 62)**

4:45pm
QThD4 • Relaxation dynamics of excitons and electron-hole pairs studied by spatiotemporal pump and probe experiments, S. Grosse, R. Arnold, A. Kriele, G. von Plessen, J. P. Kotthaus, J. Feldmann, *Ludwig-Maximilians-Univ., Germany;* R. Rettig, T. Marschner, W. Stolz, *Philipps-Univ. Marburg, Germany.* Optically performed ambipolar transport experiments on strained GaInAs/GaPAs quantum wells provide access to the formation and relaxation dynamics of excitons with $K_{\parallel} \neq 0$ in-plane wave vector. **(p. 65)**

5:00pm (Invited)
QThD5 • Locking of the stimulated emission of a microcavity laser to the electron spin precession clock, J. D. Berger, H. M. Gibbs, G. Khitrova, *Univ. Arizona;* S. Hallstein, M. Hilpert, M. Oestreich, *Max-Planck-Institut für Feskörperforschung, Germany;* H. C. Schneider, F. Jahnke, S. W. Koch, W. W. Rühle, *Fachbereich Physik der Philipps-Univ., Germany.* We synchronize the stimulated emission of a microcavity laser to the electron spin precession in a magnetic field by modulating the optical gain for the circularly polarized emission via the electron Larmor precession. **(p. 68)**

SALON B

8:00pm–10:00pm
QThE • Poster Session

QThE1 • Picosecond switching using resonant nonlinearities in a quantum well device, Patrick LiKamWa, *Univ. Central Florida;* Ayman Kan'an, *Purdue Univ.* Optical switching of signal pulses from one output port to the adjacent output port and back within 10 ps has been achieved in an overmoded Y-junction using two control pulses. **(p. 72)**

QThE2 • Quantum devices using multi-dots structures, E. A. M. Fagotto, S. M. Rossi, E. Moschim, *State Univ. Campinas, Brazil.* We examine the potential of multi-dots structures for signal processing. This is made by calculating the electronic transmission through them. **(p. 75)**

QThE3 • Spin gratings and in-well carrier transport in GaAs/AlGaAs multiple quantum wells, P. Riblet, A. R. Cameron, A. Miller, *Univ. St. Andrews, U.K.* Electron spin and concentration transient gratings are used to determine the in-well mobilities of both electrons and holes in MQW samples with different well widths. **(p. 78)**

QThE4 • New interpretation of quantum wire luminescence using a nonstandard description of the valence band states, F. Filipowitz, U. Marti, M. Glick, F. K. Reinhart, *Federal Institute of Technology, Switzerland;* J. Wang, P. von Allmen, J. P. Leburton, *Univ. Illinois–Urbana-Champaign.* We use a nonstandard description of valence band states to explain photoluminescence results. The lowest energy absorption peak of V-QWR is e1-lh1; the second is e1-hh1. **(p. 81)**

QThE5 • Observation of quantum confined Stark effect in strained compensated GaInAsSb/AlGaAsSb multiple quantum well structures, Yan Shi, Jian H. Zhao, *Rutgers Univ.;* Jiten Sarathy, Greg Olsen, *Sensors Unlimited Inc.;* Hao Lee, *SRI David Sarnoff Research Center.* The quantum confined Stark effect in the GaInAsSb/AlGaAsSb strain compensated multiple quantum well structures has been successfully demonstrated. A large absorption peak shift was observed. **(p. 84)**

QThE6 • Unidirectional radiation of spontaneous emission from 3-D photonic bandgap crystal cavity laser, Hideki Hirayama, Tetsuko Hamano, Yoshinobu Aoyagi, *The Institute of Physical and Chemical Research (RIKEN), Japan.* A novel radiation pattern from a three-dimensional photonic bandgap crystal cavity laser is demonstrated by a plane wave analysis. **(p. 87)**

QThE7 • Wavelength stabilization and trimming technologies for vertical surface-emitting lasers, F. Koyama, K. Iga, *Tokyo Institute of Technology, Japan.* We propose novel techniques of wavelength stabilization and post-process wavelength adjustment for vertical microcavity surface-emitting lasers. A possibility of drastic reduction in temperature sensitivity of wavelength as well as precise wavelength adjustment is presented. **(p. 90)**

QThE8 • Time-domain measurements of light propagation in dielectric spheres, W. B. Whitten, R. W. Shaw, M. D. Barnes, J. M. Ramsey, *Oak Ridge National Laboratory.* A formulation of optical pulse propagation in dielectric spheres is presented, and supporting experimental measurements of ps-pulses in glass spheres are described. **(p. 93)**

QThE9 • Computational modeling of ultrashort pulse propagation in semiconductor materials, Peter M. Goorjian, *NASA Ames Research Center;* Govind P. Agrawal, *Univ. Rochester.* Calculations of ultrashort optical pulse propagation in semiconductors are presented, which include Coulomb interaction effects. The Maxwell–Bloch equations are solved without the usual approximations. **(p. 95)**

QThE10 • Laser annealing of trap states in ZnSe quantum dots, Christine A. Smith, Subhash H. Risbud, *Univ. California–Davis;* J. Diane Cooke, Howard W. H. Lee, *Lawrence Livermore National Laboratory.* We have prepared ZnSe quantum dots that show visible luminescence from trap states. The results of laser annealing experiments on these trap states are reported. **(p. 98)**

SALON A

8:30am–10:00am

QFA • Physics of Mid Infrared Devices

Jurgen Kuhl, *Max Planck Institute, Germany, Presider*

8:30am (Invited)

QFA1 • Quantum cascade whispering gallery lasers, Claire Gmachl, Jérôme Faist, Federico Capasso, Carlo Sirtori, Deborah L. Sivco, Alfred Y. Cho, *Bell Laboratories, Lucent Technologies.* Low threshold, single-mode quantum cascade whispering gallery lasers with emission wavelengths from 5.0 to 11.5 micrometer are reported. Their potential for true microcavities is discussed. **(p. 102)**

9:00am

QFA2 • Simulation of high-power mid-IR interband cascade laser, I. Vurgaftman, J. R. Meyer, C. L. Felix, *U.S. Naval Research Laboratory;* L. R. Ram-Mohan, *Worcester Polytechnic Institute.* Detailed simulation of an optimized type-II interband cascade laser (T2ICL) design demonstrates that 1 W cw output power combined with low threshold current is feasible. **(p. 103)**

9:15am (Invited)

QFA3 • Type-II superlattices for infrared optoelectronics and lasers, R. H. Miles, *Hughes Research Laboratories.* Recent advances in the design of structures employing spatially indirect optical transitions promise infrared devices far outstripping conventional technology. **(p. 106)**

9:45am

QFA4 • Enhanced intersubband χ^3 in coupled InGaAs/AlGaAs multiple quantum wells, W. S. Rabinovich, G. Beadie, D. S. Katzer, *U.S. Naval Research Laboratory.* The saturation of a mid-infrared intersubband transition in coupled InGaAs/AlGaAs quantum wells and its implications for the system's χ^3 nonlinearity are studied. **(p. 109)**

10:00am–10:30am

Coffee Break

SALON A

10:30am–12:00m

QFB • Vertical Device Physics

Jerry R. Meyer, *U.S. Naval Research Laboratory, Presider*

10:30am

QFB1 • Field-dependent transverse confinement within selectively oxidized microcavities, Kent D. Choquette, G. R. Hadley, H. Q. Hou, K. M. Geib, B. E. Hammons, *Sandia National Laboratories.* We show that the transverse optical confinement produced by a buried oxide layer within an optical microcavity is dependent on the overlap of the oxide layer with the cavity longitudinal standing wave. **(p. 114)**

10:45am

QFB2 • Effects of two-photon absorption in saturable Bragg reflectors in femtosecond solid-state lasers, Amjad T. Obeidat, Jacob B. Khurgin, *The Johns Hopkins Univ.;* Wayne H. Knox, *Lucent Technologies.* We analyzed the effect of two-photon absorption on distributed Bragg reflectors. We showed that nonlinear absorption is greatly reduced in these mirrors in comparison with bulk material. **(p. 117)**

11:00am

QFB3 • Microcavity semiconductor lasers: parameter evaluation and performances, G. P. Bava, P. Debernardi, *Politecnico di Torino, Italy.* Single-mode semiconductor microcavity post lasers are studied, based on a first principle model, with a particular emphasis on the evaluation of controlled spontaneous emission. **(p. 120)**

11:15am

QFB4 • Polarization characteristics of vertical-cavity surface-emitting lasers with tilted pillar structure, Hye Yong Chu, Byueng-Su Yoo, Min Soo Park, Hyo-Hoon Park, *Electronics and Telecommunications Research Institute, Korea.* We report a precise control of the polarization states for vertical-cavity surface-emitting lasers by tilted etching of the laser pillar. **(p. 123)**

11:30am

QFB5 • Design and expected characteristics of 1.3 μm GaInNAs/GaAs vertical cavity surface emitting lasers, T. Miyamoto, T. Takada, K. Takeuchi, F. Koyama, K. Iga, *Tokyo Institute of Technology, Japan.* Long wavelength (1.3–1.55 μm) surface-emitting lasers using a GaInNAs/GaAs system have been investigated for low threshold and high temperature operation. A threshold current density of less than 300 A/cm^2 and a characteristic temperature of over 200 K are estimated. **(p. 126)**

11:45am

QFB6 • Symmetry breaking in vertical-cavity semiconductor lasers, J. P. Woerdman, A. K. Jansen van Doorn, M. P. van Exter, *Leiden Univ., The Netherlands.* We measure and manipulate the native anisotropy of a VCSEL by using a hot-spot technique. This allows us to realize any polarization state (linear, elliptical, circular). **(p. 129)**

12:00m–1:30pm

Lunch Break

SALON A

1:30pm–3:00pm

QFC • Novel Materials and Structures

Thomas Dekorsy, *RWTH Aachen, Germany, Presider*

1:30pm (Invited)

QFC1 • Red-emitting semiconductor quantum dot lasers, S. Fafard, *National Research Council, Canada.* The latest results will be presented on stimulated emission in electrically-injected laser structures based on an active region with 0-dimensional density-of-states obtained by self-assembled growth. **(p. 134)**

2:00pm

QFC2 • An all-silicon integrated light emitter technology, K. D. Hirschman, L. Tsybeskov, S. P. Duttagupta, P. M. Fauchet, *Univ. Rochester.* The design, fabrication, and optoelectronic characteristics of silicon-rich silicon oxide visible light-emitting devices integrated into silicon microelectronic circuits are reported. **(p. 135)**

2:15pm (Invited)

QFC3 • Optimization of photorefractive polymers for optical processing, K. Meerholz, *Univ. Munich, Germany.* Organic non-crystalline materials that exhibit the photorefractive effect are emerging as attractive materials for optical devices and processing systems. Recent progress in optimization of the materials for particular applications will be reported and some demonstration experiments presented. **(p. 138)**

2:45pm
QFC4 • Fabrication and characterization of Si dots prepared by self-organized recrystallization, L. Tsybeskov, K. D. Hirschman, S. P. Duttagupta, D. G. Hall, P. M. Fauchet, *Univ. Rochester.* Strong room temperature 1.1 μm photoluminescence and electroluminescence have been achieved from large Si dots prepared by recrystallization of oxidized mesoporous silicon and a-Si/a-SiO multilayers. **(p. 139)**

3:00pm–3:30pm
Coffee Break

SALON A

3:30pm–5:00pm

QFD • Quantum Optoelectronic Physics

Wayne H. Knox, *Lucent Technologies, Bell Laboratories, Presider*

3:30pm (Invited)
QFD1 • Trends in quantum optoelectronics: quantum confinement and beyond, Daniel Chemla, *Univ. California–Berkeley and Lawrence Berkeley National Laboratory.* Looking beyond the capabilities of the current generation of quantum confined heterostructures, we discuss potential approaches for molecular level design, synthesis, processing and interconnection of new functional materials and structures. **(p. 144)**

4:00pm (Invited)
QFD2 • Exciton dynamics, laser action, and cooperative emission in conducting polymer thin films, Z. V. Vardeny, *Univ. Utah.* Picosecond dynamics of exciton emission and absorption have been studied in neat thin films of a variety of poly(phenylene-vinylene) derivatives. We found that the stimulated emission band of 120 nm width and ~1 ns duration, which is observed at low exciton density, n, collapses at $n > 10^{17}$ cm^{-3} into a much narrower band of 7 nm width and lifetime $\tau \ll 10$ ps. Based on its excitation intensity dependence, polarization, lifetime, illuminated area, and film thickness dependencies, we assign this narrow band to superfluorescence rather than to amplified spontaneous emission. **(p. 145)**

4:30pm
QFD3 • Size reduction of microdisk injection lasers for spontaneous emission control, T. Baba, M. Kihara, R. Watanabe, *Yokohama National Univ., Japan.* We have demonstrated 3-μm-diameter microdisk injection laser operated with threshold current lower than 1 mA. Further reduction of the diameter to half of the device satisfies cavity single-mode condition and provides effective spontaneous emission control. **(p. 146)**

4:45pm
QFD4 • Novel configurations for optical parametric oscillators without any cavity, Yujie J. Ding, *Bowling Green State Univ.;* Jacob B. Khurgin, Seung-Joon Lee, *The Johns Hopkins Univ.* present our recent results on backward and transversely-pumped counter-propagating optical parametric oscillators. The oscillation in either configuration can occur without any cavity. **(p. 149)**

5:00pm–
Closing Remarks

Microcavity Lasers and Quantum Dots

QWA 1:30pm – 3:00pm
Salon A

Kenichi Iga, *Presider*
Tokyo Institute of Technology, Japan

Practical Microcavities?

Jack Jewell
Picolight, Inc.

Summary not available.

Vertical cavity surface emitting laser with self-assembled quantum dots

Kenichi Nishi, Hideaki Saito, and Shigeo Sugou
Opto-Electronics Research Laboratories, NEC Corporation
34 Miyukigaoka, Tsukuba, Ibaraki 305, Japan
Phone: +81-298-56-6127 Fax: +81-298-56-6140

Recently, low-dimensional quantum structures such as quantum dots (QDs) and quantum wires (QWIs), has been attracting much interest due to their novel physical properties and consequent improvements in device performances.[1] When the ideal QD or QWI structures are achieved, higher gain and lower threshold current in laser diodes are expected.[2] Among the many fabrication methods reported for such structures, self-assembled quantum-dot (SAQD) growth techniques[3-5] are particularly notable. They positively utilize the islanding growth in highly strained heteroepitaxial systems, such as InGaAs on GaAs. The SAQDs can be simply fabricated by molecular beam epitaxy (MBE)[3] or metal-organic vapor phase epitaxy (MOVPE)[4,5] and they have high crystal quality and uniform size distributions of within 10% as well as high surface densities of more than about 10^{11} cm^{-2}. Using these SAQDs, low-threshold QD edge-emitting lasers have been fabricated.[6-8] We expect to make even more advanced lasers, such as QD vertical-cavity surface-emitting lasers (VCSELs) using QDs in the active region.[9] The QD-VCSEL is especially attractive for controlling both the electron and photon modes in a microcavity structure.[10] When the cavity mode coincides with the narrow bandwidth light emission that originates from the delta-function-like density of states in uniform QDs, a high-performance light source with very low threshold current can be realized. On the other hand, the gain width, which critically determines the temperature characteristics of the VCSEL,[11] can be designated in QD-VCSELs by controlling the dot size distribution. Therefore, for improving and modifying device performances, we believe that the QD-VCSEL is the optimum optical device utilizing the QD structure. In this article, we report the fabrication of a QD-VCSEL and the observation of lasing oscillation at room temperature.

The QD-VCSEL structure (Fig. 1) was grown in a solid-source MBE chamber. Bottom 18-period AlAs/GaAs distributed Bragg reflectors (DBRs) and a spacer layer of AlGaAs were first grown on a GaAs (100) substrate. These layers were n-type doped. AlAs and GaAs layer thicknesses in the DBR were designed to be 64.9 nm and 51.5 nm, respectively. The interface layer between them was a graded composition AlGaAs layer (18 nm). Next, 10 periods of an $In_{0.5}Ga_{0.5}As$ dot / $Al_{0.25}Ga_{0.75}As$ layer (10 nm) were grown at 520°C. The dots were obtained by alternately supplying a GaAs 0.2 monolayer (ML) and an InAs 0.2 ML, including a 2-sec As pause until the RHEED pattern turned spotty. Growing an AlGaAs cover layer on the dots caused the growth surface to quickly become flat. Thus, even by the 10th period, the InGaAs dot layer was formed as well as the first layer. After the growth of the InGaAs dot active layer, a p-type AlGaAs spacer layer and top 14.5-period DBRs were grown at 600°C. Total thickness of the n- and p-AlGaAs spacers and the QD active layer was designed to be 295 nm, corresponding to the thickness of one wave cavity. A reflectivity spectrum of an As-grown wafer showed that the DBR mirror center and cavity resonant were positioned at a wavelength of around 960 nm, 2% shorter than the designed wavelength due to MBE growth fluctuation.

An atomic force microscopy (AFM) image shows the dot diameter and dot height to be about 28 nm and 3 nm, respectively. This lateral dimension is expected to be

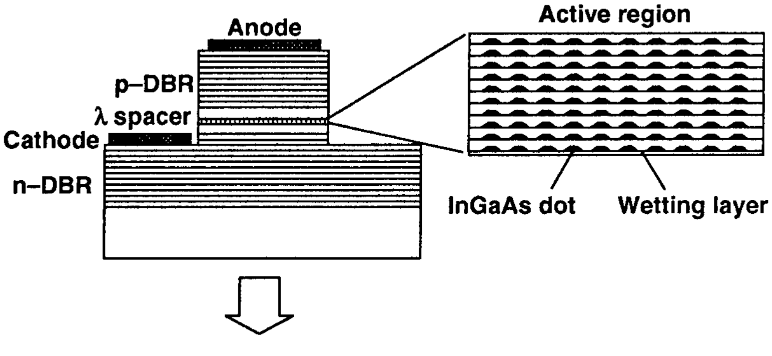

Fig. 1. QD-VCSEL with 10-period InGaAs dots in the active region.

small enough for lateral quantum confinement, which is comparable to or greater than thermal energy at room temperature. The density of dots is 2×10^{10} cm^{-2}, covering 12% of the surface. A PL measurement sample with 10-period InGaAs dots, just like the QD-VCSEL active layer, was also grown. PL from dots at 77 K is observed at 950 nm with a full width at half maximum (FWHM) of 60 meV. From the symmetric shape of the energy spectrum, the PL line width is thought to be dominated by the dot size distribution. The FWHM remains almost constant when the periods of dot layers are increased. Thus, there is little degradation of size uniformity by stacking 10 periods of dot layers. The PL spectrum at room temperature shows the quantum dot peak at 1000 nm with 100 meV FWHM. By stacking the dot layers up to 10 periods, we obtained PL intensity comparable to three period quantum well layers, which are usually used for the active layer of VCSELs.12) In the room temperature PL spectrum, a shoulder peak is observed at 920 nm, which probably corresponds to emission from a wetting layer that exists under the dots, as shown in Fig. 1. When the dot density becomes less, this 920 nm peak appears sharply and the quantum dot peak becomes small.

After the QD-VCSEL growth process, 25-μm-square devices were formed by wet etching. The current-versus-light-output characteristics of the QD-VCSEL at room temperature are shown in Fig. 2(a). The laser had a threshold current of 32 mA in the continuous wave condition with a threshold voltage of 5 V. Figure 2(b) shows the QD-VCSEL lasing spectrum. This clearly indicates lasing at 960.4 nm. In the QD-VCSELs, the gain in the active region was increased by stacking 10-period dot layers, resulting in the first demonstration of QD-VCSEL lasing oscillation at room temperature by current injection.

The VCSEL's lasing wavelengths correspond to the resonant wavelengths in the vertical cavities. The QD-VCSEL resonant wavelength shown in the reflectivity spectrum was shorter than the quantum dot PL peak wavelength by 40 nm. The QD-VCSEL device in this study, however, had a simple mesa structure and there was no heat dissipation. Thus, the resonant wavelength and the quantum dot levels shifted due to the heat under continuous wave operation. In the case of the QD-VCSEL with the 960.4-nm lasing wavelength, the resonant wavelength shift was measured to be 4.9 nm by the resonant peak shift in emission spectrum when current was increased from zero to the threshold current. Because the resonant wavelength shifts at a rate of 0.07 nm/°C,11) this 4.9-nm shift corresponds to a temperature increase of 70°C. The PL spectrum from the dots at a temperature elevated by 70°C shows the quantum-dot peak at 1020 nm and the wetting layer peak at 940 nm, which are shifted by 20 nm from the peaks at room temperature. The lasing wavelength is located between these wavelengths, indicating that a gain corresponding to the higher quantum level in the quantum dot, which is about 60 nm shorter than the ground state level, contributes to the lasing operation.

Figure 3 shows an emission spectra of 10-period dots at various currents under pulsed conditions from a sample which had an edge-emitting stripe mesa structure and was fabricated from the same wafer as that used for the QD-VCSEL devices. A small peak is observed at the vertical-cavity resonant wavelength, shown by the dashed line. As the current is increased, the main peak shifts from 1000 nm to a shorter wavelength. When the sample's edges are cleaved, an edge-emitting laser is obtained, which lases at 942 nm with a threshold current density of 820 A/cm^2 under pulsed conditions. This lasing wavelength is also about 60 nm less than the ground state transition. The peak shift and the short-wavelength lasing come from the fact that the quantum dots have several higher order quantum levels8),13),14) at wavelengths shorter than 1000 nm, as noted for the QD-VCSEL gain. In both lasers, the same quantum level, whose wavelength is 60 nm shorter than the ground state level, is used

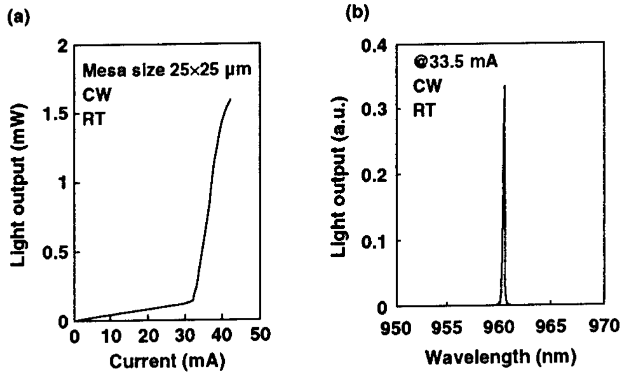

Fig. 2. Light output vs. current (a) and lasing spectrum (b) of QD-VCSEL at room temperature during cw operation.

for lasing, although the lasing wavelengths are different because the level in QD-VCSELs shifts by 20 nm due to the heat under continuous wave operation. A large current injection causes the ground-state gain to saturate and raises the emission intensity from the higher quantum levels. In other words, the gain from the transition at the higher quantum levels can become larger than that from the ground state transition as a result of high degeneracy at the higher levels.[14)] On the other hand, the ground level of the wetting layer is located at 920 nm. Even under increased current injection, there is not much gain in the longer wavelength side (lower energy side) of the peak in a two-dimensionally confined system. Therefore, its contribution to the lasing oscillation that is 28 meV apart from the peak should be negligible.

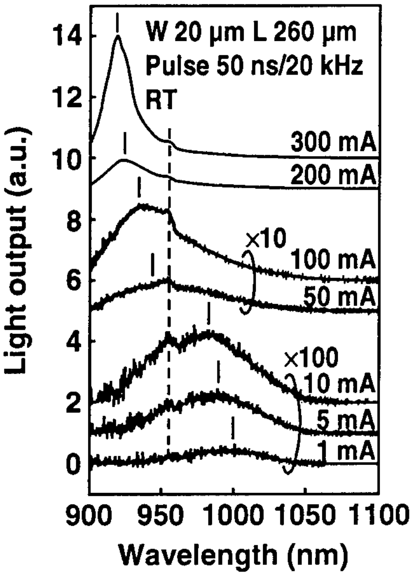

Fig. 3. Emission spectra of 10-period InGaAs dots at various current injections. The dashed line is vertical-cavity resonant wavelength.

To take advantage of the QD laser's superior properties, the gain of the quantum-dot ground state at 1000 nm should be dominant in lasing. To achieve this, loss in the cavity should be decreased (for example, by increasing reflectivity) or the gain should be increased. To obtain the higher gain from the ground state transition, more periods of dot layers should be stacked and/or dot size uniformity should be improved. We believe that more than ten periods of stacking are possible using the present growth conditions, and that size uniformity can be improved by optimizing the growth parameters or grown directions.[15)]

In summary, we have fabricated a QD-VCSEL with self-assembled quantum dots in its active region. Lasing operation at room temperature was achieved by stacking 10-period dot layers. The measurements of the emission spectrum should lead to an understanding of quantum-dot gain, which will be useful in designing the cavity wavelength of QD-VCSELs. Although the laser characteristics have not been improved by introducing QD structures, it is confirmed that room temperature continuous wave operation can be achieved under current injection and the optical gain from QDs is large enough for lasing. Thus, it is shown that, when the ideal QD structures with high uniformity are realized, great improvements in laser characteristics can be expected.

References

1). H. Sakaki, Jpn. J. Appl. Phys. **19**, L735 (1980).
2). Y. Arakawa and H. Sakaki, Appl. Phys. Lett. **40**, 939 (1982).
3). D. Leonard, M. Krishnamurthy, C. M. Reaves, S. P. Denbaars, and P. M. Petroff, Appl. Phys. Lett. 63, 3203 (1993); D. Leonard, K. Pond, and P. M. Petroff, Phys. Rev. **B 50**, 11687 (1994).
4). R. Nötzel, J. Temmyo, H. Kamada, T. Furuta, and T. Tamamura, Appl. Phys. Lett.**65**, 457 (1994).
5). J. Ahopelto, H. Lipsanen, M. Sopanen, T. Koljonen, and H. E.-M. Niemi, Appl. Phys. Lett. **65**, 1662 (1994).
6). N. Kirstaedter, N. M. Ledentsov, M. Grundmann, D. Bimberg, V. M. Ustinov, S. S. Ruvimov, M. V. Maximov, P. S. Kop'ev, Zh. I. Alferov, U. Richter, P. Werner, U. Gösele, and J. Heydenreich, Electron. Lett. **30**, 1416 (1994).
7). J. Temmyo, E. Kuramochi, M. Sugo, T. Nishiya, R. Nötzel, and T. Tamamura, Electron. Lett. **31**, 209 (1995).
8). R. Mirin, A. Gossard, and J. Bowers, in Proceedings of the 38th Electronic Materials Conference, California, 1996.
9). H. Saito, K. Nishi, I. Ogura, S. Sugou, and Y. Sugimoto, to be published in Appl. Phys. Lett.
10). T. Baba, T. Hamano, F. Koyama, and K. Iga, IEEE J. Quantum Electron. **27**, 1347 (1991).
11). M. Kajita, T. Kawakami, M. Nido, N. Kimura, T. Yoshikawa, K. Kurihara, Y. Sugimoto, and K. Kasahara, IEEE J. Sel. Top. Quantum Electron. **33**, 859 (1994).
12). H. Saito, I. Ogura, Y. Sugimoto, and K. Kasahara, Appl. Phys. Lett. **66**, 2466 (1995).
13). S. Fafard, D. Leonard, J. L. Merz, and, P. M. Petroff, Appl. Phys. Lett. **65**, 1388 (1994).
14). K. Mukai, N. Ohtsuka, H. Shoji, and M Sugawara, Appl. Phys. Lett. **68**, 3013 (1996).
15). K. Nishi, R. Mirin, D. Leonard, G. Medeiros-Ribeiro, R. M. Petroff, and A. C. Gossard, J. Appl. Phys. **80**, 3466 (1996).

Optical Probing of Mesoscopic and Nano-Structures

Yasuhiko Arakawa
University of Tokyo, Japan

We investigate the dynamics of 2D electrons in mesoscopic and point-contact structures using a micro-photoluminescence probing technique. NSOM observation of photoluminescence from quantum dots is also demonstrated.

Quantum Coherence

QWB 3:30pm – 5:15pm
Salon A

Duncan Steel, *Presider*
University of Michigan

Quantum Coherence of Hole Continuum States in GaAs Quantum Wells

T. Dekorsy, A.M.T. Kim, G.C. Cho, S. Hunsche, H.J. Bakker, H. Kurz,
S.L. Chuang [1], and K. Köhler [2]

Institut für Halbleitertechnik, RWTH Aachen, Sommerfeldstr. 24, D-52056 Aachen, Germany
Tel. +49-241-807896, FAX +49-241-8888246
[1] Department of Electrical and Computer Engineering, Univerity of Illinois at Urbana
Champaign, Urbana, Illinois 61801
[2] Fraunhofer Institut für Angewandte Festkörperphysik, D-79108 Freiburg, Germany

The investigation of quantum coherence excited by femtosecond laser pulses is one of the central topics in quantum optoelectronics. Up to now, most investigations in semiconductors and semiconductor quantum structures deal with quantum coherence of excitonic states. For two reasons the quantum coherence of continuum states has not been anticipated for a long time due to i) the expected high momentum scattering rates of continuum states and ii) the dispersion of the valence and conduction bands, which gives rise to a strong "inhomogeneous" broadening of the band-to-band transitions. Recently, optically excited quantum coherence has been observed, which was attributed to the phase coherence of continuum states in the conduction band. These observations include Bloch oscillations in superlattices [1,2] and free-electrons in Landau levels [3]. Most recently, quantum coherence in the valence band has been observed in GaAs quantum wells [4] and bulk GaAs [5]. Here, we report on the observation of quantum coherence of the first heavy and light hole subbands in a GaAs quantum well under excitation above the fundamental excitonic transitions [4].

We compare the results of three different optical technique: degenerate four-wave mixing (FWM), time-resolved transmission changes (TC) and the time-resolved detection of polarization anisotropies in the transmitted probe beam in a geometry sensitive to electro-optic transmission changes (EOTC). The laser source is a passively Kerr-lens modelocked Ti:sapphire laser delivering pulses of 50 fs duration and a spectral shape close to a Gaussian with a FWHM of <40 meV. The sample consists of 40 GaAs quantum wells of 6.5 nm width and 20 nm $Al_{0.35}Ga_{0.65}As$ barriers. The splitting of the 1s heavy-hole (HH) and 1s light-hole (LH) exciton is 21 meV. The laser spectrum is tuned between the excitonic HH and LH transitions at 10 K for resonant excitation. Off-resonant excitation with respect to the excitonic transitions is accomplished by tuning the laser central energy 47 meV above the HH resonance at 10 K and an additional tuning of the sample temperature up to 150 K.

Fig. 1 compares the data obtained by all three techniques at 10 K. For resonant excitation, all signals exhibit quantum beats due to the resonant excitation of the HH and LH exciton. However, under non-resonant excitation the FWM signal exhibits a signal at zero time delay only, which has decreased by two orders of magnitude compared to the resonant case. In contrast, the TC and EOTC signals still reveal a periodic modulation. This discrepancy between the different signals is explained as follows: FWM is very selectively sensitive towards the *third order excitonic interband polarization.* The nonlinear interband polarization associated with band-to-band transitions of continuum states is much weaker and destroyed within 100 fs compared to the ps-dephasing of the excitonic coherence [6]. Both the TC and EOTC signals for off-resonant excitation are modulated by the *intersubband coherence of HH and LH continuum states.* The dephasing time of the associated polarization persists much longer than the interband coherence of the states coupled by the band-to-band transitions.

Fig. 2 shows the oscillations extracted from the EOTC signals for different excess energies up to 75 meV above the HH exciton. For all excess energies the quantum beats are clearly resolved. The decrease of the dephasing time is only a factor of 2 between resonant

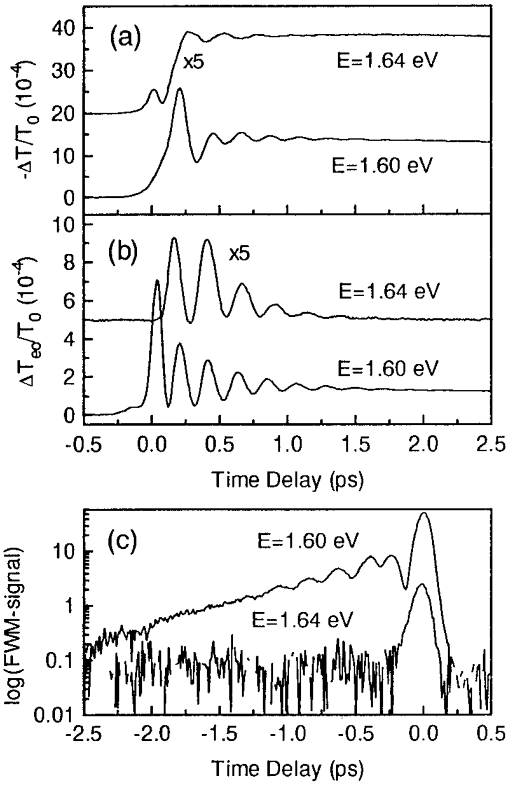

Fig. 1: (a) Transmission changes, (b) electro-optic transmission changes, and (c) FWM signal for two different excitation energies at 10 K.

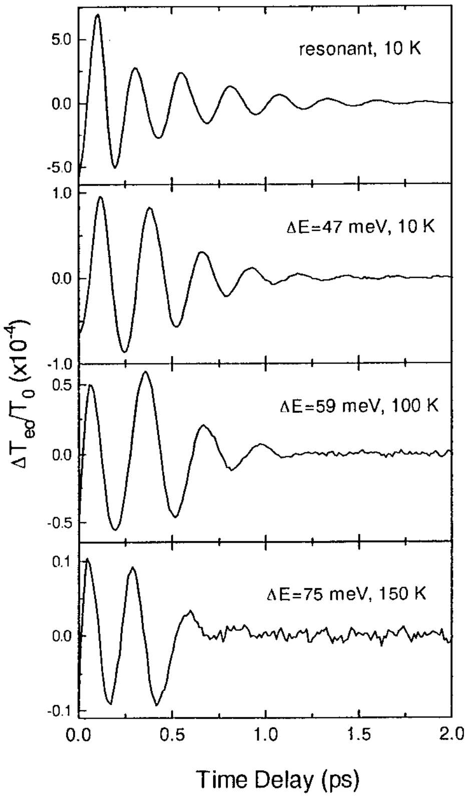

Fig. 2: Electro-optic transmission changes for different excess energies above the HH exciton.

and off-resonant excitation at 10 K. A further increase of the dephasing time with rising temperature is related to the intervalence-band thermalization by the absorption of LO phonons [7] and by the inhomogeneity of the HH-LH splitting as a function of the momentum parallel to the layers. Although the highest excess energy is more than twice the LO phonon energy in GaAs, the observed dephasing is not governed by LO phonon relaxation, since almost all of the excess energy is transferred to the conduction band. A drop in the energy of the quantum beats is observed from 21 meV for resonant excitation to 16 meV for off-resonant excitation. This drop is due to the valence band dispersion in the quantum well in quantitative agreement with theoretical calculations of the band mixing based on a Luttinger-Kohn Hamiltonian.

The observation of quantum coherence of continuum states in the valence band of quantum wells adds important information for the understanding of intraband and intersubband dephasing processes in semiconductor heterostructures. Furthermore, relevant data on the valence band mixing in GaAs quantum wells are obtained.

References

[1] H.G. Roskos, C. Waschke, R. Schwedler, P. Leisching, H. Kurz and K. Köhler, Superlattices Microstruct. **15**, 281 (1994).

[2] P. Leisching, T. Dekorsy, H.J. Bakker, H. Kurz, and K. Köhler, Phys. Rev. B **51**, 18015 (1995).

[3] D. Some and A.V. Nurmikko, Phys. Rev. B **50**, 5783 (1994).

[4] T. Dekorsy, A.M.T. Kim, G.C. Cho, S. Hunsche, H.J. Bakker, H. Kurz, S.L. Chuang, and K. Köhler, Phys. Rev. Lett. **77**, 3045 (1996).

[5] M. Joschko, M. Woerner, T. Elsaesser, R. Hey, H. Kostial, and K. Ploog, *Ultrafast Phenomena X*, eds. P.F. Barbara, J.G. Fujimoto, W.H. Knox, and W. Zinth (Springer Berlin 1996), pp.385.

[6] D.S. Kim, J. Shah, J.E. Cunningham, T.C. Damen, W. Schäfer, M. Hartmann, and S. Schmitt-Rink, Phys. Rev. Lett. **68**, 1006 (1992).

[7] A.M.T. Kim, S. Hunsche, T. Dekorsy, H. Kurz, and K. Köhler, Appl. Phys. Lett. **68**, 2956 (1996).

Interferometric Four-Wave-Mixing Spectroscopy on Semiconductors

M. U. Wehner, J. Hetzler, and M. Wegener
Institut für Angewandte Physik, Universität Karlsruhe
Kaiserstrasse 12, D-76128 Karlsruhe, Germany
Phone : 0049-721/608-3401
Fax : 0049-721/607-593

In ultrafast nonlinear spectroscopy interferometric techniques can be applied both for heterodyne detection of the signal and for the excitation of the sample by phase-locked pulses, thus delivering coherent control [1] over the system. Such techniques have been predicted to be extremely sensitive with respect to the dynamics of elementary excitation [2] and have been applied to the study of non-Markovian dynamics of molecules [3, 4]. For the case of semiconductors, interferometric sensitivity has been employed for detection purposes [5] and the use of phase-locked pulses has been reported quite recently [6]. In this paper we report the observation of a novel interference phenomenon in interferometric four-wave-mixing due to contributions beyond the third order perturbational limit. An analysis of the observed interferences allows for an estimation of the importance of these higher order contributions.

For a general discussion let us consider the four-wave-mixing setup shown in Fig. 1. The incoming beams have the wave vectors $\vec{q}_1$ and $\vec{q}_2$, respectively. While there is only a single optical pulse $\mathcal{E}(t-t_2)$ in direction $\vec{q}_2$ a phase-locked pair of pulses $\mathcal{E}(t-t_1)$ and $\mathcal{E}(t-t_{1'})$ is employed in direction $\vec{q}_1$. In the third order perturbational regime the beam in direction $\vec{q}_1$ enters linearly into the diffracted signal with wave vector $2\,\vec{q}_2-\vec{q}_1$ and consequently a simple interference with the frequency of the laser is expected as a function of the time delay $t_1 - t_{1'}$ for a resonant degenerate experiment. If formally two distinct wave vectors $\vec{q}_1$ and $\vec{q}_{1'}$ are assigned to the phase-locked pulses, further contributions of higher order propagate in the same diffracted direction, as e.g. $2\,\vec{q}_2+\vec{q}_1-2\,\vec{q}_{1'}$. By interference among themselves and with the above contribution they lead to components oscillating with twice and three times the laser frequency. The corresponding phase factors of all third and fifth order contribution are listed in Table I. In third order, the only occuring beat oscillation is $\omega(t_1 - t_{1'}) = \omega t_{11'}$, while up to fifth order terms like $2\omega t_{11'}$ come into play also. Similarly, yet higher order terms show up as yet higher harmonics in the time-delay domain. Note, that all contributions are resonant and appear within the rotating wave approximation. Hence they are not related to higher harmonics in the real-time domain.

The experimental setup is similar to the one employed in previous experiments [7, 8] except for the extension to three collinearly polarized beams of comparable intensity arranged as shown in Fig. 1. The time delays $t_{11'} \equiv t_1 - t_{1'}$ and $t_{21'} \equiv t_2 - t_{1'}$ are controlled by means of piezoelectric actuators. The center frequency of the closely transform-limited optical pulses of 15 fs in duration is tuned to the 1s-exciton resonance of bulk GaAs at T=77 K and the diffracted signal in direction $2\,\vec{q}_2 - \vec{q}_1$ is detected with a photomultiplier. All carrier densities quoted refer to the incoherent superposition of the three beams. They are determined in a fashion consistent with previous, non-interferometric experiments [7, 8].

Fig. 2(a) shows a typical set of FWM traces as a function of $t_{11'}$ for three different $t_{21'}$. Beside the simple interference with roughly the band gap frequency, additional fine structure is observed around $t_{11'} \approx 0$. From the inset in Fig. 2(a) it already becomes evident that this fine structure is related to higher frequency components. The origin of these fast oscillations becomes yet more clear when inspecting the Fourier transforms of the data with respect to $t_{11'}$. The absolute value of the Fourier transforms for four different total carrier densities, separated by one order of magnitude, plotted as a function of the energy is depicted in Fig. 2(b). It is obvious that only integer harmonics of the basic

Table 1: Phase factors of components of the polarization with wave vector $2\vec{q}_2-\vec{q}_1$ within the rotating wave approximation from a pertubational analysis.

3rd order	$e^{-i\omega(t-[2t_2-t_1])}, e^{-i\omega(t-[2t_2-t_{1'}])}$
5th order	$e^{-i\omega(t-[2t_2-t_1])}, e^{-i\omega(t-[2t_2-t_{1'}])}$
	$e^{-i\omega(t-[2t_2+t_{1'}-2t_1])}, e^{-i\omega(t-[2t_2+t_1-2t_{1'}])}$

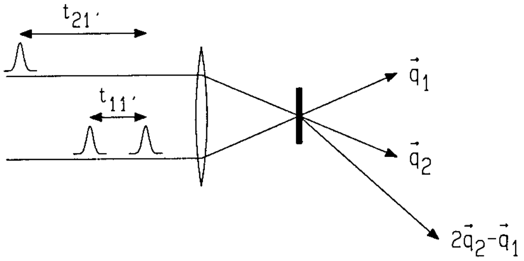

Figure 1: Schematic of the experimental setup

frequency occur. For a density of e.g. $2.9 \times 10^{15}\mathrm{cm}^{-3}$, the second harmonic is merely a factor of three weaker than the fundamental. Somewhat surprisingly, the relative weight of the harmonics shows a rather small influence on carrier density. It is only at the lowest carrier densities that the strength of the higher harmonics decreases somewhat.

Following the general discussion of the introduction the higher harmonics in the time-delay domain are interpreted as being due to resonant nonlinear optical contributions beyond the third order perturbational limit. For excitation densities lower than $5 \times 10^{15}\mathrm{cm}^{-3}$ the dominant nonlinear response in bulk GaAs has recently been shown to originate from exciton-continuum scattering [8]. A similar coupling of exciton and continuum has also been found for quantum wells [9]. The following analysis based on the model for exciton-continuum scattering [8] confirms the above interpretation. Since contributions of different orders are comparable a perturbational approach is no longer appropriate, whereas the well known wave vector selection procedure , e.g. described in Ref.10, is still meaningfull for this situation. The application of this procedure to the equation of motion of the polarization of the 1s-exciton leads to a coupled set of differential equations for its spatial Fourier components. The coupling of the different Fourier components reflects the reasoning given in the introduction. Using the parameters corresponding to the experiment the numerical solutions shown in Figs. 3(a) and 3(b) are obtained. In Fig. 3(a) again fast oscillations of the four-wave-mixing signal are observed which show up as integer harmonics of the fundamental frequency when performing a Fourier transform with respect to $t_{11'}$ (Fig. 3(b)). The overall qualitative agreement with the experiment is satisfactory (compare Figs. 2 and 3). The relative strength of the higher harmonics is found be proportional to

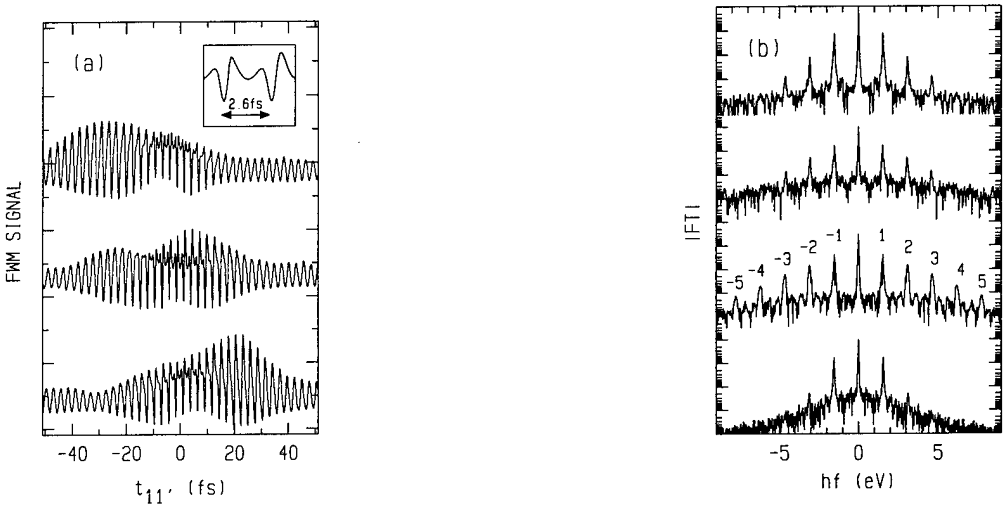

Figure 2: Experiment: (a) Interferometric four-wave-mixing signal, GaAs at 77 K and a total carrier density of $2.9 \times 10^{15}\mathrm{cm}^{-3}$, as a function of $t_{11'}$ for three fixed $t_{21'}$ (from top to the bottom $t_{21'} = -10, 0, 10\,\mathrm{fs}$). Inset: Signal for $t_{21'} = 0$ and $t_{11'} \approx 0$. (b) Absolute value of the Fourier-transform (FT) with respect to $t_{11'}$ of traces similar to those of (a) for $t_{21'} \approx 0$. The total carrier density from top to the bottom : $2.0 \times 10^{17}, 2.0 \times 10^{16}, 2.9 \times 10^{15}$, and $2.3 \times 10^{14}\mathrm{cm}^{-3}$.

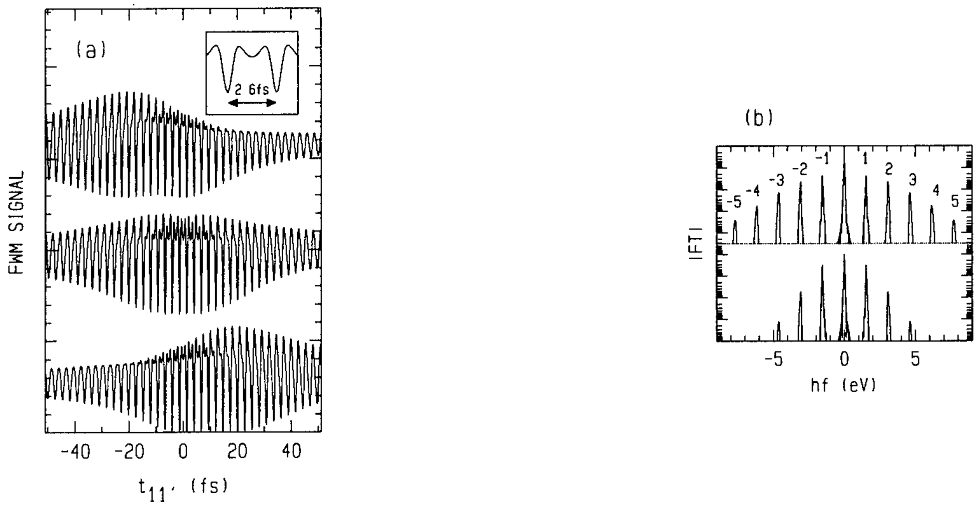

Figure 3: Model: (a) Interferometric four-wave-mixing signal as a function of $t_{11'}$ for three fixed $t_{21'}$ (from top to the bottom $t_{21'} = -10\,,0\,,10\,\mathrm{fs}$). Inset: Signal for $t_{21'} = 0$ and $t_{11'} \approx 0$. (b) Absolute value of the Fourier transform with respect to $t_{11'}$, at $t_{21'} = 0$. The excited density of the upper curve corresponds to (a), the density of the lower curve is one order of magnitude lower.

the excited carrier density and to the inverse of the 1s-exciton linewidth taken in the limit of zero excitation density. This behavior can be seen in Fig. 3(b), where the carrier density is varied by a factor of ten.

In conclusion transient four-wave-mixing employing phase-locked pairs of ultrashort pulses is a sensitive tool to quantify the influence of resonant nonlinear optical contributions beyond third order. We like to emphasize that these contributions still have considerable strength at total carrier densities of $2.3 \times 10^{14}\,\mathrm{cm}^{-3}$ which are among the lowest ever reported for semiconductors. Regarding coherent control experiments, the appearance of interferences with higher harmonics poses severe requirements to the control of the phase. Work on quantum wells is currently in progress.

References

[1] W. S. Warren, H. Rabitz, and M. Dahleh, Science **259**, 1581 (1993)

[2] M. Cho, N. F. Scherer, G. R. Fleming, and S. Mukamel, J. Chem. Phys. **96**, 5618 (1992)

[3] W. P. Boeij, M. S. Pshenichnikov, D. A. Wiersma, Chem. Phys. Lett. **247**, 264 (1995)

[4] M. S. Pshenichnikov, W. P. de Boeij, and D. A. Wiersma, Phys. Rev. Lett. **76**, 4701 (1996)

[5] J.-Y. Bigot, M.-A. Mycek, S. Weiss, R. G. Ulbrich, and D. S. Chemla, Phys. Rev. Lett. **70**, 3307 (1993); D. S. Chemla, J.-Y. Bigot, M.-A. Mycek, S. Weiss, and W. Schäfer, Phys. Rev. B **50**, 8439 (1994)

[6] A. P. Heberle, J. J. Baumberg, and K. Köhler, Phys. Rev. Lett. **75**, 2598 (1996)

[7] L. Bányai, D. B. Tran Thoai, E. Reitsamer, H. Haug, D. Steinbach, M. U. Wehner, M. Wegener, T. Marschner, and W. Stolz, Phys. Rev. Lett. **75**, 2188 (1995)

[8] M. U. Wehner, D. Steinbach, and M. Wegener, Phys. Rev. B **74**, R5211 (1996)

[9] S. T. Cundiff, M. Koch, W. H. Knox, and J. Shah, Phys. Rev. Lett. **77**, 1107 (1996)

[10] T. Rappen, U. Peter, M. Wegener and W. Schäfer, Phys. Rev. B **48**, 4879 (1993)

Coherent Control Of Semiconductor Optoelectronic Properties

A. Haché, Y. Kostoulas, R. Atanasov, J. Fraser, J. Sipe, and H.M. van Driel
Department of Physics, University of Toronto and
Ontario Laser and Lightwave Research Centre, Toronto, Canada, M5S 1A7

Historically, phase has received little attention as a parameter which can be used to control the properties of matter. Recently, however, coherence control of physical and chemical properties of simple systems using two or more laser beams has been demonstrated [1-3]. The possibility of influencing the phase of matter by controlling the phase of light arises from the fact that two or more phased perturbations which can connect the same initial and final states in a system can lead to interference effects between the different quantum mechanical pathways and therefore influence the final state of matter. In this talk we report two manifestations of this effect in bulk semiconductors, namely the generation and control of carrier density and electrical currents [3] in a <u>bulk</u>, unbiased semiconductor when both initial and final states are in the <u>continuum</u> (valence and conduction bands). The observations of such effects is not only intellectually appealing but may point the way to novel device applications. In initial experiments, control has been achieved in GaAs at room temperature using picosecond and 100 fs optical pulses at 1550 and 775 nm. The talk will focus on the description of these phenomena in terms of quantum mechanics as well as nonlinear optics. The influence of beam parameters and sample characteristics will be discussed.

References

1. Y. -Y. Yin, C. Chen, D.S. Elliot, A. V. Smith, Phys. Rev. Lett. **69**, 2353, (1992); E. Dupont, P.B. Corkum, H.C. Liu, M. Buchanan, and Z.R. Wasilewski, Phys. Rev. Lett. **74**, 3596 (1995).
2. R. Atanasov, A. Haché, J.L.P. Hughes, H.M. van Driel, and J. E. Sipe, Phys. Rev. Lett. **76**, 1703 (1996); A. Haché, Y. Kostoulas, R. Atanasov, J.L.P. Hughes, J.E. Sipe and H.M. van Driel, Phys. Rev. Lett. (in press, 1997)

Time Resolved Amplitude and Phase of Coherent Four Wave Mixing Emission from GaAs Quantum Wells

Wojciech J. Walecki, David N. Fittinghoff and Arthur L. Smirl
Laboratory for Photonics and Quantum Electronics, 100 IATL, University of Iowa,
Iowa City, IA 52242
Phone: (319)335-3460 Fax: (319)335-3462

Time integrated and time-resolved four wave mixing (FWM) techniques using ultrashort pulses have proven to be extremely powerful tools for studying coherent processes and excitonic effects in semiconductors and semiconductor multiple quantum wells (MQWs). These techniques have provided considerable information about the time dependent amplitude of the emitted FWM signal, but they provide no information about the time dependent phase. Complete characterization of the emitted electromagnetic field requires the measurement of both amplitude and phase. Moreover, it has been emphatically demonstrated[1] that the phase dynamics carry essential information about the optical interactions and the fundamental processes. Consequently, failure to measure the phase will result in a loss of this information.

Techniques for characterizing both the amplitude and phase of an isolated ultrafast signal are available,[2] however, each of these requires the use of a nonlinear process. As a result, they are relatively insensitive, requiring a few picojoules for a multishot measurement. By comparison, FWM signals are much weaker and require more sensitive measurement techniques. For this reason, the full characterization of such weak FWM signals has proven tedious, difficult and labor intensive. For example, the measurements described in Ref. 1 were an impressive tour de force. In addition to characterizations of the reference pulse, five complementary quantities were measured: the time-integrated and time resolved FWM signals, the power spectrum and the first-order interferometric auto and cross correlations. The correlations required interferometric stability and considerable experimental dexterity, since ~20 points per optical period were acquired. Recently, in partial response to this need, a method of completely measuring the intensity and phase of an almost arbitrarily weak coherent signal has been demonstrated[3,4] by combining spectral Interferometry with a well characterized reference pulse.

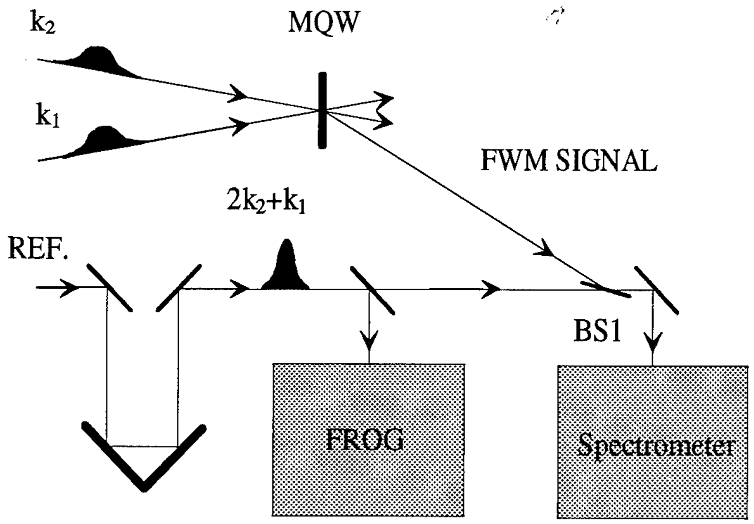

Fig. 1. Schematic of the experimental geometry for the spectral interferometric measurements.

Here, we provide the first demonstration that spectral interferometry combined with a reference pulse that is characterized by frequency resolved optical gating (FROG) can be used to obtain the dynamics of both the phase and the amplitude of weak FWM signals. We accomplish this by dividing the output from our mode-locked Ti:sapphire laser into three pulses. Two of the pulses, with wavevectors $\mathbf{k}_1$ and $\mathbf{k}_2$, were used to generate the FWM signal in the direction $2\mathbf{k}_2+\mathbf{k}_1$ as indicated in Fig. 1. The third pulse was fully characterized using second harmonic FROG techniques, and a fixed time delay was introduced between the reference pulse and the signal. The reference and the FWM signal were then allowed to collinearly interfere and, finally, the combined pulses were dispersed by a spectrometer. If the amplitude and the phase of the reference pulse are fully known, then (it is well known[3,4] that) the amplitude and phase of the signal can be retrieved from the corresponding spectral interferogram. The trick for this retrieval is to provide a fully characterized reference pulse.

Notice that for the spectral interferometry described here the phase is directly measured in the spectral domain. By comparison, for the interferometric correlations reported previously,[1] the phase was obtained in the temporal domain by measuring the relative fringe spacings of the signal and reference autocorrelations. Also notice that the present technique relaxes the requirement for interferometric stability over long time intervals and (aside from the characterization of the reference pulse) requires only a linear measurement at a single fixed time delay. Thus it is simpler than previous techniques.

To demonstrate the power and sensitivity of the technique, we have investigated the temporal dynamics of the phase and amplitude of the FWM signal emitted from several GaAs/AlGaAs MQWs as a function of the excitation fluence, of time delay between the two incident pulses, of the detuning of the laser wavelength from the heavy hole (hh) exciton, and of the orientation of the input polarizations. For example, a typical spectral interferogram with the laser tuned above the hh is shown in Fig. 2 for a MQW consisting of 40 periods of 10 nm/10 nm GaAs/$Al_{0.3}Ga_{0.7}As$ at 80 K and for a time delay of 0. Notice that the spectral fringes exhibit an obvious π phase shift near 1.54 eV. The spectral intensity and spectral phase corresponding to this interferogram are shown in Fig. 3. The spectral phase is moderately flat across the hh and light hole (lh) spectrum, but it undergoes a π phase shift in between the hh and lh. The temporal evolution of the field amplitude and phase are shown in Fig. 4. In the time domain, quantum beats are evident, and a π shift in the phase is observed at each beat minimum.

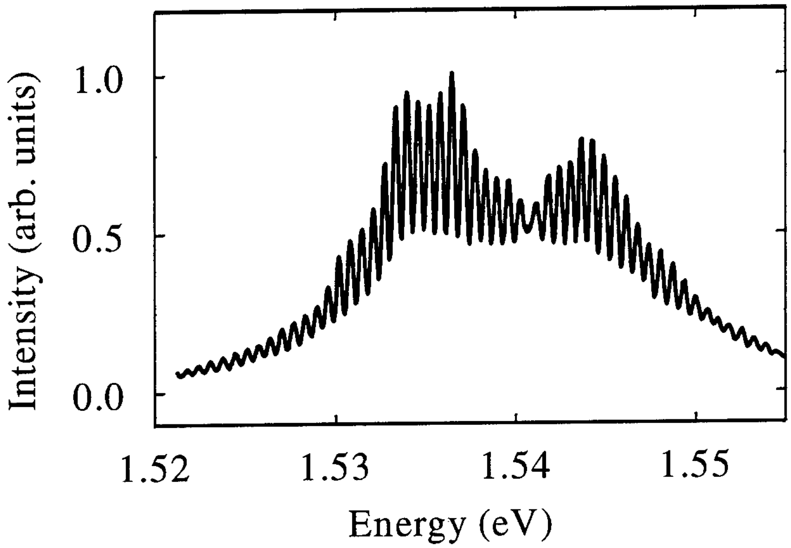

Fig. 2. Typical spectral interferogram when the laser was tuned above the heavy hole exciton in the regime of low carrier densities.

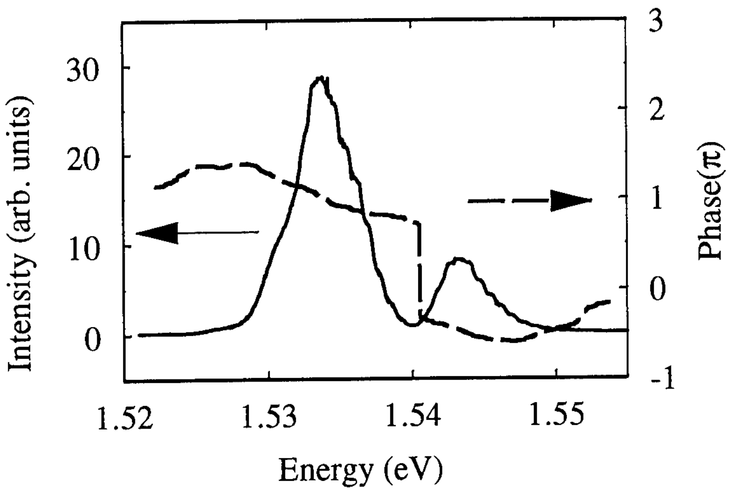

Fig. 3. The power spectrum and spectral phase corresponding to the interferogram shown in Fig. 2.

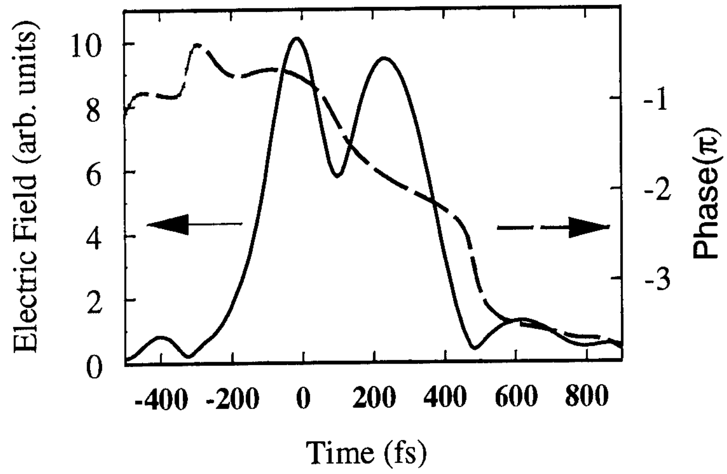

Fig. 4. The amplitude and temporal phase corresponding to the power spectrum and spectral phase shown in Fig. 3.

When the laser was tuned below the hh resonance at low fluences (not shown here), the FWM spectrum was asymmetric and narrow, and the emission wavelength was centered near the hh resonance. The temporal phase increased dramatically and linearly during the first part of the emission then leveled off. As the fluence was increased, the FWM spectrum shifted and broadened, approaching the laser spectrum. The corresponding temporal phase gradually flattened with increasing fluence. All of the features described here are consistent with (and confirm) those observed previously.[1] These features and others that we will describe also demonstrate that this technique is capable of providing the same information as the battery of measurements used previously, but with less effort in the laboratory. The accuracy, temporal resolution, and dynamic range limitations will be discussed.

1. D. S. Chemla, J. Y. Bigot, M. A. Mycek, S. Weiss, and W. Shäfer, Phys Rev. B **50**, 8439 (1994)
2. K. W. Delong, et al., J. Opt. Am. B **11**, 2206 (1994), and references therein.
3. L. Lepetit, G. Chériaux and M. Joffre, J. Opt. Soc. Am. B **12**, 2467 (1995).
4. D. N. Fittinghoff et al., Opt. Lett. **21**, June (1996).

Excitation- and Disorder-induced Reduction of the Superradiant Excitonic Decay in GaAs Quantum Well Bragg Structures

J. Kuhl and M. Hübner
Max-Planck-Institut für Festkörperforschung, D-70569 Stuttgart, Germany
Phone : (+49) 711 689 1633, FAX: (+49) 711 689 1615
e-mail: Kuhl@servix.mpi-stuttgart.mpg.de

T. Stroucken, B. Grote, A. Knorr, and S.W. Koch
Department of Physics and Materials Science Center,Philipps University,
D-35032 Marburg, Germany

R. Hey and K. Ploog
Paul-Drude-Institut für Festkörperelektronik, D-10177 Berlin, Germany

The theoretically predicted rapid superradiant decay of coherent 2D excitons on a time scale of approximately 10 ps [1] is expected to be strongly enhanced in multiple QW (MQW) Bragg structures consisting of N identical QWs separated by (Ga,Al)As barriers the thickness of which was adjusted so that the QWs had a distance d equal to one half of the heavy-hole exciton resonance wavelength λ in the medium [2]. This enhancement originates from efficient radiative coupling of excitons excited in different wells via the exchange of transverse photons. Recently we have published [3] degenerate-four-wave-mixing experiments with fs optical pulses on GaAs QW Bragg structures which demonstrate that the radiative lifetime in high-quality GaAs single QWs (SQW) is approximately 5 ps and decreases to less than 2 ps in Bragg samples with N=10. These studies revealed that radiative recombination provides the dominant contribution to the homogenous linewidth of the 2D exciton in high-quality samples and exceeds nonradiative contributions caused by scattering with sample imperfections in contrast to previous assumptions.

Here we show that high sample quality and low excitation density are crucial premises for strong radiative recombination. Rough QW interfaces (implying considerable inhomogenous line broadening or energetic disorder) or even slight mismatches between d and λ/2 (geometric disorder) result in rapidly increasing suppression of radiative interwell coupling. Density dependent DFWM experiments demonstrate that the superradiant decay is a low intensity phenomenon. At higher excitation intrawell exciton/exciton scattering leads to rapid dephasing of the coherent polarization and a corresponding reduction of radiative recombination.

We present data for a 20 nm SQW and two Bragg samples consisting of 10 identical QWs with a thickness of 20 nm separated by (Ga,Al)As barriers. Time-integrated (TI) and time-resolved (TR)-DFWM and time-resolved reflectivity experiments have been performed using σ^+ polarized, 770-fs-long pulses from a Kerr-lens mode-locked Ti:sapphire laser.

The mismatch between d and λ and thus the interwell coupling can be intentionally tuned on a given sample by tilting the sample normal with respect to the incident excitation beams used in a two-pulse self diffraction experiment. Fig.1a displays the angle dependence of the DFWM signal shape for one of our Bragg structures. For $\alpha = 0$ the signal displays a biexponential deacy. The first fast decay reflects optical dephasing of the superradiant mode due to raditive recombination, whereas the slower decay can be attributed to long-living nonradiative modes which have vanishing oscillator strength in a perfect structure and whose dephasing rate is even considerably slower than that of a single QW. The growing mismatch between d and λ with increasing α results in a gradual disappearance of the initial fast decay whereas the slow decay of the „optically inactive“ modes remains unaffected. Deviations of d from λ/2 as small as 1% lead to drastic changes of the exciton relaxation. The second Bragg sample exhibits just the opposite angle dependence of the signal shape (Fig.1b). With increasing α the contribution of the superradiant mode becomes more and more dominant. From these data we have to conclude that d is slightly smaller and larger than $\lambda/2$ for the first and second sample, respectively. The characteristic change of the signal features with α are qualitatively well reproduced by solutions of the semiconductor Maxwell Bloch equations (Fig.1c).

The high sensitivity of the interwell coupling to the mismatch between d and λ directly raises questions concerning the role of sample disorder for the radiative recombination rate of the 2D exciton. Disorder in MQW structures can be classified into two groups. Geometrical and energetic disorder. The former describes statistical and systematic deviations of d from $\lambda/2$. Geometric disorder is characterized for a given sample by the average value d_{av} of the QW distances and the width of its distribution σ_d. In a real sample, both these quantities may remarkably fluctuate across the excited sample spot. Energetic disorder is a measure for fluctuations of the exciton transition wavelength, i.e. inhomogeneous broadening of the exciton transition frequency due to well width fluctuations. It can be characterized by the inhomogeneous linewidth γ_{inh}. Signal shapes have been calculated with the semiconductor Maxwell-Bloch equations for a fs pulse reflected from a N= 10 Bragg structure in dependence of the disorder parameter σ_d. Variations of d_{av} and σ_d across the laser beam diameter were taken into account by superimposing solutions of the semiconductor Maxwell Bloch equations for 10,000 channels with statistically fluctuating values for these quantities. With increasing σ_d the signal displays a growing contribution of nonradiative modes in accordance with the observations made in the tilting experiments. If σ_d exceeds 0.01 λ the tail of the signal exhibits pronounced modulations, which probably can be used to characterize the sample disorder. The modulations are caused by simultaneous excitation of several nonradiative modes. The theory also predicts remarkable excitation of nonradiative modes in MQW Bragg structures in the presence of modest inhomogeneous broadening of the exciton transition energy as small as $\gamma_{inh}= 0.5 - 1\ \gamma_{hom}$. Such a small inhomogeneous broadening is hardly detectable on a single QW since the corresponding deviations from the exponential decay are extremely small. Systematic experimental studies of reflected pulse shapes are currently underway.

Next, we describe the density dependence of the DFWM signal shape. At very low excitation (Fig. 2a) the signal displays the biexponential decay attributed to the superposition of the superradiant and the nonradiative modes. Both the fast and slow decay are accellerated at higher excitation densities (see Figs.2b and 2c) because of competing excitation-induced dephasing of excitons caused by intrawell scattering. The slower decay of the signal tail in the MQW detectable even at 50 W/cm^{-2} proves, however, the presence of residual superradiant coupling. Fig. 2d shows plots of the intensity dependent dephasing rates of coupled nonradiative modes in the MQW and the exciton mode in the SQW. The different slope of the two curves indicates a remarkably lower excitation of the MQW at the same laser intensity because of the higher radiative recombination rate. Rapidly increasing decoupling of excitons excited in different wells is confirmed by comparison of the DFWM signal amplitudes measured on N=10 Bragg sample and a SQW in dependence on the laser beam intensities. The ratio increases from approximately 2 at low intensities (2 W/cm^{-2} to almost 70 at 50 W/cm^{-2}). The value of 2 reveals lower excitation of the MQW due to rapid radiative recombination. The value of 70 agrees fairly with the growth of the signal proportional to N^2 as expected for the incoherent superposition of the signal contributions from the indiviual QWs.

References

1. E. Hanamura, Phys.Rev. B **38**, 1228 (1988); L.C. Andreani et al., Sol.State Commun. **77**, 641 (1991); G. Björk et al., Phys. Rev. B **50**, 17336 (1994)
2. T. Stroucken et al., Phys. Rev. B **53**, 2026 (1996); E.L. Ivchenko et al., Phys. Sol. State **36**, 1156 (1994)
3. M. Hübner et al., Phys. Rev .Lett.**76**, 4199 (1996)

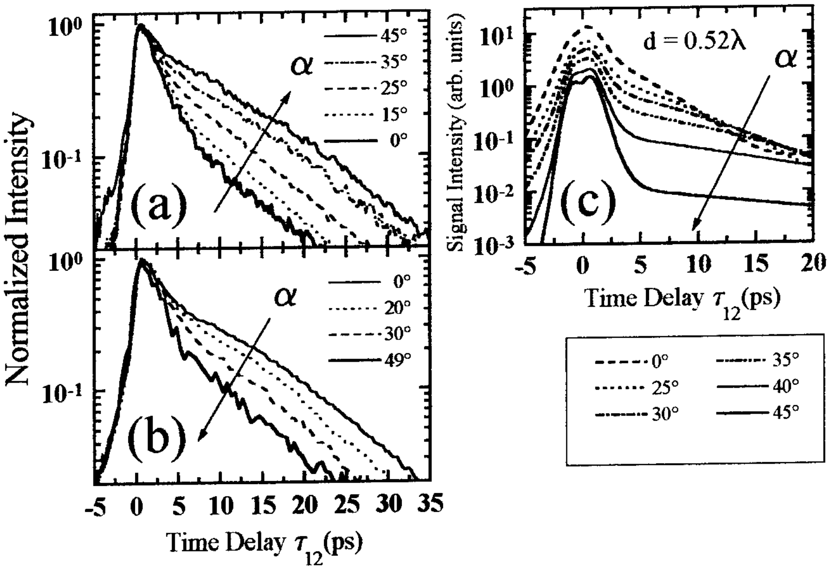

Fig. 1 :Measured angle-dependent time-integrated DFWM signals on two N=10 Bragg structures (a,b) and calculated angle-dependence for a sample with d=0.52 λ (c).

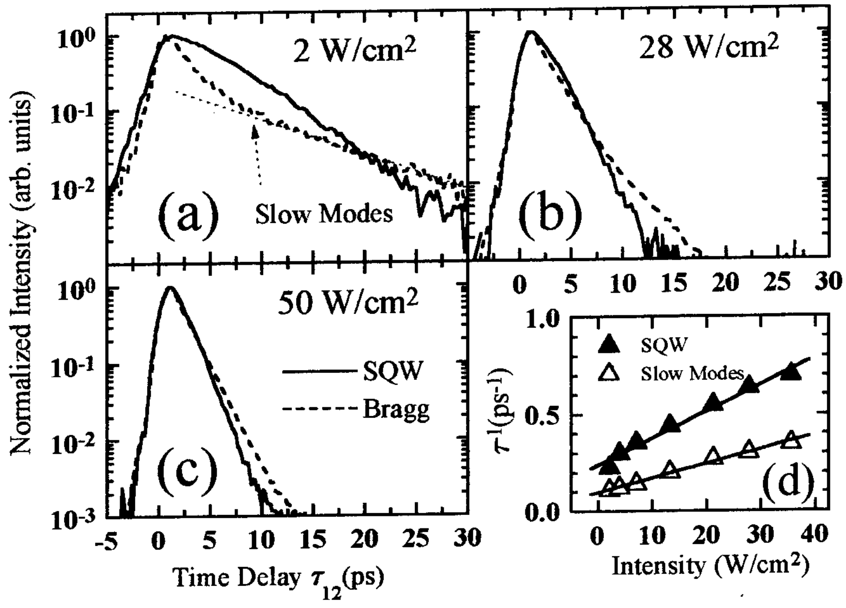

Fig. 2 : (a-c) Time-integrated DFWM signals for a SQW and a N=10 Bragg sample for 3 different excitation intensities. (d) Intensity-dependence of the signal decay rate for the SQW and the slow modes of the Bragg structure.

Probing radial electron-hole wavepacket dynamics in quantum wells with terahertz pulses

A. Maslov and D. S. Citrin

Department of Physics, Washington State University, Pullman, Washington 99164-2814

The routine availability of sub-ps laser pulses has led to the preparation and probing of electronic wavepackets in Rydberg atoms. [1] An atom – initially in the ground state – is excited optically by a short pulse to a superposition of states centered at a large principle quantum number n. Both radially [2] and angularly localized [3] electronic wavepackets have been created. The wavepacket at various time delays may then be probed by field ionization using a pulsed electric field. [2–4] In semiconductor quantum wells (QW) optically excited electron-hole (e-h) wavepackets have also been observed; [5,6] however, such wavepackets differ markedly from their Rydberg-atom counterparts. In the QW, an optical pulse centered near the QW bandedge E_0 and with a bandwidth that exceeds the $1s$-exciton binding energy coherently excites from the crystal ground state excitons with principle quantum numbers ranging from $n=1$ through the continuum. Moreover, the dipole selection rule for the excitation of e-h pairs from the crystal ground state dictates that only s states are created since these are the only states with nonzero e-h overlap. In Ref. [5], two-pulse four-wave-mixing (FWM) experiments were performed on compressively strained $\mathrm{In_{0.08}Ga_{0.92}As/GaAs}$ multiple QW's excited by 110-fs optical pulses. Compressive strain in such structures substantially increases the light-hole–heavy-hole splitting, thus allowing the excitation of e-h pairs involving only the heavy-hole. The time-integrated (TI-) FWM signal as a function of time delay between the two pulses shows distinct beating when the laser center frequency is near resonance with E_0.

Now even shorter pulses (~10 fs) with greater bandwidths are available to carry out such studies. [7] In this talk we address the *spatial* properties and the coherent dynamics of e-h wavepackets excited by sub-100-fs optical pulses and how the dynamics are expected to be manifested in the time-dependent optical emission and in the induced THz absorption associated with $s \to p$ e-h dipole transitions. [8] In addition, we elucidate the spatial dynamics of e-h wavepackets by exploiting dipole-allowed $s \to p$ transitions as evidenced by the induced absorption of half-cycle THz pulses.

An optical pulse whose bandwidth well exceeds the $1s$-exciton binding energy creates an e-h radial wavepacket initially strongly peaked at zero relative e-h displacement $\mathbf{r}$. This wavepacket then undergoes spatial spreading away from $r = 0$. At a frequency determined by the $1s$ exciton binding energy, there are partial recurrences at $r = 0$, in which the interference between the $1s$ exciton and the two-dimensional (2D) density of e-h pair states plays a major role. These recurrences correspond to *maxima* in the temporal optical-emission intensity. We also explore the effect of the wavepacket dynamics on the time dependence of the induced $s \to p$ THz absorption at various time delays following optical excitation. We show that *minima* occur at the recurrences when the e-h wavepacket projected at $r = 0$ has maxima, because the $s \to p$ transition dipole is small when the e-h separation is at a minimum. Surprisingly, in Ref. [5] the nature of the spatial wavepacket dynamics and its role in the time-integrated FWM signal was not recognized.

The model we employ is phrased in terms of the susceptibility relating the optical field to the material response of the e-h pairs. The susceptibility is expressed in the Lehman representation which allows the wavepacket dynamics to be constructed from the temporal profile of the incident optical pulse. Once the time-dependent wavepacket is obtained, we calculate the transition rate to p states induced by a half-cycle THz pulse at various time delays following optical excitation.

In Fig. 1 is shown the wavepacket for the relative motion of the photogenerated e-h pairs following impulsive excitation. Note the partial revivals (frequency given by $1s$ binding energy) which are associated with sloshing of the wavepacket back to zero relative e-h separation. The dynamics of the optical emission and time-integrated FWM will also reflect these dynamics. We will also present results for the full spatial dependence of the wavepacket and for the absorption of half-cycle THz pulses at various time delays following excitation, which is a probe of the dynamics of the first moment of the wavepacket. Thus, optical and THz probes provide direct information on the spatial dynamics of e-h wavepackets excited in semiconductors with ultrafast broadband excitation pulses.

REFERENCES

[1] For a review, see G. Alber and P. Zoller, Phys. Rep. **199**, 231 (1991).

[2] A. Ten Wolde *et al.*, Phys. Rev. Lett. **61**, 2099 (1988).

[3] J. A. Yeazell and C. R. Stroud, Phys. Rev. Lett. **60**, 1494 (1988).

[4] R. R. Jones, Phys. Rev. Lett. **76**, 3927 (1996).

[5] J. Feldmann *et al.*, Phys. Rev. Lett. **70**, 3027 (1993).

[6] The oscillatory signature in linear optics of e-h relative-motion wavepackets has also been observed in A. Knorr *et al.*, Nuovo Cimento D **17**, 1265 (1995).

[7] S. T. Cundiff *et al.*, Phys. Rev. Lett. **77**, 1107 (1996).

[8] R.H.M. Groeneveld and D. Grischkowsky, J. Opt. Soc. Am. B **11**, 2502 (1994).

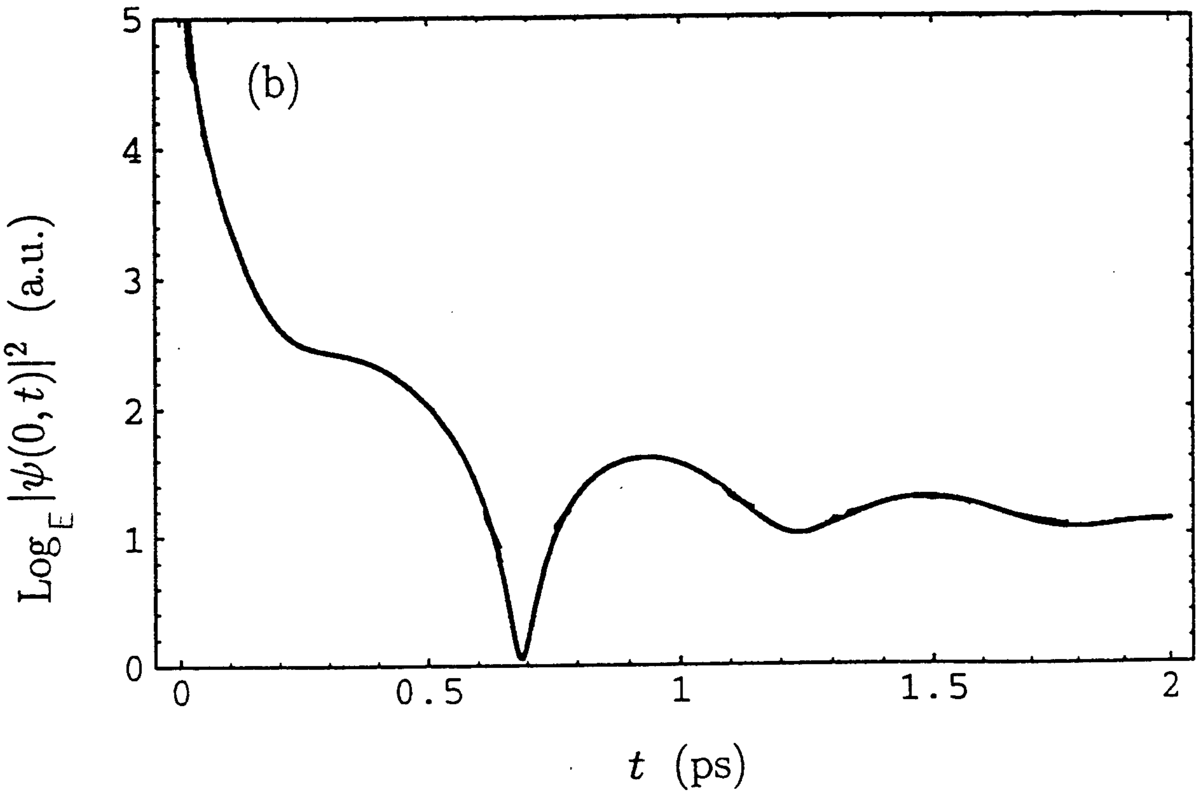

Wavepacket dynamics $\mathrm{Ln}|\psi(r=0,t)|^2$.

Thursday, March 20, 1997

Photonic Bandgaps

QThA 8:30am – 10:00am
Salon A

Eli Yablonovitch, *Presider*
University of California–Los Angeles

Reflection Properties and Defect Formation in Metallic Photonic Crystals

Ekmel Özbay, and Burak Temelkuran
Department of Physics, Bilkent University, Bilkent Ankara 06533 TURKEY
90-312-266-4397, 90-312-266-4579 (fax), e-mail: ozbay@fen.bilkent.edu.tr

M. Sigalas, G. Tuttle, C.M. Soukoulis, and K.M. Ho
Ames Laboratory and Microelectronics Research Center
Iowa State University, Ames, IA 50011 USA
515-294-1814, 515-294-9584 (fax)

Photonic crystals are three-dimensional periodic dielectric structures where the propagation of electromagnetic (EM) waves can be forbidden for a certain range of frequencies.[1-2] Early attempts to use these structures in applications like thresholdless semiconductor lasers and single-mode light-emitting diodes have suffered from the difficulties associated with fabricating sub-micron features needed to achieve a band gap at optical frequencies. On the other hand, fabricating photonic band gap (PBG) structures at microwave and millimeter-wave scales[3] have been more successful, with numerous demonstrations of PBG-based applications like high directivity millimeter wave antennas, high-quality resonators, microwave cavities for accelerators, and efficient microwave reflectors.

Although the employment of photonic crystals made of dielectric materials have been successful in various applications, some of their properties restrict the wide usage of these materials. First, the rejection from the dielectric based photonic crystals are typically limited to a maximum of 3-4 dB per layer. This means that an application requiring 40 dB isolation would need at least 10 layers, which is often too large to meet space constraints. Furthermore, for applications around 1-10 GHz range, the relatively large surface area of a photonic crystal becomes another limiting factor. As an example, a dielectric-based dielectric photonic crystal with a band gap centered at 2 GHz will have a surface area larger than one square meter which is again not practical for most applications. As has been suggested by other researchers, these problems can be solved by introducing metals to photonic crystals.[4,5] Although the metals exhibit high absorption at optical frequencies, they act like nearly perfect conductors at lower microwave and millimeter-wave frequencies which minimizes the problems related to absorption.

In our investigations of metallic photonic crystals, we first examined the face-centered-tetragonal (fct) structure. Previously, we used this structure to make dielectric-based photonic crystals with a full band gap at frequencies ranging from microwave to far-infrared.[6] In addition to the fct structure, we also used the simple tetragonal (st) structure in our examinations of metallic photonic crystals. This structure which is depicted in Figure 1, has a two-layer unit cell in the stacking direction. The metallic rods used in this study were 0.8 mm wide, 2.5 mm thick, and 120 mm long. The center to center distance between adjacent parallel rods was 7.6 mm. The rods were obtained by machining 150x150x5 mm aluminum blocks. The blocks were machined from bottom and top surfaces to create parallel rods on each side. Each block contained two layers of metallic rods, where the rods on the top side were perpendicular to the rods on the bottom side. These blocks were then stacked to form the layer-by-layer structures. Our measurements on these structures have yielded 7-8 dB/layer rejection rates along with a metallicity gap extending down to zero frequencies. We have also found out that, st type crystals yield better defect structures than fct type structures.[7]

An HP 8510C network analyzer and three microwave horn antennas were used to measure both the transmitted and reflected waves. For reflection measurements, we used a metal sheet to calibrate our measurements, where we assumed that the metal sheet is a 100% reflector at these frequencies. By changing the incidence angle θ, we could obtain the reflection and transmission properties of the photonic crystals at different propagation directions.

By using the aforementioned experimental set-up, we investigated the transmission and reflection properties of the st type metallic photonic crystal. Figure 2 shows the reflection and transmission characteristics of a 6 layer crystal along the stacking direction with an incidence angle $\theta=5^\circ$. The magnitude of the reflected and the transmitted waves were found to be independent of the polarization vector **e** of the incident EM wave. However, we found a strong polarization dependence for the phase of the reflected waves. Figure 3 shows the phase of the reflected waves as a function of frequency for both polarizations where the polarization vector e of the incident EM wave is either perpendicular or parallel to the rods of the top layer of the photonic crystal.

We used this phase information to understand and predict defect formation in photonic crystals. By separating a 12-layer photonic crystal from the middle with a separation width of L, we built planar defect structures and modeled them as Fabry-Perot resonators. We considered each 6-layer stack as the mirrors of the Fabry-Perot resonator with reflection coefficients $r_1e^{-j\phi_1}$ and $r_2e^{-j\phi_2}$, where ϕ_1 and ϕ_2 are the reflection-phase factors in radians. In a Fabry-Perot resonator the circulating electric field E_c can be written as a function of the incident electric field E_i as,

$$E_c = \frac{t_2}{1-r_1r_2e^{-j(2\beta L+\phi_1+\phi_2)}}E_i$$

where β is the propagation constant of air, and t_2 is the transmission coefficient of the second mirror. The resonant condition is satisfied when $2\beta L+\phi_1+\phi_1=2m\pi$ ($m=0, \pm1, \pm2, \pm3$), where enhancement of the circulating field results in almost unity transmission at the resonant frequency. This resonance can be used to estimate the defect frequencies for our planar defect structures.

We first measured the transmission properties and the defect frequency as a function of separation width L. Using the resonance condition, along with the measured defect frequencies, we calculated the predicted total phase contribution, ϕ_t, from the two mirrors as

$$\phi_t = \phi_1+\phi_2 = 2m\pi-4\pi L\frac{f_L}{c} \qquad (m=0, \pm1, \pm2, \pm3),$$

where f_L is the defect frequency for a separation of length L, and c is the speed of light in air. We then measured the reflection properties of the two 6-layer mirrors, and found the experimental total phase of the two mirrors $\phi_{t,exp}$ as a function of frequency. Figure 4 compares the predicted, $\phi_t(f_L)$ and the measured $\phi_{t,exp}(f)$ total phase of the two mirrors. As can be seen from the plot, the predicted phase values are in very good agreement with the measured phase values.

This work is supported by the Turkish Scientific and Technical Research Council of TURKEY (TÜBITAK) under contract No. EEEAG-156, National Science Foundation Grant No. INT-9512812, and NATO-Collaborative Research Grant No. 950079.

References

1) E. Yablonovitch, T. J. Gmitter, and K. M. Leung, Phys. Rev. Lett. **67**, 2295 (1991).

2) K. M. Ho, C. T. Chan, and C. M. Soukoulis, Phys. Rev. Lett. **65**, 3152 (1990).

3) E. Ozbay, E. Michel, G. Tuttle, M. Sigalas, R. Biswas, and K. M. Ho, Appl. Phys. Lett. **64**, 2059 (1994).

4) D. F. Sievenpiper, M.E. Sickmiller, E. Yablonovitch, Phys. Rev. Lett. **76**, 2480 (1996).

5) J. S. McCalmont, M. Sigalas, G. Tuttle, K. M. Ho, and C. M. Soukoulis Appl. Phys. Lett. **68**, 2759 (1996).

6) E. Ozbay, J. Opt. Soc. B **13**, 1945 (1996).

7) E. Ozbay, B. Temelkuran, M. Sigalas, G. Tuttle, C. M. Soukoulis , and K. M. Ho, to be published in Applied Physics Letters.

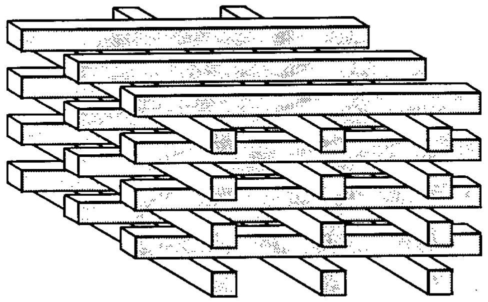

Figure 1: Schematics of simple tetragonal metallic photonic crystal.

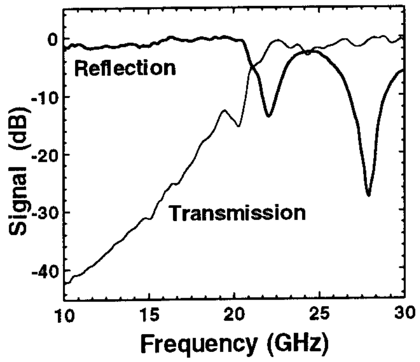

Figure 2: Transmission and reflection properties of the metallic photonic crystal.

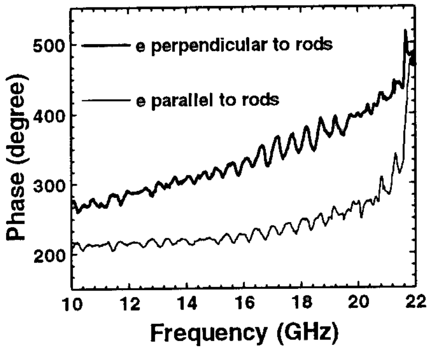

Figure 3: Reflection-phase measurements of the metallic photonic crystal.

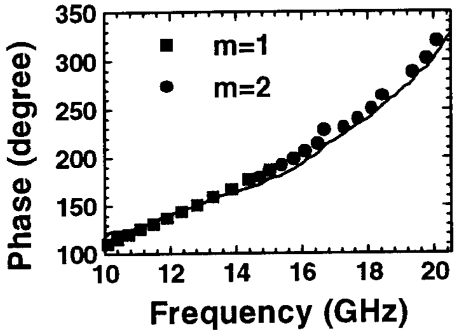

Figure 4: Comparison of the experimental reflection-phase properties(solid line), with the predicted reflection-phase properties for m=1 (squares), and m=2 (circles).

Observation of Photonic Bandgap in GaAs 2D Crystal Fabricated by Selective Growth

T. Hamano, H. Hirayama and Y. Aoyagi
The Institute of Physical and Chemical Research (RIKEN)
2-1 Hirosawa, Wako, Saitama 351-01, JAPAN
Ph.: +81 48 467 9368, Fax: +81 48 462 4659

1. Introduction

Photonic bandgap (PBG) crystals, consisting of periodic structures of two or more materials and with sizes on the order of optical wavelength have recently been extensively studied due to interest in both their physical properties and also in their possible applications to optoelectronic devices [1,2]. Analysis has shown that a 3-dimensional PBG crystal with designed-in phase shifts will control the direction of spontaneous emission due to its strong couping to localized optical modes in the bandgap. Thus a laser using a PBG crystal as its optical cavity can be expected to have a highly directional radiation pattern or high output efficiency [3]. A 1-dimensional crystal has already been utilized as a distributed Bragg reflector (DBR), and so it is necessary to demonstrate that 2-dimensional (2D) PBG crystal without phase shifts can be used as a reflector and then that a PBG crystal with inherent phase shifts may be fabricated inside a laser cavity.

A semiconductor 2D PBG crystal usually consists of either pillars of, or else holes in, a materials on top of a substrate. Various fabrication techniques for a 2D crystal have been previously tested [2,4,5], however, these all have problems associated with the fabrication of an optical cavity. As an alternatives, selective growth on masked substrates may be a suitable technique to produce GaAs pillars without the process damage and heterointerface contamination [6].

In this study, we have fabricated a semiconductor 2D PBG crystal using selective growth on (111)B GaAs, and have obtained submicron pillars of a 2D crystal of a high aspect ratio (>10) with emission layers in the middle. The existance of PBG was subsequently confirmed by the disconntinuous spectra in the photoluminescence (PL) measurement of the crystal.

2. Experiment

Selective growth by metalorganic vapor phase epitaxy (MOVPE) on a masked (111)B GaAs substrate is known to produce a hexagonal structure with (110) sidewalls [6]. The PBG structure in this work consists of hexagonal GaAs micropillars arranged in periodic 2D triangle lattice, as illustrated in Fig. 1.

GaAs substrate covered with SiO_2 masks were used for selective growth in this work. After degreasing and cleaning the GaAs substrate, a 30 nm thick SiO_2 layer was deposited by chemical vapor deposition to act as a mask, and rectangular open windows was fabricated into this by electron beam lithography and wet-etching with buffered HF. The patterned area was about 1 mm square, and the rectangular windows were 70-200 nm wide and arranged in triangle lattice of 490 nm period. The masked substrate was inserted into an MOVPE system after removing the electron beam resist.

Trimethylgallium (TMG) and arsine (AsH_3) were used as source gases, and trimethylindium (TMI) was also used for epitaxy of InGaAs quantum wells (QWs) which were introduced as emitting layers (with wavelengths of ~1.0 μm) into the middle of a GaAs hexagonal pillar. The partial pressures of AsH_3, TMG and TMI were maintained at 3.3-4.9 $\times 10^{-4}$, 6.4×10^{-7} and 6.5×10^{-8} atm, respectively. The operating pressure during growth was maintained at 38 Torr, and the substrate temperature was set at 750°C.

3. Results

The hexagonal micropillars, when grown under the appropriate growth conditions, have smooth sidewalls consisting of (110) facets and are perpendicular to the substrate, as shown in Fig. 2. The average size and height of pillars in Fig. 2 are around 103.6 nm and 1.85 μm, respectively. Thus they have a high aspect ratio of 10-15, and this may be large enough to form a 2D PBG crystal [7]. The height of pillars are dependent on the size of hexagonal section (due to the migratio fo Ga). An increasing the partial pressure of AsH_3 was found to enhance the growth rate of pillars and also to improve their uniformity.

Side-detected PL measurements were made in order to study the radiation (emission) from the QWs in the direction perpendicular to the pillars which had passed through the 2D PBG crystal where the normalized hexagonal size was ~0.23. The incident light from an Ar^+ laser with a beam spot of ~300 μmϕ was focused on the edge of the selectively grown PBG structure, and the collimated raditation was passed through a monochrometer to a Si photodiode (or an InGaAs photomultiplier) detector and analyzed by computer as usual. A 5 mm wide slit was inserted before the collimated lenses to cut out any spurious diffracted light.

In crystals of the form of triangularly arranged hexagonal pillars, the PBG can appear only in certain directions, and it along these that the PL spectra were measured in both of *H*- and *E*-polarizations. In Fig. 3, the calculated PBGs are shown along with the PL spectra in both polarizations in Γ-J and Γ-X directions in the first Brillouin zone. It is clear that the measured spectra are discontinuous and that their wavelengths are almost matched with those of the calculated PBG edges, such as 0.88 μm in *E*-polarized spectra in Γ-J direction and 0.91 μm in *H*-polarized spectra in Γ-X direction. From this we infer that it is the presence of the PBG in the fabricated crystals is the cause of the dips in the PL spectra.

4. Summary

For the first time, semiconductor 2D PBG crystals have been fabricated by selective growth on (111)B GaAs and their effects have been demonstrated in both polarizations.

Thus it has been shown that this selective growth technique is suitable for the fabrication of pillars of submicron height, however in order to produce ideal 2D PBG characteristics, it is necessary to improve the structrure of crystal by increasing the aspeact ratio and uniformity of the micropillars.

Reference

[1] K. Inoue, M. Wada, K. Sakoda, A. Yamanaka, M. Hayashi and J. W. Haus: Jpn. J. Appl. Phys. **33** (1994) L1463. [2] T. Baba and M. Koma: Jpn. J. Appl. Phys. **34** (1995) 1405. [3] H. Hirayama, T. Hamano and Y. Aoyagi: Apply. Phys. Lett. **69** (1996) 791. [4] U. Grüning, V. Lehmann, S. Ottow and K. Busch: Appl. Phys. Lett. **68** (1996) 747. [5] T. Krauss, Y.P. Song, S. Thomas, C.D. W. Wilkinson and R. M. Dela Rue: Electron. Lett. **30** (1994) 1444. [6] S. Ando, N. Kobayashi and H. Ando: J. Crystal Growth **145** (1994) 302. [7] T. Baba and T. Matsuzaki: Jpn. J. Appl. Phys. **34** (1995) 4496.

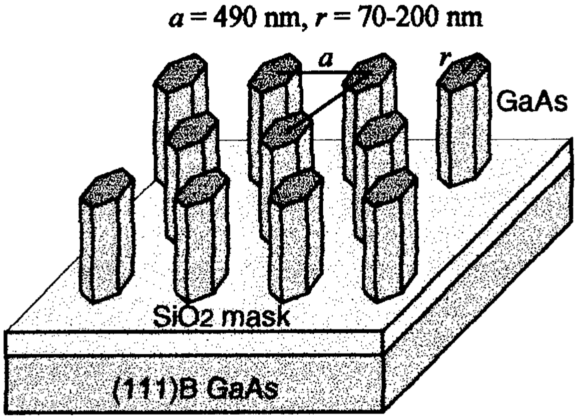

Figure 1: Schematic structure of fabricated 2-dimensional photonic bandgap crystal.

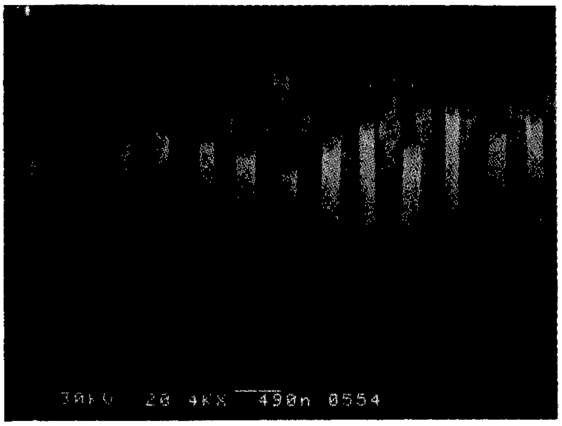

Figure 2: SEM image of hexagonal micropillars arranged in triangle lattice

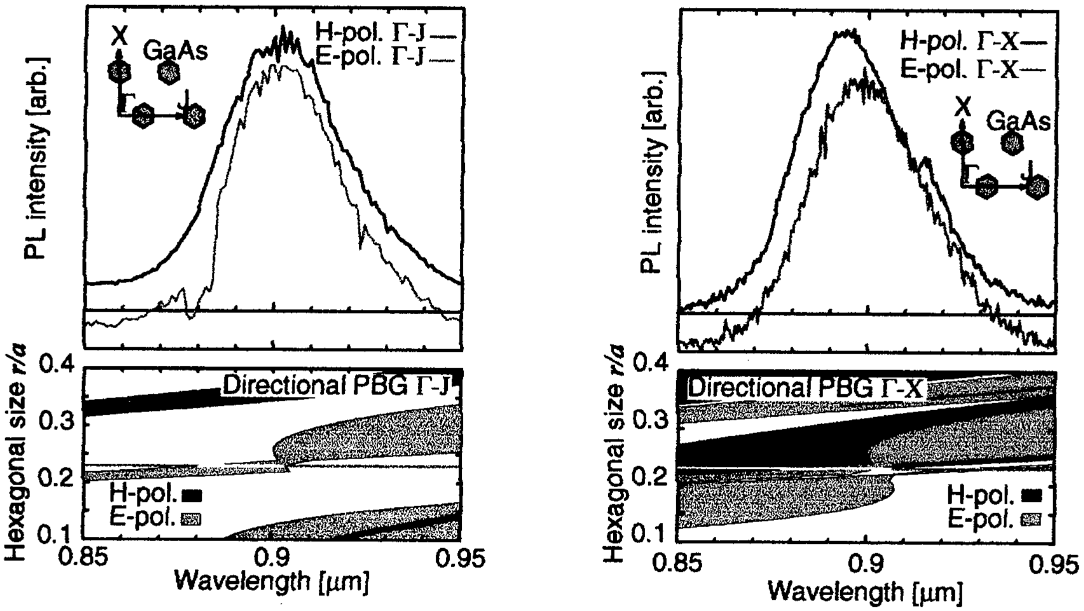

Figure 3: PL spectra detected in the direction perpendicular to the pillars and calculated results of phonic bandgap against the normalized hexagonal size. The spectra were observed in both polarizations separately. The hexagonal size of the measured crystal was ~0.23.

Observation of Photonic Bandgap in GaInAsP/InP 2D Photonic Crystals by Equivalent Transmission Measurement

T. Baba, M. Ikeda and N. Kamizawa

Yokohama National University, Div. of Electr. & Comput. Eng.
79-5 Tokiwadai, Hodogayaku, Yokohama 240, Japan
Phone +81-45-335-1451, Fax +81-45-338-1157, E-Mail baba@dnj.ynu.ac.jp

Semiconductor photonic crystals are promising candidates for realizing spontaneous emission control, i.e., enhancement of spontaneous emission rate (SER) and spontaneous emission factor. Schematic structure of various dimensions of photonic crystal and corresponding wave vector space inhibited by photonic bandgaps (PBGs) are summarized in Fig. 1. Due to the almost perfect PBG and single mode localized state, 3D structures are ideal. However, structures for optical wavelength range are still difficult to fabricate. We have studied 2D structures[1,2] to confirm preliminary effects of photonic crystals. In this study, we simply predict the spontaneous emission control in 2D structures, and report the experiment to observe PBG in GaInAsP/InP 2D photonic crystals.

Fig. 2 shows SER enhancement factor γ and SE coupling efficiency β [3], which are defined by

$$\gamma \equiv \frac{\text{total SER in photonic crystal}}{\text{total SER in bulk semiconductor}}$$

$$\beta \equiv \frac{\text{SER for a localized state in photonic crystal}}{\text{total SER in photonic crystal}}$$

They are approximately calculated as a function of normalized width $\Delta\omega_g/\omega_g$ of PBG by assuming that $\Delta\omega_g/\omega_g$ equals the interval of localized states. Such assumption is almost valid for λ-cavity 1D photonic crystals except for the effect of the change of cavity effective index. As seen in Fig. 2, increases

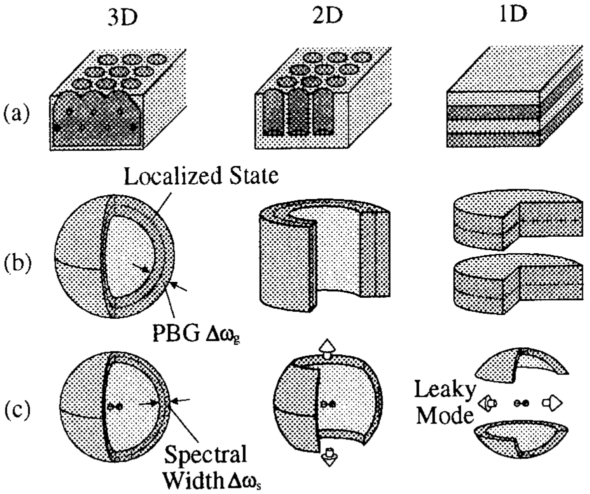

Fig. 1 Schematic structures of photonic crystal of various dimensions(a), corresponding wave vector space inhibited by PBG (b), and emission inhibited by PBG(c).

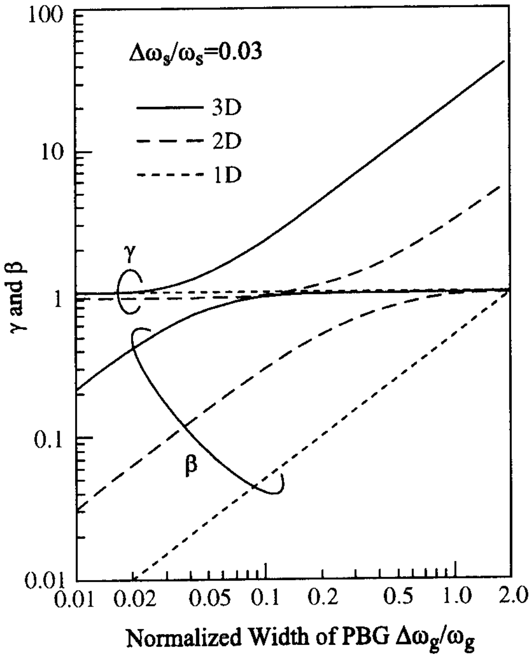

Fig. 2 SER enhancement factor γ and SE coupling efficiency β calculated with normalized width of PBG. $\Delta\lambda_s$ is spectral width of atomic radiation. Effective indexes of all modes were assumed to be equal to reference index n_{ref}.

of both γ and β are expected in 2D and 3D at $\Delta\omega_g/\omega_g > 0.2$ even though the spectral width of atomic radiation is as wide as $\Delta\omega_s/\omega_s$=0.03. It has been shown by 2D photonic band calculations that $\Delta\omega_g/\omega_g \sim 0.2$ is possible in circular holes formed on semiconductor substrate and even $\Delta\omega_g/\omega_g \sim 0.5$ is achieved for a specified polarization in semiconductor columns.$^{4)}$

So far, several authors reported the fabrication of such holes and columns made of GaAs,$^{5,6)}$ but their PBGs were not evaluated. This seems to be due to two reasons. One is the large optical absorption at their side walls deeply damaged by the dry etching process. The other is the difficulty of in-plane transmission measurement, which is often used for PBG evaluation. In this study, we fabricated columns of 0.3–0.5 µm in diameter and 1.2 µm in height by etching 1.55-µm GaInAsP/InP compressive strained MQW wafer having nearly 100 nm of emission spectral width. The SEM view of the columns are shown in Fig. 3. They were arranged with the triangular lattice of 0.7–1.2 µm in pitch so that they almost satisfied the second order PBG condition for polarization parallel to the substrate plane (TE polarization). For the etching, a methane-based reactive ion beam etching (RIBE) technique was used. From the measurement of PL characteristics, we have confirmed that the damage induced into etched side walls can be suppressed to negligible order by relatively low acceleration voltage of 200 V in the RIBE process.$^{2)}$

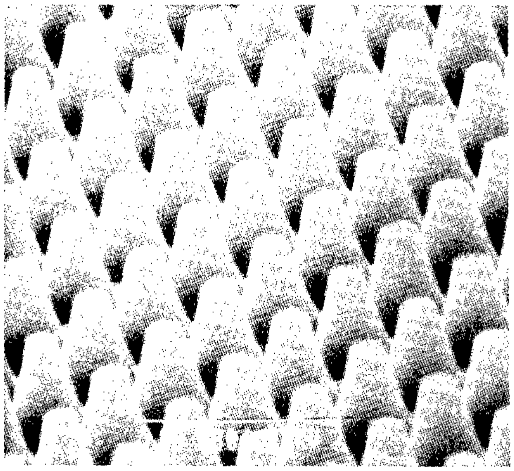

Fig. 3 Fabricated GaInAsP/InP 2D photonic crystal constructed by columns.

We evaluated the PBG of the columns by using measurement setup, as illustrated in Fig. 4. As a light source for transmission measurement, we utilized a large square region of the wafer neighboring with the columns, which was not removed by the RIBE. This region was photo-pumped from the top of the wafer. The emission in the lateral direction was detected by a single mode fiber and analyzed by an optical spectrum analyzer after passing through the columns. We prepared many samples of various column pitches *a* and repeated the measurement. By plotting all the measured spectra on the axis of normalized frequency $\omega a/2\pi c$, we can obtain the equivalent transmission characteristic of the columns. Such measurements were performed in two directions, which are expressed as Γ-X direction and Γ-J direction in Brillouin zone of the triangular lattice, as illustrated in Fig. 4.

The results are shown in Fig. 5. Here, calculated photon density of states (DOS) for TE polarization and that for the sum of 75 % TE polarization and 25 % TM one are also plotted for comparison. The polarization ratio of the latter calculation corresponds to the one experimentally observed for the used wafer. Theoretically the second order PBG for TE polarization exists at $\omega a/2\pi c$ =0.75–0.83 when assuming refractive index of columns to be 3.4. In Γ-X direction, the spectra almost overlapping with the theoretical PGB showed nearly –4 dB decrease in transmission intensity. Although the decrease in transmission intensity was ambiguous in Γ-J direction, at least –1 dB decrease could be recognized at the same frequency range. We also observed that the frequency range of low transmission intensity blue-shifted and the decrease in transmission intensity became more ambiguous when the optical fiber for detection was slightly tilted toward upper direction. This seems to be caused by the insufficient height and side wall angle of columns.

In summary, we simply predicted the spontaneous emission control effects in 2D photonic crystals and demonstrated a 2D PBG in GaInAsP/InP column arrays by evaluating equivalent transmission characteristics. For clearer evaluation, we are now trying to measure transmission characteristics directly by making columns into a wafer having much wider emission spectrum. Also, we will evaluate localized states by introducing some inuniformity in the columns.

References

1) T. Baba and T. Matsuzaki, *Electron. Lett.* **31** (1995) 1776.

2) T. Baba and T. Matsuzaki, *Jpn. J. Appl. Phys.* **35** (1996) 1348.

3) In 3D structures, β is equivalent to spontaneous emission factor *C*, while in 1D and 2D structures, β is different from *C*, since a localized state is constructed by continuous resonant modes.

4) T. Baba and T. Matsuzaki, *Jpn. J. Appl. Phys.* **34** (1995) 4496.

5) P. L. Gourley, J. R. Wendt, G. A. Vawter, T. Brennan, et.al. *Appl. Phys. Lett.* **64** (1994) 687.

6) T. Krauss, Y. P. Song, S. Thomas, C. D. Wilkinson, et.al. *Electron. Lett.* **30** (1994) 1444.

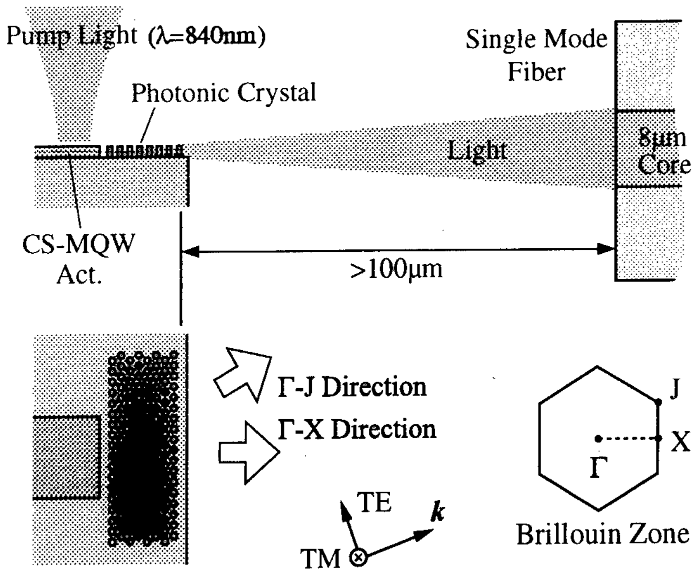

Fig. 4 Measurement setup of transmission characteristics of 2D photonic crystal constructed by columns.

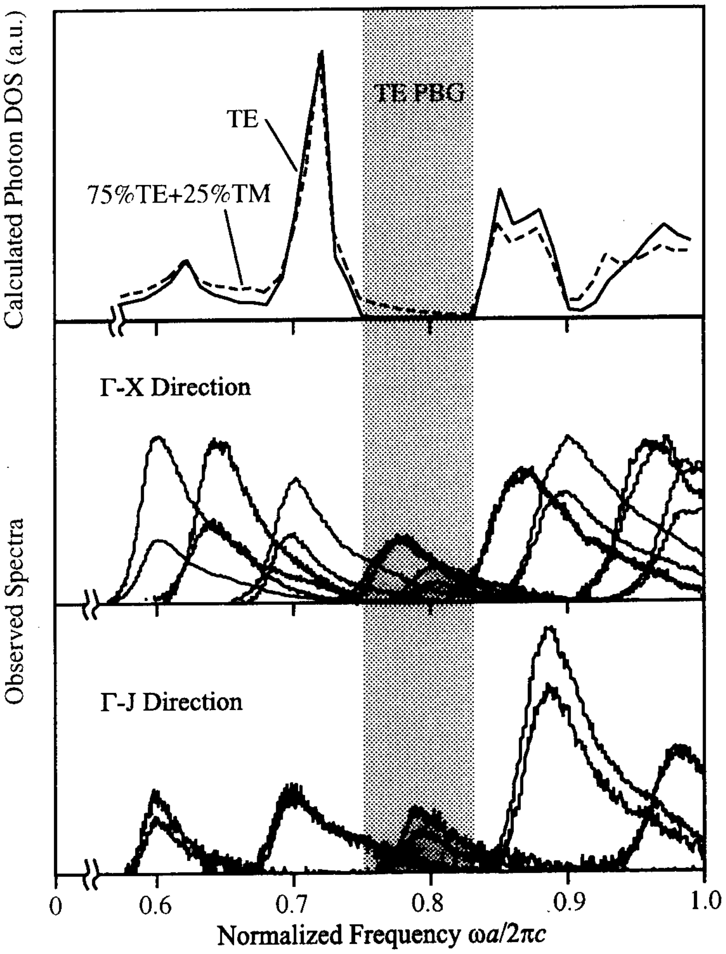

Fig. 5 Calculated photon density of states and observed emission spectra from square region after passing through columns.

Subwavelength Multilayer Binary Grating Design for Implementing Photonic Crystals

Rong-Chung Tyan, Pang-Chen Sun, Atul A. Salvekar*, Hou-Pu Chou*,
Chuan-Cheng Cheng*, Fang Xu, Axel Scherer*, and Yeshayahu Fainman

Department of Electrical and Computer Engineering, University of California at San Diego
La Jolla, CA 92093 Tel:(619)543-1893 Fax:(619)534-1225
* Department of Electrical Engineering, California Institute of Technology
Pasadena, CA 91125 Tel:(818)395-4691

1. Introduction

Subwavelength multilayer binary gratings (SMBG) can be seen as a 2-D periodic structures (see Fig.1a) with two periodic directions along the grating vector and the multilayer cascading direction. Such structures combine strong form-birefringence[1,2]of the subwavelength grating with high reflectivity due the multilayer structure allowing us to design polarization sensitive microdevices, such as polarization selective mirror and polarizing beam splitter. Recently[3] we introduce a new polarizing beam splitter (PBS) microdevice design built of SMBGs. Not only this novel design increases the angular and spectral range of the PBS microdevice in comparison to conventional PBS designs, but most importantly, our microdevice can operate with normally incident light, acting as a high-efficiency polarization-selective mirror. Microdevice with such features are critical for microlaser designs. Since the SMBG is a 2-D periodic structure, it can also be used to design a 2-D photonic crystal. In this manuscript, we summarize the design, modeling, and characterization of the SMBG structure designed to implement polarization sensitive microdevice, and also introduce and discuss a 2-D photonic crystal design based on SMBG.

2. Polarization Sensitive Microdevices

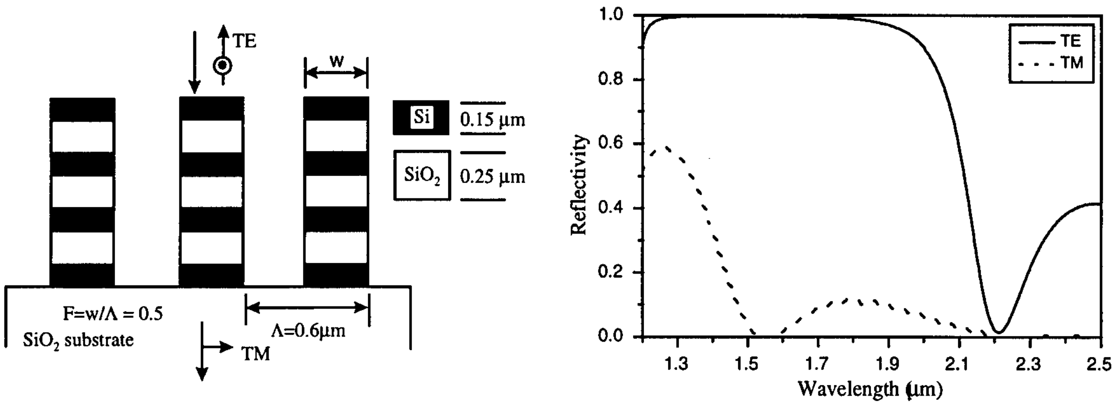

(a) (b)

Figure 1 (a) Schematic diagram of a 7-layer PBS designed for light at normal incidence. The center operating wavelength is 1.523 μm. (b) RCWA results of the reflectivity for TE and TM polarized waves vs. wavelength.

Figure 1b shows the Rigorous Couple-Wave Analysis (RCWA)[4] results of TE (E-field parallel to the grating grooves) and TM (E-field perpendicular to the grating grooves) reflectivities as a function of the wavelength for a 7-layer polarization selective mirror design shown in Fig.1a. The reflectivity spectra of TE and TM polarized light are largely separated. Furthermore, the TE reflectivity spectral band is broader and centered at a longer wavelength than those of the TM wave. Both the TE reflection efficiency and the TM transmission efficiency are higher than 99% at the design operating wavelength of 1.523 μm. The transmission polarization extinction ratios (defined as the ratio of transmittance of TM polarized light to that of TE polarized light) remain high over a broad spectral range (>200:1 over 200nm range). However, the reflection polarization extinction ratios (defined as the ratio of reflectance of TE polarized light to that of TM polarized light) are extremely high over a small spectral range (>1000:1 over 20nm range).

We have designed (see Fig. 2a) and fabricated (see Fig. 2b) a SMBG microdevice implementing PBS for incident angle of 42°. The measured and calculated efficiencies (i.e., the TM transmittance and the TE reflectance) vs. the incidence angles vary from 32° to 52° (see Fig. 3b). The experimental results and the numeric predictions are in good agreement. The experimental results show that the fabricated PBS retains high polarization extinction ratios over a large angular bandwidth

(±10°). The measured transmission polarization extinction ratios (defined as the ratio of transmittance of TM polarized light to that of TE polarized light) are higher than 220:1 with an maximum value of 830:1. The polarization extinction ratios in reflection are smaller, but still better than 40:1 with a maximum value of 70:1. The fabricated PBS element also has very high efficiencies. The measured reflection efficiency for the TE polarized light and transmission efficiency for the TM polarized light are higher than 99% and 97% respectively.

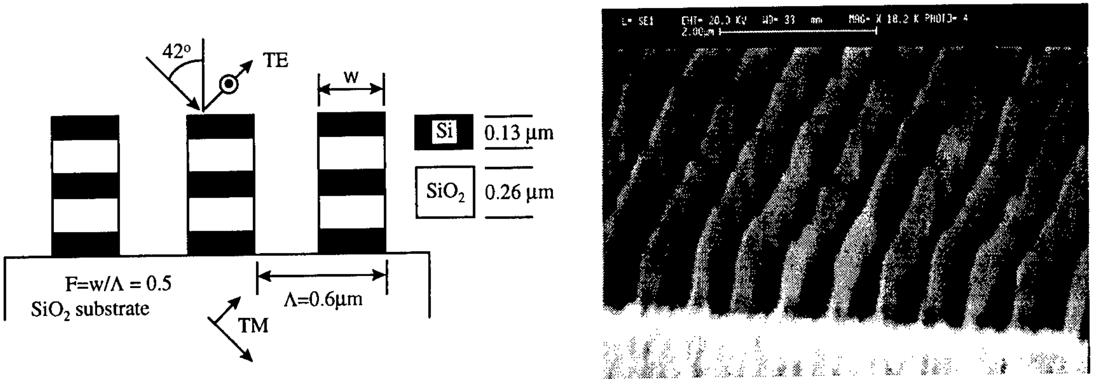

(a) (b)

Figure 2 (a) Schematic diagram of a 5-layer PBS operating with waves incident at an angle of 42°. The center operating wavelength is 1.523 μm. (b) SEM photograph of the fabricated PBS microdevice.

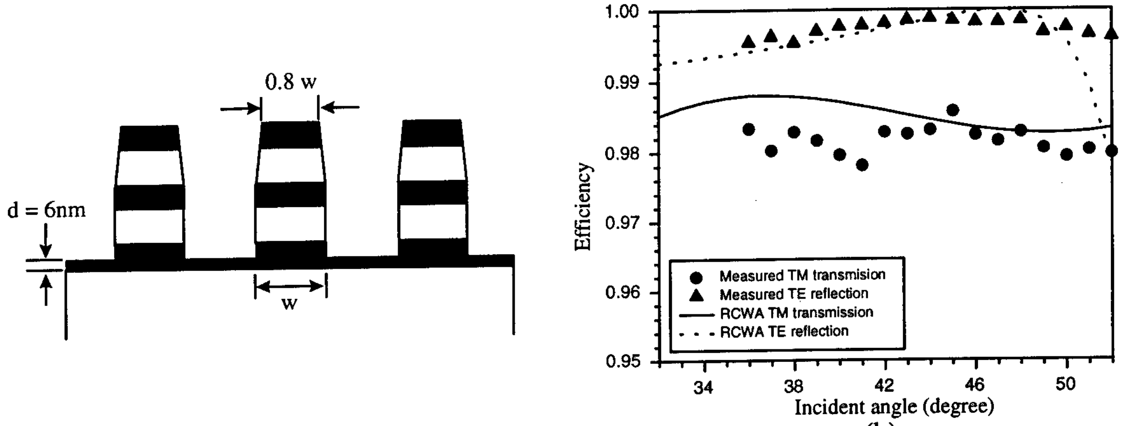

(a) (b)

Figure 3 Comparison of experimental results and numeric predictions of the fabricated PBS. (a) the device structure of Fig. 2a has been modified to encounter for the observed fabricated grating profile error and the observed under etched error. (b) the measured and the calculated efficiencies for TE and TM polarized waves.

3. Photonic Crystal

The SMBG structure shown in Fig. 1 possesses a broad reflectance band for the TE polarization in a wide angular range. This property is analogous to 2-D photonic crystals. We use three materials in contrast to most frequently used two-material design. The advantage of using three-material designs is technological. For example, some difficult to build 3-D photonic crystals can be easily fabricated with the extra supporting degree of freedom introduced by the third material. A 3-D cubic structure can be built by etching a 2-D binary grating into a multilayer mirror (see Fig. 1a).

To design photonic crystal with three materials, we use effective medium theory (EMT)[1] as a design tool similar to the method that was used in Ref.6. Later we use RCWA to validate the EMT design. Consider a simple 2-D 13-layer three-material photonic crystal shown in Fig.4a consisting of Si, SiO$_2$, and air. Our design criteria is to construct quarter-wave stacks in both x and y directions. Therefore, the grating period, Λ_y with fill factor, f_y, and the thickness of the high and low refractive indices, $d_H = f_x\Lambda_x$ and $d_L = (1-f_x)\Lambda_x$, respectively, have to satisfy the following equations,

$$\sqrt{\varepsilon_1} f_x \Lambda_x = \sqrt{\varepsilon_2}(1-f_x)\Lambda_x = \sqrt{\varepsilon_0}(1-f_y)\Lambda_y = \sqrt{\varepsilon_3} f_y \Lambda_y = \lambda/4,$$

where ε_1, ε_2, and ε_3 are the effective dielectric constants, calculated by second-order EMT[5], for each equivalent homogeneous thin layers shown in Fig.4a. From these equations, we solve for the fill factors of f_x and f_y and periods of Λ_x and Λ_y for a given incident wave at wavelength λ. For the incident field at wavelength of 1.523mm, f_x, f_y, Λ_x, and Λ_y are found as 0.319, 0.276, 0.487 μm, and 0.526 μm, respectively. As indicated above, the design is for TE polarized light.

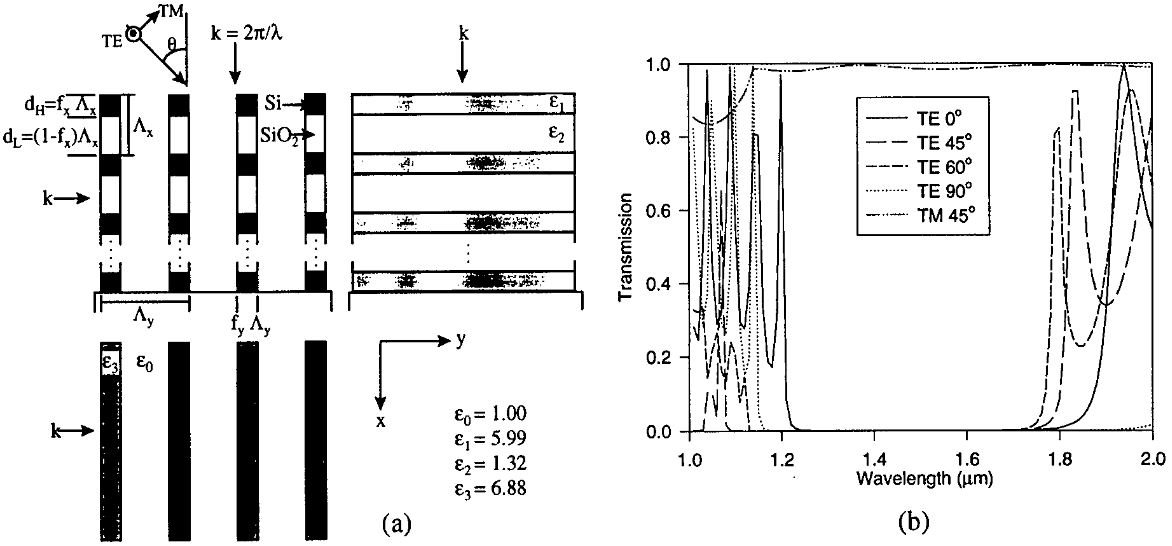

Figure 4 (a) Schematic diagram of a 2-D 13-layer two-material photonic crystal and its effective multilayer thin film stacks in vertical and horizontal directions. (b) RCWA results of transmission vs. wavelength for different incident angles. TE 90° are the results for incidence from y direction.

We use RCWA to verify the above design and the result shown in Fig.4b which shows a clear existence of a photonic band gap falling between 1.4 μm and 1.6 μm for the incidence angular range of 120° (-60° to 60°) when waves are incident from x direction. The TE 90° curve is the result for incidence from y direction and the corresponding forbidden gaps are coincident with the others. The Fig.4b also shows that, at 45° incidence angle, the structure is transparent for the TM polarized light and reflecting for the TE polarized light. Therefore, the same design can also be used for polarizing beam splitting.

4. Conclusion

SMBGs possess unique properties of strong form birefringence combined with high reflectance, making these structures superior for designing polarization sensitive microdevices. We have designed, fabricated, and experimentally evaluated a novel PBS based on such SMBG. The measurements show good performance of the element and result are well correlated with the design. We also found that our SMBG approach can be used to design 2-D photonic crystal due to its broad reflectance band for the TE polarization. We design such photonic crystal using optimization of the TE reflectivity in both x and y directions. The design verified with RCWA shows a clear photonic band structure.

References

[1] M. Born and E. Wolf, *Principles of Optics* (Pergamon, Oxford, 1975), p. 705.
[2] F. Xu, R.-C. Tyan, P.-C. Sun, Y. Fainman, C.-C. Cheng, and A. Scherer, Opt. Lett. **20**, 2457 (1995).
[3] R.-C. Tyan, P.-C. Sun, A. Scherer, and Y. Fainman, Opt. Lett. **21** 761 (1996).
[4] M. G. Moharam, and T. K. Gaylord, J. Opt. Soc. Am. **72**, 1385 (1982).
[5] S. M. Rytov, Soviet Physics JETP, **2**, 466 (1956).
[6] P. Lalanne, Appl. Opt. **35**, 5369 (1996).

Microfabrication Of Photonic Crystal Mirrors For Optoelectronic Devices.

A. Scherer, J. O'Brien, C.C. Cheng, O. Painter, R. Lee, E. Yablonovitch*
and A. Yariv

Electrical Engineering and Applied Physics
MC 200-36, Caltech, Pasadena, CA 91125
Tel.:(818) 395-4691
Fax.:(818)683-9060

* *Electrical Engineering Department, UCLA*
Los Angeles, CA 90095-1594

Photonic bandgap crystals are expected to be useful in defining microcavities for modifying spontaneous emission and as high reflectivity mirrors. Here, we use these photonic crystals as end-mirrors of edge-emitting GRINSCH lasers. These single quantum well lasers were grown by molecular beam epitaxy (MBE) and consist of waveguide structures which are in excess of 1.5 micrometers in thickness. To define a high-reflectivity photonic crystal mirror on the edge of these laser stripes, we use a surface mask of PMMA on top of an epitaxially deposited AlAs masking layer. After electron beam exposure of the resist and definition of the 100nm diameter holes through the GaAs cap layer and the 200 nm thick AlAs mask layer, high temperature field oxidation of the AlAs is performed at 340°C for 1.5 hours. This oxidizes the AlAs and forms a very robust etch mask. The hexagonal arrays of 100nm holes are then transferred to a depth of 2 microns through the laser waveguide structure so as to overlap with the optical field in the laser (Figure 1). The output mirror for the laser stripe consists of a standard cleaved facet.

The structures lased in pulsed operation. The L-I characteristic shows threshold currents of 110 mA from 180 micron long lasers. From Hakke-Paoli analyses, we find that the photonic lattice is 8 times more reflective than a dry-etched facet on a test laser. The lasers operate at about 800 nm, which is the transition due to the second quantized state in the quantum well. One fo the lasers containing a photonic grating operated in a single longtitudional mode for at least 80 mA above threshold before becoming multi-moded and eventually lased at both 850 nm and 800 nm.

We have also microfabricated 3-D photonic crystal mirrors as reflectors for laser stripes (Figure 2), and are using the laser emission from the cleaved edge to characterize the quality of these photonic bandgap structures.

Figure 1. SEM micrograph of a 2-D photonic crystal at the end of an edge-emitting laser stripe.

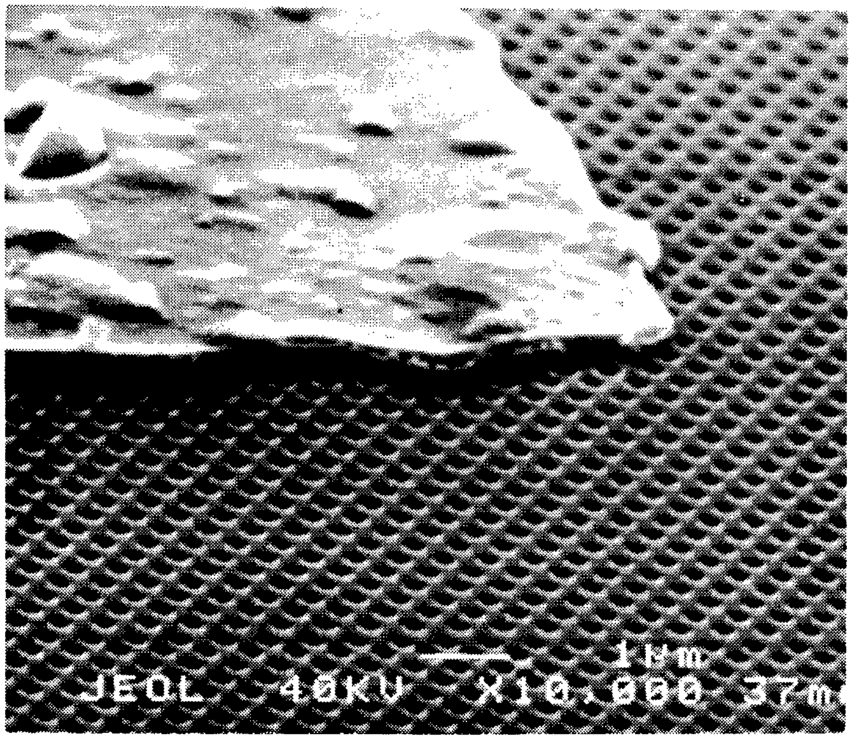

Figure 2. SEM micrograph of a 3-D photonic crystal

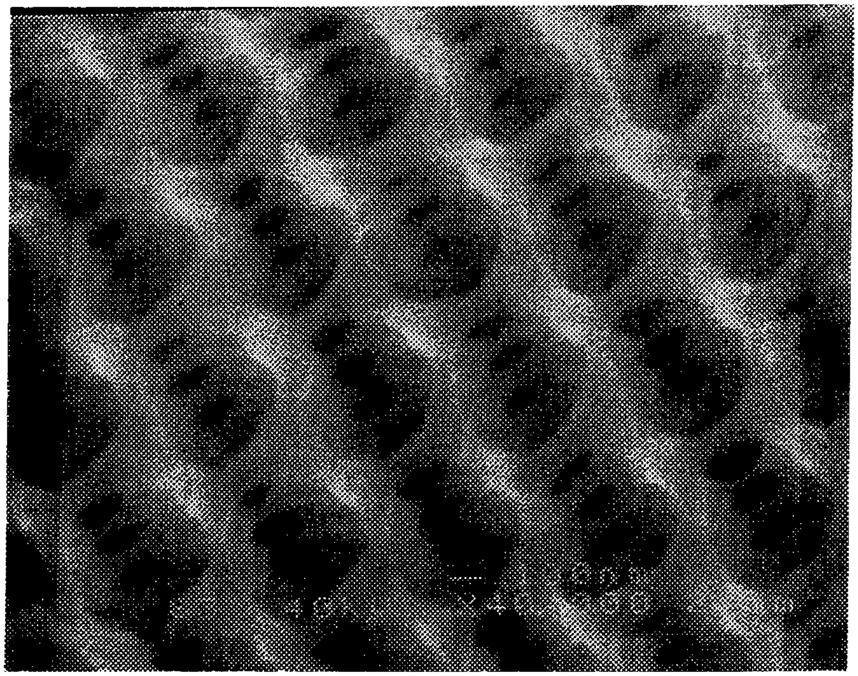

QED?

QThB 10:30am – 12:00m
Salon A

Galina Khitrova, *Presider*
University of Arizona

Quantum Statistical Effects of Microcavity Exciton Polaritons

H. Cao, S. Pau, F. Tassone, R. Huang, G. Björk[a], and Y. Yamamoto[b]
ERATO Quantum Fluctuation Project, E. L. Ginzton Laboratory
Stanford University, Stanford, CA 94305.

In the past few years there has been extensive study on exciton-photon coupling in a quantum well (QW) embedded semiconductor microcavity [1, 2]. The strong coupling between the QW exciton state and the cavity photon state results in the new eigenstates of this coupled systems, i. e. the exciton-polariton states [3]. The microcavity exciton-polaritons, as new quasiparticles, features interesting quantum statistics.

First of all, since excitons can be approximated as bosons at low density, the stimulated generation of k=0 excitons by phonon scattering is possible. Namely after the pump creates hot excitons, the k=0 excitons can stimulate the hot excitons to jump to the k=0 state by emitting phonons, and those generated k=0 excitons have the same phase as the initial k=0 excitons.

However there are two difficulties in achieving the stimulated generation of bare excitons in GaAs QW: First, the thermal de Broglie wavelength of exciton is quite small, e. g. it is comparable with the exciton Bohr radius at 4 K. Thus it is difficult to realize that the thermal de Broglie wavelength of exciton is larger than the interparticle spacing while still keeping the interparicle spacing large enough that excitons can still be approximated as bosonic quasiparticles. Secondly the fast recombination of $k_{//} = 0$ excitons makes it difficult to accumulate excitons in the k=0 state to start the stimulation process.

To increase the thermal de Broglie wavelength, we dress the exciton with photon in a semiconductor microcavity. Since the mass of the microcavity exciton-polariton is much smaller, its thermal de Broglie wavelength is much larger [4]. Thus it is much easier to achieve the stimulated generation of exciton-polaritons, i. e. the exciton polariton boser.

To overcome the rapid decay of $k_{//} = 0$ excitons, the fast longitudinal optical (LO) phonon scattering process is used as an efficient pumping scheme. Namely if only the hot excitons or electron-hole pairs, whose energy is one LO phonon energy above the bottom of the exciton band, are created by the pump light, they can be efficiently scattered into $k_{//} = 0$ exciton state by one LO phonon emission. Experimentally as we scan the pump light wavelength across the LO phonon resonance, we observed a huge enhancement of forward emission intensity of the microcavity exciton-polariton, as shown in figure 1.

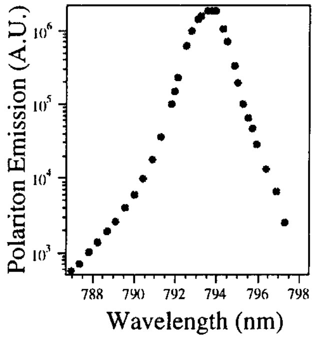

Figure 1: The normal emission intensity of microcavity exciton-polaritons as a function of pump light wavelength.

Next we set the excitation energy at one LO phonon energy above the bottom of the upper polariton band, and increase the excitation intensity. Figure 2 (a) shows the evolution of the emission spectra as we increase the pump intensity. We can see that as the exciton density increases, the upper polariton peak increases much faster than the lower polariton peak. If we plot the integrated upper polariton emission intensity as a function of pump power [see figure 2 (b)], we can clearly see a superlinear increase of the emission intensity with a threshold. This indicates a nonequilibrium buildup of upper polariton population, which we attribute to the stimulated generation of upper polaritons by LO phonon emission.

As the exciton density increases further, the exciton-exciton interaction becomes important. In GaAs QW, the monolayer fluctuations of the well thickness results in many islands [5]. If the lateral size of those islands is equal or larger than the exciton Bohr radius, an exciton tends to localize within one island. As the excitation intensity increases, the probability of two excitons occupying the same island increases. If the lateral size of the island is comparable with the exciton Bohr radius, each island can only hold one exciton due to the repulsive Coulomb interaction between excitons at such short interparticle spacing. Hence, such exciton system behaves more like a Fermionic system. However in sufficiently large islands, the attractive interaction between two excitons with opposite angular momentum is dominant, leading to the formation of biexciton. Such an attractive interaction favors more than one exciton occupation in one island, and hence the exciton

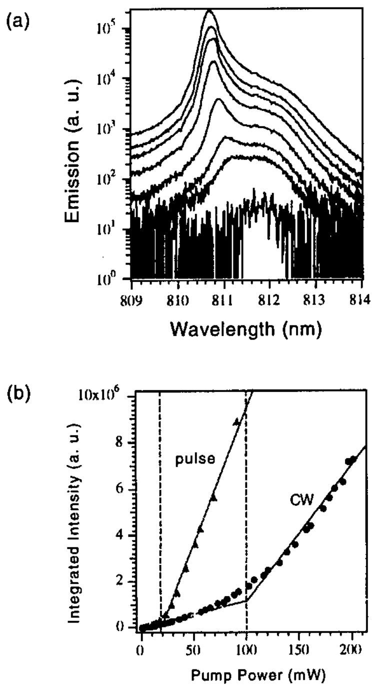

Figure 2: (a) The evolution of the exciton-polariton emission spectrum as the pump intensity increases. (b) The integrated upper polariton emission intensity as a function of pump power.

system is more like a Bosonic system. Therefore, from the quantum statistical point of view, QW exciton system is a very interesting system to study because it can demonstrate a continuous transition from a system of Fermions to a system of Bosons.

Figure 3 shows the energy levels of dressed excitons, dressed Fermions, and dressed Bosons. In the weak excitation regime where the system is excited to $N = 1$ manifold, the emission spectra due to the transitions from $N = 1$ to $N = 0$ manifold ($1 \rightarrow 0$) are identical for the dressed Fermion and dressed Boson systems. However as the excitation intensity increases, the system is excited to $N = 2$ manifold. For Fermions, the four transitions from $N = 2$ to $N = 1$ manifold ($2 \rightarrow 1$) results in additional peaks in the emission spectrum. For non-interacting Bosons, the two outlying transitions from $2 \rightarrow 1$ are forbidden (marked by cross), and the remaining four transitions are pairwise degenerate (circled together), with the transition frequencies coinciding with those two from $1 \rightarrow 0$. Therefore the emission spectrum still consists of only two peaks. In the case of excitons, the attraction between excitons with opposite angular momentum switches on the two forbidden transitions from $2 \rightarrow 1$, and red-shifts the $2 \rightarrow 1$ transition frequencies. Therefore the biexcitonic effect gives additional peaks in the emission spectrum of microcavity exciton-polaritons.

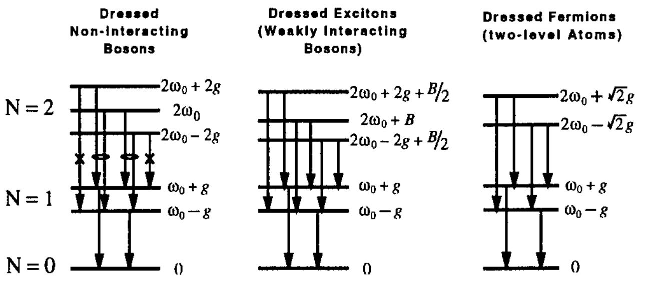

Figure 3: Dressed state level diagram of $N = 0, 1, 2$ excitation manifolds. g is the exciton-photon coupling constant. B is equal to half of the biexciton binding energy.

Experimentally we first chose the excitation spot where the cavity photon state is in resonance with one localized QW exciton state in a MOCVD grown microcavity sample, and then resonantly created the localized QW excitons by Ti:S laser pulses. Figure 4 shows the evolution of the emission spectra as we increased the intensity of the linearly polarized pump beam. In the weak excitation regime, the emission spectrum features Rabi splitting. As the excitation intensity increases, the emission spectrum becomes asymmetric, and two additional peaks emerge on the low frequency side. This indicates that the exciton-exciton interaction is mainly attractive. However as we change the pump beam polarization from linear to circular while keeping the same pump intensity, the emission spectrum changed drastically from 4 peaks to 2 peaks, as shown in figure 5. This confirms that the additional features, which appear at higher intensity of the linearly polarized pump light, indeed originates from the biexcitonic effect.

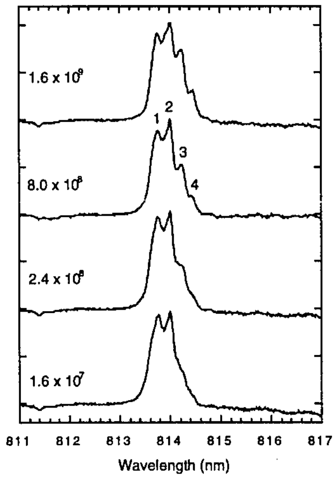

Figure 4: The observed evolution of the emission spectra as we increase the intensity of the linearly polarized pump light. The initial exciton densities created in the QW by the short laser pulses are written in the unit of cm^{-2}.

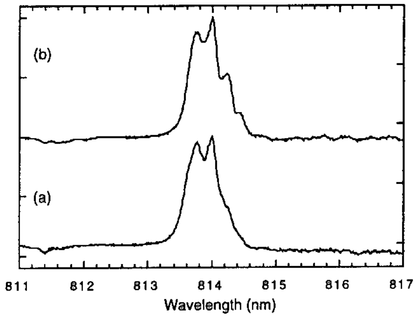

Figure 5: The observed emission spectra when the pump light is (a) circularly polarized, (b) linearly polarized. The QW exciton density is kept constant in the two cases, i. e. 8×10^8 cm^{-2}.

In conclusion, we have shown two interesting quantum statistical effects of microcavity exciton polaritons. One is the stimulated generation of exciton polaritons through LO phonon scattering process. The other is the onset of additional spectral sidebands of exciton polaritons due to the exciton-exciton interaction. This indicates a fundamental connection between a system of weakly interacting Bosons (excitons) and a system of Fermions (two-level atoms) at higher densities.

References

[1] Y. Yamamoto, and R. E. Slusher, *Physics Today* **46**, 66 (June 1993).

[2] R. E. Slusher, and C. Weisbuch, *Solid State Commun.* **92**, 149 (1994).

[3] C. Weisbuch, M. Nishioka, A. Ishikawa, and Y. Arakawa, *Phys. Rev. Lett.* **69**, 3314 (1992).

[4] A. Imamoğlu, R. J. Ram, S. Pau, and Y. Yamamoto, Phys. Rev. A **53**, 4250 (1996).

[5] H. Cao, S. Pau, Y. Yamamoto, and G. Björk, Phys. Rev. B **54**, 8083 (1996).

[a] Present address: Department of Electronics, KTH Electrum 229, S-16440 Kista, Sweden.

[b] Y. Y. is also affiliated with NTT Basic Research Laboratories, Atsugishi, Kanagawa, Japan.

Anomalous Diffusion of Repulsive Bosons in a Two-Dimensional Random Potential

T. Fukuzawa^A, S. Y. Kim^B, T. K. Gustafson^B, E. E. Haller^C, and E. Yamada^D

A) PRESTO, JST, IBM Research, Tokyo Research Laboratory, Yamato-shi, Kanagawa 242, Japan,
(phone 81-462-73-4860, FAX 81-462-73-7413)
B) University of California, Berkeley, E.E.C.S. Dept., Berkeley, CA 94720 U.S.A.
C) University of California and Lawrence Berkeley National Laboratory, Berkeley, CA 94720 U.S.A.
D) Meisei University, Faculty of Information Sciences, Nagabuchi, Ome-shi, Tokyo 198, Japan

Two-dimensional (2D) bosons can undergo a Kosterlitz-Thouless transition[1], which does not involve macroscopic occupation of a single quantum state, but which can still result in superfluidity. In addition, strongly interacting bosons subject to a random potential can also exhibit superfluidity, as in the case of charged superfluidity that occurs in high-T$_c$ superconductors. Competition between the strength of the interaction and the degree of potential disorder are among the many complicated and competing factors which determine whether superfluidity is promoted or supressed in a Bose system[2]. Strong potential disorder forces bosons to localize and can result in an insulating Bose glass phase. Alternatively, repulsive interactions among bosons act to release them from their traps, to keep their inter-particle distances as uniform as the potential allows, and to arrange the flow direction. An appropriate interaction strength can thus promote superfluidity.

To study the macroscopic quantum effects of interacting 2D-bosons in a random potential, we previously proposed an electric-dipole-oriented exciton system in GaAs/AlGaAs coupled double quantum wells[3] with an electric field applied normal to the plane of the wells, and conducted initial experiments[4]. In the experimental coupled quantum well (CQW) samples, the widths of the GaAs quantum wells and AlGaAs intermediate barriers exhibit atomic layer fluctuations dependent on the epitaxial crystal growth conditions. These heterojunciton interface irregularities impose a random potential disorder. Optical pumping at appropriate excitation energies creates direct excitons with significant spatial overlap in the electron and hole probability amplitudes. For CQW systems under an applied electric field, the direct excitons relax to indirect excitons with electrons and holes confined in adjacent quantum wells. This spatial separation of the electron and hole creates a fixed electric dipole moment. Furthermore, the radiative recombination lifetime is increased by a factor of 1000 times with respect to that of direct excitons[5]. Thus, the system can be regarded as one of quasi-equilibirum 2D bosons with dipole-dipole repulsive interactions in a random potential.

The random potential disorder causes inhomogeneous broadening of the photoluminescence (PL) spectra. The density of states $D(E)$ reflecting the spatial variation of exciton energy can be determined from the experimental exciton PL spectral curves[6]. In subsequent analyses and experiments the quantity $E_{av}(n,T)$ - the mean photon energy of the recombination emission of excitons with density n at temperature T, was used to infer the boson energy distribution. E_{av} reflects the quasi-equilibrium energy distribution $f(E,T)$ of the excitons weighted by the sample-dependent density of states $D(E)$ and the energy dependent recombination rate $\tau(E)$, which is strongly weighted towards lower energy recombination sites. We previously reported the exciton density dependence of E_{av} at different temperatures, and found possible evidence of boson correlation in the system[7].

To theoretically investigate boson diffusion in the above system, quantum Monte Carlo simulations were performed employing the Metropolis algorithm[8]. The potential randomness used in the simulation was obtained from experimental PL spectra. The diffusion of dipole oriented indirect excitons among the local minima of the random potential due to thermal activation and under the influence of mutual Coulomb repulsion was modeled by the variable-range-hopping mechanism. The total exciton energy E_{total} in the system was calculated after an adequate number of Monte Carlo steps and the exciton mean energy $E_{av} = E_{total}/N_{ex}$ was compared with the experimental results. Here, N_{ex} is the number of excitons in the simulation. Without Bose correlation effects, due to strong Coulomb repulsion the evolution of the dipole oriented excitons should correspond to classical or fermion particle diffusion.

The exciton density dependence of E_{av} in experiments and simulation were in good agreement at higher temperatures, but differed in the low temperature range[8]. In the simulation, E_{av} for lower temperatures was always larger than at higher temperatures for the entire range of exciton densities considered, which implies that excitons have less mobility at lower temperatures. For a fixed temperature, higher exciton densities also result in larger E_{av}, because excitons begin to accumulate in the higher energy sites as the lower energy sites are filled. In contrast, the experimental results at lower temperatures displayed sudden reductions in E_{av} at higher exciton densities[8][9]. This suggests that there is an unknown mechanism which promotes exciton migration to lower-energy sites. If this anomaly originates from a phase transition from the trapped boson (Bose glass) phase to the superfluid phase, one should expect to find a similar anomaly in the temperature dependence of E_{av}.

To confirm our earlier interpretation[7][8][9] of possible boson correlation effects in 2D excitons in CQW systems, the detailed temperature dependence of average PL spectra energy E_{av} was measured for temperatures between 2 to 9 K. Figure 1 shows the temperature dependence for E_{av} at these excitation levels, 23.8 μW, 53.2 μW, and 180 μW. The observed $E_{av}(T)$ in this temperature range increases with decreasing T because of reduced hopping mobility and enhanced trapping at higher-energy sites (reduced flow in energy space). However, the rate of change of E_{av} decreases prominently as the temperature is lowered below a critical temperature T_c, (4 - 6 K for the above excitation intensities). Furthermore, the critical temperature tends to increase with increasing exciton density (i.e. excitation intensity). The curves have sample-specific fine structures, but the general tendency of this change in curvature in E_{av} is universally observed, indicating the onset of an abrupt shift in the exciton energy distribution due to enhanced downward flow in energy space.

According to the simulations, without Bose correlation E_{av} is expected to become larger as temperature is decreased or exciton densities are increased. Therefore, these three curves should not cross each other, and such behavior is observed in the higher temperature range from 6 to 9 K. However, when the excitation density becomes higher and temperature becomes lower, there are inversions of the $E_{av}(n, T)$ curves.

This anomaly in E_{av} versus the temperature and exciton density provides evidence for the onset of Bose correlation - that is, contact of de Broglie wavelengths of a macroscopic number of trapped excitons - induced as the temperature is lowered below a critical temperature. Higher excitation reduces the average inter-particle distance and results in higher T_c.

References

[1] J. M. Kosterlitz and D. J. Thouless, J. Phys., **C6**, 1181 (1973).

[2] P. Nozières, *Bose-Einstein Condensation*, Eds., A. Griffin, D. W. Snoke and S. Stringari, pp. 15-30, Cambridge University Press, New York (1995); K. Huang, ibid., pp. 31-50.

[3] T. Fukuzawa, S. S. Kano, T. K. Gustafson, and T. Ogawa, *Proceedings of 4th Int. Conf. on Modulated Semiconductor Structures*, Michigan, July 17th 1989; Surface Science, **228** 482 (1990); T. Fukuzawa, T. K. Gustafson, and E. Yamada, IEEE J. of Quantum Electronics, QE Letters, **26** 811 (1990).

[4] T. Fukuzawa, E. E. Mendez, and J. M. Hong, Phys. Rev. Lett., **64** 3066 (1990)

[5] A. Alexandrou, J. A. Kash, E. E. Mendez, M. Zachau, J. M. Hong, T. Fukuzawa, and Y. Hase, Phys. Rev., **B42** 9225 (1990).

[6] J. A. Kash, M. Zachau, E. E. Mendez, J. M. Hong, and T. Fukuzawa, Phys. Rev. Lett., **66** 2247 (1991); ibid. **69**, 994 (1992).

[7] T. Fukuzawa and E. Yamada, Superlattices and Microstructures, **15** 151 (1994).

[8] T. Fukuzawa and E. Yamada, IL Nuovo Cimento, **17D**, 1459 (1995).

[9] T. Fukuzawa, S. Y. Kim, T. K. Gustafson, E. E. Haller and E. Yamada, Superlattices and Microstructures, **20** in printing (1996).

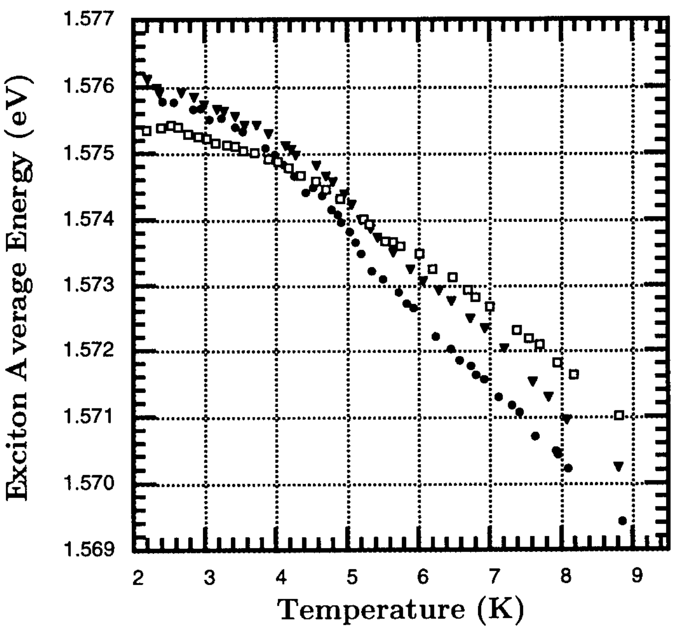

Figure 1. Temperature dependence of the average photon energy $E_{av}(n, T)$, for various excitation levels: 23.8 μW (solid circles), 53.2 μW (solid triangles), and 180 μW (open squares).

Cavity-Polariton Formation and Relaxation Dynamics in Semiconductor Microcavities

J.D. Berger[1], S. Hallstein[2], W.W. Rühle[3], O. Lyngnes[1], G. Khitrova[1], H.M. Gibbs[1],
M. Kira[3], F. Jahnke[3], and S.W. Koch[3]

[1]*Optical Sciences Center, University of Arizona, Tucson, AZ 85721, USA, Ph: 520-621-2452, FAX: 520-621-4323*
[2]*Max-Planck-Institut für Festkörperforschung, Heisenbergstraße 1, D-70569 Stuttgart, Germany*
[3]*Fachbereich Physik der Philipps-Universität, Renthof 5, D-35032 Marburg, Germany*

Semiconductor microcavities are of inherent physical importance for their ability to dramatically alter the emission properties of solid states. Of particular interest is the strong coupling regime, characterized by a cavity-exciton coupling which dominates over irreversible decay mechanisms. This regime has been the focus of abundant activity since the first observation of the normal mode splitting in a semiconductor microcavity.[1] Recent work has elucidated cavity-polariton emission properties in both the linear[2] and nonlinear[3,4,5] regimes.

Here we report on the dynamics of cavity-polariton formation and relaxation in a strongly coupled semiconductor microcavity. We measure the temporal evolution of the cavity-polariton emission spectra when the initial carrier distribution is generated far from thermal equilibrium, and find that the emission dynamics exhibit curious behavior in the presence of the cavity. The data are in accordance with a microscopic theory which includes quantization of both the material polarization and the field, and explains the observed behavior in the context of carrier cooling inside a normal mode coupling microcavity.

The quantum well (QW) microcavity consists of a $3\lambda/2$ GaAs spacer between symmetric 99.6% GaAs/AlAs Bragg mirrors, with two 80 Å $In_{0.04}Ga_{0.96}As$ QWs placed at the antinodes of the intracavity field. The cavity mode is tuned with respect to the exciton resonance by scanning across the tapered sample. The sample was held at 15 K in the center of a superconducting magnet, and oriented in Faraday geometry. The microcavity was excited in a reflection minimum 109 meV above the exciton resonance by 2ps pulses from a mode-locked Ti:Sapphire laser with 80 MHz repetition rate. The microcavity emission was dispersed in a 0.32 m spectrometer and then detected by a synchroscan streak camera. The spectral and temporal resolutions are 0.5 nm and 7 ps, respectively.

Figure 1 shows the time evolution of the microcavity exciton-polariton emission for increasing pump intensities. At low excitation, the lower polariton luminescence dominates. The upper polariton emission grows sharply with increasing excitation, while the lower polariton emission clamps at a constant value, as observed in the time-averaged emission of Fig. 2. Particularly interesting behavior occurs at a pump intensity of 135 W/cm^2. As carrier cooling takes place, the upper polariton intensity grows in time with respect to the lower polariton, and then decreases as the lower polariton intensity rises up to eventually dominate. Ultimately the Mott density is reached, and we no longer have a coupled exciton-polariton. At 450 W/cm^2 we observe lasing from the detuned cavity mode, which is part way between the two low-density luminescence peaks. The lasing threshold is characterized by a sharp increase in the emission intensity (see inset of Fig. 2) and decay rate, as well as a linewidth reduction.

The growth of the upper polariton mode in time is even more pronounced at high magnetic field, where the coupling strength increases[6] and the continuum is quantized into discrete Landau levels which are well-separated from the exciton resonance. Absorption in the continuum, which most strongly affects the high energy mode, is consequently minimized.

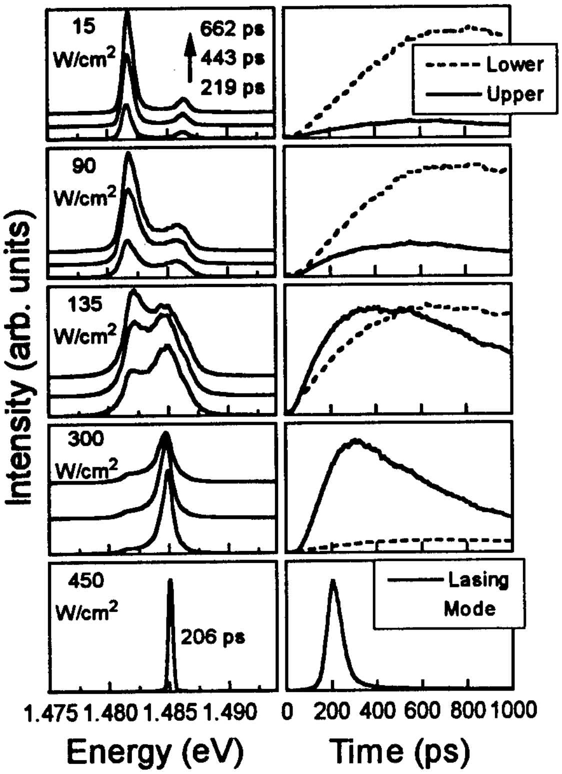

Fig. 1. Time evolution of the microcavity exciton-polariton emission after 2ps excitation with increasing intensities. The cavity mode is 2.39 meV above the exciton resonance. The left column shows emission spectra from different time windows. The right column shows the time-dependent emission from the upper (solid) and lower (dashed) polaritons.

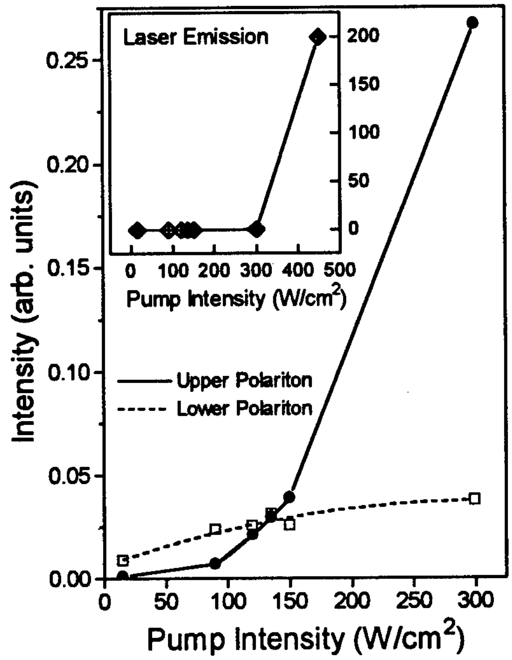

Fig. 2. Time-averaged emission versus pump intensity from the data of Fig. 1, showing a strong increase in the upper polariton emission, and clamping of the lower polariton. The inset shows the lasing threshold curve.

Figure 3 shows the time-resolved magnetoexciton polariton emission spectra under 14 T magnetic field. At early times, the emission intensity from the two modes is nearly symmetric. Then the upper polariton grows dramatically in time with respect to the lower polariton as carrier cooling takes place. Eventually we observe an intensity crossing of the two modes, after which the lower polariton emission dominates. Figure 4 details the time evolution of emission intensity, linewidth, and peak energy for the upper and lower polariton modes. The upper polariton linewidth decreases as the intensity increases, reaching a minimum when the intensity is maximum. The lower polariton, in contrast, exhibits a slowly increasing linewidth as thermalization takes place. The upper polariton also shifts to lower energies with time, reaching a minimum when the intensity is highest, while the lower polariton peak energy does not shift in time.

This interesting behavior is contrary to what one might expect in a simple picture of exciton thermalization. In the absence of the cavity, an initially broad exciton distribution narrows to lower energy states as relaxation takes place via phonon emission. Here we observe the thermal distribution in time through the eyes of the coupled cavity-polariton. The data are in excellent agreement with a microscopic theory which includes quantization of both the material polarization and the field. These calculations show that the emission dynamics can be explained as follows: Carriers are initially generated high above the band edge. As thermalization takes place, the modified exciton absorption lineshape and the corresponding index changes lead to a strong increase of the upper polariton luminescence. The gradually increasing carrier population also results in a shift of the upper polariton mode to lower energy.

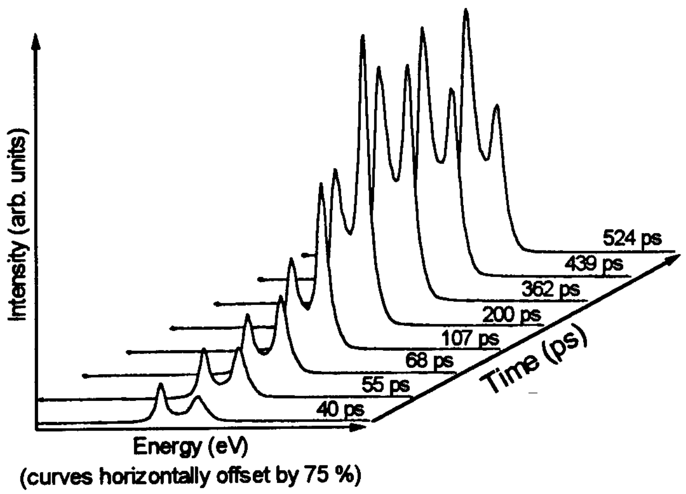

Fig. 3. Time evolution of the magnetoexciton-polariton emission spectra under 14 T magnetic field. The cavity mode is 1.05 meV above the exciton resonance.

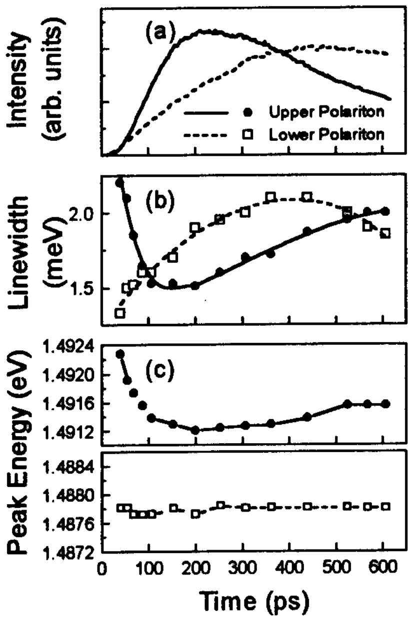

Fig. 4. Time evolution of (a) emission intensity, (b) linewidth, and (c) peak energy of the upper (circles, solid lines) and lower (squares, dashed lines) polariton modes from the spectra of Fig. 3.

In summary, we have measured the temporal evolution of the cavity-polariton emission spectra from a semiconductor microcavity in the strong coupling regime. When the initial polariton distribution is generated far from thermal equilibrium, and for positive cavity-exciton detunings, we observe the upper polariton emission escalating in time with respect to the lower polariton as carrier cooling takes place. The upper polariton also exhibits an increased emission decay rate, a sharp linewidth reduction, and a shift of the emission peak to lower energies with increased excitation. Emission from the low energy mode, in contrast, clamps at a constant value, and shows little change in decay rate, linewidth, or emission peak energy. The data are in excellent agreement with a microscopic theory which explains the observed behavior in the framework of carrier cooling inside a normal mode coupling microcavity.

References

1. C. Weisbuch, M. Nishioka, A. Ishikawa, and Y. Arakawa, Phys. Rev. Lett. **69**, 3314 (1992).
2. R.P. Stanley, R. Houdré, C. Weisbuch, U. Oesterle, and M. Ilegems, Phys. Rev. B **53**, 10995 (1996).
3. R. Houdré, J.L. Gibernon, P. Pellandini, R.P. Stanley, U. Oesterle, C. Weisbuch, J. O'Gorman, B. Roycroft, M. Ilegems, Phys. Rev. B **52**, 7810 (1995).
4. A. Imamoglu, R.J. Ram, S. Pau, and Y. Yamamoto, Phys. Rev. A **53**, 4250 (1996).
5. F. Jahnke, M. Kira, S.W. Koch, G. Khitrova, E.K. Lindmark, T.R. Nelson, Jr., D.V. Wick, J.D. Berger, O. Lyngnes, H.M. Gibbs, and K. Tai, Phys. Rev. Lett., accepted for publication.
6. J.D. Berger, O. Lyngnes, H.M. Gibbs, G. Khitrova, T.R. Nelson, E.K. Lindmark, A.V. Kavokin, M.A. Kaliteevski, and V. Zapasskii, Phys. Rev. B **54**, 1975 (1996).

Quantum Mode Correlations in Vertical Cavity Surface Emitting Lasers

D. C. Kilper, P. A. Roos, J. L. Carlsten
Montana State University, Department of Physics, Bozeman, MT 59717
phone: (406) 994-6286/fax: (406) 994-4452

K. L. Lear
Sandia National Laboratories, Albuquerque, NM 87185-0603
phone: (505) 844-6331/fax: (505) 844-8985

Considerable progress has been made during the past decade in understanding the quantum noise processes associated with the generation of photon-number squeezed light from conventional semiconductor lasers. Microcavity lasers, such as the vertical cavity surface emitting laser (VCSEL), have also been predicted to generate photon-number squeezed light based upon the high impedance pump noise suppression model[1]. Previous measurements, however, have only shown noise far above shot noise[2]. Several features of VCSELs are expected to lead to important differences from the quantum photon statistics in conventional edge-emitters. Because the cavity length is matched to the lasing wavelength, only a single longitudinal mode is present. This eliminates noise contributions from longitudinal mode competition noise. However, VCSELs often oscillate in multiple transverse modes, particularly for high efficiency devices operating at high pump rates, necessary for squeezing. Although quantum mode correlation effects between multiple longitudinal modes have been studied extensively in edge-emitting devices[3], quantum correlations between different transverse modes have not been observed. Furthermore, because of the high mirror reflectivities (>99%) squeezed output from a VCSEL can provide confirmation of the high impedance pump noise suppression model predictions in the good cavity limit, for which the theory was formulated. The enhanced spontaneous emission into the lasing mode that is characteristic of these devices can potentially lead to squeezed output at all pump rates. In present devices, the microcavity effects contribute to a low threshold current that allows for the high pump rates necessary for squeezed output to be achieved at room temperature without damage to the laser.

In this paper, we report the generation of photon-number squeezed light from a VCSEL, mediated by quantum correlations between two orthogonally polarized transverse modes. The device[4] consists of an oxide confined AlGaAs laser cavity grown to match the lasing wavelength of 960 nm. Approximately 3x3 um^2 apertures are formed in oxide layers at the top and bottom of the cavity. The active region consists of three 8nm InGaAs quantum wells.

The output of the VCSEL is directed by a high numerical aperture lens onto a large area detector. The laser is biased at 2.87 mA (12 times threshold), and the average photocurrent is 1.09 mA. Figure 1 shows the resulting photocurrent power spectrum (Laser Noise) compared against the spectrum from a red-filtered halogen lamp (SNL) with 1.07 mA photocurrent, which exhibits shot noise output and is linear for the intensities used here. The background amplifier noise has been subtracted. The laser noise spectrum is 1.3 dB below the shot noise level, SNL, trace for frequencies near 97 MHz. Squeezing was also confirmed using a balanced homodyne detector. The squeezing level is 68% of the squeezing expected from the total system efficiency of 0.38. This discrepancy with the single mode theory can be understood by examining the transverse mode behavior of the device.

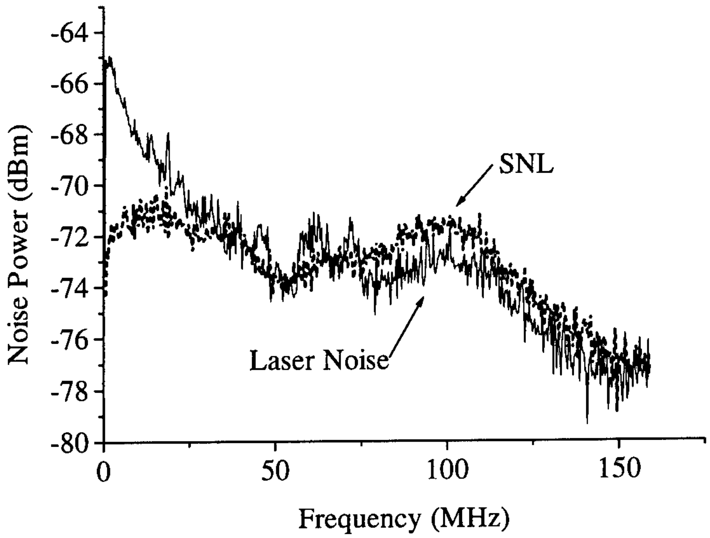

Figure 1. Amplitude power spectrum for the total VCSEL output (Laser Noise) and the shot noise level (SNL) determined from a halogen lamp.

Separate measurements using an optical spectrum analyzer (OSA) reveal that the laser is in fact oscillating in the fundamental transverse mode (0,0) and the first higher order transverse mode (0,1). Because the wavelengths of the various transverse modes differ with nm separations, they are easily identified by the OSA. Placing a polarizer in the field further demonstrates that the two lasing modes are orthogonally linearly polarized. Therefore, the photon-number statistics of the two modes can be conveniently studied by placing a polarizer before the detector. Figure 2a shows the polarization resolved laser noise (at 97.5 MHz) as a function of drive current. The noise on each individual mode is more than 10 dB above the noise of the combined (polarizer removed) fields. The SNL trace, obtained from a linear fit of the noise from a halogen lamp versus detector current, corresponds to the shot noise level for the Combined trace. For drive currents above 1 mA, the Combined trace is observed to fall below the shot noise level clearly indicating that the correlation between the two modes is nonclassical. The noise does not, however, drop to the level expected for the device efficiency. This may be due to a number of effects that can degrade the correlation, most notable are unequal mode scattering at the oxide layer edges or incomplete cross-transverse mode gain saturation in the device. The noise peak near 0.5 mA marks the onset of the (0,1) mode and the noise peak near 4 mA corresponds to the onset of additional higher order modes.

Figure 2b shows the degree of correlation γ between the two transverse modes as a function of drive current, calculated directly from the traces in Figure 2a using:

$$\gamma = \frac{Combined - (S_{(0,0)} + P_{(0,1)})}{2\sqrt{S_{(0,0)}P_{(0,1)}}}$$

The correlation is near perfect, -0.99, as the (0,1) mode turns on and remains below -0.97 up to 3.5 mA. The decrease in correlation is likely to be due to the increase in quantum noise (due to vacuum fluctuations), which increases with the average power, or the gradual increase of power into the higher order transverse modes.

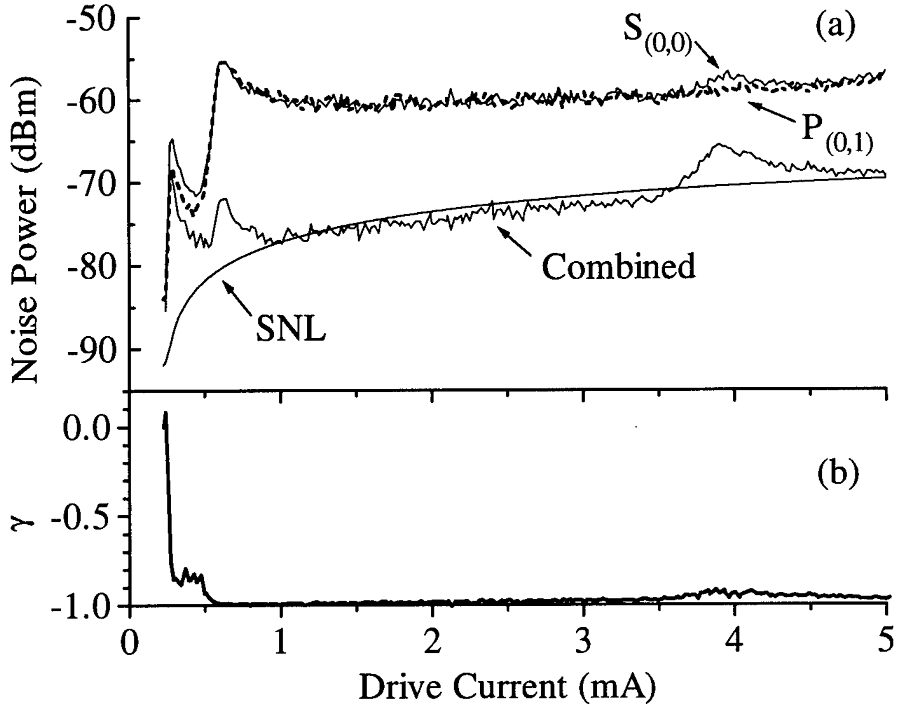

Figure 2. (a) Polarization resolved photon-number fluctuations (at 97.5 MHz) versus laser drive current (threshold is 0.24 mA). $S_{(0,0)}$ is obtained with polarizer aligned to the (0,0) mode, and for $P_{(0,1)}$ it is aligned with the (0,1) mode. Combined is obtained without a polarizer. (b) Degree of correlation $-1<\gamma<1$ between $S_{(0,0)}$ and $P_{(0,1)}$.

This work is supported by the NSF-EPSCOR, NASA-EPSCOR, ILX Lightwave and the DOE under contract #DE-AC04-94AL85000.

1. Y. Yamamoto, S. Machida, and G. Bjork, Phys. Rev. A **44**, 657 (1991).
2. E. Goobar, et. al., Appl. Phys. Lett. **67**, 3697 (1995).
3. S. Inoue, et. al., Phys. Rev. A **46**, 2757 (1992); H. Wang, M. J. Freeman, and D. G. Steel, Phys. Rev. Lett. **71**, 3951 (1993); F. Marin, et. al., Phys. Rev. Lett. **75**, 4606 (1995).
4. K. L. Lear, et. al., Appl. Phys. Lett. **66**, 2616 (1995).

Fluorescence lifetimes of Oriented Molecules in Microdroplets

M. D. Barnes, N. Lermer, W. B. Whitten and J. M. Ramsey
Chemical and Analytical Sciences Division, Oak Ridge National Laboratory
Oak Ridge, Tennessee 37831-6142

S. Arnold
Microparticle Photophysics Laboratory, Polytechnic University
Brooklyn, New York 11021

Over the last several years there has been considerable interest in the properties of atomic resonance fluorescence in an optical cavity with a primary dimension comparable to the relevant transition wavelength.[1] In particular, there has been great interest in the realization of strong atom-cavity coupling[2] and the suppression of spontaneous emission into "free-space" modes. However, an important but poorly understood issue relevant to low- or zero-threshold condensed phase optical devices is the nonradiative coupling of the emitting species to a thermal bath. Unlike experiments involving dilute atomic beams where the transition is well defined and broadening is negligible, coupling to a thermal bath induces spectral broadening which is usually much larger than the cavity resonance width and may often exceed the cavity mode spacing. Interesting examples of such systems are solvated dyes whose condensed phase dynamics are well known and characterized. To date, several studies have been made on fluorescence properties of solvated dyes in microcavities,[3, 4, 5] however additional complexities such as spatial and orientational averaging have obscured to some extent the connection between radiative and nonradiative processes in such systems. We discuss the observation of spontaneous emission rate modification (both enhancement and apparent suppression) for molecular species in a microcavity where both the molecular position *and* transition moment orientation are well defined.[6] These experiments serve as an interesting test case of molecule-cavity systems in which the emitting species is nonradiatively coupled to a thermal bath.

Liquid microspheres have received a great deal of attention in recent years in a wide variety of optical phenomena and cavity-QED.[7] High-Q (10^5 - 10^8) resonances, also called morphology dependent resonances (MDRs), in combination with high mode degeneracy have been shown to significantly enhance radiative processes in spherical microparticles. Here, we discuss fluorescence lifetime measurements for surfactant molecules in levitated glycerol microdroplets ranging in size from 3.5 to 30 μm in diameter. Polarized fluorescence imaging has provided evidence that the molecules are localized at the surface of the microspheres as well as having the (emission) transition dipole moment oriented parallel to the droplet surface. In sharp contrast with results from previous studies on homogeneously distributed dyes,[5] we find significant deviation from "bulk" behavior at both extremes of the size range. For small droplets (< 6 μm diam.), the fluorescence decay rate is enhanced by a factor roughly proportional to 1/r; for larger sizes (>12 μm diam.), the apparent fluorescence decay rate is *smaller* than the bulk by a factor of about 30%.

For small droplets (≤ 6 μm), the fluorescence decay rate has a similar size dependence as observed for rhB and rhodamine 6G. In this size regime, the resonance Q's are of the order of 10^3 - 10^4 and weak coupling is expected. Thus, within a Yokoyama-Brorson model,[ref] the decay rate should scale approximately as the ratio of the mode spacing (proportional to 1/r) to the homogeneous width. For larger droplets (>12 μm), the fluorescence decay rates deviate significantly from the predictions of the Yokoyama-Brorson model clearly indicating a different physical mechanism. One possibility is a non-perturbative molecule-cavity interaction: Q's for MDRs for glycerol droplets in this size range are known to be $\geq 5 \times 10^6$ which means that the cavity damping time, $\tau_{cav} = Q/\omega$, is approximately equal to the (bulk) fluorescence decay time implying an intermediate molecule-cavity coupling regime. However, an alternative explanation is that the deviation from bulk behavior may be related to interfacial electrodynamics.[8] At present, there is no comprehensive theory which describes spontaneous radiative decay from molecular systems in dielectric microspheres which also describes the effect of nonradiative coupling to a thermal bath. This situation therefore precludes definitive statements on the physical origin of the anomalous decay times observed at the larger sizes. It is hoped that these results will stimulate more theoretical work in this area.

This research was sponsored by the Division of Chemical Sciences, Office of Basic Energy Sciences, U.S. Department of Energy, under contract DE-AC05-96OR22464 managed by Lockheed Martin Energy Research Corporation.

---

[1] For reviews, see P. Meystre, in *Progress in Optics*, edited by E. Wolf (North Holland, Amsterdam, 1992), Vol. 30, p. 261; S. Haroche and D. Kleppner, Phys. Today **42**, 24 (1989) and references cited therein.

[2] S. E. Morin, C. C. Wu, and T. W. Mossberg, Phys. Rev. Lett. **73**, 1489 (1994); R. J. Thompson, G. Rempe, and H. J. Kimble, Phys. Rev. Lett. **68**, 1132 (1992); Y. Yamamoto and R. Slusher, Phys. Today **46** (6) 66, (1993).

[3] F. De Martini, G. Innocenti, G. R. Jacobovitz, *et al.*, Phys. Rev. Lett. **59**, 2955 (1987).

[4] H. Yokoyama, M. Suzuki, and Y. Nambu, Appl. Phys. Lett. **58**, 2598 (1991).

[5] M. D. Barnes, W. B. Whitten, S. Arnold, and J. M. Ramsey, J. Chem. Phys. **97**, 7842 (1992).

[6] M. D. Barnes, C-Y. Kung, W. B. Whitten, J. M. Ramsey, S. Holler, and S. Arnold, Phys. Rev. Lett. **76**, 3931 (1996).

[7] For a comprehensive review, see "Optical Processes in Microcavities," R. K. Chang and A. J. Campillo, ed. (World Scientific, Singapore, *in press*).

[8] J. M. Wylie and J. E. Sipe, Phys. Rev. A **30**, 1185 (1984)

Physics in Quantum Structures

QThD 3:30pm – 5:30pm
Salon A

A.L. Smirl, *Presider*
University of Iowa

Radiationless Stimulated Exciton Emission

E. Benson, E. Fortin, Physics Dept. University of Ottawa, Canada
A. Mysyrowicz, LOA, ENSTA, école polytechnique, Palaiseau, France

Experiments investigating the process of Bose-Einstein condensation of excitons in Cu2O will be reviewed. The exciton flux reaching the back surface of mm thick single crystals is investigated following creation of a high density of excitons close to the front surface with a pulsed laser. An anomalous propagation regime is observed at sufficiently low crystal temperatures and sufficiently high particle densities, in the form of a ballistic packet progressing at a velocity close to the crystal sound velocity. The ballistic packet is attributed to an excitonic superfluid, the result of a Bose-Einstein Condensation (BEC). Conditions for appearance of the ballistic excitonic transport are found to be in good agreement with the predictions of the weakly interacting Bose gas model.

When the measurements are repeated in the presence of an additional population of cold excitons, distributed throughout the sample with a tunable cw laser, a strong amplification of the excitonic packet is observed. This effect is interpreted as the radiationless emission of excitons stimulated by the superfluid excitonic packet. It represents the excitonic counterpart of light amplification by stimulated emission of radiation (boser).

Finally, recent experimental results showing interference effects between two independent excitonic condensates will be briefly described.

Femtosecond luminescence of semiconductor nanostructures

B. Deveaud, S. Haacke, M. Hartig, R. Ambigapathy, I. Bar Joseph†, R.A. Taylor*
EPFL-DP-IMO-LOEQ, CH 1015 Lausanne, Switzerland
Tel. (41) 21 693 54 96, Fax. (41) 21 693 45 25, e-mail : deveaud@eldpa.epfl.ch
† Physics Dept., Weizmannn Institute, Rehovot, Israel
*Clarendon Laboratory, Oxford University, Oxford

Luminescence has been quite widely used for the study of semiconductor nanostructures, and more especially time resolved luminescence, due to the ease to get a luminescence signal. The interpretation of the results however is sometimes quite complex, and one generally finds that some care has to be taken for the results to be meaningful. In particular, the homogeneity of the excited density over the detected luminescence signal is a quite important parameter, also it is often desirable to work at the lowest possible densities.

Luminescence Up-Conversion (LUC) provides luminescence data with a very good time resolution (basically given by the temporal width of the pulse from the laser), but this is obtained at the expense of the signal to noise ratio. We have improved the conventionnal LUC technique in two respects : by using a cooled CCD camera as a detector and by using to synchronous femtosecond laser sources at different wavelengths. The first improvement has the advantage of introducing a detector with a very high quantum efficiency (60%), and very low dark noise counts (less than 1 count per pixel perhour). Furthermore, the CCD detector can be used in a multichannel mode, thereby averaging the laser fluctuations over the entire spectrum. The use of two synchronized lasers at different wavelengths allows to perform LUC with resonant excitation, and thus to create cold distributions of carriers or excitons and to study their dynamics.

In this paper, we will briefly outline the results that we have obtained in three different directions : intersubband scattering in QWs, femtosecond resonant exciton luminescence in quantum wells, and high density plasmas in quantum wires.

Intersubband scattering :

It is expected that the intersubband scattring rate in quantum wells depends very strongly on the well thickness. In particular, it should depend on the fact that the n=1 to n=2 subband separation may be larger or smaller than the energy of the optical phonon. We have measured the decay time of the n=2 luminescence in a wide series of quantum wells. For well width of the order of 100 Å, we find scattering times of the order of 500 fs,[1] in very good agrement with theoretical expectations.[2]

We also demonstrate that the scattering time changes with the energy distance, as expected, due to the change of the q-vector of the phonon involved in the transition. If the excitation density is too high, full thermalization between the two subbands is obtained very quickly (see Fig.1).

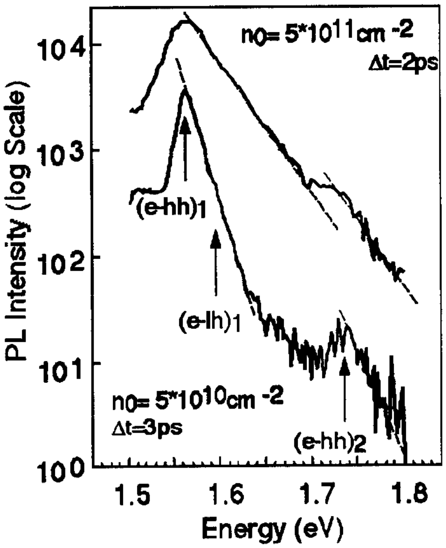

Fig. 1 : Luminescence spectrum of a 100 Å quantum well for a delay of 2 ps. Note the quasi thermal distribution in the two subbands, but the different carrier temperature for low excitation density (lower curve). At higher densities, the two subbands are fully thermalized very fast (upper curve).

For well widths above 220 Å, we also find decay times which are very short (of the order of 1 ps). We have been able to measure such times down to very low excitation densities and this result is in strong contradiction with theoretical expectations for scattering with acoustical phonons. We have then performed calculations of the scattering rate due to electron-electron and electron hole scattering. The results are in very good agreement with the experimental observations, and allow indeed to predict times of the order of 1 ps. We also find that the intra-subband electron-electron scattering is much faster that the intersubband scattering, and that, at short times and low densities, the electron temperature is not the same in the two subbands although the distribution is thermalized in each subband (see Fig.1 - lower curve).

Femtosecond resonant exciton luminescence :

It is now recognized that the excitonic luminescence behaves differently in quantum wells than it does in bulk crystals.[345] However, the process by which the energy is transferred from the laser field to the exciton luminescence is not well unerstood at this time. We have performed femtosecond resonant luminescence down to very low densities. We show a typical series of time delay curves on Fig.2 where diferent very interesting features can be evidenced.[6] The most obvious feature is the clear beating between heavy and light hole states. More interesting is the variation of the shape of the curve with density. Comparison of this shape with a theoretical model by Zimmermann and coworkers allows to interpret the signal emitted as partly due to resonant Rayleigh scattering, and partly to luminescence per se. The only way to distinguish between the two is the phase relationship with the exciting laser beam. The Rayleigh signal being coherent with the excitation pulses, and the luminescence signal is incoherent with these pulses.

In Fig. 2, the oscillations are due to the beating between heavy and light holes. As a function of the excitation density, the rise time of the signal becomes shorter and, at the same time, changes shape. The rise is more or less linear at high densities, and becomes quadratic when the intensity is low enough.

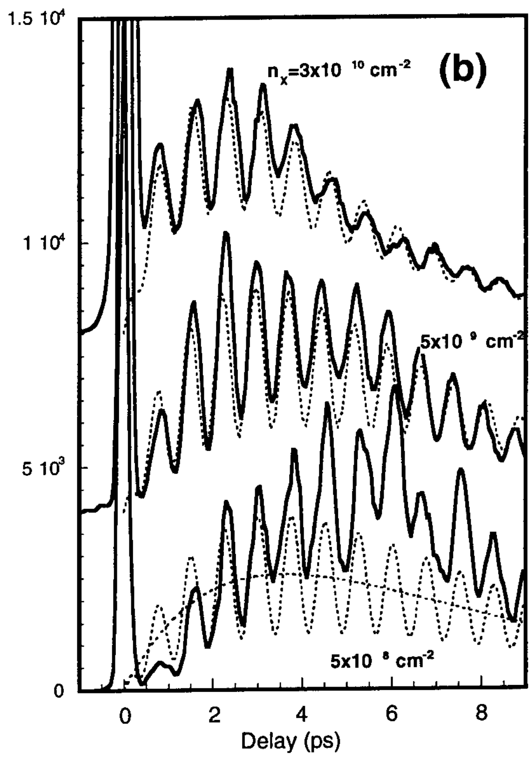

Fig. 2 : Secondary emission signal at the energy of the exciton, for a quatum well excited at resonance. The different spectra correspond to different excitation densities. Note the decrease of the dely for the maximum as well as the change in the initial shape as a function of density.

High density effects in quantum wires :

We have studied the recombination processes of high density plasmas in quantum wires because such processes will govern thebehavior of future quantum wire lasers. We use very high quality quantum wires, grown by MOCVD on non planar substrates. The quality of the samples is characterized by a narrow linewidth in luminescence, and a small Stokes shift.[7]

We observe clearly the modulation of the spectra due to the lateral subbands, up to the highest densities (see Fig. 3). We also observe that the different sturctures saturate at high densities (short times), and do not shift at all.

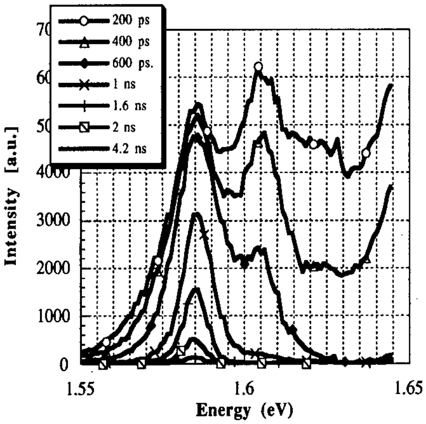

Fig. 3 : Successive time resolved luminescence spectra from a quantum wire sample after high intensity excitation. Clear signature from the successive subbands is observed, with no shift as a function of density.

All observations that we have made are only consistent with this emission being due to excitonic recombination, even at densties where all transitions are due to electron-hole pairs in quantum wells. One of the experimental evidences is given in Fig. 4 : we show the time behavior of the integrated intensity. In quantum wells, a clear break is observed at the transition from a degenerate plasma to a non degenerate one. In quantum wires, the intensity appears to decay exponentially over several orders of magnitude.[8] This is a clear indication of the excitonic behavior in wires, in agreement with some theories.[9][10]

The absence of any shift of the observed structures, and the abscence of broadenning over part of the density range points out to a very small band gap renormalization. If all these interpretations are correct, the assessment of the interest of wires for making lasers has to be reconsidered.

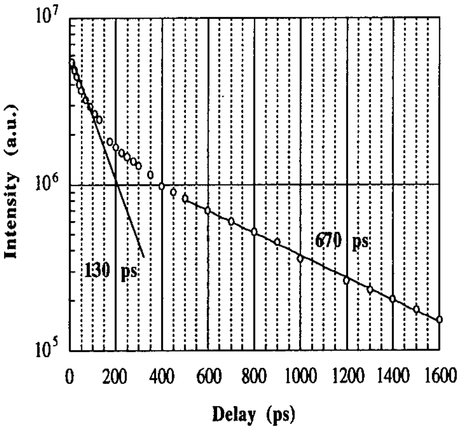

Fig. 3 : Time behavior of the integrated intensity in a) a quantum well, and b) a quantum wire. The break in the quantum well corresponds to the density is not large enough for the plasma to be degenerate.

References :

---

[1] M. Hartig, S. Haacke, L. Rota, and B. Deveaud, *Phys. Rev.*, **B** (to be published)
[[2]] R. Ferreira, G. Bastard, *Phys. Rev.*, **B40**, 1074 (1989)
[[3]] V.M. Agranovitch, O.A. Dubovskii, *JETP Lett.*, **3**, 223 (1966)
[[4]] J. Lee, E.S. Koteles, M.O. Vasell, *Phys. Rev.* , **B33**, 512 (1986)
[5] B. Deveaud, F. Clérot, N. Roy, K. Satzke, B. Sermage, D.S. Katzer, *Phys. Rev. Lett.*, **67**, 2355 (1991)
[6] S. Haacke. B. Deveaud, I. Bar Joseph, R. Zimmermann, R.A. Taylor (to be published)
[7] D.Y. Oberli et al., *Il Nuevo Cimento*, **17D**, N. 11-12, 1641 (1995)
[8] R. Ambigapathy, I. Bar Joseph, M.J. Brasil, D. Oberli, S. Haacke, E. Kapon, B. Deveaud to be published
[9] T. Ogawa, T. Takagahara, *Phys. Rev.*, **B43**, 14325 (1991) ; ibid **B44**, 8138 (1991)
[10] F. Rossi, E. Molinari, *Phys. Rev. Lett.*, **76**, 3642 (1996)

Coulomb Contributions to Exciton Saturation in Room Temperature GaAs-Al$_x$Ga$_{1-x}$As Multiple Quantum Wells

M. Holden, G.T. Kennedy and A. Miller
J.F. Allen Physics Research Laboratories, Department of Physics and Astronomy,
University of St. Andrews, Fife, Scotland, KY16 9SS.

Tel: (01334) 463158
Fax: (01334) 463104

A number of optoelectronic device applications of quantum well semiconductors depend on the saturation of exciton absorption features. Studies of exciton saturation at room temperature have resolved exciton-exciton interactions on timescales less than 300fs, and two distinct mechanisms based on phase space filling (PSF) and Coulomb effects caused by free carriers on longer timescales. Nonequilibrium carrier distributions were originally employed to separate Pauli exclusion and long range Coulomb effects [1]. More recently, optically induced circular dichroism was used to identify PSF and Coulomb exchange contributions [2]. However, Coulomb contributions can arise from both screening and collisional broadening. In this work, we have extended the use of circularly polarised ultrashort pulses to distinguish the two related Coulomb effects of screening and broadening and in addition, compared the relative contributions of excitons and free carriers to Coulomb contributions.

When the heavy-hole exciton is resonantly excited in a quantum well at room temperature using ultrashort pulses, an exciton gas is generated which rapidly ionises to an electron-hole plasma. The exciton gas and the electron-hole plasma can both saturate the exciton absorption by reducing the overall oscillator strength through PSF and screening. PSF results from the blocking of transitions which would otherwise create excitons when the band states associated with the excitons are filled. Exciton creation can only be blocked by the presence of excitons or free carriers of the same spin and thus PSF is described as spin dependent. On the other hand, it has been shown that at low carrier injection densities, Coulomb screening has no dependence on the spins of the particles. At the same time, excess free carriers cause a collisional broadening of the absorption line, which lowers the absorption at the peak while leaving the area under the line unchanged. The relative strengths of the saturation mechanisms, how they differ between free carriers and excitons, and polarisation dependencies need to be determined in order to understand the operation of devices which are contingent on saturable absorption.

We have explored the spin sensitivity in the temporal dynamics of exciton saturation of GaAs-AlGaAs MQWs by using three separate pump and probe polarisation configurations: Pump and probe beams with the same linear polarisation (SLP); pump and probe beams circularly polarised in the same sense (SCP); and pump and probe circularly polarised in the opposite sense (OCP). The selection rules for quantum wells allow only one spin orientation to be populated when a circularly polarised pump is resonant with the heavy hole exciton. A previous study [2] using these pump-probe methods used 1ps pulses with bandwidths much less than the exciton spectral linewidth. Therefore, when the laser was tuned to the absorption line centre, the Coulomb effects of broadening and screening could not be separated as they are both spin independent. An example of a set of results taken with such a source is shown in figure 1(a) for a 6.5nm well width GaAs-AlGaAs MQW sample. The rise in the SLP trace after zero delay is due to a combination of PSF, screening and broadening, which all reduce the absorption at the centre of the line. For the OCP condition, immediately after excitation, all of the opposite spin states are still available to the probe for creation of excitons, so there is no PSF. This results in less saturation initially, but as the electron spins randomise, the OCP signal rises to the SLP level. Conversely for the SCP condition, the probe interacts with spin states which are twice as full as those in the SLP case (for the same total number of excited carriers), so initially there is a doubling of the spin dependent saturation which again recovers on the spin relaxation time.

In our experiments we use a self-mode-locked Ti:sapphire laser producing 100fs pulses at a repetition rate of 83 MHz. The bandwidth of the pulses (~10nm) is greater than the linewidth of the exciton in GaAs-AlGaAs MQWs at room temperature. With the laser tuned to the heavy hole exciton peak, broadening is no longer significant for the probe pulses since the overall oscillator strength does not change in this mechanism, making a direct determination of the effect of screening alone possible. An example of a set of results using this 100fs source is shown in figure 1(b) for the same MQW sample as used in figure 1(a) with 1ps pulses. Comparison of figures 1(a) and 1(b) shows that broadening is clearly the dominant Coulomb contribution when longer pulses are employed.

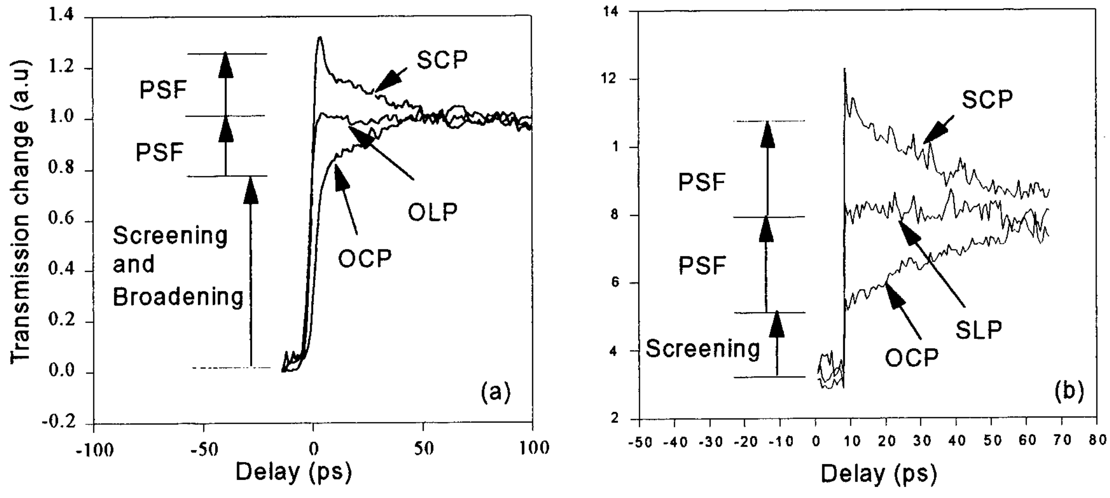

Fig 1 Changes in transmission of time delayed probe pulses using (a) 1ps and (b) 100fs pump and probe pulses, under 3 different polarisation conditions..

Using circularly polarised pulses with 100fs durations, i.e. shorter than the exciton ionisation time (<300fs), allows spin dependent and spin-independent exciton-exciton contributions to be resolved. An example of a set of higher time resolution pump-probe scans taken within 2ps of zero delay are shown in Fig 2.

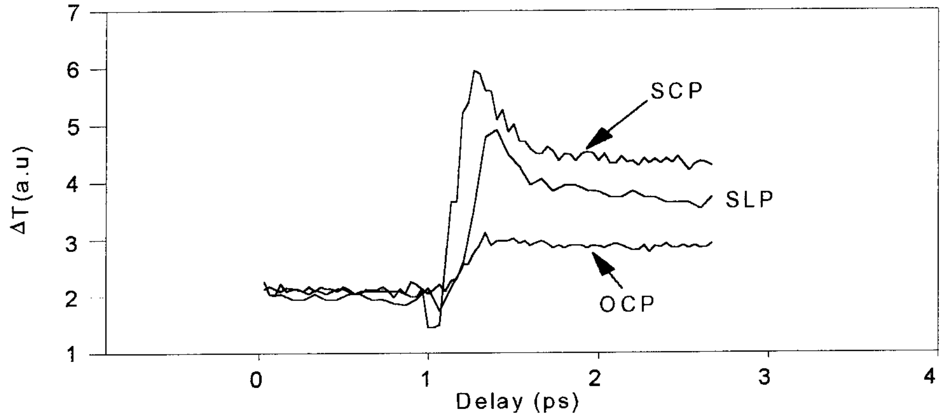

Fig 2 Changes in transmission of time delayed, 100fs probe pulses for 3 polarisation conditions at the same pump power.

Exciton ionisation produces the initial decay of approximately 300fs in the SLP configuration, consistent with early measurements [1]. The enhanced transmission change at small delays is due to the fact that the presence of excitons saturates the absorption more efficiently than the same number of free carriers. Figure 2 also shows that exciton ionisation is observed in the SCP configuration. However, surprisingly, exciton ionisation is not apparent in the OCP configuration. The implication of this result is that the spin-independent contributions to the exciton saturation is identical whether the particles are bound or free.

A simple rate equation model was used to describe the evolution of the particle sets and a fit made to each trace assuming the transmission changes are proportional to the density of each particle set. It was found that irrespective of the polarisation configuration, excitons are twice as efficient at saturating the HH exciton resonance than free carrier pairs. The measured spin dependent contribution from the excitons doubles, as predicted when SCP rather than SLP is used. However the free carrier SD saturation appears to triple for SCP. This may be due to the free carrier SD effect being small and thus difficult to measure especially when using SLP. All the saturation mechanisms were found to vary linearly with carrier density within the regime investigated.

In conclusion a method of individually resolving all of the main heavy hole exciton saturation mechanisms in a MQW semiconductor has been demonstrated. Free carrier screening mechanism has been distinguished from collisional broadening and the results suggest that spin independent screening may be identical for excitons and free carriers.

References:

[1] W. Knox, R. L. Fork, M. C. Downer, D. A. B. Miller, D. S. Chemla and C.V. Shank, Phys. Rev. Letts. **54**, 1306 (1985)
[2] M. J. Snelling, P. Perozzo, D.C. Hutchings, I. Galbraith and A. Miller, Phys. Rev. B. **49**, 17160 (1994)
[3] S. Schmitt-Rink, D.S. Chemla and D.A.B. Miller, Phys. Rev. B **32**, 6601 (1985)

Relaxation dynamics of excitons and electron-hole pairs studied by spatiotemporal pump and probe experiments

S. Grosse, R. Arnold, A. Kriele, G. von Plessen, J.P. Kotthaus, and J. Feldmann
Sektion Physik, Ludwig-Maximilians-Universität, D-80799 München, Germany.

R. Rettig, T. Marschner, and W. Stolz
Wissenschaftliches Zentrum f. Materialwissenschaften, Philipps-Universität Marburg,
D-35032 Marburg, Germany

Phone: +49-89-2180-3356 Fax: +49-89-2180-3441
www.physik.uni-muenchen.de/lmu.physik/sektion/feldmann/

Ultrafast laser spectroscopy has been used extensively to study carrier relaxation phenomena in semiconductors and semiconductor nanostructures. Accordingly, several physical issues of the carrier thermalization and recombination scenario after optical excitation are well understood. This is particularly true for many III-V quantum well structures. However, there is a basic problem when using light-matter interaction to study carrier relaxation in crystals. As a consequence of (i) the conservation law for the total momentum and (ii) the vanishing momentum of visible light as compared to the extension of the Brillouin-zone only electron-hole (e-h) pair transitions with vanishing total wavevector ($\vec{K} = 0$) can be excited and detected, provided no other quasi-particle carrying momentum is involved in the optical transition.

In quantum wells, the kinetic energy and thus the lateral velocity of excitons are directly related to the total in-plane wavevector $\vec{K}_{||}$. Accordingly, the lateral diffusion constant depends critically on the exciton distribution in $\vec{K}_{||}$-space, which changes e.g. with exciton temperature. Accordingly, the measurement of the temporal evolution of the excitonic diffusivity is expected to reveal the relaxation or cooling dynamics of the ensemble of excitons spread in $\vec{K}_{||}$-space.[1]

Here we report temporally and spatially resolved pump and probe experiments performed on quantum wells to study the lateral diffusivity of excitons and e-h pairs as a function of time, excess energy, and crystal temperature. We have chosen symmetrically strained (GaIn)As/Ga(PAs) multiple quantum wells, since the strain-induced blue-shift of the light-hole exciton allows to study of the spatiotemporal evolution of the electron–heavy-hole pair excitations without being disturbed by light-hole transitions. For spatial calibration purposes special gold structures with sizes between 0.5μm and 5μm were deposited on the sample surface. To guarantee high temporal resolution we use a Kerr-lens mode-locked Ti:sapphire laser providing $\approx$ 100 fs pulses with a spectral width of $\approx$ 20 meV. A microscope objective is used to focus pump and probe beams into a helium-flow cryostat, where a spot diameter of 1.8μm is obtained on the sample surface. A steering lens placed in the path of the probe beam is used to laterally displace pump and probe spots with sub-μm accuracy. We limit the maximum e-h pair density to $4 \cdot 10^{10}$ cm^{-2} to stay in the regime, where the carrier density is proportional to the detected optical nonlinearity. By measuring pump and probe transients at different lateral displacements it is possible to map out the propagation profile of carriers with respect to time. An example is shown in Fig.1, where the pump-probe signal (differential transmission) is plotted versus the lateral displacement for various time delays. Assuming Gaussian distributions for the carrier populations and the probe beam the profiles can be nicely fitted as shown by the solid lines in Fig.1. From the fits we deduce the spatial width Δx of the carrier population defined by the exp(-1/2)-values of the respective Gaussian distribution.

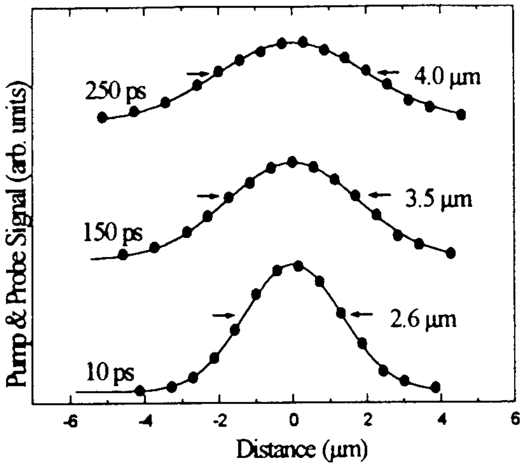

Fig.1: Pump-probe signal versus lateral displacement for three time delays. The solid lines represent Gaussian fits.

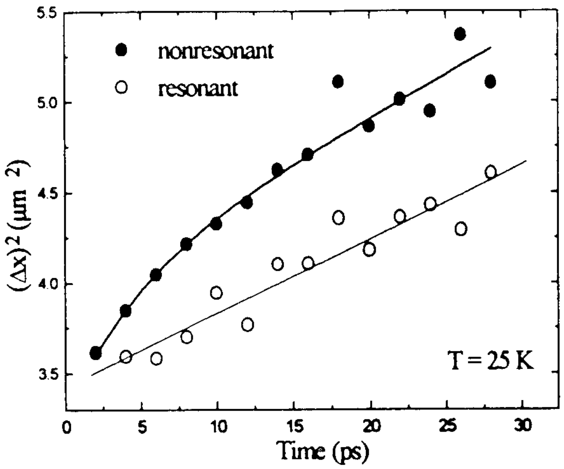

Fig.2: $[\Delta x(t)]^2$ for resonant (hollow circles) and nonresonant excitation (full circles).

In Fig.2 the squared Δx-values are plotted versus time delay for a lattice temperature of 25K ($kT \approx$ 2.2meV) and for two excitation conditions: energetically resonant with the 1s exciton (hollow circles) and 14meV above the 1s exciton (full circles). Due to the spectral width of the pump pulse a mean excess energy E_{exc} of $\approx$ 3meV is deposited into the exciton system for resonant excitation, whereas for non-resonant excitation $E_{exc} \approx$ 13meV. We note that the slope of $[\Delta x(t)]^2$ is directly proportional to the diffusion constant D. On this time scale we find a linear increase of $(\Delta x)^2$, i.e. a constant diffusivity of $D = 60$cm^2/s for resonant excitation. In contrast, the diffusivity for non-resonant excitation starts with a value of $D \approx 200$cm^2/s and then slows down to the same value as found for resonant excitation. This initial slow down may be explained by two processes, first by the relaxation of thermalized electron-hole pairs and excitons to $K_{||} = 0$ and second by the formation of excitons, since the mobility of bound excitons is an order of magnitude smaller than the mobility of quasi-free carriers.[2] This interpretation implies an exciton formation time of less than 10ps.

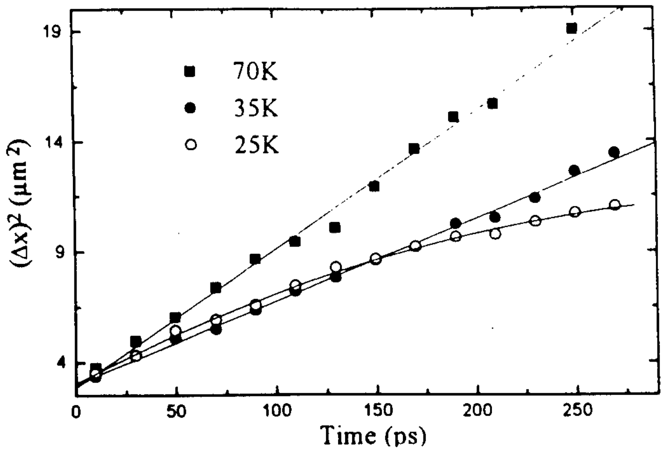

Fig.3: $[\Delta x(t)]^2$ for three different crystal temperatures under resonant excitation. Diffusion constants of 46cm^2/s and 80cm^2/s are obtained for 35K and 70K, respectively.

The temporal evolution of $(\Delta x)^2$ is shown for resonant excitation and for three crystal temperatures on a larger time scale in Fig.3. We note that on this time scale the 25K curve is not linear (compare to Fig.2). The decrease of the diffusivity with time is attributed to exciton cooling, since E_{exc} is larger than kT. In addition, disorder induced potential fluctuations may lead to exciton localization reducing the overall diffusion. As can be seen in Fig.3 we find time-independent diffusion constants for crystal temperatures higher than 35K. Since E_{exc} is smaller than kT for $T \geq 35$K, excitonic cooling processes do not occur anymore. In addition, exciton localization in shallow potential minima become less important with increasing temperature.

This work is supported by the Deutsche Forschungsgemeinschaft (Grant No. Fe 323/5-1).

1. H.W. Yoon et al., Phys. Rev. **B46**, 13461 (1992).
2. H. Hillmer et al., Phys. Rev. **B39**, 10901 (1989).

Locking of the Stimulated Emission of a Microcavity Laser to the Electron Spin Precession Clock

J.D. Berger[1], S. Hallstein[2], C. Schneider[3], M. Hilpert[2], W.W. Rühle[3],
H.M. Gibbs[1], G. Khitrova[1], F. Jahnke[3], S.W. Koch[3], and M. Oestreich[2]

[1]*Optical Sciences Center, University of Arizona, Tucson, AZ 85721, USA, Ph: 520-621-2452, FAX: 520-621-4323*
[2]*Max-Planck-Institut für Festkörperforschung, Heisenbergstraße 1, D-70569 Stuttgart, Germany*
[3]*Fachbereich Physik der Philipps-Universität, Renthof 5, D-35032 Marburg, Germany*

Spontaneous and stimulated emission properties of electronic states depend intimately on the electromagnetic environment to which they are coupled. Microcavities are of great fundamental and practical interest largely thanks to their ability to influence these emission properties. In the weak coupling regime of cavity quantum electrodynamics, a microcavity can either enhance or inhibit spontaneous emission, while the strong coupling regime is characterized by reversible vacuum Rabi oscillations. Stimulated emission properties are also greatly influenced by the nature of the intracavity field.

In this paper, we report on a novel manifestation of cavity-modified photon emission. The circularly polarized spontaneous emission from a semiconductor in a parallel magnetic field has recently been shown to exhibit temporal oscillations after circularly polarized excitation.[1] The oscillations can be explained as a quantum beating between the Zeeman-split electron spin states in a magnetic field, and have been used to study various properties of the electron Landé g-factor in semiconductors.[2,3,4] Here we demonstrate how circularly polarized excitation of a semiconductor microcavity in a parallel magnetic field leads to fast oscillations in the stimulated laser emission with alternating circular polarization. The oscillations originate from optical gain modulation via Larmor precession of the electron spins, and their frequency is determined by the internal electron spin precession clock. They are a novel example of how photon emission is modified in a semiconductor microcavity. Besides synchronization of the stimulated emission to the electron spin precession, this experiment is a tool to transfer electron spin coherence to the coherence of an optical field. We demonstrate 22 GHz oscillation frequencies with high modulation depth in the laser emission. The frequency depends only on magnetic field strength and the absolute value of the electron g-factor in the semiconductor material.

The quantum well (QW) microcavity consists of a $3\lambda/2$ GaAs spacer between symmetric 99.6% GaAs/AlAs Bragg mirrors, with two 80 Å $In_{0.04}Ga_{0.96}As$ QWs placed at the antinodes of the intracavity field. The sample was held at 15 K in the center of a superconducting magnet, and was oriented in Voigt geometry with the magnetic field parallel to the QW plane and to the normally incident excitation. The microcavity was excited in a reflection minimum at 780 nm by 2ps pulses from a mode-locked Ti:Sapphire laser with 80 MHz repetition rate. The 835 nm microcavity emission was detected antiparallel to the excitation and analyzed with a circular polarizer. The emission was then dispersed in a 0.32 m spectrometer and detected by a synchroscan streak camera with 7 ps temporal resolution.

Figures 1a and 1b show oscillations with high modulation depth in the time-resolved, circularly polarized microcavity emission. The total emission of Fig. 1c oscillates with twice the Larmor frequency, and the circular polarization alternates. The modulation depth is far greater than that observed at a comparable carrier density in the QWs without a microcavity.

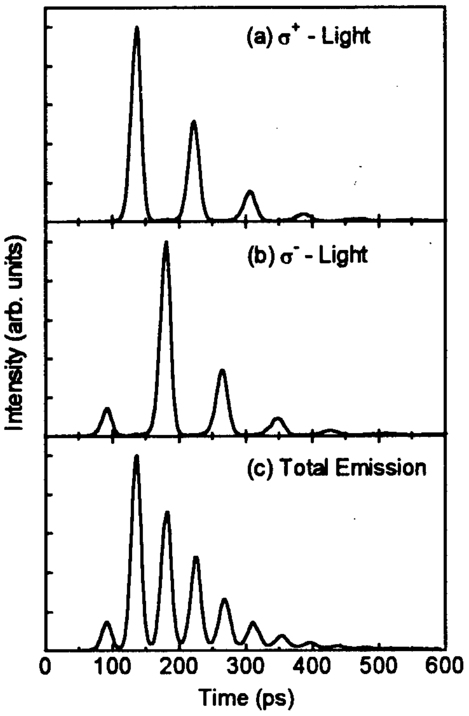

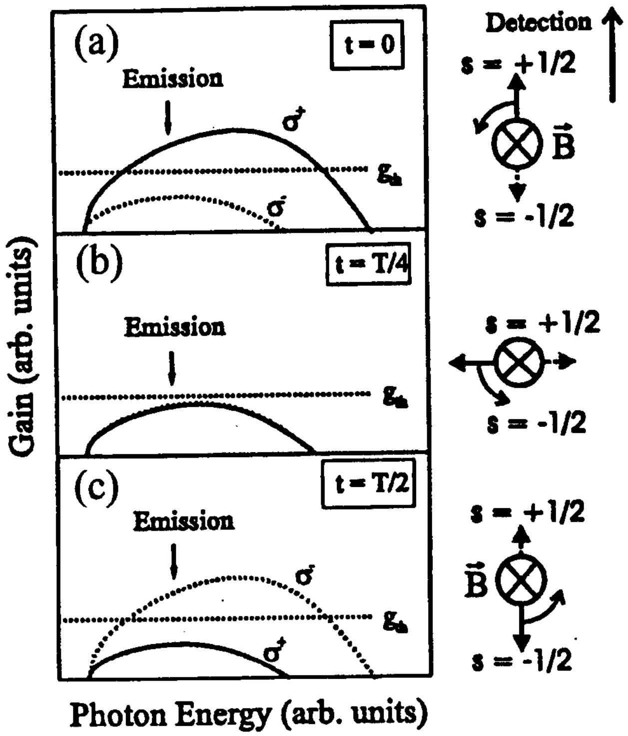

Fig. 1 Time-resolved stimulated emission of the microcavity laser in 2 Tesla magnetic field, after circularly polarized, 2 ps pulsed excitation. (a) and (b) show the circularly polarized emission components, while (c) shows the total emission without analyzer.

Fig. 2 Schematic gain spectra (a) at excitation (t=0), (b) after a quarter Larmor precession period (t=T/4), and (c) after a half Larmor precession period (t=T/2). The right side demonstrates the spin precession about the magnetic field.

The fast oscillations in the total emission without an analyzer can be explained as follows: The initial circularly polarized excitation creates a large population of spin up electrons and only a small population of spin down electrons. Two different gain curves are therefore established at time zero, as depicted in Fig. 2a. Just after excitation, only σ^+ polarized light sees gain that exceeds the losses at the emission energy and is therefore strongly amplified. Here we observe a maximum in Figs. 1a and 1c, and a minimum in Fig. 1b. After a quarter precession period (t = T/4), both spin states are populated equally and the corresponding gain curve drops below threshold (Fig. 2b). Lasing is switched off and we observe spontaneous emission of polarization $\frac{1}{2}(\sigma^+ + \sigma^-)$. In this situation the total microcavity emission of Fig. 1c reaches a minimum. After a half Larmor precession period (t = T/2), the laser exceeds threshold only for σ^- light (Fig. 2c), since the initial spin up electrons have precessed to have spin down. At this point a maximum appears in Figs. 1b and 1c, while Fig. 1a exhibits a minimum.

The total laser emission therefore pulses with twice the Larmor frequency and with alternating circular polarization. It is locked to the completely internal spin precession, which depends on the magnetic field and the electron g-factor. With 2 Tesla magnetic field and a 22 GHz modulation frequency of the unpolarized emission, we deduce a value $g_e = -0.411$. Since spin precession is caused by a coherent superposition of two spin states, this experiment is a novel tool to transfer spin coherence to the coherence of the optical field.

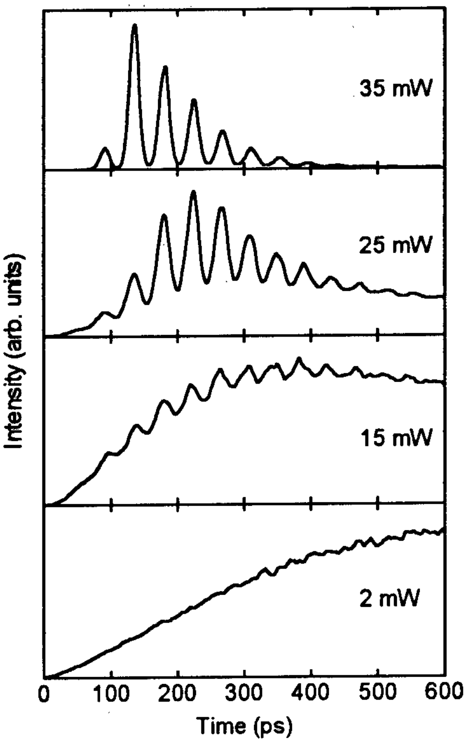

Fig. 3. Time-resolved total laser emission for increasing excitation powers at 2 Tesla magnetic field.

The modulation depth depends strongly on excitation power since oscillations in the total emission arise from a modulation of the optical gain. Figure 3 demonstrates the excitation power dependence of the total microcavity laser emission. At low excitation power, the laser remains below threshold at all times, and no modulation is observed. Higher excitation leads to an increased maximum gain for σ^+ and σ^- light and to a larger stimulated part in the total emission. Oscillations begin to appear on top of a spontaneous emission background. The modulation depth then increases with increasing excitation.

In summary, we have demonstrated that light emission from a QW in a magnetic field is strongly modified by the presence of a semiconductor microcavity. The stimulated emission is synchronized to the stable electron spin precession about the magnetic field axis. Transfer of the electron spin coherence to the coherence of the optical field yields a pulsed total emission with twice the Larmor frequency and alternating circular polarization.

References

1. A.P. Heberle, W.W. Rühle, and K. Ploog, Phys. Rev. Lett. **72**, 3387 (1994).
2. M. Oestreich and W.W. Rühle, Phys. Rev. Lett. **74**, 2315 (1995).
3. M. Oestreich, S. Hallstein, A.P. Heberle, K. Eberl, E. Bauser, and W.W. Rühle, Phys. Rev. B **53**, 7911 (1995).
4. R.M. Hannak, M. Oestreich, A.P. Heberle, and W.W. Rühle, Solid State Commun. **93**, 331 (1995).

Poster Session

QThE 8:00pm – 10:00pm
Salon B

Picosecond Switching using Resonant Nonlinearities in a Quantum Well Device

Patrick LiKamWa
CREOL - Center for Research and Education in Optics and Lasers
and Electrical and Computer Engineering
University of Central Florida, Orlando, FL 32816-2700.
Tel: (407) 823-6816. Fax: (407) 823-6880. E-mail: likamwa@creol.ucf.edu

Ayman Kan'an
School of Electrical and Computer Engineering
Purdue University, Lafayette, IN 47907-1968
Tel: (317) 494-3392. Fax: (317) 494-6951. E-mail: kanan@ecn.purdue.edu

Resonant nonlinearities in quantum well structures arise from exciton saturation and band-filling due to photogeneration of free carriers. Through the Kramers-Kronig's relation, a corresponding change in refractive index occurs close to the bandgap energy where the absorption change occurs. The change in refractive index can effectively be used to produce optical switching in devices that can convert phase changes into intensity changes or directional switching[1]. Although the turn-on of carrier induced nonlinearities is effectively an instantaneous effect which follows the photon pulse, these photogenerated carriers tend to linger on well after the photon pulse has passed. The recovery time is usually governed by carrier relaxation times[2,3] or carrier removal rates[4]. In this work, we demonstrate all-optical switching in a Y-junction device in which two control optical pulses are used for each switching event. The first control pulse flips the state of the switch while the second control pulse turns the switch back to its initial state. The switch dynamics is related to other carrier induced devices demonstrated by other independent researchers[5, 6].

The multiple quantum wells which consisted of 38 pairs of 8nm GaAs and 8nm $Al_{0.3}Ga_{0.7}As$ were grown by molecular beam epitaxy and formed the core of a single mode slab waveguide with a 0.5μm thick AlGaAs cladding layer on the top and a 2.5μm thick $Al_{0.3}Ga_{0.7}As$ cladding layer on the bottom. Y-junction ridge structures were delineated by photolithography and wet chemical etching. The ridges were 0.4μm high and 2.5μm wide. The center to center separation of the branching waveguides was 20μm and the half angle between them was 0.8°. The straight input waveguide was 450μm long. Since the waveguides were slightly overmoded, exciting the waveguide with a focused off-center input spot effectively launches the symmetric and anti-symmetric modes of the structure. These propagate along the device with different phase velocities and hence, a split ratio that is different from 50:50 is possible. This split ratio is dependent on the distance between the center of the waveguide and the focusing point at the input facet of the device (which determines the relative amplitudes of the two excited modes), and on the length of the overmoded region.

The device switching characteristics were measured using a conventional pump-probe set-up employing pulses from a self-modelocked Ti-sapphire laser that produced 200fs pulses at a repetition frequency of 80MHz. By using a combination of mirrors and beamsplitters, a pair of control pulses separated by a manually adjustable temporal delay are launched into the device for each signal pulse. The control pulses can be adjusted separately so that they are either collinear or non-collinear. The signal pulses are distinguished from the control pulses by arranging the polarization of control pulses to be orthogonal to that of the signal pulses. In the experiments described in this work, the control pulses were polarized with E-field parallel to the MQW layers thus exciting the TE modes. All three laser beams were coupled into the device using a single 40X microscope objective lens that has a numerical aperture of 0.65. The output facet was simultaneously imaged onto both a video camera and a photodetector. The pump beams were blocked from the probe detector using a crossed polarizer. Additionally, a mechanical chopper was used to modulate the signal beam at 290Hz and lock-in detection ensured high rejection of remnant control pulses and other background noise.

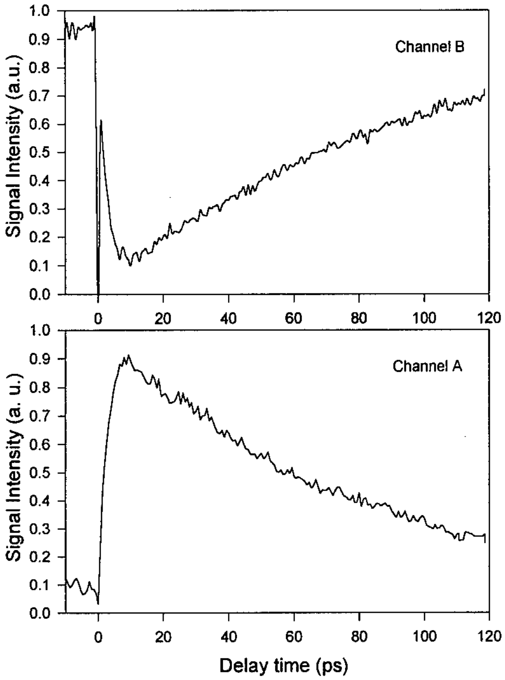

Figure 1. Switching of signal pulses in response to a single control pulse.

The lateral position of the signal beam was adjusted until an unequal split in the intensity of the output ports was detected. Then the position of the first control beam position at the input waveguide is set so that switching causes the signal intensity to be transferred from the port that had the larger split of the probe power into the adjacent one. The second control beam is launched into the waveguide after a short time delay of approximately 10ps, in such a position at the input, that the signal beam is switched back to the original state.

The temporal response of the device to a switching event induced by a single control pulse is recorded by scanning the signal delay stage. From the switching characteristic shown in figure 1, the signal intensity is switched from channel B into channel A, and the recovery of the switch fits well to an exponential decay that has a time constant of about 255ps. The switching is believed to be caused by free carriers that are created by two photon absorption of the control pulse. This notion is substantiated by the fact that similar behavior is observed when the wavelength of the laser was tuned to 890nm, although optimum switching was obtained at a wavelength of 875nm in the devices reported here. As the control beam propagates along the switching region, an asymmetric distribution of photogenerated carriers is created by the two photon absorption. This results in a nonlinear change in the refractive index of the high intensity region, and a consequent change in the power division at the output channels ensues. The nonlinear refractive index change is determined by the distribution of the carriers which, in turn, is dependent on the propagating modes of the control beam.

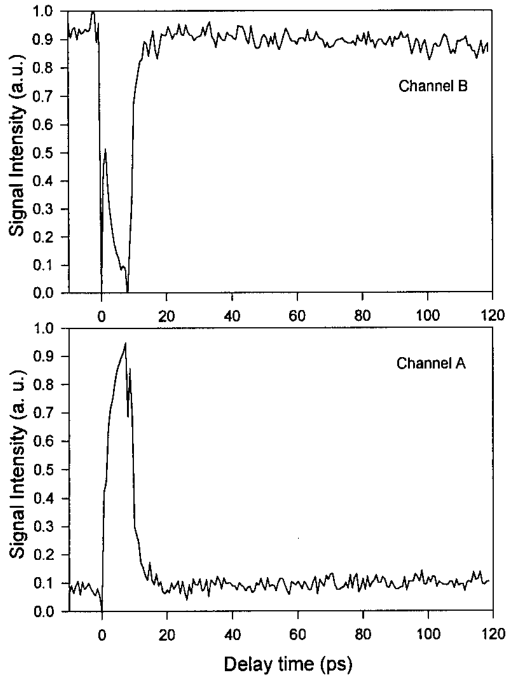

Figure 2. On and off switching of signal pulses caused by two control pulses.

By positioning a second pump beam appropriately at the input of the device, the probe intensity was made to switch back into the initially higher throughput exit port well before the carrier recovery time. Figure 2 shows the time-resolved pump-probe measurement of the device using two control pulses that were temporally separated by 9 ps. Approximately $3GW/cm^2$ of optical intensity corresponding to 9pJ of optical energy, from each of the pump pulses were launched into the device for the switching. The first control pulse created a local population of free carriers asymmetrically across the branching region causing a switch in the power division between the two output ports. The second control pulse created an equal density of free carriers as produced by the first one with a mirror image spatial distribution so as to cancel the effect of the first pulse. Consequently, the initial switching was turned off well before the recovery or removal of the free carriers and ultrafast switch-on as well as ultrafast switch-off is achieved. Hence the switching window is no longer limited by the recovery time, but it depends instead on the temporal separation between the two control pulses. On the other hand a lower limit is imposed by the rise time of the nonlinearity which is due to the cooling time of the hot carriers generated by two photon absorption, and is measured to be 2ps.

In conclusion, we have demonstrated an ultrafast integrated all-optical switch in which the switching window is not restricted by the relatively slow relaxation time in the nonlinearity of the medium. The energy required to achieve a switching contrast of better than 9:1, was around 9pJ. A switching window of <10ps for gating signal pulses has been realized. Two-photon absorption was used to create the free carriers that caused the nonlinear refractive index changes and consequently, nonlinear absorption of the signal pulses at zero time delay was observed in all the measurements.

Acknowledgments:

The authors are extremely grateful to Dr. Mitra-Dutta (now at the Army Research Office) and Dr. Jagadeesh Pamulapati of the Army Research Laboratory for the provision of MBE grown wafers of GaAs/AlGaAs multiple quantum well structures and for helpful discussions.

References

1. R. Jin, C.C. Chuang, H.M. Gibbs, S. W. Koch, “Picosecond all-optical switching in single-mode GaAs/AlGaAs strip-loaded nonlinear directional coupler”, Appl. Phys. Lett., 53 (19), pp1791-1793, (1988).
2. Y. Silberberg, P.W. Smith, D.A.B. Miller, B. Tell, A.C. Gossard, W. Wiegmann, “Fast nonlinear optical response from proton-bombarded multiple quantum well structures”, Appl. Phys. Lett., 46(8), pp701-703, 1985.
3. T. Mishima, T. Tanoue, K. Uomi, “Low temperature MBE growth of high quality modulation doped AlGaAs/GaAs MQWs for ultra-high-speed laser diodes”, J. Crystal Growth, 95(1), p382, 1989.
4. P. Li Kam Wa, A. Miller, J.S. Roberts, P.N. Robson: “130ps recovery of all-optical switching in a GaAs multi-quantum well directional coupler”, Appl. Phys. Lett., 58 (19), pp2055-2057, 1991.
5. J. P. Sokoloff, P. R. Prucnal, I. Glesk and M. Kane,” A terahertz optical asymmetric demultiplexer (TOAD),” IEEE Photonics Tech. Lett., 5, p 787-790 (1993).
6. K. Tajima, S. Nakamura, Y. Sugimoto, “Ultrafast polarization-discriminating Mach-Zehnder all-optical switch”, Appl. Phys. Lett., 67 (25), pp3709-3711, 1995.

Quantum Devices Using Multi-Dots Structures

E. A. M. Fagotto, S. M. Rossi and E. Moschim
School of Electrical and Computer Engineering, State University of Campinas
13083-970 Campinas, SP, Brazil
Phone: 55-19-2398361, Fax: 55-19-2391395

I. INTRODUCTION

Nowadays, due to the advances in nanolithography technology it is possible to fabricate structures whose electronic properties correspond to that of a quasi-one-dimensional electron gas. Such structures allow us to observe ballistic quantum transport at low temperatures, and remarkable experimental observations have resulted[1]. Many theoretical studies have investigated conductance fluctuations[2] and voltage controlled defects. Cahay et al[3] studied the problem of localization associated with the conductance fluctuations of an array of elastic scatterers. Joe et al[4] discussed the effects of a voltage controlled impurity for the conductance of a single open quantum box. As the impurity size is changed, it causes conductance oscillations due to the interference of circulating and bound states of the quantum box. In this paper we analyze how changes in geometry of a structure with three open dots affect its electronic properties.

II. THE MULTI-OPEN DOTS STRUCTURE

In Fig. 1 we have the potential profile for the structure discussed in this work. In order to determinate the electronic transmission through the structure, we perfomed a multichannel scattering calculation[5].

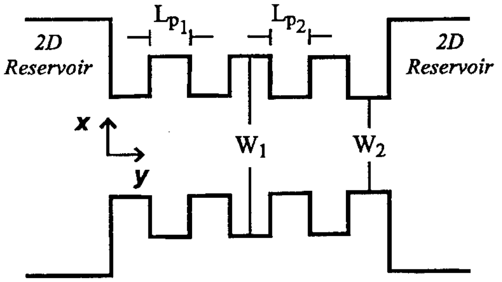

Figure 1: Potential profile for the structure discussed in this paper.The dimensions are $L_{p1}=L_{p2}=500Å$, $W_1=800$ Å e $W_2=500$ Å.

The symmetric and asymmetric multi-open dots structures were discussed by Brum[6]. We can understand their electronic properties in terms of two kinds of states. One strongly localized at the dot regions and the other extended along the channel. We call the former a dot-like state and the latter as channel-like state. In this picture the states formed at the dots generate narrow minibands and those formed at the channels give origin to wide minibands. At certain energies these narrow and wide minibands are degenerate, and, if there is a coupling among them, it opens gaps on the electronic structure. Since we can control this coupling by acting on the structure geometry, we also can control the transmission through the structure. Because this structure is periodic also there will be gaps due to the Bragg reflections at the structure internal interfaces. Therefore, we can say for this kind of structure there will be gaps due to the periodicity, and other ones due to the minibands anticrossing[6,8]. From this point we will always use the term *miniband* for the electronic structure and the term *band* for a transmission width.

III. RESULTS AND DISCUSSIONS

In Fig.2 are the transmission spectra for a symmetric (solid line) and an asymmetric (dashed line) one dot structure. For both structures the first transmission bands are narrow because they are due to their ground dot-like states. The first transmission band for the asymmetric structure occurs at higher energies because its lateral confinement is larger than that for the symmetric structure. For both structures the second transmission bands are much larger than the first ones because they are due to their channel-like states. One can notice a smooth valley centered at the energy of 4 meV that will become more defined as the structure will have a large number of periods because it is a periodicity gap. For the symmetric structure, one can distinguish a sharp peak around the energy of 5 meV. This peak comes from the first excited dot-like state that is superposed on the transmission continuum from the channel-like states.

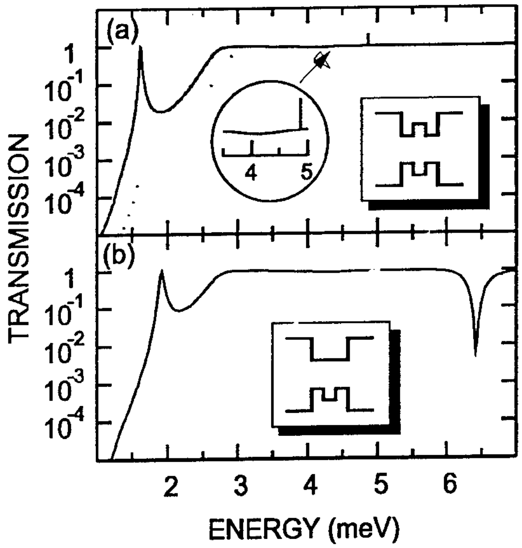

Figure 2: Transmission spectra for a symmetric (solid line) and an asymmetric one dot structure (dashed line). The upper inset shows the symmetric and the lower inset shows the asymmetric structure.

If one considers the asymmetric structure one can see a sharp drop (a cusp) in the transmission close to the energy of 6.5 meV. It occurs because due to the asymmetrization of the structure the first excited dot-like state and the channel-like continuum couple, which causes an anticrossing. One should observe that this is a typical Fano resonance situation[7]. Other small oscillations presents in the transmission spectra should be identified as Fabry-Perot oscillations at the structure boundaries.

To discuss the geometry effects on multi-open dots structure we choose to use a three open dots structure (TODS), since for this number of dots the superlattice features are already present and the computational time for numerical evaluations is not quite extensive[8]. At this point we should notice there are twenty six different geometry configurations for a TODS if only one consider geometric changes in the dots regions[9]. By these changes we mean if the dots are kept empty or full to the channel border.These twenty six different configurations will also produce twenty six different transmission spectra, which can be tailored by the structure geometry. In such a one can program one structure to perform ain signal processing by defining the structure ometry (logical or decoding operations for instance). For this paper we selected five from the twenty six spectra to discuss the physics involved.

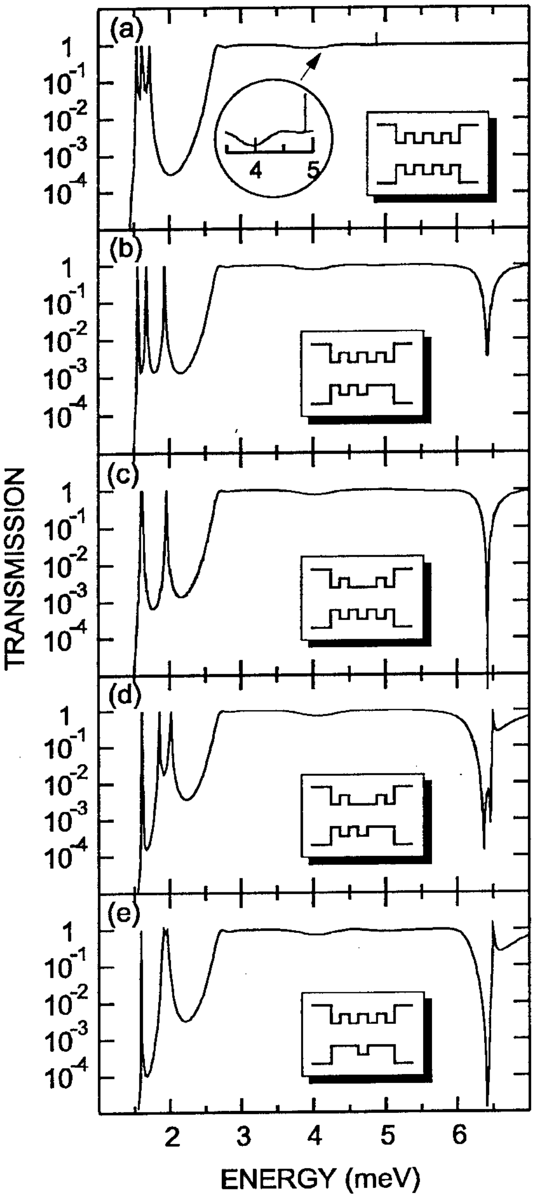

Figure 3: Transmission spectra for five geometry configurations. The insets show geometries for each spectrum.

In Fig.3 are the transmission spectra for these five geometry configurations (see insets) calculated for a three open dots structure (TODS). We are going to designate the dots, from the left to the right, as first, second and third one. In Fig 3(a) is the spectrum for a symmetric TODS, which can be basically understood in the same way that for a single dot structure. However, at this time since there are three dots also there are three dot-like levels for the dot-like ground miniband. Therefore, that is why there are three peaks in the first transmission band. Also, as observed before, due to the existence of a larger number of periods, the superlattice gap centered at energy of 4 meV becomes more evident. The first excited dot-like state can be observed superposed on the transmission continuum, about the energy of 5meV. In Fig.3(b), by increasing the third dot lateral confinement its ground level is displaced to higher energies which separates it from the other miniband levels. Around the energy of 6.5 meV that occurs a dramatic change on the transmission spectrum. It happens because the dot-like third excited miniband couples to the channel continuum in consequence of the third dot asymmetrization. In Fig.3(c), with the second dot asymmetrized its ground level is led to higher energies and the two levels become almost degenerate. We really can not distinguish them in the figure. As before, the first excited dot-like miniband couples to the channel continuum and we have again an anticrossing gap at the energy of 6.5 meV. In Fig.3(d), with the second and the third dot asymmetrized (on opposite sides of the channel) we recover the three peaks for the first transmission band, although two of them have been displaced to higher energies as should be expected. Two valleys appear at the anticrossing gap region which should be understood inside the Fano resonance schema[7]. The first dot is weakly coupled to the second and the third dot as can be seen through their ground states. The same occurs to their first excited states which gives origin to two anticrossing centers, one of them from the interaction between the first dot and the continuum and the other from the interaction among the second and third dot with the continuum. The peak seen close to the higher energy valley is a signature of the Fano resonance. Fano showed when a continuum interacts with localized we can observe resonances and antiresonances as a result of this interaction depending on the nature of coupling potential[7]. In Fig.3(e), with the first and the third dot asymmetrized their ground levels are displaced to higher energies and again they are almost degenerate. However, at this time we find only one antiresonance at the gap region because the structure is now an asymmtric one, perturbed by one symmetric dot at its center and the superlattice features are kept.

IV. CONCLUSIONS

In this work we discussed the geometry effects on the electronic properties of a multi-open dots structure. It was shown by changing the structure geometry one can change the coupling between dot and channel states and hence control the transmission through the structure. Such a way, this kind of structure appears as promising for quantum devices, specially for signal processing.

REFERENCES

[1]B. J. Van Wees, H. Van Houten, C. W. J. Beenaker, J. G. Williamson, L. P Van Der Marel, and C. T. Foxon, *Phys. Rev. Lett.* **60**, 848 (1988). R. C. Ashoori, H. L. Stormer, J. S. Weiner, L. N. Pfeiffer, S. J. Pearton, K. W. Baldwin, and K. W. West, *Phys. Rev. Lett.* **68**, 3089 (1992).

[2]H. Xu, *Phys. Rev. B* **50**, 12254 (1994).

[3]M. Cahay, M. McLennan, and S. Datta, *Phys. Rev. B* **37**, 10215 (1988).

[4]Y. S. Joe, R. M. Crosby, M. W. C. D. Wardana, and S. Ulloa, *J. Appl. Phys.* **76**, 4676 (1994).

[5]G. Bastard, J. A. Brum and R. Ferreira, *"Solid State Physics"* **44**, 382 (1991).

[6]J. A. Brum, *Phys. Rev. B* **43**, 12082 (1991).

[7]U. Fano, *Phy. Rev.* **124**, 1866 (1961).

[8]E.A.M. Fagotto, P.A. Schulz and J.A. Brum, *Solid-State Eletronics* **37**, 1171 (1994). E.A.M. Fagotto, S.M. Rossi and E. Moschim, submitted to the *J. Appl. Phys.*

[9]The structure has inversion of simetry along the x- and y-axes.

Spin-Gratings and In-Well Carrier Transport Measurements in GaAs/AlGaAs Multiple Quantum Wells

P. Riblet, A.R. Cameron, A. Miller

School of Physics and Astronomy
University of St Andrews
North Haugh, St Andrews, Fife, KY16 9SS
Scotland
Tel: +44 -1334-463122
Fax: +44-1334-463104

We have recently demonstrated [1] that transient electron spin gratings created by cross-polarised excitation pulses at a wavelength resonant with the heavy hole exciton, can provide a new and unique way of measuring in-well *electron* drift mobilities in semiconductor multiple quantum well structures. This compares with the usual transient grating method in which only the *ambipolar* diffusion coefficient can be determined [2]. A comparison of concentration and spin grating decay rates allows the direct measurement of both the electron and hole drift mobilities in the same sample. In this work we extend these measurements to GaAs/AlGaAs multiple quantum wells with different well widths and compare results obtained under conditions of exciton saturation and broadening.

Transient gratings are formed when two noncollinear pulses interfere to produce a spatial modulation of the optical properties due to carrier generation. A third, time-delayed pulse is diffracted from the temporary grating. Two types of interference of the optical pulses can be produced depending on the relative polarisations of the beams [3]. An amplitude modulation results from two beams with parallel linear polarisations which creates a free carrier concentration grating in the material. A modulation of electron spin can be created using crossed linear polarisations, figure 1.

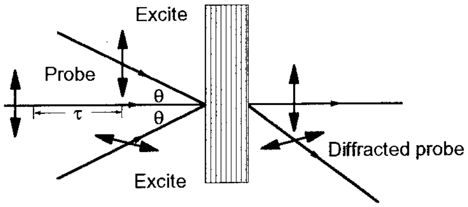

Fig. 1 Transient grating configuration used to produce electron spin gratings.

The creation of electron spin gratings in quantum well semiconductors relies on (a) the selection rules for optical transitions between the heavy hole valence and conduction bands in quantum wells, (b) the spin-dependent nonlinear optical contribution to exciton saturation, (c) the polarisation modulation produced by cross-polarised laser beams and (d) the large difference between spin-relaxation rates for electrons and holes. Circular polarised light resonant with the heavy hole exciton transition produces spin polarised electrons and holes. Since phase space filling is spin-dependent, a polarisation grating, figure 2 (a) can diffract light even although the overall concentrations of electrons and holes are uniform. Electron spin relaxation times in room temperature quantum wells are in the range 10 to 100ps while hole spin relaxation times are sub-picosecond because of the mixed-spin nature of the light hole valence bands. Thus, a modulation of electron spin can be maintained on picosecond timescales.

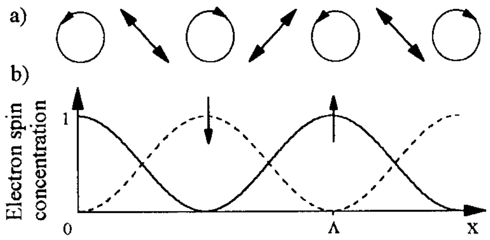

Fig. 2 (a) Polarisation modulation produced by cross-polarised beams and (b) electron spin-up and spin-down concentrations.

Concentration gratings decay by a combination of carrier recombination and diffusion from regions of high to low population. Since equal numbers of electrons and holes are generated, monitoring the grating decay for different grating spacings allows the ambipolar diffusion coefficient to be determined. Electron spin gratings will decay by a combination of spin relaxation and electron diffusion, given by a decay rate, Γ, where,

$$\Gamma = \frac{4\pi^2 D_e}{\Lambda^2} + \frac{1}{\tau_s}$$

Figures 3 and 4 show population and spin grating results for a 4.4nm well width GaAs/AlGaAs sample using a 1ps self-mode-locked Ti:sapphire laser operating at 80MHz.

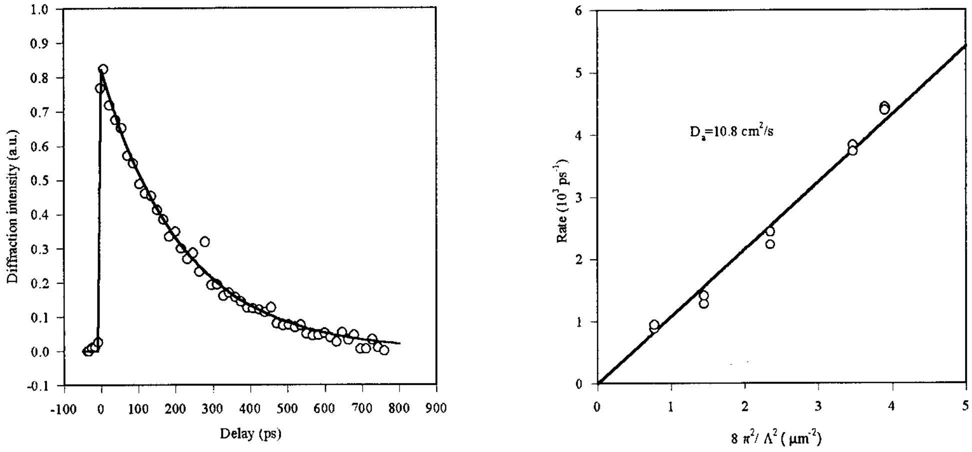

Fig. 3 (a) Diffracted probe signal as a function of delay for parallel polarisations and (b) concentration grating decay rate plotted to give ambipolar diffusion coefficient.

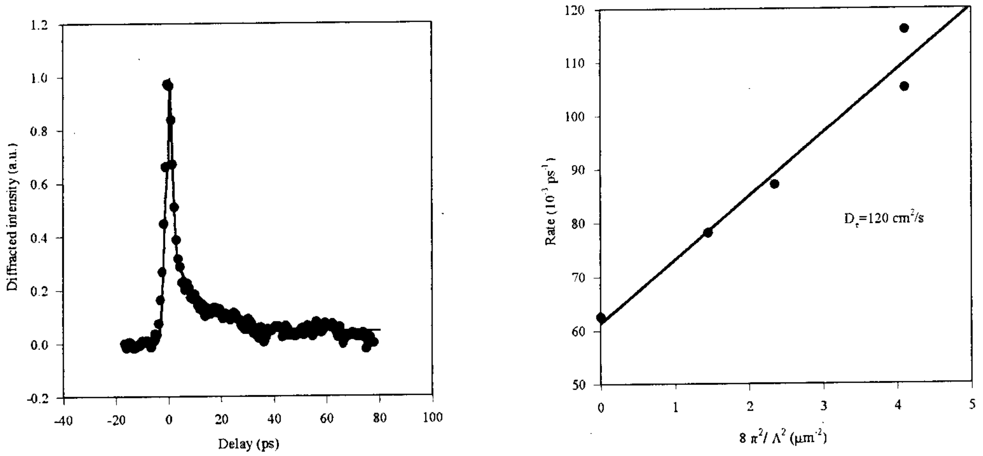

Fig. 4 (a) Diffracted probe signal as a function of delay for crossed polarisations and (b) spin grating decay rate plotted to give electron diffusion coefficient.

The polarisation of a linearly polarised probe pulse is rotated by 90^0 from the spin grating since the modulation consists of two out-of-phase populations of spin-up and spin-down electrons. The in-well electron mobility deduced from the spin grating of fig. 4 is 4600cm^2/Vs which is close to that obtained in a sample with 6.5nm wide wells [1]. The 4.4nm sample has a low background doping level so that a higher mobility may have been expected. Since both well widths give a lower mobility than pure bulk GaAs the limitation on mobility may be interface and alloy scattering. The hole mobilities deduced for the 4.4nm sample from spin and concentration gratings is 450cm^2/Vs which is significantly higher than we observe in wider wells. In the interpretation of hole mobilities, it is important to take into account the effects of exciton broadening on the diffracted signal. In a separate study, we have found that broadening dominates the Coulomb contribution to exciton saturation in narrower GaAs/AlGaAs MQWs. Broadening results in a nonlinear dependence of diffraction efficiency with carrier density in concentration gratings. Although different hole mobilities are expected in quantum wells due to the difference of the in-well effective masses for different well widths, these values are lower than expected for calculated zone centre, in-well masses. This can be explained by considering the room temperature carrier distribution and the nonparabolicity of the heavy hole band which results in a drift mobility close to the bulk GaAs value.

References

[1] A.R. Cameron, P. Riblet and A. Miller Phys. Rev. Lett. **76** 4793 (1996)
[2] A. Miller, R.J. Manning, P.K. Milsom, D.C. Hutchings, D.W. Crust and K. Woodbridge J. Opt. Soc. Am. B **6** 567 (1989)
[3] A.L. Smirl, T.F. Boggess, B.S. Wherrett, G.P. Perryman and A. Miller Phys. Rev. Lett. **49** 933 (1982)

New interpretation of quantum wire luminescence using a non standard description of the valence band states

F. Filipowitz, U. Marti, M. Glick, F.K. Reinhart
Institute of Micro- and Optoelectronics, Federal Institute of Technology, CH-1015 Lausanne, Switzerland, FAX:0041 (21) 6935480

J. Wang, P. von Allmen, J.P. Leburton
Beckman Institute for Advanced Science and Technology, University of Illinois at Urbana-Champain, Urbana, Illinois 61801, USA, FAX: 001 (217) 2444333

I. INTRODUCTION

Theoretical predictions[1] have shown that confined structures, quantum wires (QWR) or quantum dots (QD), should have higher gain and absorption, compared to quantum wells, owing to the discontinuity in the joint density of states. We use a non standard description of the valence band states[2] to evaluate the absorption of V-shaped quantum wires close to the band edge. We choose the projection axis of the angular momentum of the valence band states along the non-confined direction of the wire. This description has two advantages: (i) the masses are isotropic along the two confined directions and (ii) the light hole (lh) and heavy hole (hh) states are decoupled at $k_z=0$, if the kinetic energy of the confined holes is the same along both confined directions and the energy separation between the $\{lh,hh\}_i$ and $\{lh,hh\}_{i+1}$ subbands is high. This description is particularly advantageous close to the band edge where transitions are mostly excitonic. Photoluminescence (PL) and photoluminescence excitation (PLE) measurements made on V-shaped quantum wires are reinterpreted: the lowest energy transition is a e1-lh1 excitonic transition and the second lowest is a e1-hh1 excitonic transition. This new interpretation is the first to explain the lower intensity of the lowest energy peak observed in PL and PLE measurements. To assess the impact of the non-uniformity of the wires, we evaluate the absorption of V-shaped QWR (V-QWR) grown by MBE deposition over a non-planar substrate[3].

II. VALENCE BAND MIXING

With the standard definition of lh and hh, the mixing at the band edge is non negligible. If the energy separation between the $\{lh,hh\}_i$ and $\{lh,hh\}_{i+1}$ subbands is high, the only non-diagonal terms in the Luttinger-Kohn Hamiltonian[4] describing the valence band at the band edge (under the axial approximation) is given by: $R = \sqrt{3} \cdot \gamma_2 \cdot (-\partial_y^2 + \partial_x^2)$, where x and y are directions perpendicular to z, the direction of projection of the angular momentum of the valence band states (we define the lh (hh) as the valence band state whose projection of the angular momentum along z gives $\pm \hbar \cdot \frac{1}{2}$ ($\pm \hbar \cdot \frac{3}{2}$)). At the band edge, the R term is minimized if z is chosen along the wire axis, leading to a significantly smaller coupling between the newly defined lh and hh states.

III. ABSORPTION EVALUATION

We have evaluated the absorption of optical transitions close to bulk band gap. As in Ref.5, we separately describe the initial and final electron states as eigenstates in the valence band Γ_8 and the conduction band Γ_6, respectively, in the effective mass Hamiltonian approximation. We use the envelope function approximation and neglect the split-off band (Γ_7). x and y are the confinement directions, y being the growth direction (see Fig.1). The wire axis is parallel to the z direction. We assume a translational invariance along z. The projection of the angular momentum is chosen along z. Two contributions to the absorption are assumed: (i) a bound excitonic contribution at $k_z=0$ below the onset of the continuum; and (ii) a continuum contribution ($k_z>0$) drastically modified from the free carriers contribution due to Coulomb-correlation. To account for this modification, we use the energy dependent Sommerfeld factor calculated by Rossi[6]. The usual variational approach is used to calculate the binding energy and Bohr radius of the bound excitons.[7] Details of the numerical work are described elsewhere.[8,9]

IV. RESULTS

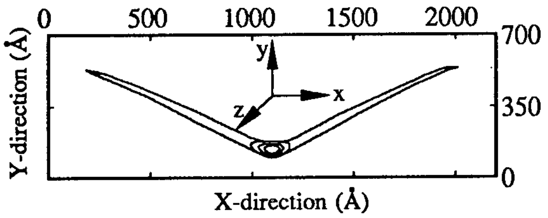

Fig.1. Cross section of the V-QWR-50Å as observed by the transmission electron micrograph. The surface of the wire is 83600Å^2. The charge-density contour plot of the lh1 state represented in the center of the V-QWR. The charge-density contour plot of the e1 and hh1 states are similar.

We have evaluated the absorption of a GaAs V-QWR embedded in a $(AlAs)_4$ / $(GaAs)_8$ superlattice grown by MBE deposition of a nominally 50 Å GaAs QW over a non-planar substrate (V-QWR-50Å). The excitonic character of the lowest energy transitions between 1D conduction and valence states has been demonstrated[10,11]. The good photoluminescence (PL) intensity (compared to QW) demonstrates the high quality interface of these V-QWR[12,13]. The superlattice is approximated by the ternary compound $Al_{0.33}Ga_{0.67}As$. The valence band effective masses along the confined directions in the V-QWR, defined by the Luttinger parameters, are $m^*_{lh}=0.211$, $m^*_{hh}=0.112$. The mixing of the lh and hh states has been evaluated with a perturbation method. The lowest energy valence band state is strongly lh1 (87%). Using the coupled valence band states obtained by the perturbation method, the absorption spectra of the V-QWR-50Å were evaluated. The excitonic and continuum contributions to the absorption spectra and their sum are plotted in Fig.2. The filling factor Γ_{wire} is set to 1. The broadening parameter of 2 meV is chosen to easily distinguish the different contributions. The lowest energy transition (peak labeled e1-lh1) has a strong e1-lh1 excitonic character, the second lowest energy transition (peak labeled e1-hh1) has two contributions: a strong e1-hh1 excitonic character and a small continuum e1-lh1 contribution. The very low contribution of the continuum states is in complete contrast to what is expected from the 1D density of states. This unexpected behavior has two sources: (i) the broadening due to the non uniformity of the wires and (ii) the Coulomb correlation (CC). A comparison of the continuum contribution calculated with or without CC is given in Fig.3. The diminution of the absorption due to CC is clearly visible.

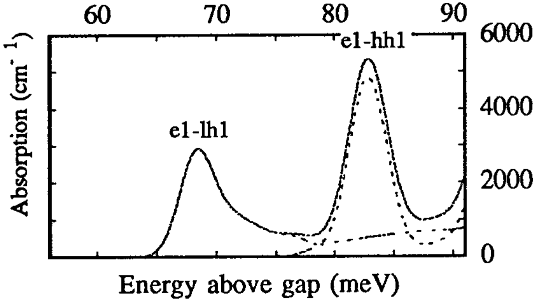

Fig.2. Absorption of light propagating along the y direction ($\Gamma_{wire}=1$). $\Gamma_0=2$ meV. The absorption (solid line) is the sum of the excitonic (dashed line) and continuum (dashed-solid line) contributions.

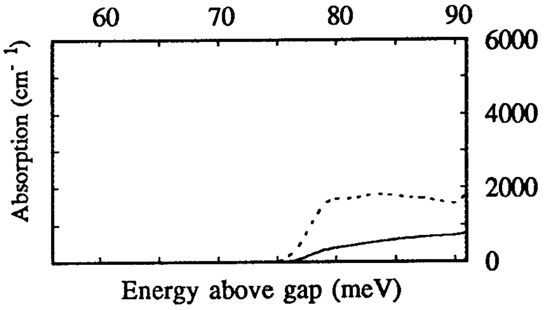

Fig.3. Comparison of the continuum contribution to the absorption ($\Gamma_{wire}=1$) of light propagating along the y direction calculated with the Coulomb-correlation (solid line) or without (dashed line). $\Gamma_0=2$ meV.

Fig.4 is a plot of the absorption spectrum with a more realistic broadening parameter of 6 meV which agrees well with the measured PL spectrum given in Fig.5. Four major results appear on this plot:

(i) The energy difference between the two peaks is 13.5 meV, this value is in good agreement with the 15 meV obtained by PL measurements[12]. The difference may be explained by the approximation of the superlattice barrier by the ternary compound $Al_{0.33}Ga_{0.67}As$.

(ii) The two lowest energy absorption peaks are mainly excitonic: this result agrees with the diamagnetic shift measured by magneto-PL.[13]
(iii) At high excitation intensity, the first and second PL peaks are saturated due to band -filling. When this saturation regime is obtained, the intensity ratio of these two peaks is equal to the intensity ratio of the two absorption peaks. This situation is nearly reached in the PL spectrum of Fig.5 where the intensity ratio equals 1.50. This PL intensity ratio lies between the calculated absorption ratio of 1.48 (ratio of purely excitonic transitions) and 1.84 (ratio of the total absorption). The smaller absorption value of the e1-lh1 transition (compared to the e1-hh1 transition) is due to its smaller optical matrix element.
(iv) The value of the absorption coefficient of the V-QWR-50Å is much lower than that of QW, furthermore the filling factor Γ_{wire} is lower for QWR than for QW. This unexpected result can be explained by the large surface area of 86400 Å^2 of the V-QWR-50Å and has drastic implications for application in lasers and modulators where a high absorption at the band edge is required. As the lowest energy transition can easily be saturated, QWR can be investigated for non linear optical applications.

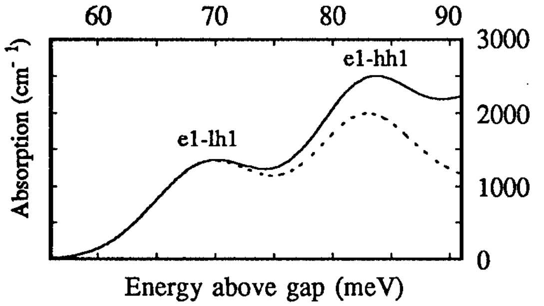

Fig.4. Absorption (Γ_{wire}=1) of light propagating along the y direction. Γ_0=6 meV. The absorption (solid line) is the sum of the excitonic (dashed line) and continuum contributions.

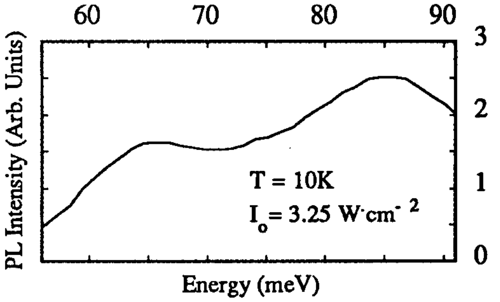

Fig.5. PL spectra adapted from Ref 12. The excitation intensity is 3.25 W·cm^{-2}.

V. CONCLUSION

A non standard description of valence band states leads to an intuitive understanding of the lowest energy transitions of V-QWR. The first transition has a e1-lh1 character. The second lowest energy transition has a e1-hh1 character. Very good agreement is obtained between measurements and theory allowing a new interpretation of PL results without ambiguity.

VI. REFERENCES

[1] D.A.B. Miller, D.S. Chemla and S. Schmitt-Rink, Appl. Phys. Lett., **52**, 2154 (1988).

[2] P.C. Sercel and K.J. Vahala, Phys. Rev. B, **42**, 3690 (1990).

[3] U. Marti, M. Proctor, D. Martin, F. Morier-Genoud, B. Senior and F.K. Reinhart, Microelectr. Eng., **13**, 391 (1991).

[4] see, for example, Eqs.(5-10) of Ref.5

[5] U. Bockelmann and G. Bastard, Phys. Rev. B, **45**, 1688 (1992).

[6] F. Rossi and E. Molinari, Phys. Rev. Lett., **76**, 3642 (1996).

[7] F.L. Madarasz, F.Szmulowicz, F.K. Hopkins and D.L. Dorsey, Phys. Rev. B, **49**, 13528 (1994).

[8] J. Wang, J.P. Leburton and J.E. Zucker, IEEE J. Quantum Electron., **30**, 989 (1994).

[9] J. Wang, J.E. Zucker, J.P. Leburton, T.Y. Chang and N.J. Sauer, Appl. Phys. Lett., **65**, 2196 (1994).

[10] R. Rinaldi, P.V. Giugno, R. Cingolani, F. Rossi, E. Molinari, U. Marti and F.K. Reinhart, Phys. Rev. B, **53**, 13710 (1996).

[11] R. Cingolani, R. Rinaldi, P.V. Giugno, M. Devittorio, M. Lomascolo, M. Didio, U. Marti and F.K. Reinhart, Nuovo Cimento Del. Soc. Ital. Di Fis. D, **17**, 1219 (1995).

[12] A.C. Maciel, J.F. Ryan, R. Rinaldi, R. Cingolani, M. Ferrara, U. Marti, D. Martin, F. Morier-Genoud and F.K. Reinhart, Semicond. Sci. Technol., **9**, 893 (1994).

[13] R. Rinaldi, M. Ferrara, R. Cingolani, U. Marti, D. Martin, F. Morier-Genoud, P. Ruterana and F.K. Reinhart, Phys. Rev. B, **50**, 11795 (1994).

Observation of Quantum Confined Stark Effect in Strain Compensated GaInAsSb/AlGaAsSb Multiple Quantum Well Structures

Yan Shi and Jian H. Zhao
Department of Electrical and Computer Engineering, Rutgers University, Piscataway, NJ 08855
Phone: (908)445-5242 Fax: (908)445-2820

Jiten Sarathy and Greg Olsen
Sensors Unlimited Inc., Princeton, NJ 08540
Phone: (609)520-0610 Fax: (609)520-0638

Hao Lee
SRI David Sarnoff Research Center, Princeton, NJ 08543
Phone: (609)734-2721 Fax: (609)734-2039

I. Introduction

The quantum confined Stark effect (QCSE) has been observed in quantum well structures of many different material systems, such as GaAs/AlGaAs [1]-[3] and InGaAs/InP [4]. Because of the steep rise at the absorption edge, coupled with the very high excitonic resonance peak, and its shift with the applied electric field, the QCSE has many applications in optoelectronics.

In recent years, the quaternary III-V alloy of GaInAsSb lattice matched to GaSb has attracted increased attention because it is a promising material for mid-IR applications [5],[6]. GaInAsSb lasers and photodetectors operating in the 2 to 5 μm wavelength region have been successfully fabricated [7]-[9]. It is therefore interesting to study the QCSE in GaInAsSb MQW structures in order to fabricate the optoelectronic devices utilizing the QCSE with GaInAsSb MQW structures, which have many potential applications. In this paper, we present the first observation of the QCSE in the GaInAsSb/AlGaAsSb strain compensated MQW p-i-n structures grown by molecular beam epitaxy (MBE) on GaSb substrates. The values of excitonic absorption peak shifts agree well with the calculated results. The application of the QCSE to resonant cavity enhanced (RCE) photodetectors is also discussed.

II. QCSE in GaInAsSb/AlGaAsSb MQW Structures

The GaInAsSb/AlGaAsSb strained MQW p-i-n structures were grown by an Intevac modular GEN-II solid-source MBE system on n^+-GaSb (100) substrates. The schematic diagram of the MQW p-i-n structure is shown in Fig. 1. The MQW layers consist of 20 pairs of undoped $In_{0.25}Ga_{0.75}As_ySb_{1-y}$ wells and $Al_{0.25}Ga_{0.75}As_xSb_{1-x}$ barriers. The compressive strain was incorporated into the wells by intentionally increasing the Sb/As ration from the lattice-matched value. To compensate the large compressive strain in the wells, $Al_{0.25}Ga_{0.75}As_xSb_{1-x}$ barriers with tensile strain were employed by intentionally increasing the As/Sb ratio from the lattice-matched value.

To measure the photoresponse of the MQW structures, the samples were fabricated into p-i-n photodiodes. The spectral response of the GaInAsSb/AlGaAsSb MQW p-i-n photodiodes was measured from 1.6 μm to 2.6 μm with reverse bias voltages from 2 V to 10 V. With a reverse bias voltage larger than 4 V, excitonic absorption peaks were observed, and the peaks shift to longer wavelength and broaden with the increasing bias voltage. The peak near the 1.75 μm is due to the e1-hh1 heavy hole excitonic transition, and the peak near the 1.65 μm is due to the e1-lh1 light hole excitonic transition. The spectral photoresponse and the QCSE shift with reverse bias are shown in Fig. 2.

By using the perturbation theory, the e1-hh1 transition energy shift as a function of applied field was calculated. The experimental results are in a very good agreement with the calculated values.

There have been increased interests in resonant cavity enhanced (RCE) photodetectors, because they may have high quantum efficiency, high speed response, and wavelength selectivity [10]. By incorporating a MQW structure into the active region and utilizing the QCSE, RCE photodetectors with wavelength tunability can be achieved [11]. We have reported resonant cavity enhanced (RCE) GaInAsSb photodetectors with high quantum efficiency operating in the wavelength region of 1.8 to 2.0 μm and of 2.35 μm at room temperature [12], [13]. Currently, we are studying electrically tunable GaInAsSb RCE p-i-n photodiodes utilizing the QCSE observed in this report.

III. Summary

The QCSE in GaInAsSb/AlGaAsSb strain compensated MQW p-i-n structures grown by MBE has been successfully demonstrated for the first time. A large excitonic absorption peak shift up to 30 meV in photon energy, or 80 nm in wavelength, under a reverse bias up to 10 V was observed by photocurrent measurement. The values of excitonic absorption peak shifts agree well with the theoretically calculated results. The observed QCSE can be used in GaInAsSb tunable RCE photodetectors, which have potential applications in gas sensing, pollution detection, and future mid-IR high speed optical communications.

References

[1] D. A. B. Miller, D. S. Chemla, T. C. Damen, A. C. Gossard, W. Wiegmann, T. H. Wood, and C. A. Burrus, *Phys. Rev. Lett.*, vol. 53, p. 2173, 1984.

[2] D. A. B. Miller, D. S. Chemla, T. C. Damen, A. C. Gossard, W. Wiegmann, T. H. Wood, and C. A. Burrus, *Phys. Rev.*, vol. B32, p. 1043, 1985.

[3] C. Alibert, S. Gaillard, J. A. Brum, G. Bastard, P. Frijlink, and M. Erman, *Solid State Commun.*, vol. 53, p.457, 1985.

[4] I. Bar-Joseph, C. Kingshirn, D. A. B. Miller, D. S. Chemla, U. Koren, and B. I. Miller, *Appl. Phys. Lett.*, vol. 50, p. 1010, 1987.

[5] R. V. Ewyk and B. M. Willatt, in *Techniques and Mechanisms in Gas Sensing*, P. T. Moseley, J. O. W. Noris and D. E. Williams, Ed. Bristol: IOP Publishing Ltd, 1991.

[6] D. C. Tran, G. H. Siegel Jr., and B. Bendow, *J. Lightwave Technol.*, vol. LT-2, p. 566, 1984.

[7] A. K. Srivastava, J. C. de Winter, C. Caneau, M. A. Pollack, and J. L. Zyskind, *Appl. Phys. Lett.*, vol. 48, pp. 903-904, 1986.

[8] C. Caneau, J. L. Zyskind, J. W. Sulhoff, T. E. Glover, J. Centanni, C. A. Burrus, A. G. Dentai, and M. A. Pollack, *Appl. Phys. Lett.*, vol. 51, p. 764, 1987.

[9] H. Lee, P. K. York, R. J. Menna, R. U. Martinelli, D. Garbuzov, S. Y. Narayan, *J. Cryst. Growth*, vol. 150, p. 1534, 1995.

[10] M. S. Ünlü and S. Strite, *J. Appl. Phys.*, vol. 78, p. 607, 1995.

[11] K. Lai and J. C. Campell, *IEEE J. Quantum Electron*. vol. 30, p. 108, 1994.

[12] K. Xie, J. H. Zhao, Y. Shi, H. Lee, and G. Olsen, *IEEE Photonics Technol. Lett.*, vol. 8, p. 667, 1996.

[13] Y. Shi, J. H. Zhao, H. Lee, J. Sarathy, M. Cohen and G. Olsen, to be published.

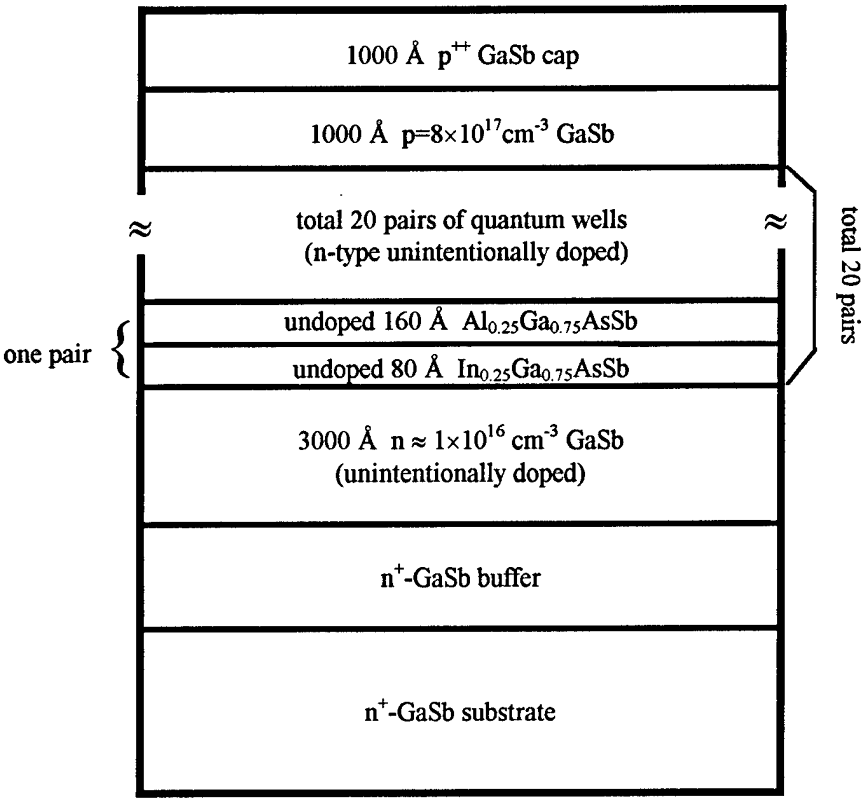

Fig. 1 Schematic diagram of the GaInAsSb/AlGaAsSb MQW structure.

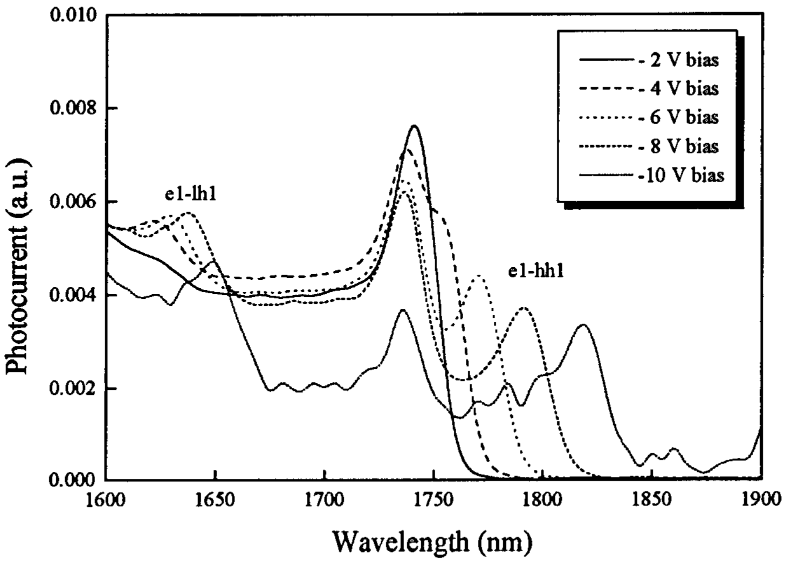

Fig. 2 Spectral photoresponse and the QCSE shift with reverse bias.

Uni-Directional Radiation of Spontaneous Emission from 3D-Photonic Bandgap Crystal Cavity Laser

Hideki HIRAYAMA, Tetsuko HAMANO and Yoshinobu AOYAGI
The Institute of Physical and Chemical Research(RIKEN)
Hirosawa 2-1, Wako-shi, Saitama, 351-01, Japan
Telephone:+81-484-62-1111 ex.3364, FAX:+81-484-62-4659

3-dimensional(3D) photonic bandgap crystal is very attractive for the realization of thresholdless light sources because of controlling the lifetime and the radiation pattern of spontaneous emission by forming the localized impurity mode in the absolute forbidden band[1-3]. We proposed novel surface emitting laser diode consist of a 3-dimensional(3D) photonic bandgap crystal cavity[4]. The spontaneous emission is controlled to radiate into the lasing direction with narrow radiation angle by introducing a plane phase shift region into the photonic crystal. In this report, we for the first time show uni-directional radiation of the spontaneous emission from a 3D photonic bandgap crystal cavity laser by using a plane-wave method.

Figure 1 shows a schematic view of a photonic bandgap crystal cavity laser structure. A diamond- or nonspherical-face-centerd-cubic-crystal dielectric media is used as a cavity in order to form absolute optical forbidden band. In the center of photonic crystal, a plane phase shift region (λ cavity) with light emitting active area is assumed in order to make a lasing level in the forbidden band.

The photonic crystal media works as both laser mirror and the spatial filter of spontaneous emission, and then the spontaneous emission radiate to lasing direction with narrow angle by tuning the emission wavelength of active region to that of phase shift level.

Figure 2 shows a schematic of $I-L$ characteristics comparing between a photonic bandgap crystal cavity laser and a conventional surface emitting laser. Since, almost all emitting power including spontaneous and stimulated emission couple to one direction in the photonic cavity, there is no kink in the $I-L$ curve for photonic crystal cavity laser. Then photonic crystal cavity laser operates as a light source without threshold and spatial-emission-noise. Since there are no optical modes in the forbidden band in contrast to conventional surface emitting lasers, the threshold (lasing) current is much reduced due to the reduction of total spontaneous recombination rate.

We analyze the radiation pattern of the localized lasing level in the photonic crystal cavity. A diamond crystal consisting of circular sphere of air(n=1) in a dielectric atmosphere(GaAs:n=3.6) is assumed with the plane phase shift and active layer. The layer number of the photonic crystal is assumed as 5, taking its refractivity as a cavity mirror into consideration. The thickness of phase shift and active layer is determined as the phase shift level energy approaches to the center of forbidden band. These are analyzed by expanding H with the plain wave basis sets. Then we obtained the average mode energy density[5] and the radiation pattern of the photonic crystal cavity.

Figure 3 shows the calculated results of the mode energy density as functions of normalized frequency and radiation angle. We can see the photonic forbidden bandgap in all directions. A high density phase shift level appears in the middle of the forbidden band. The lasing level density is especially high along the perpendicular direction of phase shift layer and its energy is changed by the radiation angle.

The radiation pattern is obtained by integrating the mode density and the spontaneous emission spectrum in $\boldsymbol{k}$-space. Figure 4 shows the calculated radiation pattern of the spontaneous emission. The wavelength of the lasing level is assumed as $1.0\mu m$ (lattice constant $a=0.47\mu m$). The full width at half maximum (FWHM) of the emission spectrum is assumed as 50meV. As seen in Fig.4 , the spontaneous emission pattern is very sharp and the leakage power, which emitted to the slanting angle, is 2 orders of magnitude smaller than the forward power. The emission angle is less than 10° for FWHM 50meV.

In conclusion, we have proposed a novel surface emitting laser diode consisting of a 3D photonic bandgap crystal cavity. The spontaneous emission is shown to be controlled so as to radiate along the lasing direction with narrow radiation angle, by the analysis using plane-wave method. The photonic bandgap crystal cavity laser operates as a light source without threshold and spatial emission noise, and is very attractive for sue as the light source in the spatially integrated optical circuits.

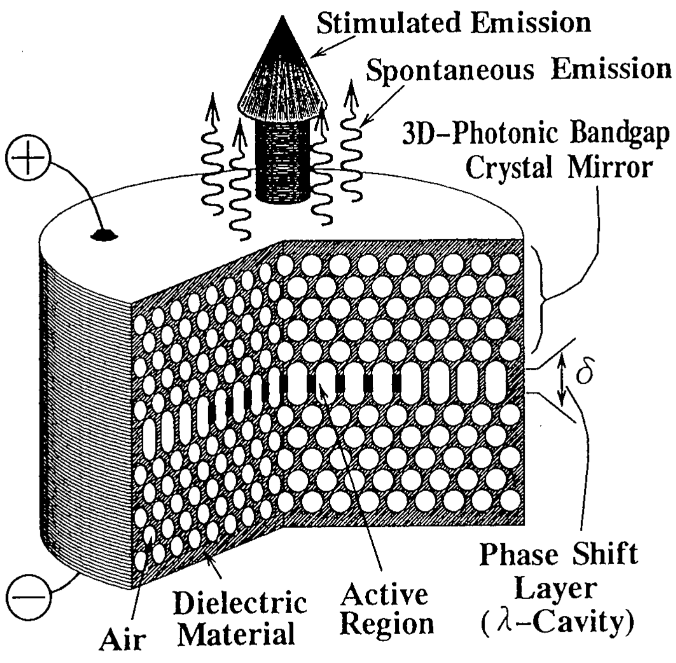

Fig.1 A schematic view of a photonic bandgap crystal cavity laser structure

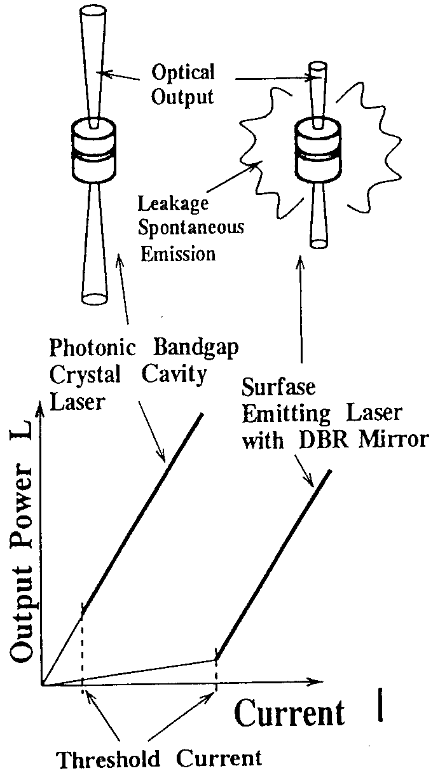

Fig.2 A schematic of $I-L$ characteristics comparing between a photonic bandgap crystal cavity laser and a conventional surface emitting laser.

References

[1] E.Yablonovitch.: *Phys. Rev. Lett.*, **58**, 2059 (1987).

[2] E.Yablonovitch, T.J.Gmitter, and K.M.Leung, *Phys. Rev. Lett.*, **67**, p.2295 (1991).

[3] K.M.Ho, C.T.Chan, and C.M.Soukoulisl, *Phys. Rev. Lett.*, **65**, p.3152 (1990).

[4] H.Hirayama, T.Hamano, and Y.Aoyagi, *Appl. Phys. Lett.*, **69**, p.791 (1996).

[5] T.Baba, T.Hamano, F.Koyama, and K.Iga, *J. Quantum Electron.*, **27**, 1347 (1991).

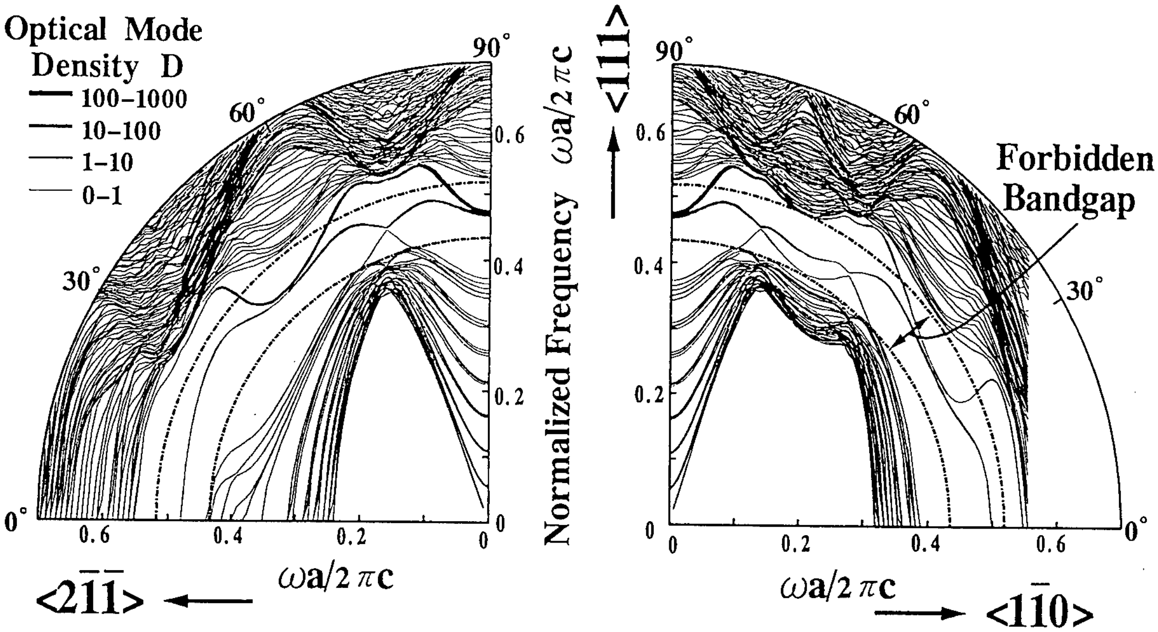

Fig.3 Calculated results of the mode density of diamond photonic crystal cavity laser as functions of normalized frequency and radiation angle.

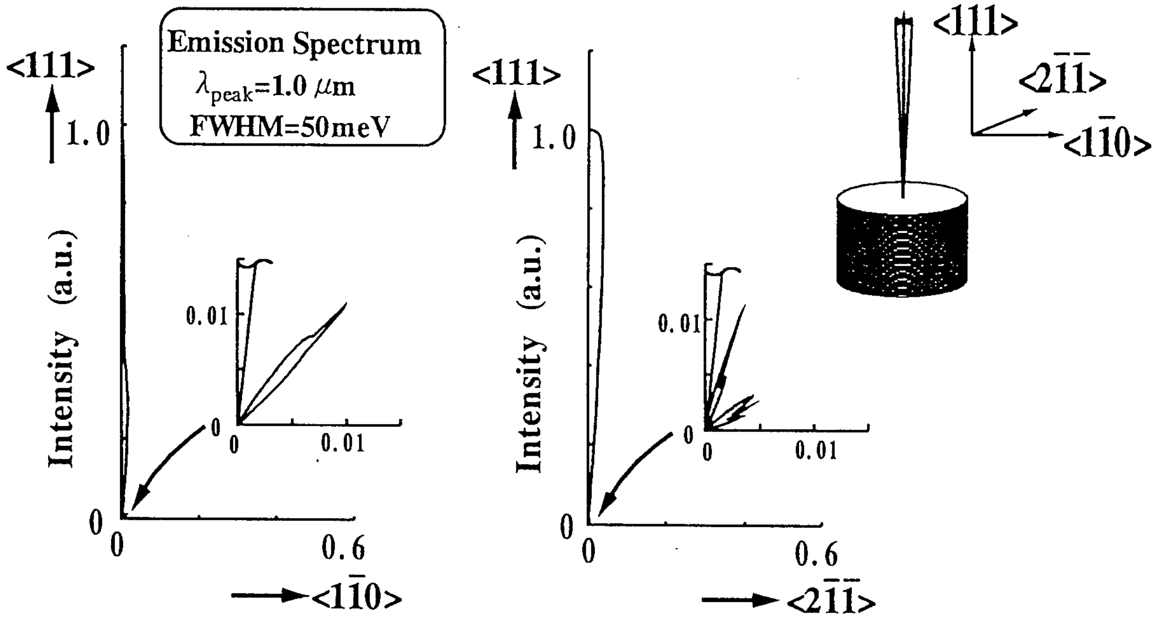

Fig.4 Calculated radiation pattern of the spontaneous emission from the diamond photonic bandgap crystal cavity laser.

Wavelength Stabilization and Trimming Technologies for Vertical Cavity Surface Emitting Lasers

F. Koyama and K. Iga
Precision &Intelligence Laboratory, Tokyo Institute of Technology
4259 Nagatsuta, Midori-ku, Yokohama 226, Japan
Tel: +81-45-924-5068, Fax: +81-45-921-0898
Email: koyama@pi.titech.ac.jp

1. Introduction

Multi-wavelength integrated light sources are key devices for future large scale wavelength division multiplexing (WDM) systems. One of important issues is precise control of lasing wavelength of each element. Large temperature sensitivity of lasing wavelength is also a remaining problem. Recently, wavelength stabilization of semiconductor lasers using strain was demonstrated [1]. Also, wavelength trimming technique was proposed for post-process precise control of wavelength [2].

On the other hand, vertical cavity surface emitting lasers (VCSELs) have been studied also for WDM applications, including multi-wavelength VCSEL arrays and tunable wavelength sources [3]-[6]. Multi-wavelength VCSELs are attractive due to their large wavelength span, easy fabrication process and on-wafer testing in array integration. However, drawback will be insufficient accuracy in wavelength control. The lasing wavelength of VCSELs is predominantly determined by the thickness of cavities. Thus, run-to-run or on-wafer fluctuations of growth rates provides a fairly large deviation of wavelength (~1% or larger). Also, the elimination of costly and unreliable thermoelectric coolers will be desirable for multi-wavelength arrays.

In this paper, we propose a wavelength stabilization technique for VCSELs using a michromachined DBR mirror movable with differential thermal expansion. Also, we discuss on possibilities of post-fabrication adjustment of lasing wavelength using controlled strain. Design and results on simulation are presented.

2. Wavelength stabilization using a micromachined DBR mirror movable by a differential thermal expansion

Figure 1 shows the proposed structure of temperature insensitive VCSELs with a micromachined DBR mirror, which is mechanically deflected by differential thermal expansion. The structure is similar to that developed for tunable wavelength VCSELs with a micromachined cantilever [6]. A difference is in adding one additional layer with a larger thermal expansion coefficient on a top DBR than that of the DBR. Figure 2 shows the operation concept of the proposed device. Temperature decrease causes mechanical deflection of the DBR to the opposite side of the substrate, resulting in the increase of resonant wavelengths. This means the compensation of the wavelength change due to temperature variations. The amount of the compensation can be controlled by the arm length L, the difference in thermal expansion coefficient, and the thickness of the top layer. Figure 2 shows the calculated temperature dependence of the wavelength. We assume that a 0.5μm thick GaAs top layer is loaded on the top of GaAs/AlAsP DBR lattice-matched to a GaAs substrate to obtain differential thermal expansion. The differential thermal expansion coefficient between the top GaAs layer and the averaged GaAs/AlAsP DBR is 8×10^{-7}/K. We can expect 100-hold reduction in temperature sensitivity of lasing wavelength.

3. Post-process adjustment of lasing wavelength

A similar concept using a strain-induced displacement of the DBR can be used for post-process adjustment of lasing wavelength. Figure 4 shows the concept of the proposed scheme using a strain for "wavelength trimming" . A trimming layer with a slightly smaller lattice constant than that of the DBR is loaded on the DBR. By etching the trimming layer, the resonant wavelength can be controlled after the completed fabrication process. Figure 5 shows the result of simulation for post-process adjustment of wavelength. In this calculation, a GaAs trimming layer and a GaAs/AlAsP DBR are assumed, where the composition of P (a few %) in the DBR is a parameter to control the average lattice constant of the DBR. A large wavelength span for post-process adjustment exceeding 10 nm can be expected.

4. Conclusion

The proposed method might be effective to realize temperature insensitive muti-wavelength VCSEL arrays with potential of post-process wavelength adjustment. Precise control in thermal expansion and stress in vertical microcavities may open up potential applications of VCSELs for WDM networks.

Acknowledgment

The authors would like to acknowledge Professor Emeritus Y. Suematsu for encouragement. This study was supported by Grant-in-Aid for COE Research from the Ministry of Education, Science, Sports and Culture (#07CE2003, "Ultra-parallel Optoelectronics").

References

[1] D.A. Cohen and L.A. Coldren, ISLC'96, W1.6, pp.135-136, 1996.
[2] T. Sudoh, Y. Nakano and K. Tada, ISLC'96, W1.5, pp.133-134, 1996.
[3] C.J. Chang-Hasnain, J.P. Harbison, C.E. Zah, M.W. Maeda, L.T. Florez, N.G. Stoffel and T.P. Lee, IEEE J. Quantum Electron., vol.27, pp.1368-1376, 1991.
[4] L.E. Eng, K. Toh and C. J. Chang-Hasnain, Summer Topical Meeting Digest of LEOS 1994, W1.5, ,1994.
[5] F. Koyama, T. Mukaihara, Y. Hayashi, N. Ohnoki, N. Hatori and K. Iga, IEEE Photon. Tech. Lett., vol.7, pp.10-12, 1995.
[6] M.S. Wu, E.C. Vail, G.S. Li, W. Yuen and C.J. Chang-Hasnain, Electron. Lett., vol.31, pp.1671-1672, 1995.

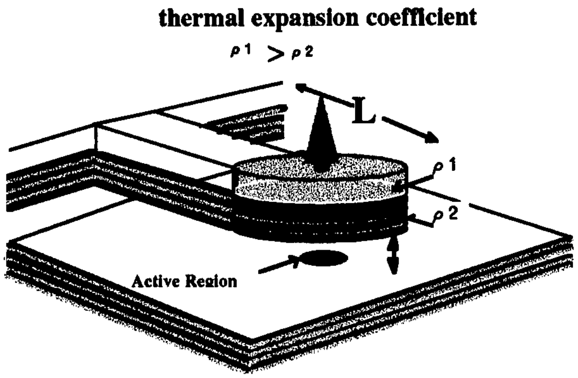

Fig.1 Schematic structure for wavelength stabilization VCSELs with micro-machined DBR deflected by differential thermal expansion.

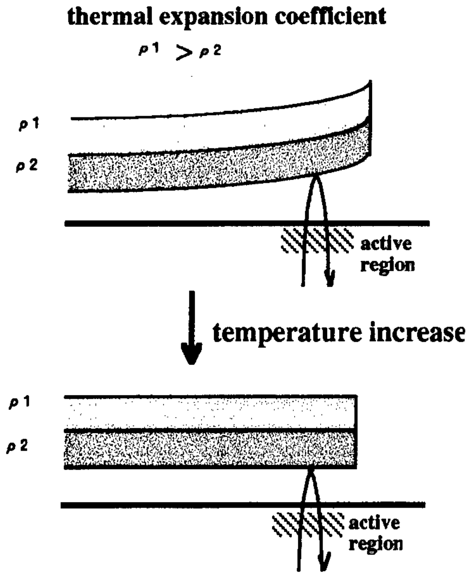

Fig. 2 Operation principle of temperature insensitive VCSELs.

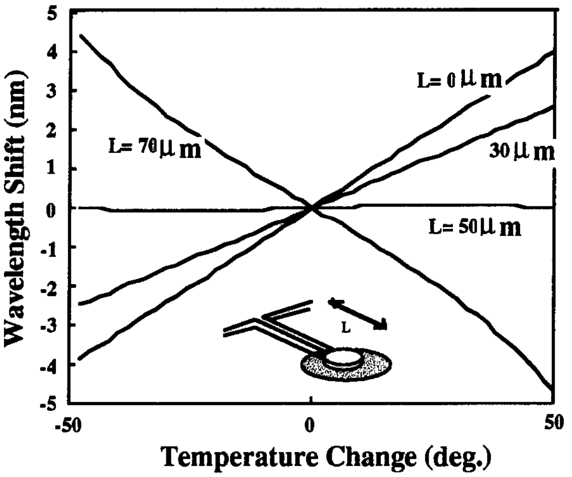

Fig. 3 Calculated temperature dependence of lasing wavelength.

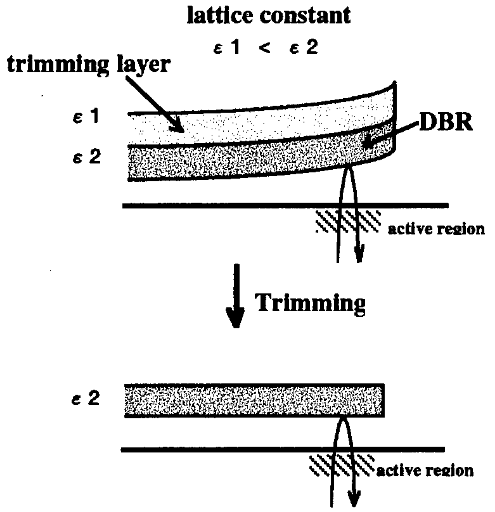

Fig. 4 Schematic concept of wavelength trimming technique for VCSELs.

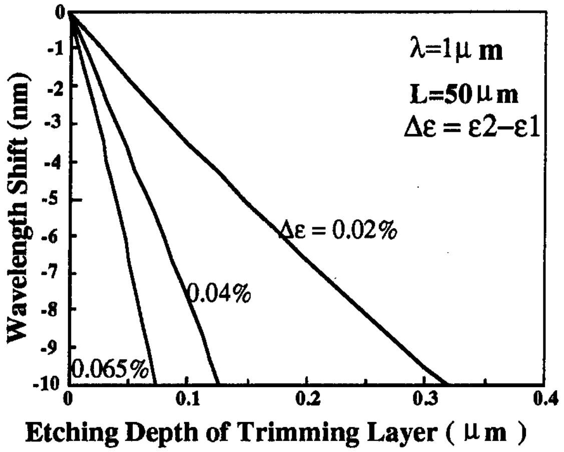

Fig. 5 Post-process wavelength adjustment by etching a trimming layer.

Time-Domain Measurements of Light Propagation in Dielectric Spheres

W. B. Whitten, R. W. Shaw, M. D. Barnes, and J. M. Ramsey
Chemical and Analytical Sciences Division, Oak Ridge National Laboratory
P.O Box 2008, Oak Ridge, Tennessee 37831-6142
Tel: (423) 574-4921, FAX: (423) 574-8363, email: wbw@ornl.gov

There has been increasing fundamental and practical interest in the properties of dielectric microspheres in recent years. High-Q structural resonances that occur when the round trip optical path is an integral number of wavelengths can be exploited for quantum measurement and the observation of cavity QED effects. The spherical microparticle is also an important component of the earth's atmosphere, contributing both to visual displays and global change. In this paper, we describe theoretical and experimental applications of optical pulse techniques to the characterization of dielectric spheres.

Microparticles are traditionally characterized by measuring the angular or wavelength dependence of scattered monochromatic light. In the present work, we have formulated the propagation of short optical pulses in dielectric spheres. Time-domain measurements in the backscattering direction should be equivalent to CW measurements at a large number of scattering angles but permit remote morphological characterization. We show that the nonlinear wave equation for pulse propagation in whispering gallery modes of a sphere is of the same form as for a linear optical fiber and that bright soliton propagation should be possible under suitable dispersive conditions.

Solutions to the spherical wave equation are obtained in the asymptotic limit $a \gg \lambda$ with the assumption of negligible leakage from the sphere. Spherical wave packets are then formed from a superposition of the wave equation solutions. The boundary conditions on the solution to the radial wave equation give a relation for the material and modal dispersion of the group velocity.

Pulse propagation should be observable when the pulse duration is shorter than the round trip time. The conditions for such visibility can be estimated from the above dispersion relation. We have explored these ideas experimentally using time-domain measurements of ps-pulse propagation in glass spheres of millimeter dimension.

Pulses from a mode-locked Ti:Al_2O_3 laser were coupled into whispering-gallery modes of a glass sphere by frustrated total internal reflection from a high-index prism. Scattered radiation leaking tangentially from the sphere was collected and focussed onto a diode detector by a lens. The signal from the photodiode could be measured with an oscilloscope in the time domain, or with a microwave spectrum analyzer. The results of these experiments should be interpretable in terms of the material properties and morphology of the samples.

This research was sponsored by the Division of Chemical Sciences, Office of Energy Research, U.S. Department of Energy, under contract DE-AC05-96OR22464 managed by Lockheed Martin Energy Research Corporation.

Computational Modeling of Ultrashort Pulse Propagation in Semiconductor Materials

Peter M. Goorjian
NASA Ames Research Center, M.S. T27B-1, Moffett Field, CA 94035-1000
Phone: (415) 604-5547, Fax: (415) 604-1095, Email: goorjian@nas.nasa.gov
Govind P. Agrawal
Institute of Optics, University of Rochester, Rochester, NY 14627
Phone: (716) 275-4846, Fax: (716) 244-4936, Email: gpa@optics.rochester.edu

An algorithm has been developed that solves the semiconductor Maxwell-Bloch equations [1], without making the standard slowly-varying envelope (SVEA) and rotating-wave (RWA) approximations. This more exact formulation is applied to simulations of the propagation of ultrashort pulses for which the standard approximations reach their limits. This development was motivated by the generation of optical pulses as short as 8 fs, which has become possible due to recent progress in ultrafast technology.

Previously, an algorithm was developed for the Maxwell equations [2,3], without making the SVEA for calculations of pulse propagation in nonlinear glasses, which exhibit Kerr-like instantaneous nonlinearities. It was found that significant differences can occur when the SVEA is not made in Maxwell equations. Specifically, light bullets, of 25 fs duration, were found to be stable [4] with the full Maxwell equations, whereas previously, calculations with the nonlinear Schroedinger equation had shown them to be unstable [5]. More recently [6], using the algorithm developed in references 2 and 3, calculations showed the formation of shock waves on the optical carrier wave. Such results are impossible with the SVEA since the carrier wave is eliminated from the calculations.

In this paper, this new algorithm is applied to studies of ultrafast optical pulse propagation in nonlinear semiconductor materials, in which many-body effects due to Coulomb interactions must be included. In addition to the algorithm for Maxwell's equations, a new algorithm has been developed for the semiconductor Bloch equations that does not make the RWA and the two algorithms have been combined into one for the coupled semiconductor Maxwell-Bloch equations. In the Bloch equations the relaxation-time approximation [1] has been made for the various intraband scattering processes.

The Maxwell-Bloch equations for pulse propagation in one spatial dimension are obtained by assuming that the electric field of the pulse propagates along the z direction and is polarized along the x axis. Ignoring the transverse effects, the Maxwell equations become

$$\frac{\partial D_x}{\partial t} = -\frac{\partial H_y}{\partial z}, \qquad \mu_0 \frac{\partial H_y}{\partial t} = -\frac{\partial E_x}{\partial z}, \qquad D_x = \epsilon_0 \epsilon_r E_x + P_x ,$$

where P_x is the induced polarization.

In the case of semiconductors, P_x is calculated by using the semiconductor Bloch equations [1] for a two band model (one conduction and one valence band):

$$\frac{dn_k^e}{dt} = -\frac{n_k^e - \bar{n}_k^e}{\tau_c} - 2\mathrm{Im}(\Omega_k p_k^*) , \qquad \frac{dn_k^h}{dt} = -\frac{n_k^h - \bar{n}_k^h}{\tau_v} - 2\mathrm{Im}(\Omega_k p_k^*) ,$$

$$\frac{dp_{1,k}}{dt} = -\frac{p_{1,k}}{\tau_2} + \Delta_k p_{2,k} + \Omega_{2,k} w_k , \qquad \frac{dp_{2,k}}{dt} = -\frac{p_{2,k}}{\tau_2} - \Delta_k p_{1,k} - \Omega_{1,k} w_k ,$$

where n_k^e and n_k^h are the occupation probabilities for electron and holes of the momentum $\hbar k$, $w_k = n_k^e + n_k^h - 1$ is the inversion, $p_k = p_{1,k} + ip_{2,k}$ is the interband transition expectation function, and the τ parameters govern various decay processes. The transition energy $\hbar\omega_k$ is varied over a sufficiently large range to accurately describe the interaction of an ultrashort optical pulse with the semiconductor. $\bar{n}_k^e(t)$ and $\bar{n}_k^h(t)$ are determined by first computing the chemical potentials $\mu^e(t)$ and $\mu^h(t)$ from $n_k^e(t)$ and $n_k^h(t)$ respectively and then using the Fermi-Dirac distribution to find the quasi-equilibrium values $\bar{n}_k^e(t)$ and $\bar{n}_k^h(t)$

The generalized Rabi frequency $\Omega_k = \Omega_{1,k} + i\Omega_{2,k}$, the effective transition energy $\hbar\Delta_k$ after the band-gap renormalization, and the induced polarization P_x are given respectively by

$$\Omega_k = \frac{1}{\hbar}(\mu E_x(t) + \sum_{q\neq k} V_{|k-q|}p_q), \quad \hbar\Delta_k = \hbar\omega_k - \sum_{q\neq k} V_{|k-q|}(n_q^c + n_q^h), \quad P_x(t) = \frac{2\mu}{\pi^2}\int_0^\infty p_{1,k}k^2 dk.$$

Initially an algorithm was developed for the simpler optical Maxwell-Bloch equations for two-level atomic systems [7]. A calculation of self-induced transparency was made for a a 10 fs pulse [8]. Figure 1 shows the electric field of the pulse at several moments during its propagation inside the medium. The top curve on the right side in figure 2 shows the corresponding population inversion at some location as the pulse goes by. The top curve on the left side in figure 2 shows the resulting population inversion for self-induced transparency when the SVEA and the RWA are made. The remaining curves are a comparison of the two methods when the atomic transition frequency is detuned away from the optical carrier frequency. The exact method is able to capture the off resonance details that the approximate method is incapable of modeling.

Next the semiconductor Maxwell-Bloch equations were solved [8] without including the Coulomb interaction (the free-carrier assumption) and there were no relaxation terms in the equations for the evolution of n_k^e and n_k^h. Figures 3–6 show colliding pulses, including constructive and destructive interference. These results show the possibility of soliton formation in a semiconductor because these nonlinear pulses remain essentially unchanged after undergoing collision. Figure 7 shows gain curves that were obtained under the free-carrier assumption.

Finally, figure 8 shows the linear exciton absorption results obtained by including the Coulomb interaction. Notice the 1s and 2s absorption peaks for a 2-ps dipole decay time. Here $w_k = -1$, the generalized Rabi frequency was used but the transition energy was not renormalized. The presentation shall include additional calculations of propagating and colliding pulses in which all the Coulomb and relaxation terms are included [9].

We would like to thank Rolf Binder, Optical Sciences Center, University of Arizona, for his many helpful comments concerning algorithm development for the semiconductor Bloch equations.

References

1. Haug, H., and Koch, S. W., *Quantum Theory of the Optical and Electronic Properties of Semiconductors* , World Scientific Press, 2nd Ed., 1993.
2. Goorjian, P. M. and Taflove, A.,"Direct Time Integration of Maxwell's Equations in Nonlinear Dispersive Media for Propagation of Femtosecond Electromagnetic Solitons," *Optics Letters* , Vol. 17, No. 3, Feb. 1, 1992.
3. Goorjian, P. M., Taflove, A., Joseph, R. M., and Hagness, S. C., "Computational Modeling of Femtosecond Optical Solitons from Maxwell's Equations," *IEEE Journal of Quantum Electronics* , special issue on "Ultrafast Optics and Electronics," vol. 28, No. 10, pp. 2416-2422, Oct., 1992.
4. Goorjian, P. M. and Silberberg, Y.: "Numerical simulation of light bullets, using the full vector, time dependent Maxwell equations," Nonlinear Optics Topical Meeting, Waikoloa, Hawaii, July 24-29, 1994 and Integrated Photonics Research Topical Meeting, (IPR'95), February 23-25, 1995, at Dana Point, CA., both cosponsored by Optical Society of America and IEEE/Lasers and Electro-Optics Society.
5. Silberberg, Y.: "Collapse of optical pulses," *Optics Letters*, Vol. 15, No. 22, pp. 1282-1284, November 15, 1990.
6. Flesch, R. G., Pushkarev, A. and Moloney, J. V.: "Carrier Wave Shocking of Femtosecond Optical Pulses," *Phy. Rev. Lett.*, Vol. 76, No. 14, pp. 2488-2499, April 1, 1996.
7. Allen, L. and Eberly, J. H., *Optical Resonance and Two-Level Atoms* , Dover Press, 1987.
8. Goorjian, P. M. and Agrawal, G. P.: "Computational Modeling of Ultrashort Optical Pulse Propagation in Nonlinear Optical Materials," Paper NME31, Nonlinear Optics Topical Meeting, Maui, HI, July 8-12, 1996
9. Indik, R. A., Moloney, J. V., Binder, R., Knorr, A. and Koch, S. W.: "Self-Induced Channeling of Sub-Picosecond Optical Pulses in Broad Area Bulk Semiconductor Amplifiers," *Optics Letters*, Vol. 20, No. 22, pp. 2315-2317, November 15, 1995.

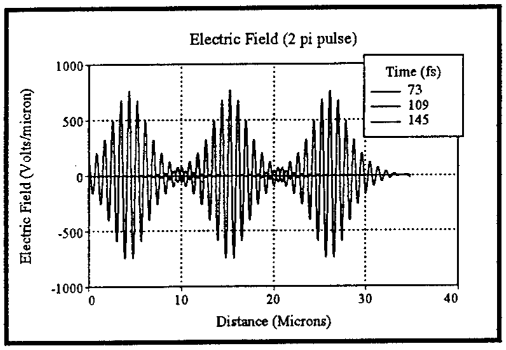

Fig. 1. Two-level atom. Self induced transparency.

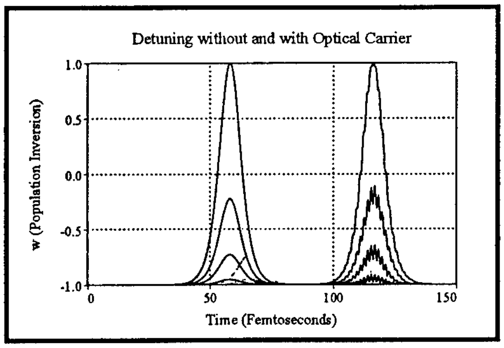

Fig. 2. Two-level atom. Population inversion.

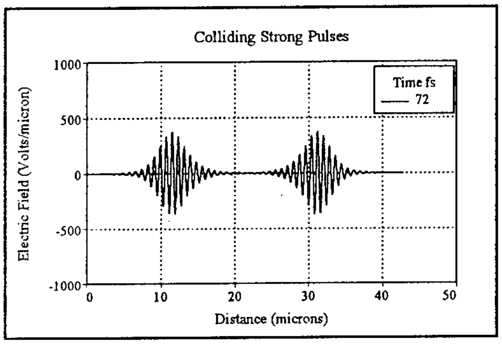

Fig. 3. Approaching Pulses

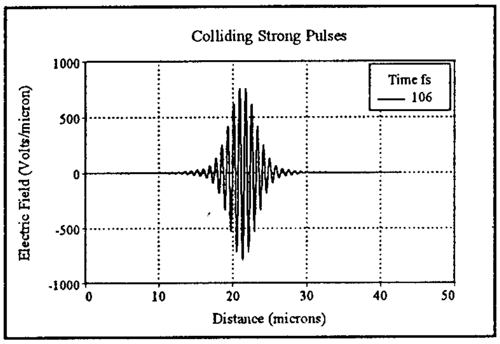

Fig. 4. Constructive Interference

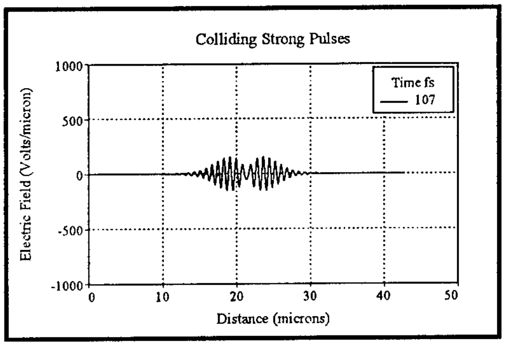

Fig. 5. Destructive Interference

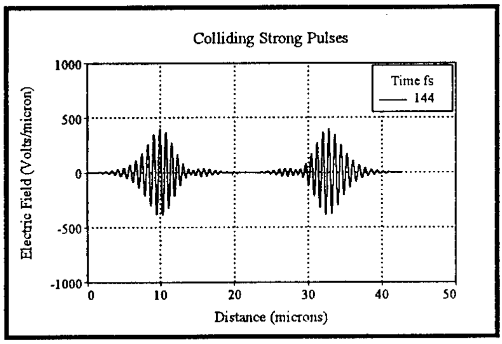

Fig. 6. Separating Pulses

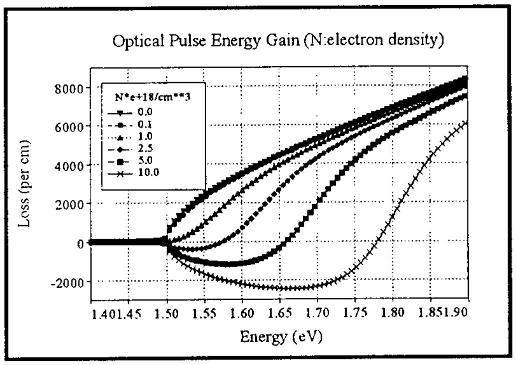

Fig. 7. Gain Curves

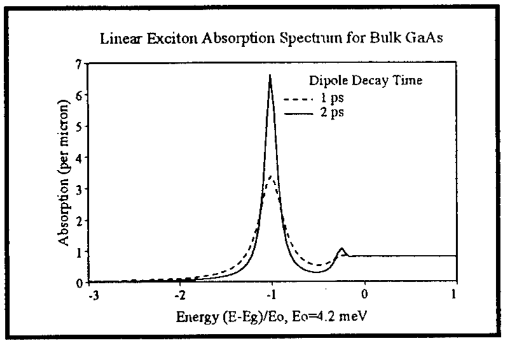

Fig. 8. Linear Exciton Absorption Spectrum

Laser Annealing of Trap States in ZnSe Quantum Dots

Christine A. Smith and Subhash H. Risbud
Dept. of Chemical Engineering & Materials Science, University of California, Davis, CA 95616

J. Diane Cooke and Howard W. H. Lee
Lawrence Livermore National Laboratory
P.O. Box 808, L-174, Livermore, CA. 94551
(510) 423-5877
(510) 422-1066 (FAX)

Our study of ZnSe quantum dots is motivated by the inherent interest in quantum confined systems and by the potential for shorter wavelength laser operation enabled by blue-shifted quantum confined energy levels. The optical and electronic properties of these nanocrystals as a function of the fabrication process were investigated with various optical techniques including photoluminescence (PL) lifetimes, and absorption, PL , and excitation spectroscopy.

ZnSe nanocrystals in a potassium borosilicate glass matrix were prepared by first melting a base glass composition formulated specifically for compatibility with II-VI semiconductors as reported in earlier work on CdS, CdSe, and CdTe [1-3]. The base glass consisted of (in wt%): 56% silica, 24% potassium oxide, 9% barium oxide, 8% boron oxide, and 3% calcium oxide. Twenty-five to thirty gram batches of this oxide powder mixture were melted in alumina crucibles and refined to remove bubbles at 1400°C for several hours. Following melt casting, the glasses were ground into a fine powder, ZnSe powder was added, and the blended mixture was re-melted again at 1400°C for approximately one and a half hours before casting the melt into small slabs. In all cases, excess ZnSe was added to compensate for the expected volatilization losses from the melting process. The as-cast sample (which we will refer to as Z0) appeared reddish-orange in color after overnight annealing at ~350 °C. A portion of this as-cast sample was successively cycled through a process of re-melting and rapid quenching. Quenching was accomplished by pouring the melt between two metal plates. Samples Z1, Z2, and Z3 resulted from successive heating and quenching cycles. Thin flakes of this quenched material appear blue-shifted from reddish-orange to orange-yellow.

The absorption spectrum of sample Z2 reveals an apparent exciton peak near 3.1 eV, which is blue-shifted by ~ 0.45 eV from the bulk's band-gap of 2.65 eV. This feature is also observed in samples Z1 and Z3. The position and width of this absorption peak increase monotonically with the number of processing cycles. Transmission electron microscopy data show an average nanocrystal size of 50 Å in diameter [4]. Since the ZnSe exciton Bohr diameter is approximately 90 Å [5], quantum confinement of the particle excitation is suggested and is supported by the blue-shifted absorption of the ZnSe nanocrystals. The color change observed, as more heat treatment is applied, also supports this interpretation. The absorption peak likely originates from discrete quantum confined electron-hole pair states in the ZnSe nanocrystals and may correspond to the 1S-1S transition. The broad absorption peak, roughly 1.0 eV, possibly reflects a wide distribution of particle sizes in the sample, along with phonon broadening at room temperature.

The PL spectra of the ZnSe nanocrystals from samples Z2 and Z3 are highly red-shifted from the absorption edge, appearing between 700-900 nm. This large red-shift is indicative of rapid trapping of the initial excitation and emission from low lying impurities or trap states. Raman studies have shown that the red-shifted PL between 700 and 900 nm originates from Se_2^- molecules [6]. This would indicate that the initial excitation in samples Z2 and Z3 relax via trapping in Se_2^- molecules, followed by radiative relaxation. In contrast, sample Z1 shows a different PL spectrum with a peak near 570 nm. This peak has been reported to result from Se vacancies in the sample [7]. A blue emission (near 425 nm) is also observed near the bandedge for samples Z2, Z3, and the potassium borosilicate glass matrix. We assign this luminescence to the direct free exciton decay, and it is this blue bandedge emission that is desirable. Our results show that trap emission competes effectively with bandedge emission. Hence, a method to eliminate these traps is needed.

In the past, laser annealing has proven effective in eliminating traps. Our motivation for utilizing a laser annealing process is to eliminate the deep trap states and thereby lead to a greater bandedge emission in the blue. The laser annealing process (0.14 W to 6.5 W over 10 min.) produces a dramatic decrease in the intensity of the PL from these trap states. Specifically, relative changes in the PL in the spectral region around 500-700 nm and 775-900 nm are observed. Since the strength of the luminescence, as viewed by the naked eye, decreases greatly after the annealing process we can conclude that Se_2^- molecules are responsible for trapping of the excitation.

UC Davis research supported by NSF grant DMR 94-11179 (Electronic Materials Program). Work at LLNL performed under the auspices of the USDoE under contract number W-7405-ENG-48.

References

1. L. C. Liu and Subhash H. Risbud, J. of Appl. Phys., **76**, 4576 (1994).
2. P. Rodrigues, P. Y. Yu, and S. H. Risbud, Solid State Communications, **94**, 583 (1995).
3. V. Esch, B. Fluegel, G. Khitrova, H. Gibbs, X. Jiajin, K. Kang, S. Koch, L. C. Liu, S. H. Risbud, and N. Peyghambarian, Phys. Rev. B, **42**, 7450 (1990).
4. While the average diameter is quoted as 50 Å the TEM data shows a broad distribution of ZnSe nanocrystals ranging from ~35 to up to 100 Å; Valerie J. Leppert, M. Fendorf, and Subhash H. Risbud, Phil. Mag. Lett., submitted.
5. F. Henneberger, S. Schmitt-Rink, and E. O. Gobel, eds. "Optics of Semiconductor Nanostructures," (Akademie Verlag; Berlin; 1993).
6. Z. Su, P. A. M. Rodrigues, P. Y. Yu, and S. H. Risbud, J. Appl. Phys., **80**, 1054(1996).
7. G. Li and M. Nogami, J. Appl. Phys., **75**, 4276 (1994).

Physics of Mid-Infrared Devices

QFA 8:30am – 10:00am
Salon A

Jurgen Kuhl, *Presider*
Max Planck Institute, Germany

Quantum Cascade Whispering Gallery Lasers

Claire Gmachl, Jérôme Faist, Frederico Capasso, Carlo Sirtori, Deborah L. Sivco, and Alfred Y. Cho

Bell Laboratories, Lucent Technologies
700 Mountain Avenue, Murray Hill, NJ 07974

Phone: (908) 582-6164
Fax: (908) 582-7660
E-mail: cgmachl@lucent.com

Low threshold, single-mode quantum cascade whispering gallery lasers with emission wavelengths from 5.0 to 11.5 micrometer are reported. Their potential for true microcavities is discussed.

Simulation of High-Power Mid-IR Interband Cascade Laser

I. Vurgaftman, J. R. Meyer, and C. L. Felix
Code 5613, Naval Research Laboratory, Washington, DC 20375

L. R. Ram-Mohan
Worcester Polytechnic Institute, Worcester, MA 01609

There is a critical need for high-power mid-infrared diode lasers to be used in such military and commercial applications as IR countermeasures, IR illumination, and long-range chemical sensing. To date, the highest reported cw output power from a semiconductor diode emitting in the 3-5 μm spectral region has been 215 mW/facet. This was obtained from a 250-μm stripe at 80 K,[1] and cw operation has never been observed in a III-V diode laser above 175 K.[2] Although output powers exceeding 1 W are readily attainable from near-IR ($\lambda \approx 1$ μm) lasers operating at or near ambient temperature, mid-IR emitters are inherently at a disadvantage due to the inverse scaling of the differential slope efficiency (dP/dI) with wavelength. That is, while the same current is required to inject one electron-hole pair as in a near-IR diode laser, the energy of the photon that results is 3-5 times smaller. A recent breakthrough has been the demonstration that this fundamental limitation may be circumvented by employing a cascade geometry. The unipolar quantum cascade laser (QCL) of Faist *et al.*,[3] which achieves lasing due to optical intersubband transitions, can in principle emit as many photons for each injected electron as there are periods in the structure. However, high cw operating temperatures and large cw output powers have not yet been reported, in part because the threshold current density is inevitably rather large owing to a rapid nonradiative phonon relaxation of the population inversion.

Here we discuss an alternative configuration, the type-II interband cascade laser (T2ICL),[4,5,6] which eliminates the phonon relaxation path while retaining the advantages of electron recycling. Detailed simulation of the operation for an optimized design shows that the T2ICL has the potential to combine low threshold current densities with mid-IR output powers exceeding 1 W/facet. The staircase device consists of many active regions separated from one another by injection regions, each of which serves as the collector for one active region and the emitter for the next. Figure 1 shows conduction and valence band profiles, along with quantized energy levels from an 8-band $k \cdot p$ finite-element formalism, for one period of the modeled structure under bias. An electron injected into the 19-Å InAs QW from an adjacent period at left emits a photon by making a type-II radiative transition to the valence band of the $In_{0.3}Ga_{0.7}Sb$ hole QW. It then tunnels into the GaSb QW (whose function is to prevent electron escape from the active region by tunneling), followed by elastic or nearly-elastic scattering into the 120 Å InAs QW which begins the injection region. This crucial step can only be accomplished in systems with a semimetallic type-II band offset. From the 120-Å well the electron traverses the n-doped superlattice miniband and is finally injected into the active region of the next period. A cascade of photons results as the electrons descend the staircase in this manner, since a separate radiative transition occurs in each active region of the device.

For a 15-period structure (964 Å period) surrounded by 1.5-μm-thick n-doped InAs/AlSb optical cladding layers, Fermi levels and electronic heat capacities have been calculated as a function of carrier concentration for each well of a given period. Electron-hole recombination is taken to result from spontaneous and stimulated radiative emission, as well as Shockley-Read and Auger nonradiative processes. Accounting for the optical confinement factor of 78%, the optical gain is determined as a function of electron and hole densities and carrier temperature in the active wells. These dependences are then input to the coupled time-dependent equations for interwell carrier transfer and photon propagation in the presence of carrier and lattice heating. Internal electric fields are self-consistently adjusted according to the spatial build-up of excess charge in the various quantum wells.

The simulation was carried out for cw pumping of the T2ICL structure, mounted junction-side-down with one facet coated for 95% reflectivity. For threshold conditions at 300 K, the net losses due to mirror transmission, free carrier absorption, and interband absorption at the type-II interface between the active and injection regions is conservatively estimated to be 52 cm^{-1}, although this value can almost surely be reduced somewhat in fully-optimized structures. The solid curves of Fig. 2 illustrate the predicted T2ICL cw output powers as a function of injection current at 100 K and 300 K, which are compared with analogous 100 K and 200 K results for a non-cascade type-II quantum well laser (T2QWL). The T2ICL threshold currents are seen to be much lower (1.1 kA/cm^2 at 300 K), and the differential slope efficiency much higher (up to 0.9 W/A per facet at 300 K) since 15 photons are generated for every electron injected. Especially encouraging is the prediction that cw output powers exceeding 1 W may be feasible.

1. H. K. Choi, G. W. Turner, and M. J. Manfra, Electron. Lett. 32, 1296 (1996).
2. H. K. Choi, G. W. Turner, M. J. Manfra, and M. K. Connors, Appl. Phys. Lett. 68, 2936 (1996).
3. J. Faist, F. Capasso, C. Sirtori, D. L. Sivco, J. N. Baillargeon, A. L. Hutchinson, S.-N. G. Chu, and A. Y. Cho, Appl. Phys. Lett. 68, 3680 (1996).
4. R. Q. Yang, Superlatt. Microstruct. 17, 77 (1995).
5. J. R. Meyer, I. Vurgaftman, R. Q. Yang, and L. R. Ram-Mohan, Electron. Lett. 32, 45 (1996).
6. I. Vurgaftman, J. R. Meyer, and L. R. Ram-Mohan, IEEE Phot. Tech. Lett. (in press).

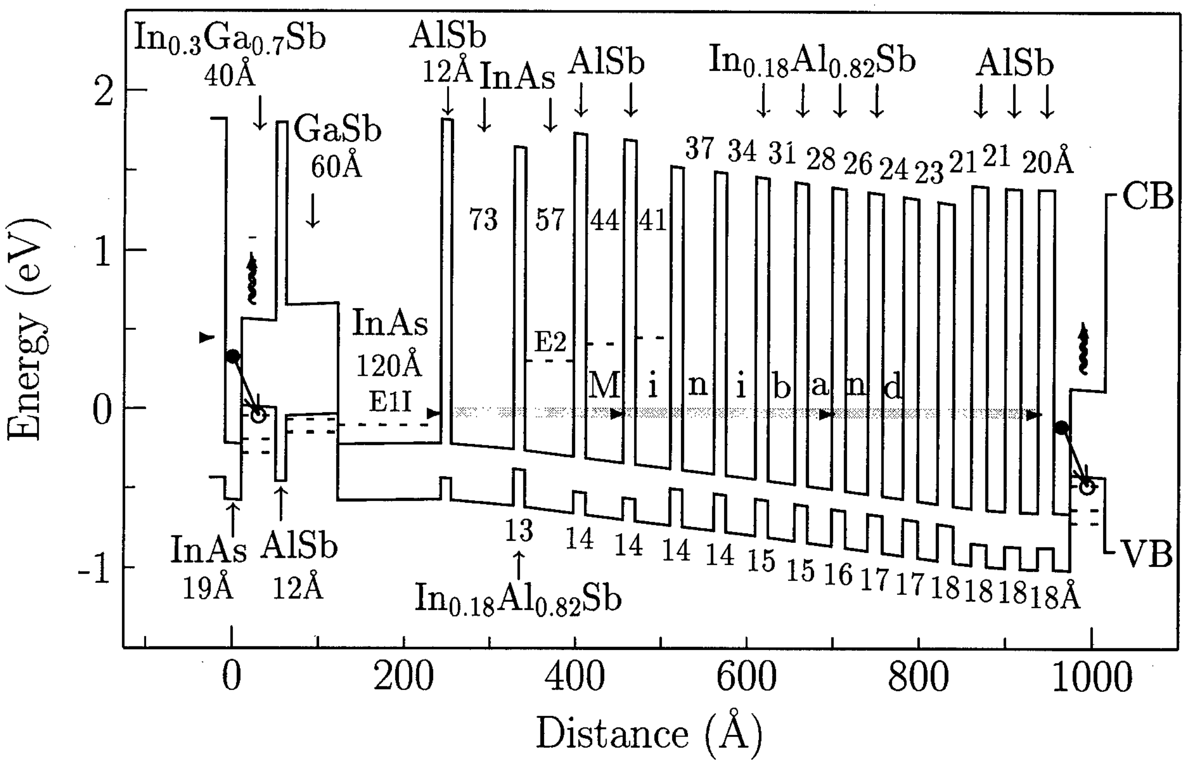

Figure 1. Conduction and valence band profiles and energy levels for the T2ICL under bias corresponding to the lasing threshold at room temperature.

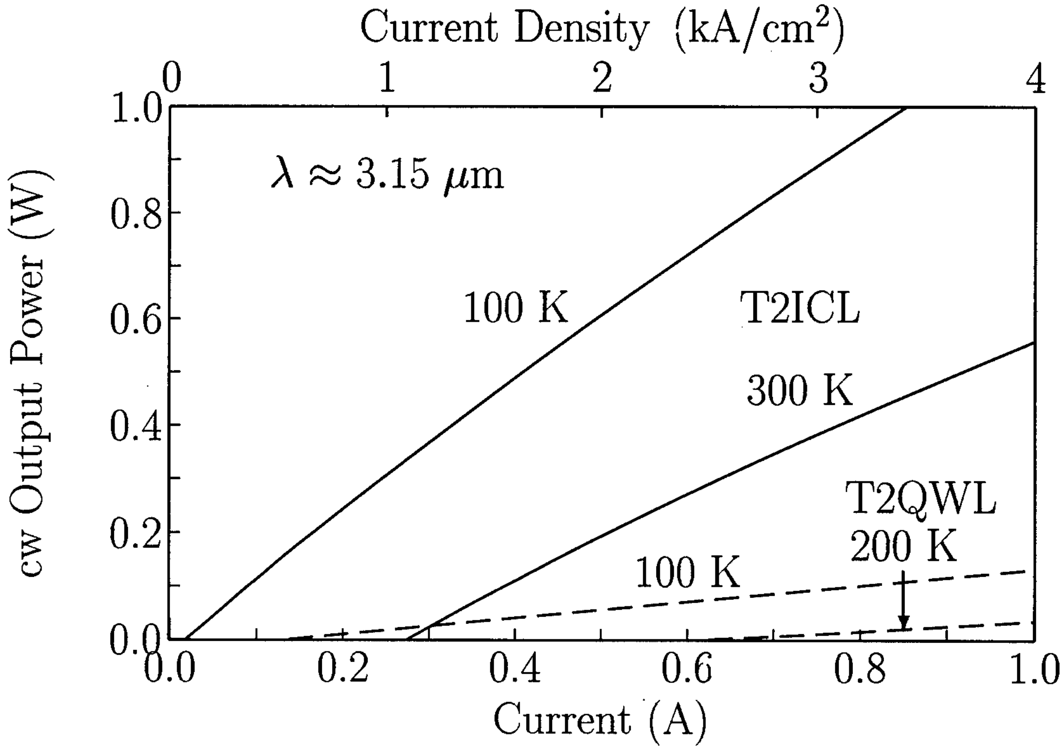

Figure 2. Theoretical output power per facet vs injected current density for a T2ICL[6] and a T2QWL. Cavity lengths are 500 μm and stripe widths are 50 μm.

Type-II Superlattices for Infrared Optoelectronics and Lasers

*R. H. Miles and M. E. Flatté**

Hughes Research Laboratories
Malibu, California 90265

*Department of Physics and Astronomy, University of Iowa
Iowa City, Iowa

Interest in broken-gap, type-II heterostructures for optoelectronic applications is predicated largely on their promise as infrared lasers, detectors, and modulators appreciably outperforming conventional devices. Cryogenic imaging arrays based on these structures are projected to perform with higher detectivities and/or at higher operating temperatures than competing systems based on HgCdTe or extrinsic materials. Lasers in the 3-5μm spectral band are expected to operate at or near room temperature with significant output powers, and modulators with unusually low insertion losses and high dynamic range have been proposed. Brought to maturity, applications of such devices would be numerous, ranging from environmental monitoring systems to short-link, high bandwidth optical communications.

Critical to obtaining high performance lasers and detectors is the promotion of radiative recombination at the expense of Shockley-Read and Auger processes. Our work has focused upon GaInSb/InAs structures, which benefit from particularly deep electron and hole wells and a broken gap band alignment, depicted in Figure 1. The broken gap band alignment is desirable as small energy gaps can be achieved in superlattices with thin constituent layers, effectively delocalizing electrons in the structure. Such delocalization raises electron-hole overlap and hence radiative cross sections. The depth of the wells in this system is desirable for reducing Auger recombination as it allows the joint densities of states for both CCCH and CHHH processes to be greatly reduced. Deep wells allow wide minigaps to be introduced at energies one fundamental gap above and below the conduction and valence band edges, respectively, eliminating Auger processes for which $\Delta k_{||}$ is small. Dispersion lowers carrier occupation for states with significant $k_{||}$, suppressing these processes except at unusually high temperatures and/or carrier densities.

Despite the utility of bilayer superlattices such as GaInSb/InAs in the long wavelength infrared, more sophisticated structures are desirable in the mid-infrared. Requirements of fixing the energy gap to set cutoff or emission wavelength, suppressing Auger recombination, and lattice matching to a GaSb substrate overconstrain the design of optimal structures, and the compromises that result particularly erode gains relative to competitors in the 3-5μm spectral range. This has led to design of superlattices consisting of three or more layers per period. We find structures such as that illustrated in Figure 2 to be particularly desirable in the mid-wave infrared, and are actively developing devices based on these active layers.

While devices based on 3+ constituent superlattices have not yet been tested, milestones achieved with simpler GaInSb/InAs superlattices already include single element detectors slightly outperforming HgCdTe arrays (*i.e.* $R_0A = 10\ \Omega\text{-cm}^2$ for $\lambda_c = 12\mu m$ at 85K, as opposed to 77K for HgCdTe) and 3.2μm lasers operating near CW at 255K. Significant improvements in these figures are to be expected with implementation of the more sophisticated superlattices outlined here, and with continued improvements in the extrinsic characteristics of these materials.

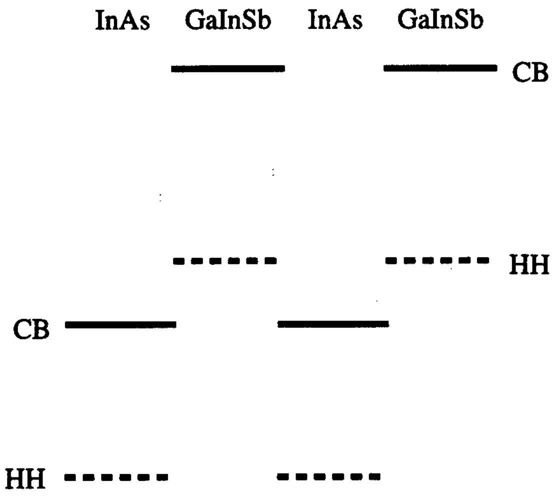

Figure 1. Band edge alignments in the GaInSb/InAs system.

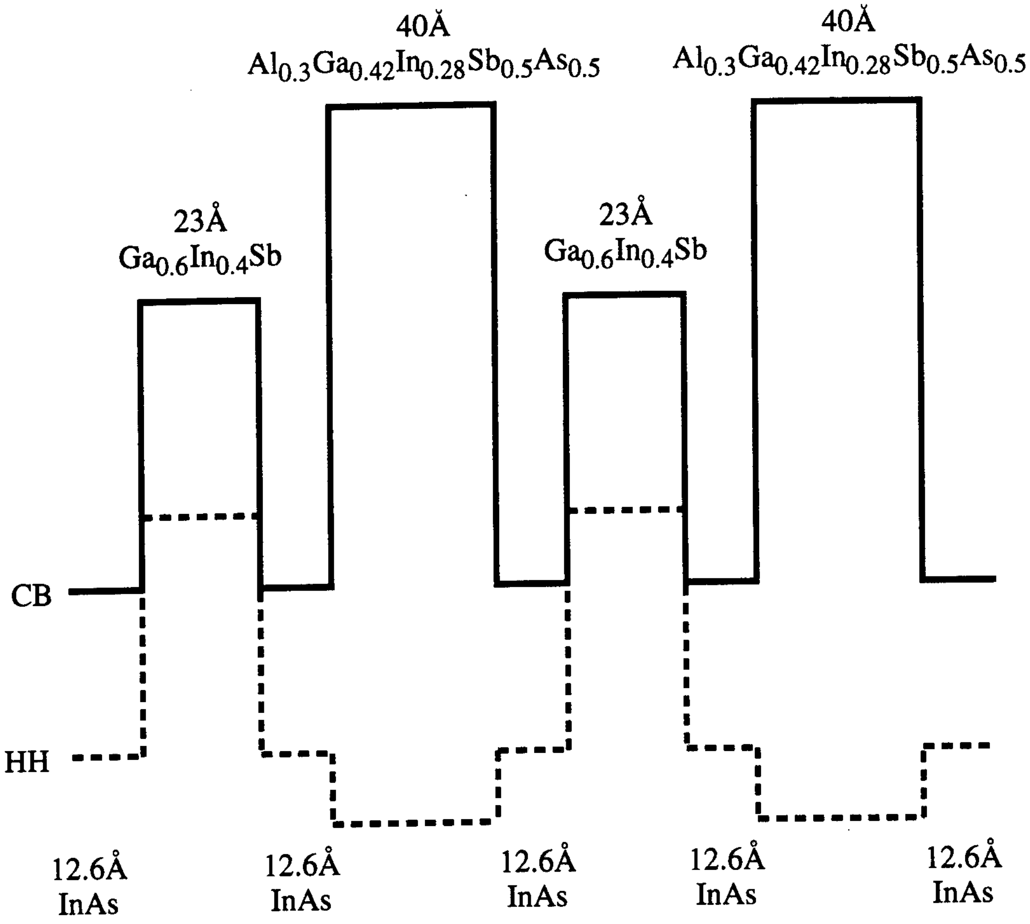

Figure 2. Schematic of a 4-constituent superlattice designed for 3.4μm emission with low Auger recombination.

Enhanced intersubband χ^3 in coupled InGaAs/AlGaAs multiple quantum wells

W. S. Rabinovich, G. Beadie
Code 5642

D. S. Katzer
Code 6850

U. S. Naval Research Laboratory
Washington, DC 20375
202-767-9413
FAX: 202-404-7530

Intersubband transitions in quantum wells have been actively studied in the past several years both as "testbed" systems for quantum mechanics and for their practical applications. The ability to tailor the structure of these materials to produce systems with desired properties, as well as the very large dipole moments exhibited in the mid and near infrared, leads to a great versatility for such applications as detectors[1], lasers[2] and nonlinear optical materials[3].

Among these applications are those that make use of the saturation of the intersubband absorption such as saturable absorbers for mid-infrared lasers and single-photon $\chi3$ effects such as the optical Kerr effect[4]. These effects have been well studied in square quantum wells, but less work has been done, particularly experimentally, on more complex structures. In addition most work has focussed on the 10 µm region of the spectrum rather than shorter wavelengths. Square quantum wells allow only limited flexibility in the control of the saturation intensity of an intersubband system. In general the saturation intensity in square quantum wells depends on the intersubband linewidth and the degree of inhomogeneous broadening, both of which may be difficult to control. The saturation intensity depends only weakly on the well width because both the cross-section and intersubband lifetime have similar dependencies on wavefunction overlap. Thus the figure of merit, $\chi3/\alpha$, is difficult to optimize.

In this work we study the saturation of the optical absorption in coupled InGaAs/AlGaAs multiple quantum wells. This structure allows us to design a four level system that contains a metastable trapping level, decoupling the intersubband absorption matrix element from the relaxation rate.

The sample we studied consisted of 100 repeats of a 1.4 nm $In_{0.45}Ga_{0.55}As$ well followed by a 7.7 nm $Al_{0.4}Ga_{0.60}As$ barrier delta doped with silicon in its center to a sheet carrier density of 1.6×10^{12} /cm^2, followed by a 3.1 nm $In_{0.45}Ga_{0.55}As$ well, followed by a 7 nm AlAs barrier. The multiple quantum well was grown on a semi-insulating GaAs substrate. Because of the

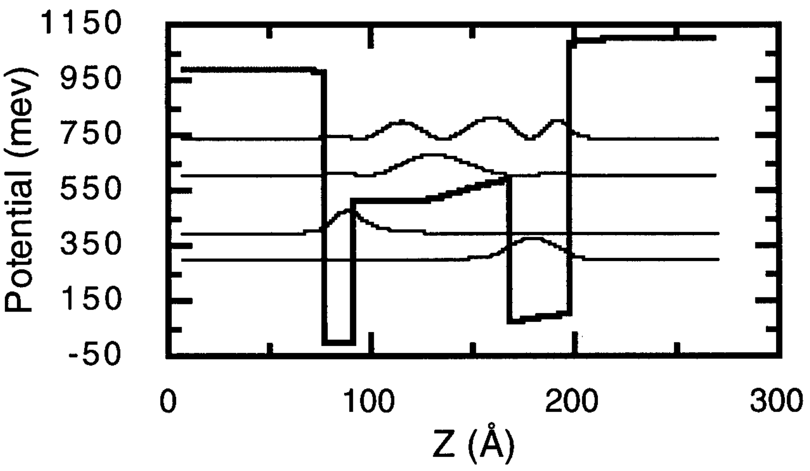

Fig 1

large lattice mismatch of $\mathrm{In_{0.45}Ga_{0.55}As}$ to GaAs, a buffer, linearly graded from GaAs to $\mathrm{In_{0.20}Ga_{0.80}As}$ at a grading rate of 15% In /μm, was first grown[5]. This buffer matches the average lattice constant of the multiple quantum well when residual strain is taken into account[6]. The surface quality of the material is good and the intersubband linewidths are characteristic of good quality material.

The InGaAs/AlGaAs system offers a large conduction band offset which is useful for controlling tunneling rates and for producing intersubband transitions in the technologically important near and mid-infrared region of the spectrum.

The structure was modeled with a self-consistent transfer matrix code that includes the effects of strain and nonparabolicity as well as many-body effects such as the Hartree potential, the exchange correlation energy and the depolarization shift. Intersubband transition rates were calculated based upon phonon scattering. The model has been successfully used for a variety of structures in this material system. The self-consistent potential in equilibrium, with no optical field, as well as the confined energy levels predicted by the model are shown in figure 1.

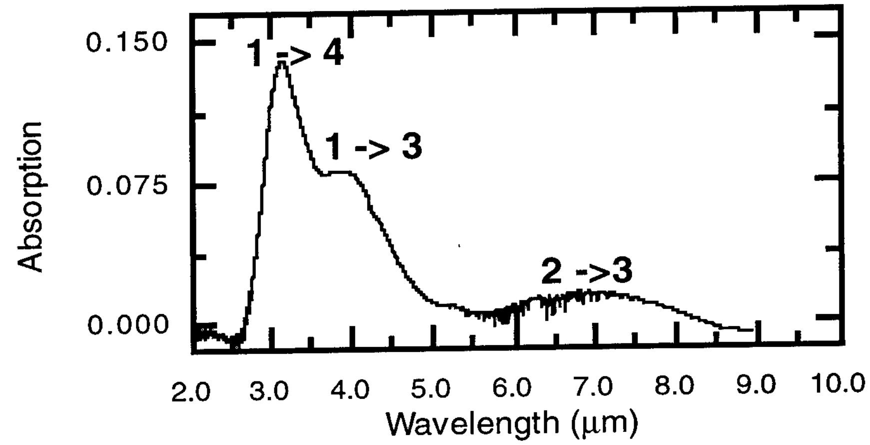

Fig 2

The absorption spectra of the sample, taken at Brewster's angle with p-polarized light, is shown in figure 2 along with transition assignments. The model produces a good match to the observed transition energies and strengths. The 2-> 3 transition is observable because the high doping level results in a carrier population in the second subband even without an optical field.

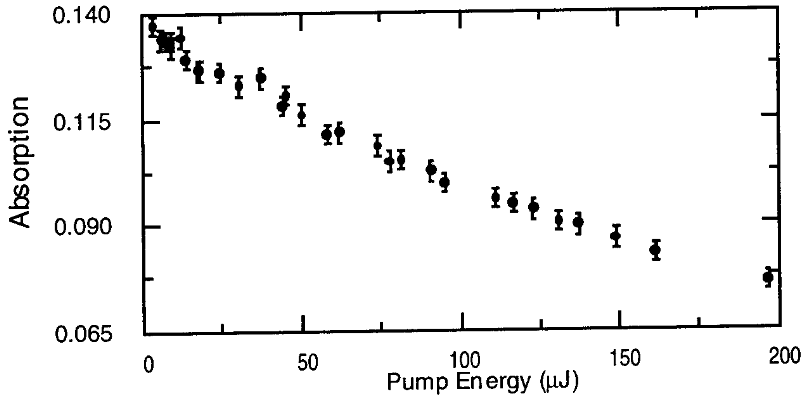

Figure 3

The sample structure is similar to ones proposed for the observation of optical bistability by Khurgin [7] as well as Seto and Helm[8]. It is also similar to a structure used for optical rectification[9]. Unlike these prior works we are interested in the effects of this structure on the saturation of the 1->4 transition. The level dynamics of this system are such that a carrier excited into the fourth subband rapidly relaxes to the third subband from which it can further relax either to the first or second subband. Carriers that relax to the second subband are trapped there for hundreds of picoseconds due to the large barrier separating this state from level one.

We have experimentally studied the saturation of the 1-> 4 transition using a mid-infrared optical parametric oscillator at a wavelength of about 3 μm. The absorption as a function of pump energy is shown in figure 3. The saturation intensity is more than ten times lower than would be expected from "two-level" saturation of the 1->4 transition alone. We have also modeled the population dynamics using a four level rate model. The system is complex because as carriers are transferred into level two, the Hartree potential changes, shifting energy levels, absorption strengths and relaxation rates. Further complexities result from the fact that, as we have shown in prior work, short wavelength intersubband transitions in this material system are heavily inhomogeneously broadened.[7]

Because this coupled well structure decreases the effective intersubband relaxation rate without decreasing the strength of the intersubband absorption, Kerr type nonlinearities will be much stronger. One does pay a price in response time, but sub-nanosecond times are still possible.

Finally because the InGaAs/AlGaAs system allows such short wavelength intersubband transitions structures similar to the one described may offer high off-resonant nonlinearities even in the near infrared.

Acknowledgements

The authors acknowledge the suppoprt of the Office of Naval Research. G. B. acknowledges the support of an NRC-NRL Cooperative Postdoctoral Fellowship.

[1]B. F. Levine, K. K. Choi, C. G. Bethea,, J. Walker and R. J. Malik, Appl. Phys. Lett., **50** 1092, (1987)

[2]J. Faist, F. Capasso, D. L. Sivco, A. L. Hutchinson, C. Sirtori, and A. Y. Cho, Science, **264**, 553 (1994)

[3]M. M. Fejer, S. J. B. Yoo, R. L. Byer, A. Harwit and J. S. Harris, Phys. Rev. Lett., **62** 1041 (1989)

[4]Amir Sa'ar, Nao Kuze, Jing Feng, I. Grave, Amnon Yariv, *Intersubband transitions in quantum wells*, 197-207, (Plenum Press, New York, NY 1992)

[5]H. C. Chui and J. S. Harris, Jr., J. Vac Sci Technol. B, **12**, 1019 (1994)

[6]A. Sacedon, F. Gonzalez-Sanz, E. Calleja, E. Munoz, S. I. Molina, F. J. Pacheco, D. Araujo, R. Garcia, M. Lourenco, Z. Yang, P. Kidd and D. Dunstan, Appl. Phys. Lett., **66**, 3334 (1995)

[7]G. Beadie, W. S. Rabinovich, D. S. Kkatzer and M. Goldenberg, submitted for publication to Phys. Rev. B

Friday, March 21, 1997

Vertical Device Physics

QFB 10:30am – 12:00m
Salon A

Jerry R. Meyer, *Presider*
U.S. Naval Research Laboratory

Field-Dependent Transverse Confinement within Selectively Oxidized Microcavities

Kent D. Choquette, G. R. Hadley, H. Q. Hou, K. M. Geib, and B. E. Hammons

Center for Compound Semiconductor Technology
Sandia National Laboratories
Albuquerque, NM 87185
(505)844-7287
kdchoqu@sandia.gov

Buried oxide apertures within microcavities such as vertical-cavity surface emitting lasers (VCSELs)[1,2], are effective to transversely confine both carriers and photons within the cavity.[3,4] For small cross section area microcavities, the buried oxide layers will also introduce additional optical loss due to aperture scattering.[5,6] To reduce the index confinement and optical scattering, the oxide apertures can be thinned and/or pulled away from the optical cavity to diminish the interaction between the fields and the oxide layers.[5,6] We show that the induced transverse index confinement from the oxide apertures is dependent upon the relative overlap of the oxide with the longitudinal standing wave intensity within the cavity, regardless of the position or thickness of the oxide layers. The index confinement induced by the oxide apertures is determined from examination of the "oxide" lasing modes present under the oxide layers.[3,7]

To examine the effects of oxide placement relative to the microcavity standing wave intensity, on each side of the 1-λ thick optical cavity we introduce a 3/4-λ thick low index layer in which a thin oxide layer is embedded. As shown in Figure 1, oxide layers centered at 1/4-λ from the edge of the optical cavity are positioned at nulls of the longitudinal standing wave intensity, while oxide layers centered at 1/2-λ from the optical cavity are positioned at antinodes of the standing wave. To produce the confining and "transparent" oxide layers sketched in Fig. 1, two VCSEL samples were fabricated containing ≈20 nm thick oxide layers converted from $Al_{0.98}Ga_{0.08}As$ and positioned at 1/4-λ and 1/2-λ from the optical cavity, respectively, within the 3/4-λ thick $Al_{0.92}Ga_{0.08}As$ layers. The selectively oxidized monolithic VCSELs were fabricated as previously described.[8]

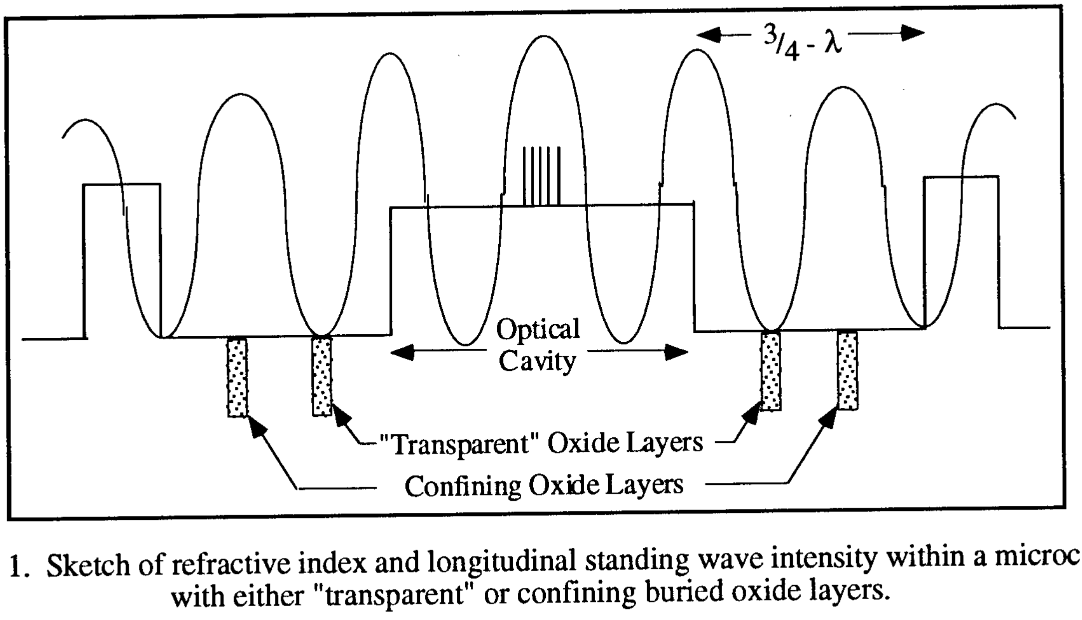

Figure 1. Sketch of refractive index and longitudinal standing wave intensity within a microcavity with either "transparent" or confining buried oxide layers.

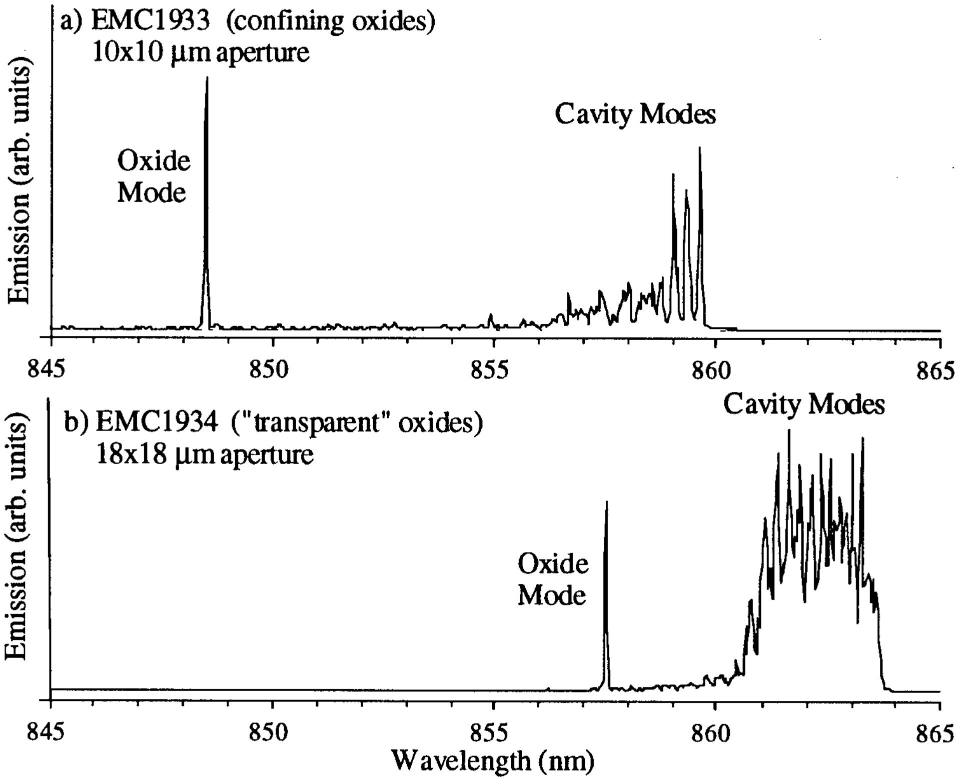

Figure 2. VCSEL emission spectra near threshold for: (a) EMC1933 which contains confining oxide layers; and (b) EMC1934 which contains "transparent" oxide layers.

In Figure 2 we show the emission spectra just above lasing threshold for broad area VCSELs. Multiple transverse modes are apparent in Fig. 2 near the nominally 860 nm as–grown cavity resonance of the two VCSEL samples. In addition, a dominant blue-shifted lasing mode is often observed corresponding to an "oxide" mode originating from under the oxide region.[3] The oxide modes arise due to the influence of the oxide's low refractive index on the effective cavity resonance and increased mirror reflectivity under the oxide as compared to the as-grown mirror. To promote the oxide modes, the as-grown cavity resonance is red-shifted relative to the peak laser gain to enhance the overlap of the oxide mode with the laser gain. In addition, broad area lasers are characterized to exploit the current crowding at the aperture edges which results in the injection of carriers under the oxide aperture. In addition to the dominant oxide mode, sometimes other subsidiary oxide modes can be observed with frequencies between the dominant oxide and cavity modes, presumably arising from regions of thinner oxide at the aperture periphery.

In Fig. 2(a), the dominant oxide mode of sample EMC1934 is blue-shifted 11 nm from the fundamental mode frequency, while in Fig. 2(b) the oxide mode of EMC1933 is shifted only 6 nm. The same frequency shift of the dominant oxide mode is found for a range of VCSEL sizes from these samples. Within a microcavity, the transverse effective index producing waveguiding is dependent only on lateral changes in the Fabry-Perot resonance frequency.[7] Thus the transverse index step in a VCSEL is equal to the normalized shift between the oxide mode and the as-grown cavity resonance. In Fig. 3 we plot the calculated spectral shift of the oxide mode relative to the as-grown resonance for a 20 nm thick oxide at various positions within a 3/4-λ thick $Al_{0.92}Ga_{0.08}As$ layer. From Figs. 1 and 3 we see the spectral shift and induced Δn is greatest (vanishing) for an oxide centered at a standing wave antinode (null). Interestingly, the spectral shift from an oxide layer centered on a standing wave null remains zero regardless of the thickness of the oxide.

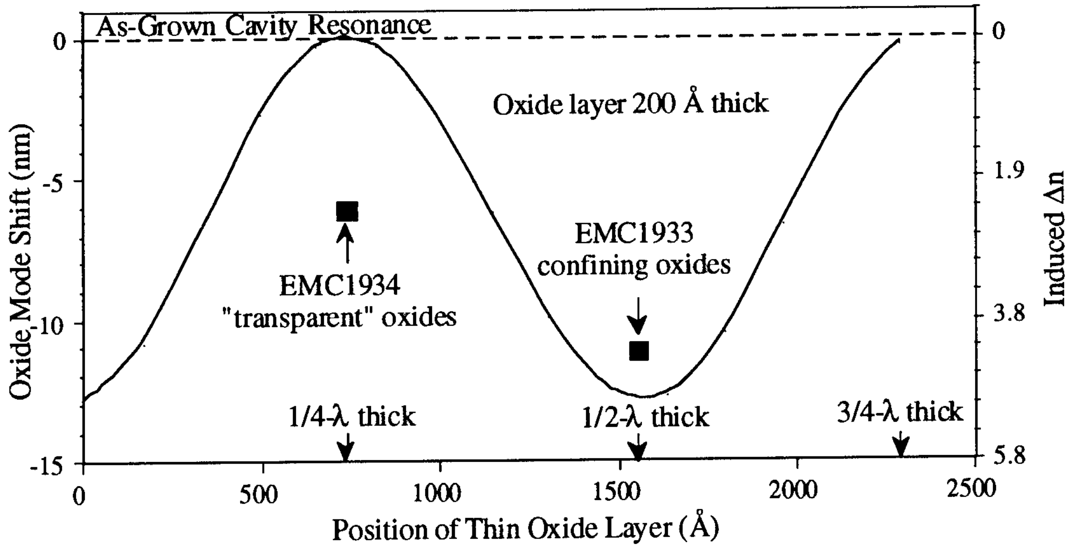

Figure 3. Theoretical and experimental oxide mode shift from the fundamental and the induced Δn for VCSELs containing 20 nm thick oxides embedded within 3/4-λ thick low index layers.

Also shown in Fig. 3 are the experimental values from the VCSEL samples shown in Fig. 2. The measurements are in qualitative agreement with the theory, where sample EMC1933 has an induced Δn nearly twice as great as sample EMC1934. Note that EMC1933 has the larger induced Δn in spite of its oxide layers being positioned farther away from the optical cavity, in contrast to previous results.[3,6] However, the effective index difference for both samples is relatively large as compared to implanted gain-guided VCSELs (typically $\Delta n \approx 10^{-3}$), making both samples strongly index-guided. The deviation from theory of our samples likely arises from the stringent growth tolerances necessary to achieve the precise positioning of the thin oxide layers relative to the optical standing wave as well as localized oxide thickness nonuniformities. We are currently exploring other designs for robust transparent oxides.

In summary, we have demonstrated that the optical confinement arising from buried oxide apertures within a microcavity is dependent upon the relative overlap of the oxide with the longitudinal standing wave intensity. Thus the insertion of oxide apertures within a microcavity which minimally perturb the optical fields is possible, while maintaining strong confinement of charge carriers. Exploiting this effect may enable new designs for microcavity modal engineering.

This work was supported by the United States Department of Energy under contract No. DE-AC04-94AL85000. Sandia is a multiprogram laboratory operated by Sandia Corporation, a Lockheed Martin Company, for the United States Department of Energy.

References

[1] D. L. Huffaker, *et al.*, Appl. Phys. Lett. **65**, 97 (1994).
[2] K. D. Choquette, *et al.*, Electron. Lett. **30**, 2043 (1994).
[3] K. D. Choquette, *et al.*, Appl. Phys. Lett. **66**, 3413 (1995).
[4] K. L. Lear, *et al.*, Appl. Phys. Lett. **66**, 2616 (1995).
[5] B. J. Thibeault, *et al.*, Photon. Tech. Lett. **8**, 593 (1995).
[6] K. D. Choquette, *et al.*, submitted to Appl. Phys. Lett. (1996).
[7] G. R. Hadley, Opt. Lett. **20**, 1484 (1995).
[8] K. D. Choquette, *et al.*, Photon. Tech. Lett. **7**, 1237 (1995).

Effects Of Two-Photon Absorption In Saturable Bragg Reflectors In Femtosecond Solid State Lasers

Amjad T. Obeidat, Wayne H. Knox[a], Jacob B. Khurgin
Department of Electrical and Computer Engineering
The Johns Hopkins University, Baltimore, MD 21218

The process of two-photon absorption (TPA) in semiconductors plays an important role at frequencies below the bandgap where it can dominate other absorption processes. TPA has been observed and studied in semiconductor materials of different composition and dimensionality[1-3], and, while TPA may have useful applications in such devices as optical memories and switches, more often than not it can severely limit the performance of electro-optic devices, especially at high intensities. For example, due to TPA, the insertion loss of saturable absorbers and other optical switches can become prohibitively high for intra-cavity applications requiring minimal losses. In this paper we will discuss TPA in a saturable distributed Bragg reflectors (DBR) recently used for mode-locking in a femtosecond, a diode-pumped Cr:LiSAF laser[4]. The focused intensity on the DBR is about 5 GW/cm^2, well into the regime for strong TPA. Yet the DBR exhibits a reflectivity in excess of 99%. Clearly, the DBR structure itself must be minimizing the effects of tpa.The saturable DBR used in ref.(4) is simply a DBR with a single quantum well in the first quarter-wavelength layer. However, we will study TPA in a simple DBR structure since the quantum well is very thin. The DBR is made of GaAs/AlAs, a material with a TPA coefficient of $\beta = 0.05$cm/MW[1]. Thus, one expects to see absorption in excess of $\alpha = 10^4$ cm^{-1} (i.e 45% per round trip through reflector) which would certainly degrade the reflectivity of the saturable DBR.

In order to understand the results observed in ref.(4) we modeled TPA in the DBR which was a non-trivial task given the non-reciprocity between the intensities of the counter-propagating fields. Figure 1 shows the incident and reflected intensities inside the DBR in the

---

[a] Bell Laboratories, Lucent Technologies, Holmdel, NJ 07733.

high index layers. The device structure is overlayed on the figure. It is clear from the figure that the field penetration depth in the DBR is rather small, thus TPA absorption practically takes place in the first few layers. Figure 2 shows the reflectivity of the GaAs/AlAs DBR at 850 nm. It is clear that the reflectivity of the DBR is uneffected by TPA for a wide range of intensities, obviously due to the small penetration depth. However, as absorption increases in the first few layers of the DBR, its reflectivity drops the Fresnel value for the front face, $((n-1)/(n+1))^2$, where n is the index of refraction of GaAs. In other words all the subsequent reflections from the DBR are absorbed and the medium behaves as if it were semi-infinite with only one boundary present.

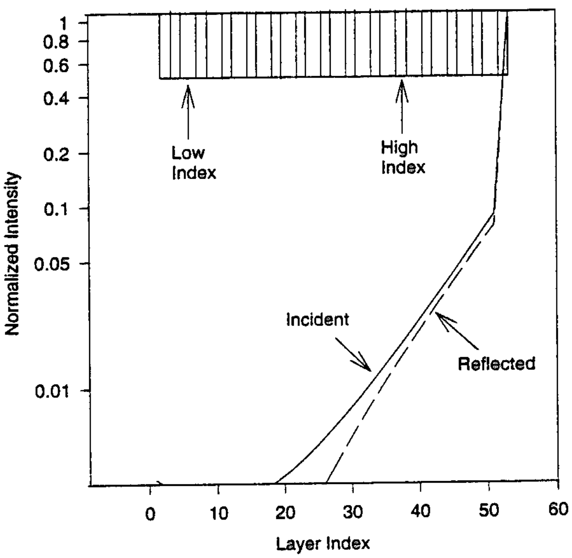

Fig. 1: The incident and reflected intensities inside the DBR. Both intensities are normalized to the incident field intensity. The device structure is overlayed on the curve.

For comparison, we also plot the reflectivity of a more conventional saturable absorber mode-locker, consisting of a bulk cell (of thickness equal to that of the DBR) placed in front of an ideal reflector. It is easy to see that its reflectivity decreases drastically at intensities two orders of magnitude below that of the saturable DBR. The value of the critical intensity in the DBR where the sharp decrease in reflectivity takes place can be found to first order by considering the TPA length in the material which is defined as $l_a = 1/\beta I_0$. When the TPA length is equal to half of the field penetration depth, then one would expect only a few reflections to make it back to the front face bringing the reflectivity to its Fresnel value. Simple calculations show that I_{cr} =400 GW/cm^2 i.e. well in excess of 5 GW/cm^2 as confirmed by Fig. 2.

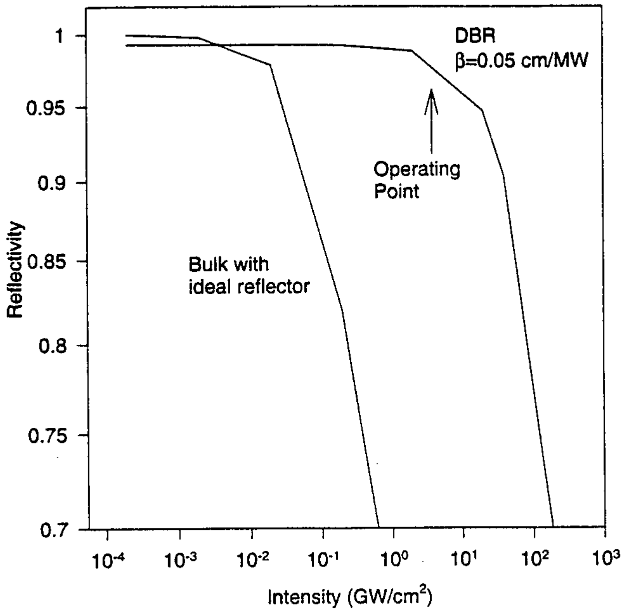

Fig. 2: Reflectivity of the DBR in comparison with a similar piece of bulk GaAs in front of an ideal reflector. The operating point of 5 GW/cm^2 is shown.

In conclusion, we have shown theoretically that in saturable DBRs the detrimental effects of TPA are dramatically reduced in comparison to conventional saturable absorbers. Our theoretical predictions are confirmed by the experiment.

References

1. B. S. Wherrett, J. Opt. Soc. Am. B **1**, 67 (1984).
2. J. B. Khurgin, J. Opt. Soc. Am. B **11**, 624 (1994).
3. A. T. Obeidat, J. B. Khurgin, J. Opt. Soc. Am. B **12**, 1222 (1995).
4. S. Tsuda, W. H. Knox, E. A. de Souza, W. Y. Jan, J. E. Cunningham, Opt. Lett. **20**, 1406 (1995).

Microcavity Semiconductor Lasers: Parameter Evaluation and Performances

G. P. Bava (1) **P. Debernardi** (2)
(1) Dip. di Elettronica, (2) Cespa-CNR, Politecnico di Torino,
Corso Duca degli Abruzzi, 24 10129, TORINO, ITALY
Tel. 011/5644063, Fax 011/5644089, E-mail: Pierluigi@polito.it

Microcavity lasers have been shown to be promising devices owing to their characteristics such as very low threshold current, large modulation bandwidth, noise properties, etc. [1, 2, 3].

These attracting features are connected with the possibility of controlling the spontaneous emission in the microcavity structure, and in particular of enhancing the emission in the lasing mode.

In this paper a complete model for the evaluation of a single mode semiconductor microcavity post laser is presented (see Fig. 1); it includes the computation of the electromagnetic mode spectrum in presence of the Bragg mirrors, the band structure of the Quantum Well region, taking into account valence band mixing, gain and spontaneous emission.

The carrier density N satisfies the following equation [4, 5]:

$$\frac{dN}{dt} = N_i - R_{nr} - \beta R_{sp} - (1-\beta) R_{sp} - nG(\omega, N) + \text{Noise} \quad (1)$$

where N_i is the injected carrier density, R_{nr} are the nonradiative recombinations, R_{sp} the total spontaneous radiative recombinations, β is the fraction of spontaneous emission going into the lasing mode, n are the photons of the lasing mode. The gain G is given by:

$$G = \sum_k \left(\frac{g_l}{\hbar}\right)^2 (n_{ck} - n_{vk}) \frac{2\gamma_k}{(\omega_{cvk} - \omega_l)^2 + \gamma_k^2} \quad (2)$$

where the suffix l refers to the lasing mode and γ_k accounts for intraband relaxation; $\sum_k$ accounts for the carrier wavevectors, $n_{c,v}$ are the carrier distribution functions in conduction and valence bands, ω_{cvk} is the angular frequency corresponding to the conduction-valence band transition at a given k. In the following the quasi equilibrium assumption is adopted and for $n_{c,v}$ Fermi-Dirac distributions are used; this introduces an N dependence of all the parameters.

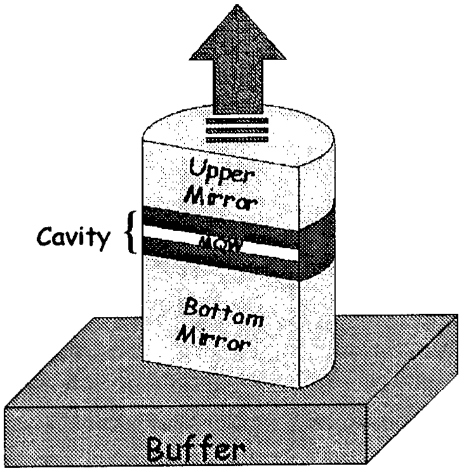

Figure 1: Schematic representation of the semiconductor post microcavity laser

The g parameter acconts for Field-Carrier interaction; assuming a uniform carrier distribution in the active layer, it reads as:

$$g_i^2 = \frac{(\hbar\omega_{cvk})^2}{2\hbar C_i \omega_i} \frac{1}{V_a} \int_{V_a} |\underline{E}_i \cdot \underline{\mu}_{cvk}|^2 dV \quad (3)$$

where V_a is the active volume, μ_{cvk} is the dipole

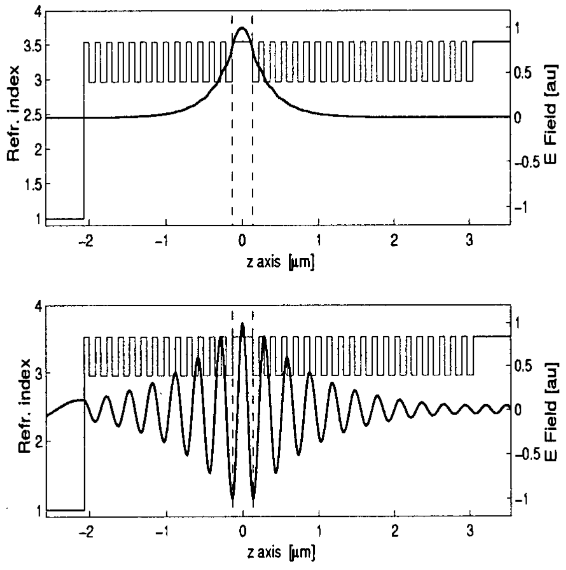

Figure 2: Refractive index (left axis, thin line) and electric field (rigth axis, thick line) in two different cases: upper part, TE modal field on B curve of Fig. 3, lower part, lasing mode longitudinal field distribution (A in Fig. 3).

matrix element of the considered transition, E_i is the electric field of the i mode and C_i is a proper normalization constant (energy stored in the i mode).

The unit volume spontaneous radiative recombination rate of carriers is given by [4, 5]:

$$R_{sp} = 2\pi \sum_i \sum_k \left(\frac{g_i}{\hbar}\right)^2 n_{ck}(1 - n_{vk})\, \delta(\omega_{cvk} - \omega_i) \tag{4}$$

where $\sum_i$ refers to the electromagnetic continuous mode spectrum of the post laser.

Since the gain computation is conventional, only a discussion of spontaneous emission and β factor is presented in the following. For this, a relevant part of the work is the computation of the electromagnetic radiation mode spectrum of the microcavity post laser, which appears in the expression of g_i.

Since an analytical solution for the fields in a post structure with Bragg mirrors is not available, some approximation have been introduced in order to simplify the evaluations. This is done as follows: the transverse and longitudinal field dependence has been splitted. In the transverse cross section the field distribution is computed by means of Bessel-Hankel functions, by defining a proper z-independent cylindrical waveguide. For the longitudinal dependence, the HE and EH modes of the dielectric waveguide are approximated by TM and TE distributions; then the z-dependence is computed by a simple transmission matrix technique.

In the numerical examples some cases of realistic structures are considered, including electromagnetic field confinement in the transverse direction. The active region is a two InGaAs/GaAs quantum well structure, embedded in a λ cavity (high index structure). The schematic drawing of the post laser is depicted in Fig. 1. For the Bragg mirrors and refractive index profile, see Fig. 2.

The upper part of Fig. 2 reports the longitudinal field distribution for typical transverse radiative modes (B in Fig. 3) while the lower part shows the field profile of the lasing mode (A in Fig.3). We have considered this example of high index cavity since it allows to clarify the problem of lateral spontaneous emission [6]. This problem can be avoided in a low index configuration which is of more interest in practice [7].

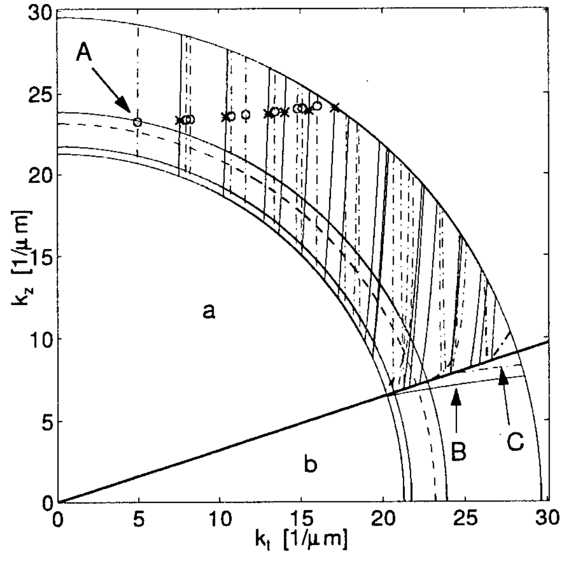

Figure 3: Dispersion relations in the plane $k_t - k_z$ (continuous lines, EH modes; dashed dotted lines, HE modes) for a 1 μm diameter post structure; the circles and the asterisks refer to the resonances of the longitudinal fields.

Fig. 3 shows the dispersion relation for the electromagnetic modes in the $k_z - k_t$ plane. The ring stripe represents the spontaneous emission bandwidth; the internal ring stripe delimited by continuous lines shows the variation interval for the maximum of the spontaneous emission spectrum when changing carrier density; the dashed line corresponds to the Bragg condition ($\lambda_B = 0.96\mu$m in the considered case).

The a-region refers to tranverse confined modes (longitudinal radiation) which includes the lasing mode A (see Fig.2 down). In the b-region there is no lateral confinement, while longitudinally there are strongly confined discrete modes (due to exponential tails in the mirrors, see Fig. 2 up); such modes are not present in the low index cavity; the B curve shows the dispersion relation for quasi-TE mode, the C curve for the quasi-TM.

In Fig. 4 the results for spontaneous emission as a function of carrier density are reported. On the left the β factor is shown; the continuous line is computed disregarding the lateral emission while the dashed curve includes longitudinal and lateral radiation. The initial sudden decrease of β at increasing carrier density is due to bandgap renormalization; the subsequent maximum is connected to band-filling which tunes the lasing mode with the Bragg condition (see Fig. 3). On the rigth the total spontaneous emission rate vs. carrier density is plotted; the dashed line corresponds to lateral radiation, the dashed dotted curve refers to longitudinal emission and the solid line represents the total rate.

On the basis of such preliminary results, a single mode microcavity laser model has been developed (eq. (1) coupled with the lasing mode equation). With respect to similar models [3] found in the literature, in this paper a completely realistic device structure is considered and the carrier density dependence of the spontaneous emission and β factor is included.

This work is performed in the framework of the ESPRIT long term research project ACQUIRE.

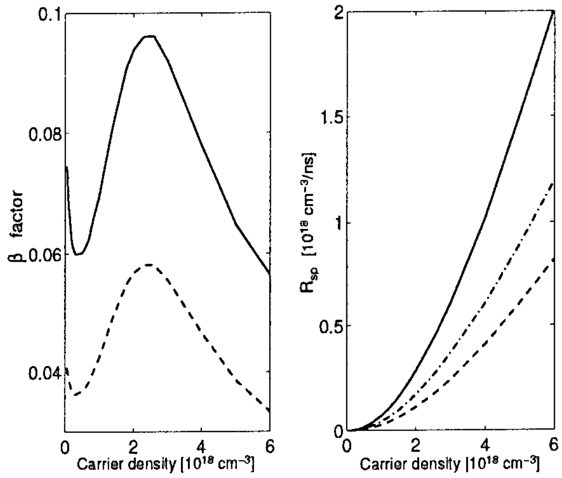

Figure 4: β factor as a function of carrier density (left graph) accounting (dashed line) or not accounting (continuous curve) for lateral spontaneous emission. On the right, total spontaneous emission rate (continuous line), contributions of spontaneous emission in longitudinal direction (dashed line) and in lateral direction (dashed line).

References

[1] Y. Yamamoto, S. Machida, G. Björk: "Microcavity semiconductor laser with enhanced spontaneous emission"; Phys. Rev. A, 44, 1991, p. 657

[2] T. Baba, T. Hamano, F. Koyama and K. Iga: "Spontaneous Emission Factor of a Microcavity DBR Surface Emitting Laser (II)– Effects of Electron Quantum Confinements", IEEE J. QE, 28, 1992, p. 1310

[3] G. Björk, H. Heitmann, Y. Yamamoto: "Spontaneous-emission coupling factor and mode characteristics of planar dielectric microcavity lasers"; Phys. Rev. A, 47, 1993, p. 4451

[4] H. Haug: "Quantum Mechanical Theory of Fluctuations and Relaxation in Semiconductor Lasers", Z. Physik 200, 1967, p. 57

[5] Y. Yamamoto: "AM and FM Quantum Noise in Semiconductor Lasers–Part I: Theoretical Analysis", IEEE J. QE, 19, 1983, p. 34-46

[6] T. Zhang, J.G.. Wohlbier, K.D. Choquette and N. Tabatabaie: "Microcavity Vacuum-Field Configuration and Spontaneous Emission Power ", IEEE J. of Selected Topics in QE, 1, 1995, p. 606

[7] I. Abram et al.: "Nonguiding half-wave semiconductor microcavities displaying the exciton-photon mode splitting", Appl, Phys. Lett., 65 1994, p. 2516-2518.

Polarization characteristics of vertical-cavity surface-emitting lasers with tilted waveguide region

Hye Yong Chu, Byueng-Su Yoo, Min Soo Park, and Hyo-Hoon Park

Electronics and Telecommunications Research Institute (ETRI),
Yusong P. O. Box 106, Taejon 305-600, Korea
(Tel)+82-42-860-5774, (Fax)+82-42-860-6836, (e-mail) hhpark@utopia.etri.re.kr

Control of the polarization state for vertical-cavity surface-emitting lasers (VCSELs) is one of the critical issues for polarization sensitive optical systems. In conventional VCSEL structures, the nearly degenerated orthogonal polarization states with fundamental mode are observed at and above threshold. However, in the absence of the selectivity of a polarization state, unstable polarization switching occurs and results in an excess intensity noise by mode hopping. A stable polarization operation over wide current range is required for low noise applications. Several attempts have been made to control the polarization of VCSELs.[1-3] A birefringent metal/dielectric polarizer on the top distributed Bragger reflector (DBR)[1] and an anisotropic gain medium of fractional-layer superlattice structure[2] were introduced. Choquette *et al.*[3] examined anisotropic transverse cavity like rhombus- or dumbbell-shape and obtained strong polarization selectivity for a specific direction. In this work, we propose a simple method to control the polarization direction by tilted-etching of laser pillar. This structure can select a single dominant polarization state with an electric field perpendicular to the tilted direction. We also demonstrate switching of the two polarized beams in form of 2x4 array in which a switching unit consists of a pair of laser devices tilted with different directions.

For this work, we used a periodic gain InGaAs/GaAs structure with a two-wavelength-thick cavity. The top and bottom DBR mirrors consist of, respectively, 16 and 23.5 periods of AlAs/GaAs quarter wave stacks. The detailed laser structure was described in previous reports [4]. Tilted laser pillar structures were formed using reactive ion beam etching (RIBE) with chlorine, by tilting the substrate toward [110] or $[\bar{1}10]$ direction with an angle of 15° ~ 20° against the ion-beam direction. The laser posts were etched through the active region. Figure 1 shows a schematic diagram of tilted VCSEL device. The tilted angle is denoted by α. Two orthogonal polarization characteristics of VCSELs were simultaneously measured using a polarized beam splitter. The device characteristics were measured at room temperature without a heat sink.

Figure 2 shows the light output power against current (L-I) characteristics measured under continuous wave operation for 10-μm-diameter devices with a tilted etching angle of 20° toward [110] and $[\bar{1}10]$ direction, respectively. The polarization directions indicated by ⊥ and // represent those of electric fields perpendicular and parallel to the tilted direction of laser posts, respectively. Figure 2 shows that the light polarized perpendicularly to the tilted direction is predominantly emitted. This tendency was observed in the whole range of injection current and for most of the tested devices with diameters of 7 and 10 μm. For the devices of 10 μm diameter, the orthogonal polarization suppression ratio was around 10 ~ 20 dB. As the diameters of the devices increased more than 15 μm, the polarization selectivity was reduced and the switching of polarization with bias current was observed. The result indicates that the polarization selectivity by the tilted geometry become larger for smaller devices.

In conventional InGaAs VCSELs, a single dominant polarization to specific [110] direction was usually observed.[3,5] We observed also that most devices with vertically etched pillar polarized to [110] direction. By tilting the laser post toward [110] direction we could change the dominant polarization direction to $[1\bar{1}0]$. However, a few devices tilted toward [110] direction with an angle of 15 ° emitted lights polarized to the reverse direction ([110]) or showed unstable polarization states. As the tilted angle is increased, such confusion of the polarization characteristics for the devices tilted toward [110] direction disappeared. On the other hand, in spite of the tilted geometry of the waveguding region, the near field pattern indicated a circular beam in spontaneous emission for the device sizes and shapes mentioned above.

Figures 3(a) and 3(b) show the emission spectra of VCSELs tilted 20° toward [110] and $[1\bar{1}0]$ directions, respectively. The cavity diameters are 10 μm. The emission spectra just above the threshold current show slightly split two dominant peaks which correspond to the two orthogonal polarization of the fundamental mode. For the [110] tilted device, the wavelength of the main peak at a current of 2.2 mA was 0.25 Å longer than the weaker emission peak, as seen in Fig. 3(a). However, the dominant peak at a current of 2.2 mA for the $[1\bar{1}0]$ tilted device appears at a wavelength, 0.3 Å shorter than the weaker peak, as seen in Fig. 3(b). These spectra indicate a competition stage of the orthogonal polarization states. In our index-guided structure, we expect a higher optical loss to be induced along the tilted surface of the laser post. Thus, the polarization state along the directions of the higher optical loss would be suppressed and rapidly disappear with increasing the current.

We fabricated a 4x4 laser array in which differently polarized devices are formed on the same wafer by two step etching. Defining a switching unit with a pair of laser devices tilted with different directions, we successfully attained switching between the two polarized states with 2x4 beam array for each polarization state.

In summary, we have demonstrated a simple polarization control of VCSELs by tilted-etching of the laser post toward [110] or $[1\bar{1}0]$ direction. For the laser devices with diameters of 7~10 μm and tilted angles of 15 °~20°, we observed outstanding selectivity of the polarization states. The results can be attributed to the different of optical losses between the two waves polarized in the tilted waveguide region. Using this laser structure, we could attain switching of the polarization states in a VCSEL array.

REFERENCES

[1] T. Mukaihara, N. Ohnoki, Y. Hayashi, N. Hatori, F. Koyama and K. Iga, *IEEE J. Selected Topics in Quantum Electron.* vol.1, p.667 (1995).

[2] A. Chavez-Pirson, H. Ando, H. Saito and H. Kanbe, *Appl. Phys. Lett.*, vol. 64, p.1759 (1994).

[3] K. D. Choquette and R. E. Leibenguth, *IEEE Photon. Technol. Lett.*, vol. 6, p.40 (1994).

[4] B.-S. Yoo, H.-H. Park, and E.-H. Lee, *Electron Lett.*, vol. 30, p.1060 (1994).

[5] C. J. Chang-Hasnain, J. P. Harbison, G. Hasnain, A. C. Von Lehmen, L. T. Florez and N. G. Stoffel, *IEEE J. Quantum Electron.*, vol. 27, p.1402 (1991).

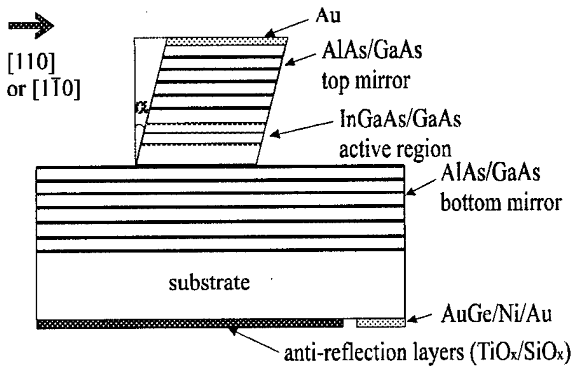

Fig. 1. Schematic diagram of a tilted-VCSEL.

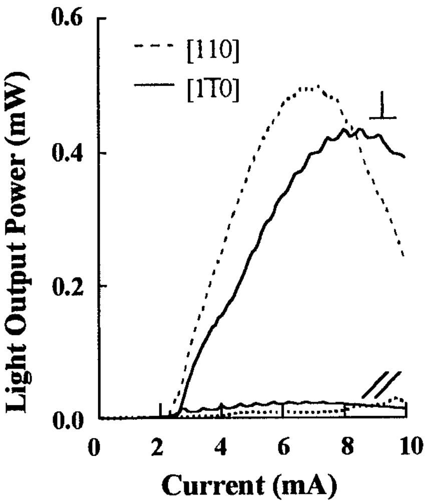

Fig. 2. L-I characteristics for 10-μm-diameter VCSELs with a tilted angle of 20° toward [110] and [1$\bar{1}$0] directions.

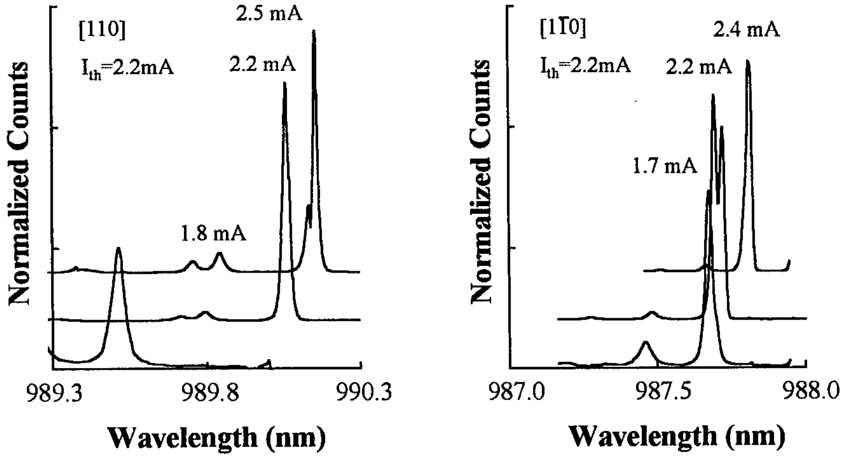

Fig. 3. Emission spectra for 10-μm-diameter VCSELs tilted toward (a) [110] and (b) [1$\bar{1}$0] directions with an angle of 20°.

Design and Expected Characteristics of 1.3μm GaInNAs/GaAs Vertical Cavity Surface Emitting Lasers

T. Miyamoto, T. Takada, K. Takeuchi, F. Koyama, and K. Iga

Tokyo Institute of Technology, Precision and Intelligence Lab.
4259 Nagatsuta, Midori-ku, Yokohama 226, JAPAN
TEL +81-45-924-5026 FAX +81-45-921-0898

The long wavelength vertical cavity surface emitting laser (VCSEL) is becoming one of key devices for future optical communication and interconnection systems. Room temperature (RT) continuous-wave (CW) operations were demonstrated for long wavelength VCSELs with a reduced threshold current and an increased operating temperature [1, 2]. However, temperature characteristics such as characteristic temperature T_0 and the maximum operating temperature are not sufficient for use in actual systems. These are due to carrier leakage related to the small conduction-band discontinuity of GaInAsP/InP systems, difficulties in fabrication of small current confining structures and high reflective mirrors, a large non-radiative absorption, and so on. Recently, the GaInNAs material was proposed as a new long wavelength system emitting 1.3μm and 1.55μm grown on GaAs substrates [3] and 1.2μm RT-CW operations of edge emitting lasers have been demonstrated [4]. The bandgap bowing between arsenide and nitride system is very large and thus long wavelength emission and large conduction-band offset are expected for this material system.

In this study, we propose a new long wavelength surface emitting laser using this GaInNAs/GaAs material. We can design the long wavelength surface emitting lasers with the same device configurations as the 0.98μm GaInAs/GaAs system. Figure 1 shows a schematic view of the proposed GaInNAs/GaAs VCSEL with GaAs/AlAs DBRs and oxidized AlAs layer for small current confinement structures. To realize this new long

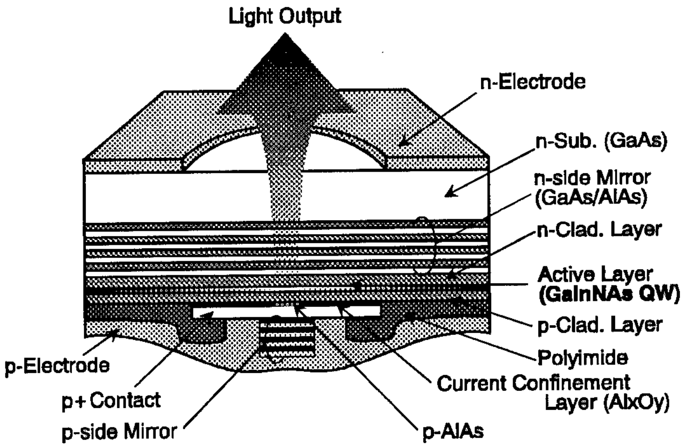

Fig. 1 Proposed structure of GaInNAs/GaAs VCSEL.

wavelength VCSEL, we designed the GaInNAs/GaAs quantum well (QW) structure and estimated its lasing characteristics.

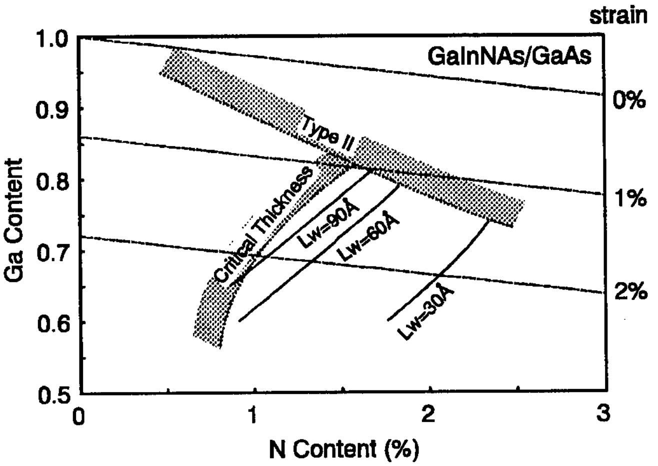

Fig. 2 The GaInNAs composition is shown for 1.3μm QW structure. The well is variable and determined for 1.3μm emission.

Figure 2 shows the relation between Ga and N composition for 1.3μm emission QWs. The dashed lines show the relation for various compressive strains. To realize 1.3μm lasing, it is required to choose suitable well widths for each GaInNAs well composition. Due to the type-II heterostructure and critical thickness, the allowed area for 1.3μm QW structures is limited. However, by introducing a small amount of nitrogen ranging from 1% to 2%, we can obtain 1.3μm lasing by the strained QW. The following analysis of liner gain coefficient and threshold current density were carried out by assuming the $Ga_{0.75}In_{0.25}N_{0.014}As_{0.986}/Al_{0.1}Ga_{0.9}As$ QWs with a well width of 65Å and a strain of 1.4%. The AlGaAs barrier is effective to increase a valence band offset and thus reducing hole leakage.

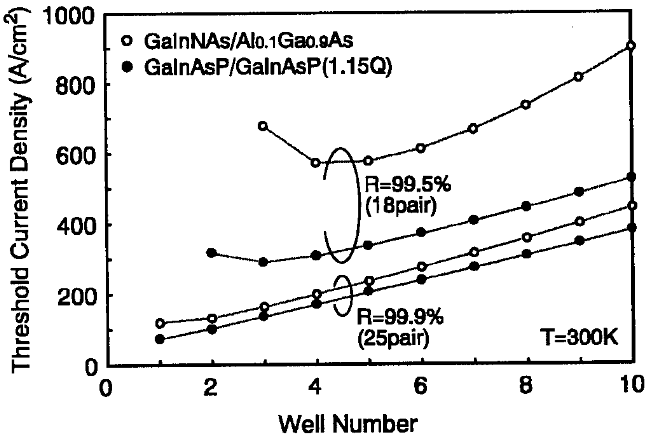

Fig. 3 Calculated threshold current density against well number for GaInNAs and GaInAsP VCSELs. The pair number means corresponding GaAs/AlAs DBR pair.

Figure 3 shows the calculated threshold current density against a well number for GaInNAs/GaAs and GaInAsP/InP VCSELs. In this calculation, both the intervalence band absorption and the auger nonradiative recombination are considered as a function of carrier density. For the case of extremely low loss (high reflectivity) condition, the threshold current density for each structure are not so different and the optimum well number is one with about 100A/cm^2 of a threshold current. On the

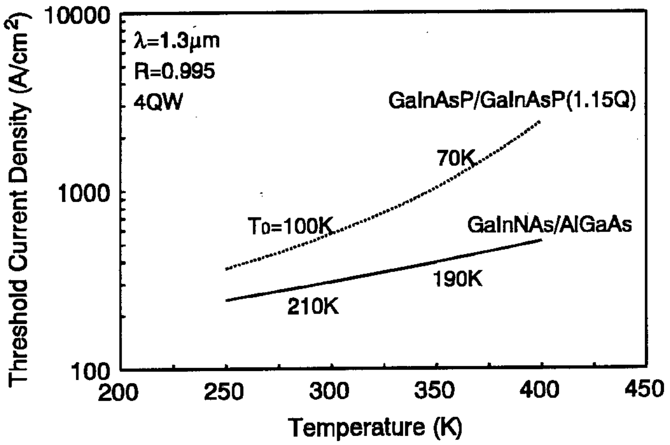

Fig. 4 Temperature characteristics of threshold current density for 4-QW GaInNAs and GaInAsP VCSELs.

other hand, threshold current densities are increased for increasing the cavity loss. However, the increase for GaInNAs/GaAs QWs is much less than that for GaInAsP/InP QWs. These are due to small carrier leakage over barriers because the conduction band barrier height is estimated to be 500meV for GaInNAs/AlGaAs though that for GaInAsP is 65meV. The optimum well number for this case is increased to 3-4.

The temperature characteristic of threshold current densities was analyzed. Figure 4 shows temperature characteristics for GaInNAs/GaAs and GaInAsP/InP VCSELs. The mirror reflectivity is assumed to be 99.5%. The well number is fixed to be 4 which is the condition for obtaining a low threshold at 300K, though the characteristic temperature T_0 is superior for large well number. A GaInAsP/InP VCSEL shows the characteristic temperature of 70K above room temperature which is good agreement with reported edge emitting long wavelength lasers. The characteristic temperature for GaInNAs VCSEL is expected over 200K. This is also due to small carrier leakage over barriers. Good lasing characteristics of optimally designed GaInNAs/GaAs VCSELs can be expected which might be comparable to GaInAs/GaAs VCSELs.

We are now growing the GaInNAs VCSELs by chemical beam epitaxy (CBE) with N-radical cell and MOCVD with dimethylhydrazine (DMHy).

This study was supported by Grant-in-Aid for COE Research from the Ministry of Education, Science, Sports and Culture (• 07CE2003, "Ultra-parallel Optoelectronics").

References

[1] T. Baba, Y. Yogo, K. Suzuki, F. Koyama, and K. Iga, *Electron. Lett.*, 29, pp. 913-914, 1993.

[2] N. M. Margalit, D. I. Babic, K. Streubel, R. P. Mirin, R. L. Naone, J. E. Bowers and E. L. Hu, *Electron. Lett.*, 32, pp. 1675-1677, 1996.

[3] M. Kondow, K. Uomi, A. Niwa, T. Kitatani, S. Watahiki and Y. Yazawa, *Jpn. J. Appl. Phys.*, 35, pp. 1273-1275, 1996.

[4] K. Nakahara, K. Kondow, T. Kitatani, Y. Yazawa and K. Uomi, *Electron. Lett.*, 32, pp. 1585-1586, 1996.

SYMMETRY BREAKING IN VERTICAL-CAVITY SEMICONDUCTOR LASERS

J.P. Woerdman, A.K. Jansen van Doorn and M.P. van Exter
Huygens Laboratory, Leiden University, P.O. Box 9504
2300 RA Leiden, The Netherlands
Tel:+31 71 5275823, Fax:+31 71 5275819, E-mail: mfqo@rulhml.leidenuniv.nl

It seems fair to say that the polarization behavior of semiconductor Vertical-Cavity Surface-Emitting Lasers (VCSELs) is not understood on a fundamental level. In spite of the nominal anisotropy of a VCSEL the polarization is usually reported as being linear, but not very stable. Most authors associate this behavior with native anisotropies due to imperfect device fabrication although also intrinsic nonlinearities of the gain medium have been put forward for explaining the linear polarization. We are involved in a detailed study [1–4] of the various anisotropies of a VCSEL, their interplay, their manipulation and the consequences thereof for the VCSEL polarization. We have found experimentally that the polarization of a practical VCSEL can be largely explained as a consequence of linear anisotropies; nonlinearities play at most a minor role.

If we neglect nonlinearities (i.e. gain saturation) the behavior of the laser polarization $\vec{E}$ is described by

$$\frac{\partial \vec{E}}{\partial t} = i\tilde{M}\vec{E} \tag{1}$$

where $\tilde{M}$ is a complex 2×2 matrix which describes the resonator and the gain medium. $\tilde{M}$ has generally elliptically polarized eigenmodes. If we transform away the isotropic part of Eq. (1), i.e. if we set trace $\tilde{M} = 0$, we are left with 6 real parameters in $\tilde{M}$. If we

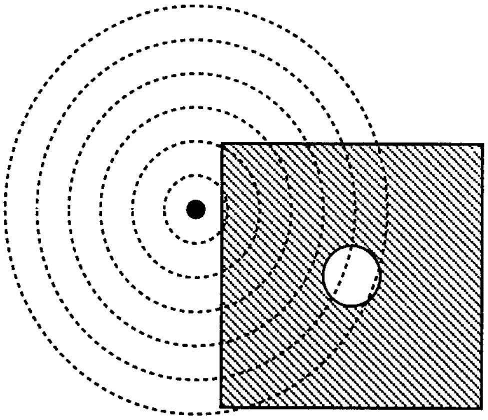

Fig. 1
Top view of VCSEL; the black dot next to the electrical contact represents the hot spot.

furthermore require time-reversal invariance (i.e. zero magnetic field) this number reduces to 4. These 4 parameters correspond to birefringence (strength and orientation) and dichroism (strength and orientation). In fact, only the relative orientation of birefringence and dichroism is important, reducing the number of free parameters to 3.

Experimentally, we have a handle on 2 of these by means of our hot-spot technique (Fig. 1). A heating laser beam is focussed on the wafer near the VCSEL, thus producing a uniaxial strain and thus birefringence in the VCSEL aperture [1]. In this way the strength and the orientation of the birefringence can be changed at will, not only on a transient but also on a permanent basis [3]. The elasto-optic tensor of the device can be deduced from such measurements; we have found it to be highly anisotropic [1]. This explains the natural preference of the polarization for the [110] crystalline axis in spite of an isotropic distribution of native strains [1,4].

We have also found that practical VCSELs possess a (small) dichroism, oriented roughly along the [110] axis. The origin of this dichroism is still unclear; however, by suitably combining it with the proper amount of birefringence we can produce any state of polarization (see Fig. 2, where we demonstrate almost circularly polarized VCSEL light).

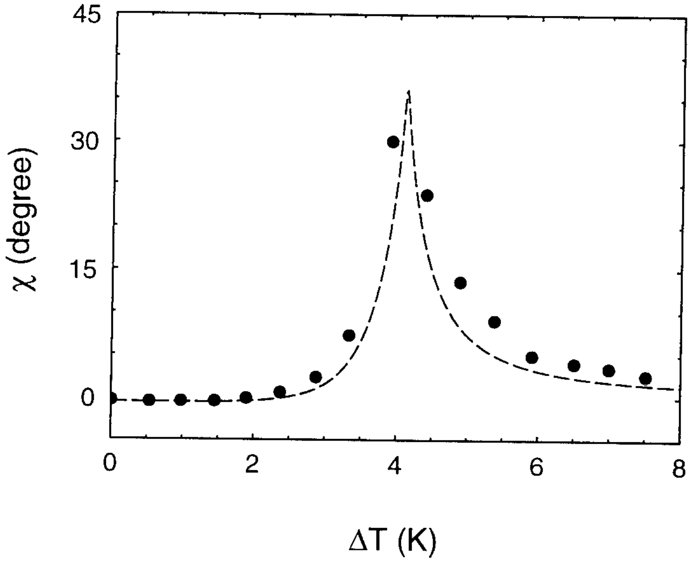

Fig. 2
Ellipticity angle of the VCSEL output beam as a function of the VCSEL temperature rise ΔT produced by the hot spot. An angle $2\chi = 90^0$ corresponds to circularly polarized light (from ref. [4]).

Presently, we are extending our techniques towards realizing a perfectly isotropic VCSEL. What will happen in this case? Will a nonlinear anisotropy show up in the end? Or will the VCSEL output become "unpolarized" due to the (vectorial) quantum noise? We hope to find answers to these intriguing questions in the near future.

References

[1] A.K. Jansen van Doorn, M.P. van Exter and J.P. Woerdman, Appl. Phys. Lett. 69, 1041 (1996).

[2] A.K. Jansen van Doorn, M.P. van Exter, M. Travagnin and J.P. Woerdman, Opt. Comm., accepted for publication.

[3] A.K. Jansen van Doorn, M.P. van Exter and J.P. Woerdman, Appl. Phys. Lett., Dec. 9, 1996.

[4] A.K. Jansen van Doorn, M.P. van Exter and J.P. Woerdman, submitted for publication.

Friday, March 21, 1997

Novel Materials and Structures

QFC 1:30pm – 3:00pm
Salon A

Thomas Dekorsy, *Presider*
RWTH Aachen, Germany

Red-Emitting Semiconductor Quantum Dot Lasers

S. Fafard
National Research Council of Canada

The latest results will be presented on stimulated emission in electrically-injected laser structures based on an active region with 0-dimensional density-of-states obtained by self-assembled growth.

An All-Silicon Integrated Light Emitter Technology

K.D. Hirschman, L. Tsybeskov, S.P. Duttagupta and P.M. Fauchet

Department of Electrical Engineering, University of Rochester, Rochester, NY 14627

The need for optoelectronic devices that are compatible with integrated circuit manufacturing technology has stimulated research in all-silicon light-emitting devices. Since crystalline silicon is an indirect bandgap semiconductor, its luminescence efficiency is low (~10^{-6}%). Several approaches have been proposed to correct this deficiency [1,2], but so far porous silicon, which produces high-efficiency room-temperature visible photoluminescence [3], has attracted the most interest. Figure 1 shows the range of wavelengths over which strong luminescence can be achieved [4]. A major limitation of this material is that it is very reactive and inherently fragile, and thus cannot readily be integrated with conventional silicon process technology. We have overcome these limitations and we show that silicon-rich silicon oxide (SRSO) prepared by partial oxidation of porous silicon exhibits appropriate light-emitting and carrier transport properties and is compatible with conventional processing techniques. SRSO-based visible light-emitting devices (LEDs) have been successfully integrated into a standard bipolar fabrication sequence. This is the first demonstration of an all-silicon visible light emitter / bipolar transistor optoelectronic integrated circuit.

Our surface-emitting SRSO-based LEDs have characteristics among the best reported in silicon-based technology with respect to electroluminescence efficiency, operating threshold conditions and frequency response, and demonstrate a significant improvement over porous silicon based device structures with respect to device stability [5,6]. In contrast to porous silicon, the active SRSO layer satisfies several critical microelectronic material processing requirements including tolerance to thermal processing (T~1000°C) and chemical resistance. The fabrication sequence and resulting device structure are shown in Figure 2. The resulting multilayer structure enables the injection of electrons and holes into the semi-insulating SRSO layer. Adequate nanocrystallite surface passivation and improved carrier injection have resulted in an increase in the quantum efficiency and significant improvements in the electroluminescence. So far, the SRSO-based devices have the following specifications at room temperature: detectable light emission at an applied voltage of ~ 2V and a current density of ≤ 10mA/cm^2 ; maximum light intensity of ~ 1mW/cm^2 ; highest external power efficiency ~ 0.1%; modulation bandwidth of ~ 10 MHz; and stability without degradation for several weeks of continuous operation.

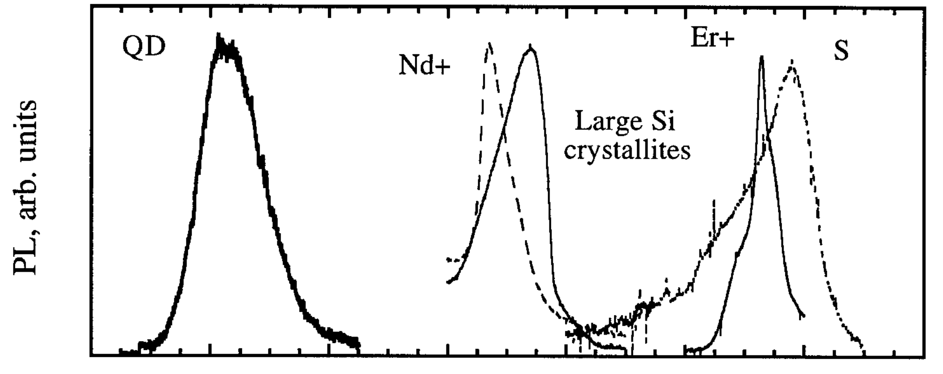

Figure 1
Photoluminescence from various porous silicon samples prepared and/or processed in different ways. From short to long wavelengths, the luminescence is due to recombination of carriers confined to quantum dots, within the Nd ion energy levels, of carriers confined to large (~100 nm) crystallites, within the Er ion energy levels, and involving the S energy levels.

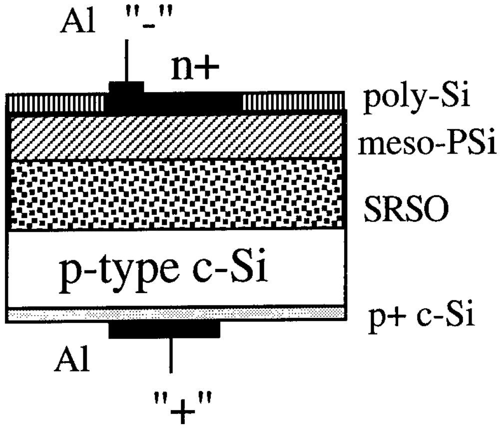

Figure 2
After anodization in an HF/ethanol solution, the top p+ region is transformed into a mesoporous buffer layer, and a ~1 μm thick layer of the p-type Si substrate into the light emitting nanoporous silicon region. After annealing in dilute oxygen at ~850°C, the porous silicon is transformed into SRSO. The top contact is made of Al and a 0.3 μm, n+ polysilicon film deposited by LPCVD at 610°C, and annealed at 950°C. The back contact is made of Al.

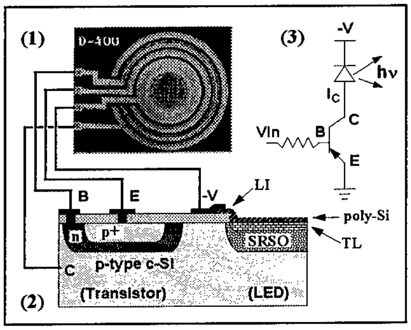

Figure 3
Micrograph of an integrated LED-bipolar transistor structure (1) along with the cross section (2), and equivalent circuit (3). The LED is in the center of the structure, and has a 400 μm diameter active light-emitting area. The surrounding bipolar transistor is identified by the concentric emitter (E), base (B) and collector (C) terminals. The right half of the cross section shows the multilayer structure of the LED, including the polysilicon local interconnect (LI) and cathode, the transition layer (TL) and the SRSO layer.

A significant milestone for silicon-based optoelectronics, namely the integration of SRSO-based LEDs into a microelectronic circuit, has now been reached [7]. We have designed and fabricated an integrated SRSO-based LED with a surrounding bipolar driver transistor, as shown in Figure 3. To accommodate bipolar transistor fabrication, isolated SRSO-based LED fabrication, and formation of the transistor-LED local interconnects, the standard bipolar process was modified to include five additional lithography levels and several processing steps. The driver transistor is connected in a common-emitter configuration and modulates light emission by amplifying a small base input signal and controlling current flow through the LED. Fig. 3 shows a micrograph of an integrated structure along with its cross section and equivalent circuit. The circular design is area-efficient and scalable, provides effective electrical isolation and demonstrates a truly integrated structure. Various sized structures were fabricated, with the active area ranging from 0.005 to 2 mm^2.

The performance of both the LED and the bipolar device is consistent with the performance of the individual devices. For example, the LED I-V characteristic demonstrates efficient carrier injection under forward bias, with a rectifying ratio of ~ 10^5 under light-emitting conditions. Applying a current density of ~ $100A/cm^2$ (total dissipated power of ~ $1KW/cm^2$) for several minutes of continuous operation was nondestructive which indicates effective heat dissipation in the improved device structures. Figure 4 shows that the LED electroluminescence response in both DC and pulsed modes of operation is identical, which confirms that the light is not due to a thermal emission process. The inset shows the electroluminescence spectrum at different levels of applied current. This is quite different from the spectra produced from a reverse-biased p-n junction [8] where the electroluminescence spans the entire visible range. The integrated structures also demonstrated functionality as driver/LED pairs. The drivers were able to amplify low-level base input signals to current pulses of ~ 100-200mA, and modulate the LEDs.

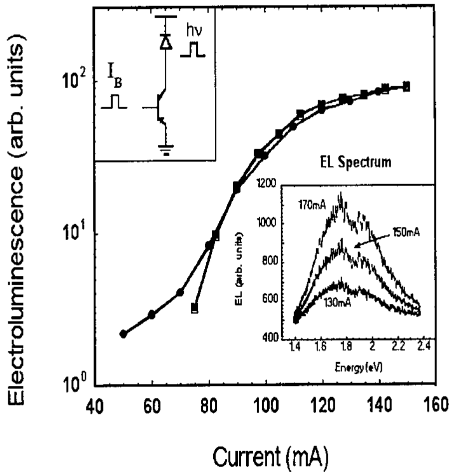

Figure 4
Electroluminescence of the LED as a function of the drive current in both the DC mode (circles) and pulsed mode (squares) of operation. The inset shows that the peak position (near 1.8 eV) and shape of the electroluminescence spectrum are independent of the applied current.

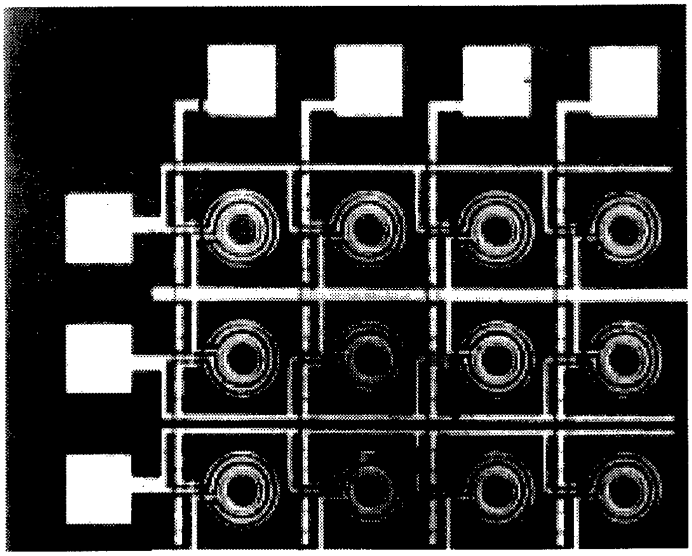

Figure 5
Micrograph of an addressable LED array utilizing the integrated driver transistors. In the array, each device is the same as the structure shown in fig. 3, except that the LEDs are smaller (active area of 0.005 mm^2), and placed at a pitch of 0.35 mm. An individual LED is addressed by the unique intersection of row (emitter) and column (base) select lines.

The improvements made in the active SRSO light-emitting material and the LED device design are renewing the prospect for commercial Si electroluminescent devices. Further improvements in efficiency and power dissipation are necessary for display applications, while increased modulation speed is critical for high speed optical interconnects. In addition, the device structures must be integrated with other optoelectronic components. The development of silicon-based integrated optoelectronic components will enable the incorporation of such structures into advanced systems, including arrays. Figure 5 shows a small addressable LED array utilizing the integrated local drivers. This array could be fabricated at much smaller dimensions and coupled with peripheral control circuitry.

This work was supported by the US Army Research Office.

REFERENCES

1. S.S. Iyer & Y.-H. Xie, *Science* **260**, 40 (1993)
2. Z.H. Lu, D.J. Lockwood, & J.-M. Baribeau, *Nature* **378**, 258 (1996)
3. L.T. Canham, *Appl. Phys. Lett.* **57**, 1046 (1990)
4. P.M. Fauchet, in *Light Emission from Silicon*, ed. D.J. Lockwood, *Semiconductors and Semimetals* (Academic Press, 1997)
5. L. Tsybeskov *et al*, *Appl. Phys. Lett.* **68**, 2058 (1996)
6. L. Tsybeskov *et al*, in *Advanced Luminescent Materials*, eds D.J. Lockwood, P.M. Fauchet, N. Koshida, & S.R.J. Brueck, (The Electrochemical Society, Pennington, NJ, 1996). p 34
7. K.D. Hirschman *et al*, to appear in *Nature* (1996)
8. G. Deboy & J. Kolzer, *Semicond. Sci. Technol.* **9**, 1017 (1994)

Optimization of Photorefractive Polymers for Optical Processing

K. Meerholz
Physical Chemistry Dept., Univ. of Munich
Sophienstr. 11, 80333 Munich, GERMANY

Photorefractive materials have many potential photonic applications, including dynamic holographic storage and image processing. Recently, the new class of amorphous organic photorefractive materials has emerged, offering wide structural flexibility, easy processability, and low cost at very high performance levels. Progress in this field has led to absorption-limited complete diffraction for the readout of a hologram stored in materials of only 100-150 μm thickness and to extremely large net gain coefficients of more than 200 cm^{-1} compared to 40-50 cm^{-1} in the best inorganic photorefractive crystals known to date. These excellent properties occur in materials with low glass transition temperatures and result from refractive index modulations as large as $\Delta n \approx 10^{-2}$, mostly originating from a Kerr-type orientational birefringence rather than the electro-optic effect as in traditional photorefractive crystals. The materials can be adjusted for photorefractivity over the entire visible spectrum and in the near infrared. The sensitivity is excellent enabling the use of low-power laser sources, such as HeNe laser or laser diodes.

In this presentation, the photorefractive effect in amorphous organic photorefractive materials will be reviewed with emphasis on poly(N-vinylcarbazole)-based composites which have shown the best performance up to date. The influence of the materials' chemical composition (e.g. by using different electro-optic chromophores, photoconductors, or photosensitizers) and the glass transition temperature on the performance of these composites will be addressed.

Proof-of-principle experiments demonstrating the excellent properties of the high-performance PR polymers as the holographic storage medium for real-time interferometry applications and optical correlation will be presented.

Fabrication and Characterization of Si Dots Prepared by Self-Organized Recrystallization

L. Tsybeskov, K. D. Hirschman[a)], S. P. Duttagupta, D. G. Hall[b)]
and P. M. Fauchet[a, b, c)]

Department of Electrical Engineering, University of Rochester, Rochester NY 14627

[a)] also Department of Microelectronic Engineering, Rochester Institute of Technology, Rochester NY 14623

[b)] The Institute of Optics, University of Rochester, Rochester NY 14627

[c)] also Laboratory for Laser Energetics, Department of Physics & Astronomy, and The Institute of Optics, University of Rochester, Rochester NY 14627

The photoluminescence (PL) in crystalline silicon (c-Si) has been investigated during the last decades. Interest has focused on the visible PL that is observed in Si nanoclusters and in porous Si (PSi), the infrared PL in silicon-germanium superlattices, and the subgap PL due to impurities in c-Si [1]. Whereas strong room-temperature PL has been demonstrated in the visible with porous silicon, band edge PL in bulk Si is inefficient and usually observed only at low temperatures. The electroluminescence (EL) is as inefficient as the PL, and, in addition, the EL is quenched by an electric field $E \geq 10^4$ V/cm due to field-induced dissociation of the exciton [2]. A result of the indirect bandgap of Si, bandgap luminescence is extremely weakly reabsorbed by Si. It follows that the light generated, propagated, and detected at the Si bandgap would not disturb the Si microelectronic circuitry with which it shares a chip, a situation that is very desirable for systems applications.

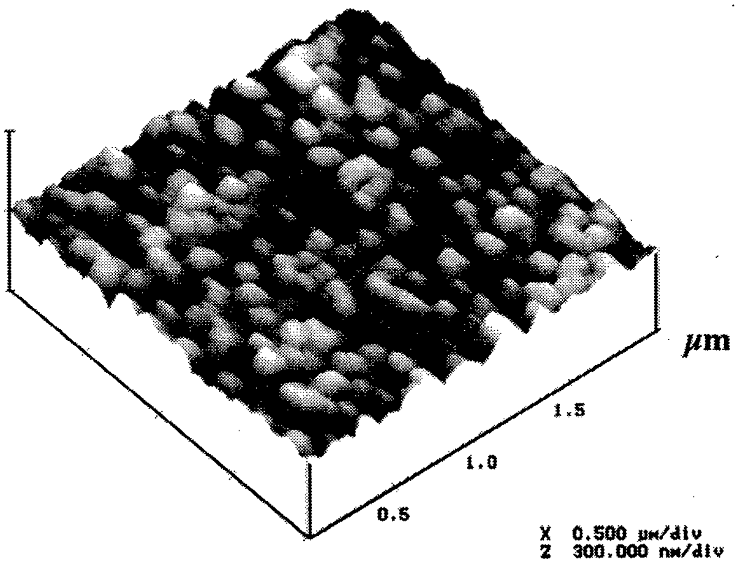

Figure 1. AFM image of HF-etched surface of recrystallized mesoporous Si.

In this presentation, we demonstrate how to achieve strong room temperature 1.1 μm photoluminescence and electroluminescence from *large* Si dots prepared by various techniques. Although most of the work on Si and other semiconductors has focused on *nm-size* quantum dots, nanocrystals or clusters [3], we will show that larger dots exhibit interesting, unexpected, and useful optical properties.

The first approach consists of recrystallizing mesoporous Si [4]. The details and the optimization of the entire procedure are outlined in Ref. 4 and will be discussed in the presentation. As shown in Figure 1, the resulting material is composed of a dense packing of Si crystallites with an average size of 100 nm, embedded in an oxide matrix. We model it as a composite material made of Si and SiO, in which the band gap varies from 1.1 eV (bulk Si) to several eV (SiO_{2-X}), with giant contravariant fluctuations due to different chemical compositions. These fluctuations produce spatial confinement, but not quantum confinement, of the injected electrons and holes. The observed weak PL (and EL) temperature dependence and the exponential PL reduction in the presence of an external electric field E (by a factor of 10 for $E \leq 10^6$ V/cm) are consistent with spatial confinement. Low-temperature luminescence spectra show all the expected phonon replica, as expected from bandedge radiative recombination in large extra-pure silicon clusters (Figure 2). LEDs were made using this material as the active medium. The voltage threshold for EL is ≥ 1 V (close to the c-Si bandgap) corresponding to a current density of less than 10 mA/cm^2. The EL is observed under forward bias, when charge injection is efficient, but for several samples with a strong leakage current, the EL at ~ 1.1 eV is also observed under a large reverse bias > 10 V. The EL intensity is slightly superlinear with respect to current and no saturation is observed over more than two orders of magnitude (Figure 3), indicating the rugedness of the device and the relative lack of importance of Auger recombination. When a bias of several volts was applied, the electric field within the active layer is close to 10^5 V/cm. At this value of the field, the optical bandgap of c-Si decreases by ~ 10 meV due to the Franz-Keldysh effect, in agreement with the observed red EL shift.

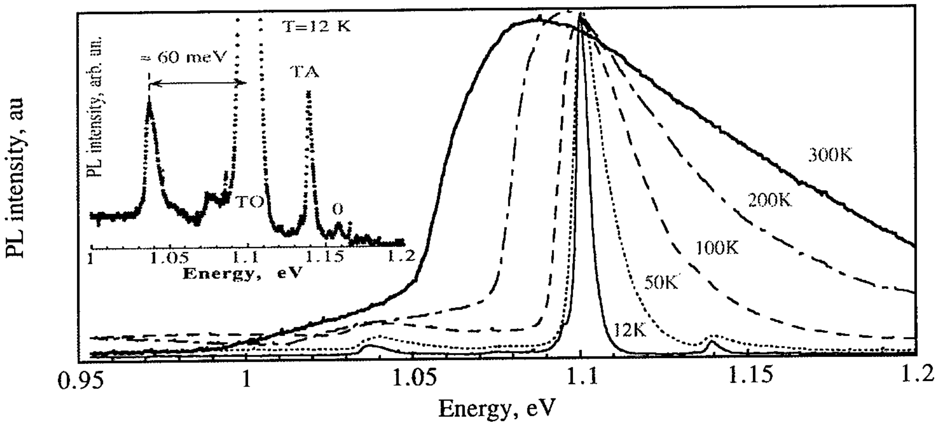

Figure 2. The PL spectra in recrystallized mesoporous Si measured at different temperatures. The inset shows the fine PL structure with typical phonon lines: NP at 1.158 eV, TA phonon at 1.14 eV, and TO line with a replica at ~ 1.04 eV.

The second approach consists of fabricating somewhat smaller Si dots by low-pressure (LP) and plasma-enhanced (PE) chemical vapor deposition (CVD) of multilayer structures consisting of amorphous Si (a-Si) layers less than 10 nm-thick sandwiched between SiO_2 layers followed by high-temperature recrystallization. The recrystallization has been performed in two steps: rapid thermal pulse annealing (nucleation) and conventional furnace annealing (complete crystallization), and has been monitored by various techniques, including Raman scattering. The recrystallized a-Si single layer is made of nearly spherical, densely packed Si clusters with a diameter equal to thickness of deposited a-Si layer. The room temperature PL quantum efficiency of these structures is approaching 0.1%. The PL spectra of samples with initial thicknesses of a-Si less than 5 nm indicate a small blue shift associated with a small amount of quantum confinement (Figure 4). A quantitative comparison between PL peak energy and crystallite size must await the determination of the effect of strain.

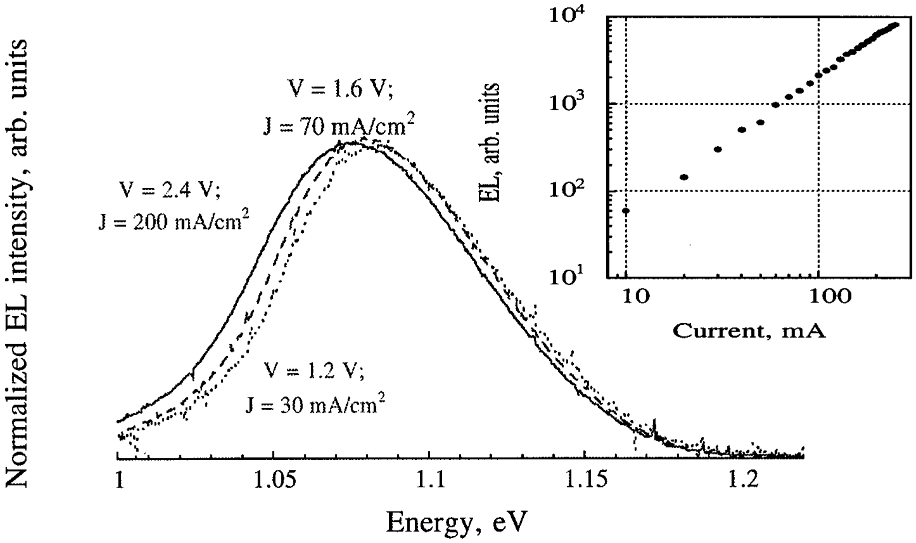

Figure 3. Room temperature EL spectra at different driving conditions. The inset shows EL intensity as function of current.

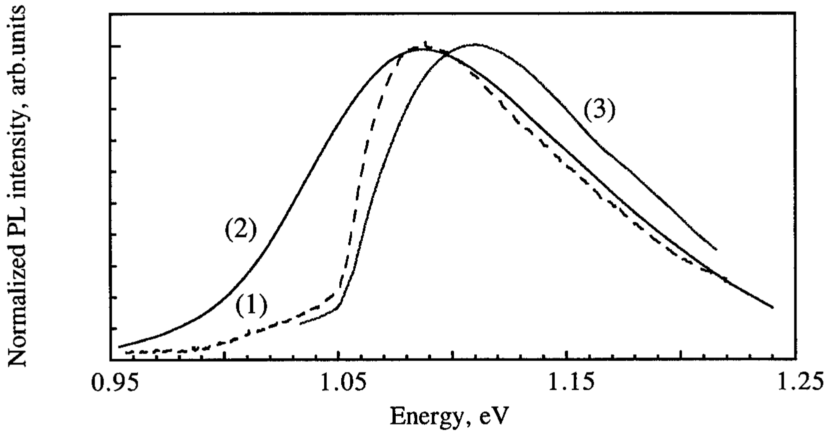

Figure 4. Room temperature PL spectra of recrystallized mesoporous Si (1) and a-Si layers with initial thicknesses 10 nm (2) and 4 nm (3).

This research was supported in part by the Army Research Office and the Air Force Office of Scientific Research.

REFERENCES

1. L. T. Canham, MRS Bulletin, **XVIII**, 22 (1993)
2. G. Davis, Physics Reports, **176**, 84 (1989)
3. A.P. Alivisatos, Science, **271**, 933 (1996)
4. L. Tsybeskov *et al.*, Phys. Rev. **B 54**, R8361 (1996)
5. L. Tsybeskov *et al*, Appl. Phys. Lett., in press (1996)

Quantum Optoelectronic Physics

QFD 3:30pm – 5:00pm
Salon A

Wayne H. Knox, *Presider*
Lucent Technologies–Bell Laboratories

Trends in Quantum Optoelectronics: Quantum Confinement and Beyond

Daniel Chemla
Department of Physics, University of California at Berkeley, and
Materials Sciences Division, Lawrence Berkeley National Laboratory

Looking beyond the capabilities of the current generation of quantum confined heterostructures, we discuss potential approaches for molecular level design, synthesis, processing and interconnection of new functional materials and structures.

Exciton Dynamics, Laser Action, and Cooperative Emission in Conducting Polymer Thin Films

Z.V. Vardeny
University of Utah

Picosecond dynamics of exciton emission and absorption have been studied in neat thin films of a variety of poly (phenylene-vinylene) derivatives. We found that the stimulated emission band of 120 nm width and ~1 ns duration, which is observed at low exciton density, n, collapses at $n > 10^{17}$ cm^{-3} into a much narrower band of 7 nm width and lifetime $\tau \ll 10$ ps. Based on its excitation intensity dependence, polarization, lifetime, illuminated area, and film thickness dependencies, we assign this narrow band to superfluorescence rather than to amplified spontaneous emission.

Size Reduction of Microdisk Injection Lasers for Spontaneous Emission Control

T. Baba, M. Kihara and R. Watanabe

Yokohama National University, Div. of Electr. & Comput. Eng.
79-5 Tokiwadai, Hodogayaku, Yokohama 240, Japan
Phone +81-45-335-1451, Fax +81-45-338-1157, E-Mail baba@dnj.ynu.ac.jp

Spontaneous emission control$^{1)}$ is of great interest since it provides novel high performance in laser diodes, e.g., thresholdless operation and high speed modulation without relaxation oscillation. It is realized in a microcavity whose volume V satisfies single mode condition $V \leqq \lambda^4/(4\pi n^3 \Delta\lambda)$, where n is the effective refractive index of cavity and $\Delta\lambda$ is the spectral width of atomic radiation. It is easier in microdisk lasers$^{2)}$ than in VCSELs to realize this condition since vertical cavity size of microdisk lasers is easily reduced by the strong optical confinement into thin disk layer. In this study, we demonstrate injection devices of 3 – 10 µm in diameter and 0.2 µm in disk thickness, which are close to the single mode condition. We compare the diameter dependence of lasing characteristics between experiment and theory, and discuss the potential of this kind of device for spontaneous emission control.

In the experiment, we prepared GaInAsP/InP compressive-strained MQW wafer having SCH layer of 0.2 µm in total thickness and peak emission wavelength of 1.55 µm. After metalization, we formed circular mesas of 4 µm in height using methane-based reactive ion beam etching technique. Finally we formed the disk shape by selective wet chemical etching of InP claddings using HCl solution. Fig. 1 shows SEM photograph of 3-µm-diameter device as well as schematic device structure. The current was flowed from a tungsten probe directly touching the top metal. The disk width was controlled to less than 1 µm to accelerate carrier diffusion to the edge of the disk. The light output that might be obtained by the scattering of whispering gallery modes at the unperfected disk surface and edge was detected by a sharpened single mode fiber and analyzed by an optical spectrum analyzer. Fig. 2 shows lasing characteristic of device shown in Fig. 1. Threshold current at room temperature under pulsed condition was 0.9 mA. Above threshold, linewidth of lasing spectrum was 0.1 nm, the resolution limit of the measurement. CW operation was not obtained mainly due to large series resistance of 3 – 6 kΩ.

Theoretical threshold current was plotted with experimental data, as shown in Fig. 3. In this calculation, we took the following 8 properties of microdisk lasers into account: i) large optical confinement factor into MQW, ii) no absorption loss in the air cladding of microdisk, iii) scattering loss at disk surfaces and edges of nearly 50 cm^{-1} (evaluated from an AFM measurement of disk roughness and perturbation analysis), iv) diffraction loss approximated by[3] $k_0 n \exp\left[-2k_0 nr\left(\tanh^{-1}\sqrt{1-n^{-2}}-\sqrt{1-n^{-2}}\right)\right]$, where k_0 is the wave number and r is the disk radius, v) surface recombination at disk surfaces with velocity v_S, vi) current passing through the center region, which does not contribute to laser oscillation, vii) exponential decay of carrier concentration toward disk edge, and viii) long spontaneous emission lifetime due to small effective index n of nearly 2.6. We noticed in this calculation that threshold current is sensitive to the change of surface recombination velocity v_S. As seen in Fig. 3, experimental data almost fit to theoretical curve of $v_S=4\times10^4$cm/s, which is typical for quaternary material system. Low threshold of 40 μA is expected for disk diameter of 2 μm if the surface recombination is suppressed to negligible order.

Cavity modes of microdisk lasers were calculated by a simple 2D model, in which a circular region having guided-wave effective index of microdisk is surrounded by an outer region having index of 1. The effective volume of whispering gallery mode in the 3-μm-diameter device was estimated to be 0.8 μm^3. This value seems to be the smallest among those of various types of microcavity injection lasers ever reported. Fig. 4 shows spontaneous emission spectra under cw condition and arrows indicate calculated resonant wavelengths for mode number Ms. It is seen that many peaks observed in the spectra well coincide with calculated resonant wavelengths, and that the number of peaks simply decreases as the disk diameter decreases. The spectral width of the observed spectra was as wide as 200 nm. This seems to be caused by the heating under cw condition. If the spectral width is reduced to less than 100 nm, which is typical for quaternary lasers, the number of modes in the spectra will be limited to 4 – 5. Reduction of disk diameter to less than 1.5 μm almost satisfies the single mode condition of spontaneous emission except for a small amount of free mode radiation in the vertical direction. This results in the spontaneous emission factor[4] for single polarization of 0.5 or larger due to the polarization anisotropy of emission from the compressive-strained MQW used in the experiment.

In summary, we demonstrated the smallest microdisk injection laser operated with threshold current lower than 1 mA. Further reduction of disk diameter to half of the demonstrated device will achieve large spontaneous emission factor close to 1. It will be realized by some improvement of the etching process. CW lasing and suppression of surface recombination at disk surfaces are key issues to clearly evaluate this factor and expected effects of spontaneous emission control.

References

1) Y. Yamamoto, S. Machida, et.al., *Coherence, Amplification, and Quantum Effects in Semiconductor Lasers* (Ed. by Y. Yamamoto), Wiley Interscience (1991) 561

2) A. F. J. Levi, R. E. Slusher, S. L. McCall, et.al., *Electron. Lett.* **28** (1992) 1010.

3) S. L. McCall, A. F. J. Levi, R. E. Slusher, et.al., *Appl. Phys. Lett.* **60** (1992) 289.

4) T. Baba, T. Hamano, F. Koyama and K. Iga, *IEEE J. Quantum Electron.* **27** (1991) 1347.

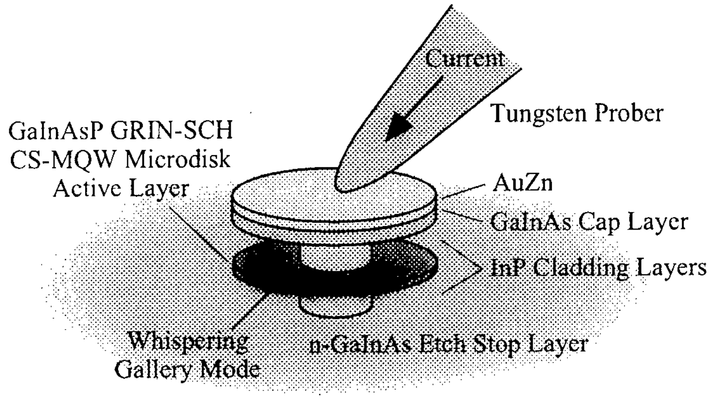

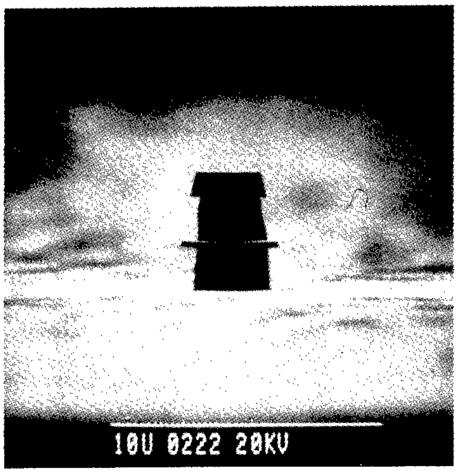

Fig. 1 Schematic structure microdisk laser and SEM photograph of fabricated 3-μm-diameter device.

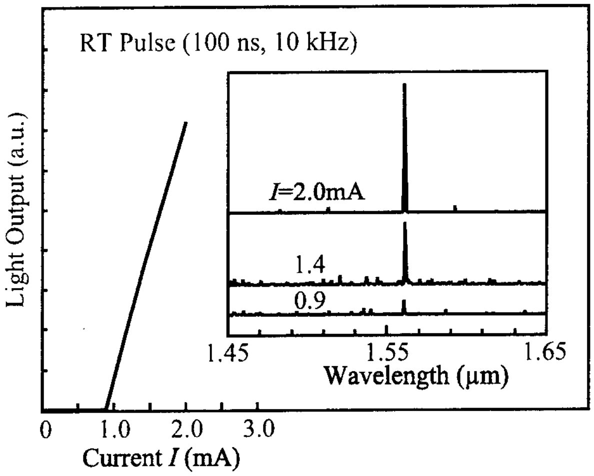

Fig. 2 Measured light output versus injection current characteristics of 3-μm-diameter device

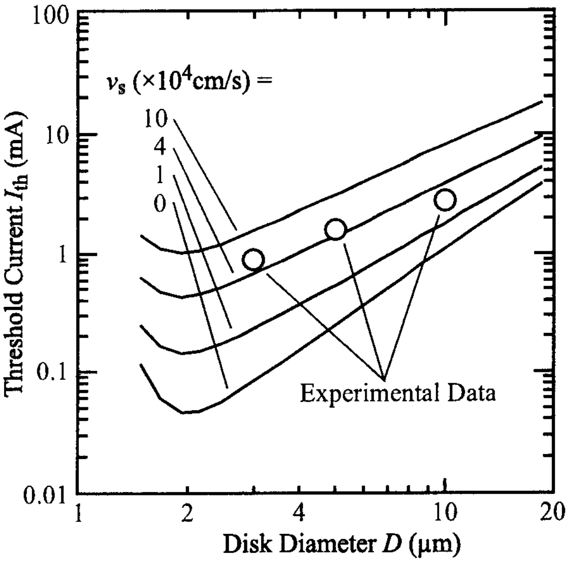

Fig. 3 Theoretical and experimental dependence of threshold current on microdisk diameter.

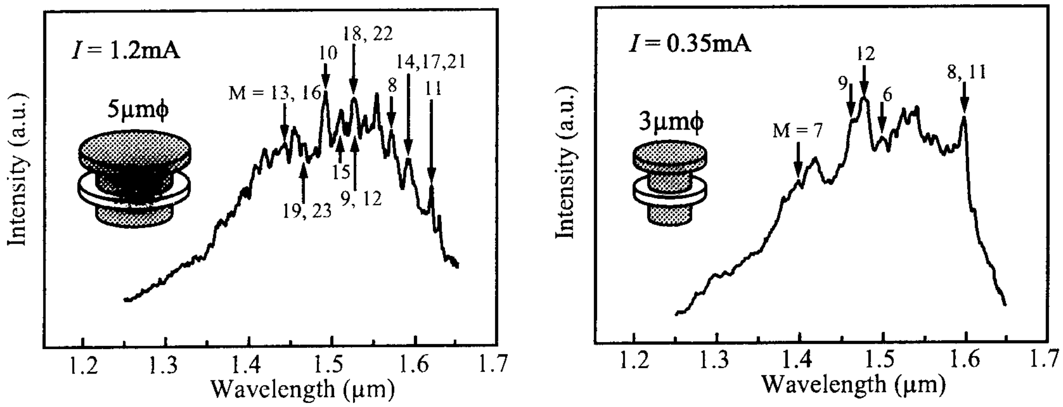

Fig. 4 Spontaneous emission spectra observed under cw condition.

Novel configurations for optical parametric oscillators without any cavity

Yujie J. Ding[a)], Jacob B. Khurgin[b)], and Seung-Joon Lee[b)]
[(a)]Department of Physics and Astronomy; Centers for Materials and Photochemical Sciences
Bowling Green State University, Bowling Green, OH 43403.
[b)]Department of Electrical and Computer Engineering
The Johns Hopkins University, Baltimore, MD 21218.
Tel. (419) 372-8785 Fax (419) 372-9938

Forward optical parametric oscillators (OPO's) based on quasi-phase matching (QPM) were implemented in $LiNbO_3$ [1]. However, a forward OPO requires a cavity to establish oscillation. Harris [2] introduced the concept of a backward OPO (BOPO) based on conventional phase matching: a cavity is not required to establish oscillation. However, in Ref. [2], only a threshold condition was obtained. Here, we present our results on BOPO's [3] and transversely-pumped counter-propagating OPO's (TPCOPO's) [4]. A TPCOPO does not require a cavity to establish oscillation either. Second-order susceptibility of a nonlinear medium is spatially modulated with a period the pump wavelength in the medium to achieve QPM. A pump wave at the wavelength in vacuum λ_3 propagates along a waveguide for a BOPO or onto the surface for a TPCOPO. Two counter-propagating waves at the wavelengths λ_1 and λ_2 can be generated in the nonlinear medium. To tune the output frequencies of the signal and idler, we can change the incident angle of the pump wave in the TPCOPO or BOPO. The gain for the signal or idler is effectively balanced by the loss of the signal or idler at the respective exit plane to reach a steady-state oscillation. Because a cavity is eliminated, a BOPO or TPCOPO is more stable while a forward OPO is sensitive to the slight mirror translation. For a TPCOPO [4], there is an optimal pump power $\approx 3.4\,P_{th}$ (where P_{th} is the threshold pump power) at which η reaches the maximum value of 44%. If $P_3 \gg P_{th}$, there is a huge build-up of the oscillating fields inside the medium. The efficient sum-frequency generation saturates the TPCOPO. Consider $GaAs/Al_{0.8}Ga_{0.2}As$ multilayers [5] with the optimized structure dimensions: if $\lambda_3 \approx 0.9\,\mu m$, $P_{th} \approx 7.3\,kW$ and tuning range: 1.4–2.6 μm (or 3.1-5.8 μm if $\lambda_3 \approx 2\,\mu m$). Consider ZnSe/ZnS multilayers: if $\lambda_3 \approx 0.49\,\mu m$, $P_{th} \approx 0.92\,kW$ and the tuning range: 0.7–1.7 μm. Consider GaAs/AlAs asymmetric coupled quantum-well domain structure [6]: if $\lambda_3 \approx 10\,\mu m$, $P_{th} \approx 10\,W$ and the tuning range: 15–29 μm. Consider a nondegenerate BOPO: $|k_1 - k_2| \gg 1/L$, where $k_{1,2}$ are the corresponding wave vectors and L is the length of the medium. If $P_3 \approx 1.1\,P_{th}$, the conversion efficiency for the BOPO is $\eta \approx 20\%$. When $P_3 \approx 3.4\,P_{th}$, $\eta \approx 44\%$ for the TPCOPO and $\eta \approx 95\%$ for the BOPO. Consider a degenerate BOPO: $\lambda_1 = \lambda_2$. A mirror for the pump wave with the reflectivity $R_{2\omega}$ is attached to the right facet to increase the conversion efficiencies. However, it is not required for the oscillation to occur. When the pump intensity is $I_p \approx 4\,I'_{th} \approx I_{th}/4$, where I_{th} and I'_{th} are the thresholds for a nearly-degenerate and degenerate BOPO, $\eta \approx 99.7\%$ if $R_{2\omega} = 99\%$. Therefore, compared with the nondegenerate BOPO, the degenerate BOPO offers higher conversion efficiencies. The decrease of the conversion efficiency as I_p ($> 4\,I'_{th}$) increases is due to generation of a backward wave at the pump wavelength, which propagates along the direction opposite to that of the pump wave. Consider a poled $LiNbO_3$ [1]. If the spatial period of the domains is $\Lambda \approx 4\,\mu m$, $\lambda_3 \approx 1.1\,\mu m$, $\lambda_{1,2} \approx 2.2\,\mu m$, and $L \approx 2.6\,cm$, the threshold pump intensity for the degenerate BOPO is $I'_{th} \approx 2.9 \times 10^8\,W/cm^2$. For a QPM KTP [7]: $\Lambda \approx 0.7\,\mu m$, $\lambda_3 \approx 1.3\,\mu m$, $\lambda_{1,2} \approx 2.6\,\mu m$, and $L \approx 3\,cm$, $I'_{th} \approx 2.8 \times 10^6\,W/cm^2$. In the presence of a cavity for the signal and idler, the thresholds can be reduced by several orders of magnitude. Both the BOPO and TPCOPO can be also implemented in nonlinear optical polymers. Our parametric processes can be used to achieve large amplifications and difference-frequency generation [8].

This work is supported by AFOSR and NSF.

[1] M. L. Bortz, M. A. Arbore, and M. M. Fejer, Opt. Lett. 20, 49 (1995).

[2] S. E. Harris, Appl. Phys. Lett. 9, 114 (1966).

[3] Y. J. Ding and J. B. Khurgin, IEEE J. Quantum Electron. 32, 1574 (1996); J. Nonl. Opt. Phys. Mat. 5, 223 (1996).

[4] Y. J. Ding, S. J. Lee, and J. B. Khurgin, Phys. Rev. Lett. 75, 429 (1995); IEEE J. Quant. Electr. 31, 1648 (1995).

[5] R. Normandin *et al*., Electr. Lett. 26, 2088 (1990).

[6] J. B. Khurgin, Phys. Rev. B38, 4056 (1988); S. Janz *et al*., Opt. Lett. 19, 622 (1994).

[7] W. P. Risk, S. D. Lau, and M. A. McCord, IEEE Photon. Tech. Lett. 6, 406 (1994).

[8] Y. J. Ding and J. B. Khurgin, submitted to J. Opt. Soc. Am. B.

Quantum Optoelectronics
Technical Program Committee

Wayne Knox, *Bell Laboratories, Lucent Technologies, General Co-Chair*
Jurgen Kuhl, *Max-Planck Institut, Stuttgart, Germany, General Co-Chair*
Kohroh Kobayashi, *NEC Corporation, Japan, General Co-Chair*
Philippe Fauchet, *University of Rochester, Program Co-Chair*
Shigehisa Arai, *Tokyo Institute of Technology, Japan*
Yasuhiko Arakawa, *University of Tokyo, Japan*
Israel Bar-Joseph, *Weizmann Institute of Science, Israel*
Moungi Bawendi, *Massachusetts Institute of Technology*
David Citrin, *Washington State University*
Jochen Feldmann, *Ludwig-Maximilians Universitat, Munich, Germany*
Steve Forrest, *Princeton University*
Manuel Joffre, *ENSTA-Ecole Polytechnique, France*
Jacob Khurgin, *Johns Hopkins University*
Jerry Meyer, *U.S. Naval Research Laboratory*
John Ryan, *Oxford University, U.K.*
Arthur Smirl, *University of Iowa*
Toshihide Takagahara, *NTT Basic Research Laboratories, Japan*